An investigation of variability and its associated synchrotron emission in relativistic AGN jets using numerical hydrodynamic simulations

Izak Petrus van der Westhuizen

Submitted in fulfillment of the requirements for the degree

Magister Scientiae

in the Faculty of Natural and Agricultural Sciences,

Department of Physics,

University of the Free State,

South Africa

March 2017

Supervised by: Dr. Brian van Soelen

Co-supervised by: Prof. Petrus Johannes Meintjes

The financial assistance of the National Research Foundation (NRF) towards this research is hereby acknowledged. Opinions expressed and conclusions arrived at, are those of the author and are not necessarily to be attributed to the NRF.

Abstract

Active regions at the centres of certain galaxies known as Active Galactic Nuclei (AGN) are some of the most energetic and violent sources of emission in the universe. Certain types of AGN can produce jet-like emission structures that extend hundreds of kiloparsec in length. The jet-like sources show intricate time dependent structure and are believed to consist of collimated flows of relativistic plasma. Many studies have focused on investigating the structure and emission of these sources. The evolution time scale of the jets are much longer than their recorded history which makes observational studies of their evolution challenging and, due to the relativistic nature of these jets, they have not been accurately reproduced in laboratory experiments. Instead many studies have employed fluid dynamic numerical simulations of these sources to study their properties. To accurately compare a fluid dynamic simulation to that of observational data the emission emitted by such an environment must be modelled. In this study a fluid dynamic simulations of a relativistic jet is constructed and a synchrotron emission model is applied to the simulations to reproduce intensity maps at radio frequencies which is comparable to observational data of AGN jet sources. The numerical fluid dynamic simulation was created and evolved using the PLUTO software and consisted of a three dimensional environment containing ambient medium, into which a jet is injected through a nozzle on the lower z boundary. The injected material consisted of a less dense medium with a super-sonic bulk motion of Lorentz factor $\Gamma = 10$. The simulation reproduced a jet structure containing a relativistic beam of material propagating through the ambient medium. The beam of material was surrounded by a turbulent cocoon region with asymmetric structure. The entire structure was encased in a bow shock. Intensity maps of the three dimensional fluid simulation were created by applying a post-processing code to the simulation data. The emission model estimated the synchrotron emission by assuming that the entire population of electrons in the jet had a power-law energy distribution. The intensity maps were able to reproduce emission structures that resemble those of FR II type radio galaxies with a dominant cocoon region containing time dependent hot spots and filaments. To investigate the effects of Doppler boosting, intensity maps were calculated at different polar angles and the results were consistent with the current unified model of AGN and showed a significant increase in the intensity of the relativistic beam at small polar angels. The intensity maps were able to reproduce time dependent emission structures due to fluid dynamic instabilities that formed during the simulation. The time dependent structure led to the production of variability with an amplitude of $\approx 10\%$ in the total intensity. It was therefore shown that some variability observed within these sources occurs due to fluid dynamic instabilities rather than a change in the injection parameters. However, large flares which have been observed from these sources require additional perturbations in the flow. This study serves as a good basis for future in depth investigation of AGN emission.

Keywords: Active Galactic Nuclei, Relativistic hydrodynamics, Synchrotron emission, PLUTO, Numerical simulation, Radio jets

Opsomming

Die aktiewe gedeeltes in die middel van sommige sterrestelsels wat bekend staan as Aktiewe Galaktiese Kerne (AGK) is van die mees geweldadigste en energieke stralingsbronne in die heelal. Sekere AGK tipes produseer spuitstraal-agtige strukture wat oor honderde kiloparseks kan uitstrek. Die spuitstraalbronne toon ingewikkelde tyd afhanklike strukture en daar word vermoed dat hierdie bronne uit gekollimeerde vloeie van relativistiese plasma bestaan. Baie studies het al die struktuur en straling van hierdie bronne bestudeer om hulle aard beter te verstaan. Die leeftyd van hierdie spuitstrale strek egter oor 'n baie langer tydperk as hulle opgetekende geskiedenis wat waarnemingstudies van die evolusie van die bronne uitdagend maak en, vanweë hulle relativisties natuur, kon hulle tot dus ver nie gereproduseer word in laboratorium eksperimente nie. As gevolg hiervan het baie studies van die bronne na fluïeddinamiese rekenaar simulasies gedraai om hulle eienskappe beter te bestudeer. Om die simulasies op 'n akurate wyse met waarnemings te kan vergelyk moet die straling wat hierdie omgewings produseer gemoduleer word. In hierdie studie word daar 'n fluïeddinamiese simulasie van 'n relativistiese spuitstraal geskep en 'n stralings model word daarop toegepas om intensiteitskaarte wat vergelyk kan word met waargenome data in radio golflengtes te produseer. Die fluïeddinamiese simulasie het bestaan uit 'n drie dimensionele ruimte wat 'n agtergrond medium in rus bevat het. 'n Relativistiese spuitstraal medium was in die ruimte ingespuit deur 'n spuitstuk op die onderste z-grens. Die simulasie was geskep en ontwikkel met tyd deur gebruik te maak van die PLUTO rekenaar sagteware. Die ingespuitde materiaal het bestaan uit 'n supersoniese medium wat minder dig as die agtergrond medium was met 'n Lorentz faktor van $\Gamma = 10$. Die simulasie het 'n spuitstraal geproduseer met 'n relativistiese gekolimeerde straal wat omring was deur 'n asemetriese, turbulente koekon. 'n Boogskok het gevorm om die hele struktuur en het die spuitstraal van die agtergrond medium geskei. Die intensiteitskaarte was uitgewerk deur 'n na-proseseerings program op die simulasie data toe te pas. Die stralings model in na-proseseerings program het 'n beraming van die sinchrotronstraling uitgewerk onder die aname dat die populasie van elektrone in die spuitstaal 'n magswet verspreiding van energie besit. Die intensiteitskaarte wat uitgewerk was het sootgelyke struktuur getoon aan FR II tipe radio sterrestelsels met 'n dominate koekon wat tydsafhanklike variasies bevat het. Om die effek van relativistiese groepssnelheid op die gemeete straaling te bestudeer was intensiteitskaarte teen verskillende poolhoeke bepaal. Die resultate

het ooreengetem met die huidige verenigde model van AGK's wat 'n merkbare toemane in intensiteit voorspel by laë poolhoeke. Die intensiteits kaarte kon van die tydsafhankilke strukture wat wwargeneem is in AGN bronne herproduseer. Hierdie variasies het ontstaan as gevolg van fluïeddinamiese onstabiliteite in die omgewing en het amplitudes van $\approx 10\%$ van die totale intensiteit geproduseer. Daar word dus in hierdie studie gewys dat sekere van die variasies in die straling wat gemeet word vanaf AGN bronne afkomstig is van fluïeddinamiese onstabiliteite in die spuitstraal eerder as perturbasies in the inspuitings tempo van die medium. Die model verduidelik egter nie die groot skaalse uitbarsting wat waargeneem word in hierdie bronne nie. Die studie vorm 'n goeie basis waarop toekomstige in-diepte studies gebaseer kan word.

Acknowledgements

I hereby wish to acknowledge the following parties for their contributions towards this study.

- My supervisor and co-supervisor, Dr. B. van Soelen and Prof. P.J. Meintjes, for the knowledge, wisdom and guidance that they have imparted to me during my time of study as well as all of the opportunities which they have granted me to do this research.
- S.J.P.K. Riekert and A. van Eck at the UFS HPC for their technical support.
- My family for their love and support throughout all of my endeavours. Without them my studies would not be possible.
- A special word of gratitude to M. van Zyl, L. de ridder, Q. van Dyk, E. Botma and L. Klindt for their friendship and motivation.
- Finally, the financial assistance of the National Research Foundation (NRF) towards this research is hereby acknowledged. Opinions expressed and conclusions arrived at, are those of the author and are not necessarily to be attributed to the NRF.

Contents

List of Acronyms

AGN	Active Galactic Nuclei
AMR	Adaptive Mesh Refinement
AUSM	Advective Upstream Splitting Method
BC	Boundary Conditions
BLR	Broad Line Region
BLRG	Broad Line Radio Galaxy
BPT	Baldwin, Phillips and Terlevich
CFL	Courant-Friedrichs-Lewy
CGRO	Compton Gamma-Ray Observatory
CIR	Courant, Isaacson and Rees
EGRET	Energetic Gamma-Ray Experiment Telescope
EM	Electromagnetic
ENO	Essentially Non-oscillatory
FR	Fanaroff-Riley
FSRQ	Flat Spectrum Radio Quasar
HBL	High-frequency peaked BL Lac
HPC	High Performance Cluster
HD	Hydrodynamics
hdf5	Hierarchical Data Format library
HRSC	High Resolution Shock Capturing
HLL	Harten, Lax van Leer
IACT	Imaging Atmospheric Cherenkov Telescope
IBL	Intermediate-frequency peaked BL Lac
IBVP	Initial Boundary Value Problem
IC	Inverse Compton
IGM	Inter Galactic Medium
ISM	Inter Stellar Medium
IV	Initial Value

LAT	Large Area Telescope
LBL	Low-frequency peaked BL Lac
LINER	Low Ionization Nuclear Emission Region
MHD	Magnetohydrodynamics
MOJAVE	Monitoring of jets in AGN with VLBA
MPI	Message Passing Interface
MUSCL	Monotone Upstream-centred Scheme for Conservation Laws
NLR	Narrow Line Region
NLRG	Narrow Line Radio Galaxy
PLM	Piecewise Linear Method
PPM	Piecewise Parabolic Method
PVRS	Primitive Variable Riemann Solver
Quasars	Quasi-stellar radio sources
RHD	Relativistic Hydrodynamics
RMHD	Relativistic Magnetohydrodynamics
RRFID	Radio Reference Frame Image Database
RXTE	Rossi X-ray Timing Explorer
SED	Spectral Energy Distribution
SMBH	Super-Massive Black Hole
SRSQ	Steep Radio Spectrum Quasars
SPH	Smooth Particle Hydrodynamics
TSRS	Two Shock Riemann Solver
TVD	Time Variation Diminishing
TVDLF	Time Variation Diminishing Lax-Friedrichs
UV	Ultraviolet
VHE	Very High Energy
VLBA	Very Long Baseline Array
WENO	Weighted Essentially Non-oscillatory
WLRG	Weak Line Radio Galaxy

Chapter 1

Introduction

One of the fundamental questions of the study of galaxies is the formation and evolution of active emission regions within galactic cores. These emission sources are referred to as Active Galactic Nuclei (AGN) and are a unique class of astronomical objects. These sources are very luminous compact regions that produce emission over a wide range of the electromagnetic (EM) spectrum. Many studies have been undertaken to classify these sources and design physical models to explain their emission characteristics, however, their origin and relation to their host galaxies are not fully understood at present (see for example Beckmann and Shrader, 2012, chapter 4 and references therein). Even within the AGN class of sources the relation between the different types of AGN (such as the radio-loud, radio-quiet division) is not well defined (Beckmann and Shrader, 2012).

Certain types of AGN produce emission from jet-like structures protruding from the core of the galaxy. The jet-like structures are produced by relativistic plasma flowing along a collimated channel with small opening angle. They consist of particles ejected from an accreting super-massive black hole (SMBH) in the central region of the galaxy. The jets are often observed in pairs on opposing sides of the galactic core. An example of such a source is Hercules A, shown in Figure 1.1, which is a giant elliptical galaxy containing an AGN. In Figure 1.1 the size of the AGN jets extend far beyond that of the galaxy and is of the order of 200 kpc (Sadun and Morrison, 2002).

The jets associated with AGN are found in a variety of forms with intricate internal structure. The structure is time dependent and many of these sources show flares and outbursts of emission over both long (yearly) and short term (intra-day) time scales. The outbursts may occur over a wide range of the EM spectrum or may be limited to a single wavelength regime, suggesting a complex jet structure with multiple emission regions. Despite the presence of short term variability found within the jets, the large scale morphology evolves over time-scales longer than their recorded history (see e.g. Carilli et al., 1991). This leads to difficulties in designing a model that describes the overall evolution of these sources. To overcome these difficulties many studies

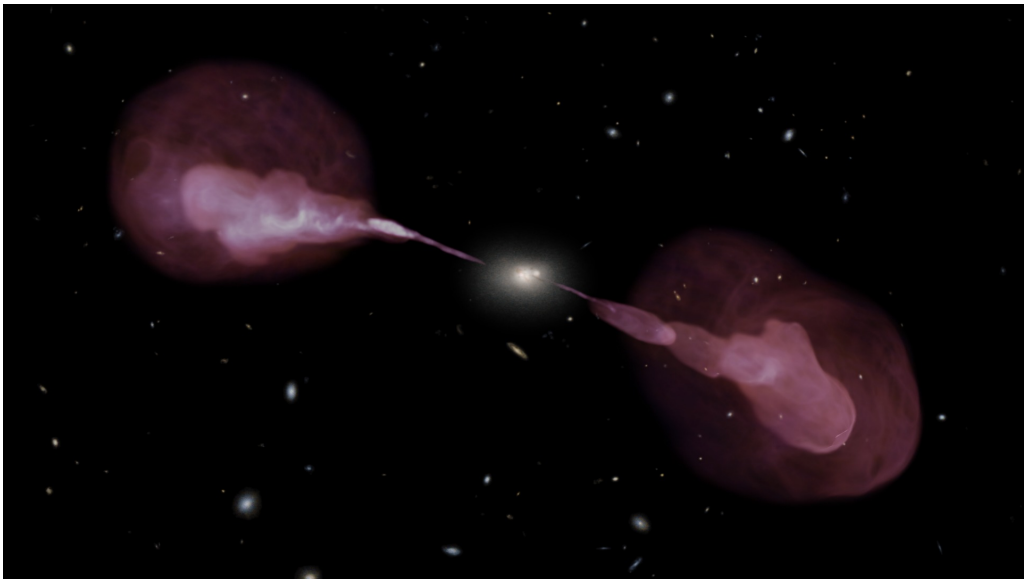

Figure 1.1: Composite image of the bilateral jet-like structures in the radio galaxy Hercules A taken by the HST and VLA telescopes. Image source: NASA (retrieved on 15/01/2017).

employ numerical simulations, in which the macroscopic dynamics of the jet is approximated as a fluid that is evolved according to the fluid dynamic conservation equations. These simulations can not only be used to investigate the evolution of these sources but also areas such as how the physical properties of the jet fluid influence the morphology, how time dependent structures form and evolve within the jet, and how interaction between the jet and ambient medium takes place. To study all of these aspects it must, however, be shown that the simulation that was run is able to reproduce an environment similar to that revealed by observational studies.

The aim of this study is to reproduce and investigate a jet-like structures similar to those that have been associated with AGN using fluid dynamic simulations. To achieve this aim the numerical software PLUTO [i] (Mignone et al., 2007) was used to create the simulations. From the results the properties of the jet fluid that is required to create these structures can be determined and compared to those predicted by observational data. In order to determine the similarity between the structures that form in the fluid dynamic simulations and observational radio data, an electron synchrotron emission model is applied to the simulated fluid dynamic environment. This is implemented by producing approximate two dimensional intensity maps of the three dimensional fluid dynamic simulations at radio-optical frequencies. Light curves can be calculated from the two dimensional intensity maps to investigate the evolution of the relative flux of the system. These simulations may lead to a better overall understanding of the large scale structures that form within these jets and how different jet morphologies observed for different AGN types relate to the initial injection and hence the central engine of the AGN. If

[i] Code website: http://plutocode.ph.unito.it/

the model implemented in the simulation reproduces the general morphology of AGN jets, future studies can be done to investigate the internal structure with more depth. An example of this would be to inject perturbations within the model to investigate probable causes of flares that have been associated with these sources.

Studies which simulate relativistic jets with numerical fluid dynamics have previously been done by many different authors (see for example Böttcher et al., 2012, chapters 10 and 11 and references therein), however, with the advance of computing technology and numerical algorithms it remains imperative that these models are continuously tested and developed. This project aims to differentiate itself from previous studies by the design of the emission estimation code that determines two dimensional image maps from the three dimensional simulation. The code can produce an intensity image at any arbitrary viewing angle and takes into account the effects of the relativistic nature of the emitting particles, resulting in boosted emission at certain viewing angles.

The research done in this study has been presented at several local and international conferences and the conference contributions, written at different stages in project, are shown in Appendix C.

The structure of this text is set out as follows. Chapter 2 contains a literature review of observational data from AGN, the unified AGN model used to define the relationship between different types of AGN, the mechanisms responsible for the production of AGN jets and the morphology of these jets according to observational studies. Chapter 3 provides an overview of fluid dynamics and the numerical methods used to simulate a fluid dynamic environment. Chapter 4 contains the set-up of the numerical simulation that was created for this study as well as the testing of different models, to ensure an accurate solution to the problem, and the results that were obtained. Chapter 5 described the emission modelling that was applied in order to estimate the intensity of the emission received from the simulated source. Finally Chapter 6 contains a final discussion of the results including the disadvantages of the current model and how it can be improved in future work.

Chapter 2

Active Galactic Nuclei

Active Galactic Nuclei (AGN) are compact regions in the centre of certain galaxies which are extremely luminous. They are some of the most energetic sources of radiation in the night sky and they can produce photons from radio wavelengths to above TeV energies. The radiation that AGN emit is not only due to the stellar and thermal contributions from the nucleus of the host galaxy. The continuum spectrum of the nucleus is mostly shaped by non-thermal radiation in the form of synchrotron emission, Inverse Compton (IC) scattering and photohadronic processes. Some AGN produce extended jet-like emission structures containing well collimated plasma flows with relativistic bulk velocities. These jet structures may extend up to megaparsec scales, making them some of the largest extended emission sources present in the universe. By investigating the processes that occur within these systems we can better understand the engines that drive them and in turn the universe as a whole. For a detailed overview on AGN the reader is referred to Beckmann and Shrader (2012) and Böttcher et al. (2012).

AGN are currently the subject of many ongoing studies and although the general model is well established there are still many missing aspects in our current understanding of these sources. This chapter contains a review of AGN, starting with the discovery and a brief observational summary of these sources. We discuss the different classes of AGN that are currently recognised and the current unified model to explain the different characteristics of each class. Finally we provide a section on the radiative processes which generate the observed emission from these sources.

2.1 The observational history of Active Galactic Nuclei

The first evidence of an AGN was recorded in 1908 by Edward Fath when he reported the presence of broad emission lines in the spectrum of the spiral galaxy of NGC 1068 (Carroll and Ostlie, 2013, see Figure 2.1 for an image of NGC 1068). The nature of galaxies (first referred to as nebulae) was poorly understood at that time and most astronomers were convinced that

Figure 2.1: Composite image of NGC 1068 consisting of data from the Hubble Space Telescope (HST) and Sloan Digital Sky Survey (SDSS) at optical wavelengths and the Nuclear Spectroscopic Telescope Array (NuSTAR) at X-ray wavelengths. Image source: http://www.jpl.nasa.gov/spaceimages/ (retrieved on 07/11/2016).

these sources were structures within our own Milky Way galaxy. Therefore, the initial discovery was not seen as significant. In 1918 Herber Curtis noted the presence of "a curious straight ray" seemingly connected to the nucleus of the M87 nebula (now known to be a giant elliptical galaxy of type E1, Curtis et al., 1918). This was the first detection of a relativistic jet within a galaxy, however its true nature would remain a mystery to astronomers for years.

It was only during the 1920s that Edwin Hubble was able to show that some of these nebulae were in fact galaxies of their own, similar to the Milky Way, containing billions of stars. He calculated the distances to M31 and M33 using the period luminosity relationship of Cepheid variable stars and found a distance to M31 of 285 kpc. Although his results were about a factor of three smaller than the current measured distance of 778 kpc, it was much further than any of the galactic stars, showing that M31 was a completely separate structure from the Milky Way. Hubble extended his studies to other newly found galaxies and their structures, which led him to propose the Hubble sequence, dividing galaxies into elliptical, spiral and irregular types (Hubble, 1926).

In 1943 Carl Seyfert published the spectra of 6 spiral galaxies (including NGC 1068 earlier observed by Fath) which showed high excitation emission lines superimposed on the continuum associated with combined stellar spectra (Seyfert, 1943). The emission lines that were recorded showed line broadening in excess of 1000 $\mathrm{km\,s^{-1}}$, far larger than any known class of object at that time. Hubble had shown that these objects were spiral galaxies similar to the Milky Way, however, it was clear that the broad emission lines could not be intrinsic to the stellar population of the galaxies and it was later discovered that they originated from their nuclei (see e.g. Woltjer, 1959). These galaxies became the first class of active galaxies that contained AGN, known as Seyfert galaxies. Seyfert also noted that the galaxies could be further subdivided into two subclasses. One subclass showed a narrow and broad component in its emission lines (Seyfert I) while the other subclass showed only a narrow component in its emission lines (Seyfert II, Seyfert, 1943). As telescopes became more sensitive, a result of technological advance, a large number of these sources were identified. This showed that Seyfert galaxies were regular phenomenon in the universe.

The next shift in the detection of AGN came with the discovery of the multi-wavelength components of astronomical sources starting with the invention of radio telescopes. Karl Jansky became the first person to observe radio emission from a celestial source in the 1930s. He discovered that the static interfering with short wave transatlantic voice transmissions was in fact radio emission from the Milky Way (Jansky, 1933). After this discovery, astronomers were quick to adopt radio telescopes to study this new found emission from the sky. Radio observations detected new AGN sources with different emission characteristics to the already known Seyfert galaxies. Reber (1944) published radio observations at 160 MHz showing radio sources were present in the constellations of Cygnus, Cassiopeia, Canis Major and Puppis. The radio emission in the Cygnus constellation was later identified as the radio galaxy Cyg A (Baade and Minkowski, 1954). Not long after the discovery of the radio source in Cyg A, it was suggested that the radio emission could be due to synchrotron radiation of electrons in a magnetic field (Alfvén and Herlofson, 1950).

Quasi-stellar radio sources or quasars were also discovered by radio surveys done between the 1950s and 1960s. These sources showed strong radio emission but they had a similar appearance to that of blue stars on optical images. Optical spectroscopy of these sources showed broad emission lines similar to those of Seyfert galaxies, but with high red shifts indicating that these sources were found at large cosmological distances and were in fact a new class of AGN (see e.g. Schmidt, 1963). Schmidt (1963) was also able to identify that the extended radio emission from the quasar 3C 273 had the form of a "wispy" jet. As the angular resolution of radio telescopes improved with the development of interferometers many of these galaxies were shown to exhibit extended radio sources, later associated with jets (van Breugel and Miley, 1977). The first observation of a stable well-collimated radio jet stretching over 100 kpc was shown by Waggett et al. (1977) (see Figure 2.2).

The first X-ray detections of astronomical sources were made in the 1960s using sounding

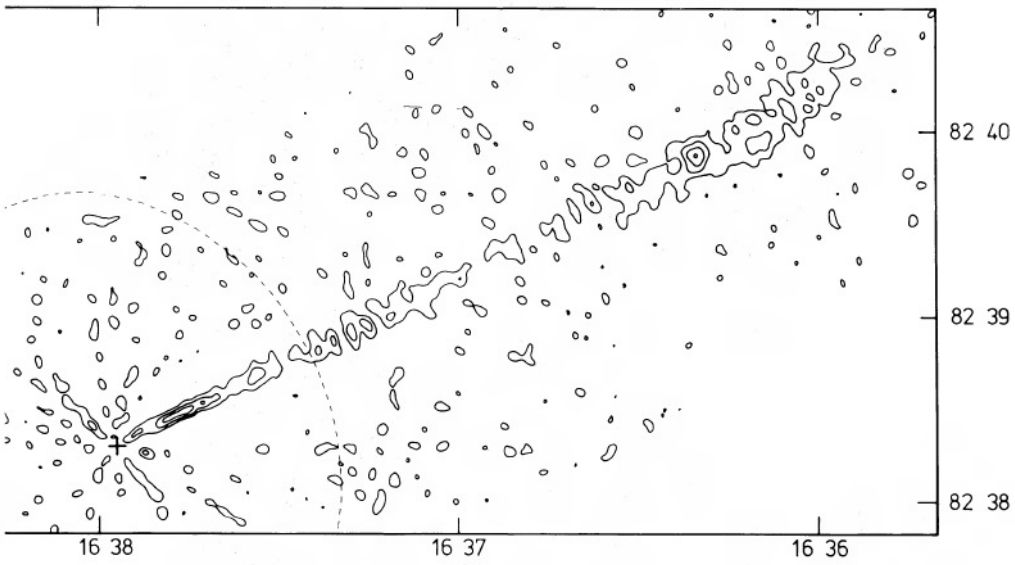

Figure 2.2: The extended well collimated radio jet of NGC 6251 at a frequency of 2689.5 MHz. The contribution of the compact central source was subtracted from the plot and replaced by the cross. The contour interval is plotted at 5 mJy/beam area with the minimum contour at 2.5 mJy. Figure adopted from Waggett et al. (1977).

rockets with X-ray detectors, in the form of Geiger counters, attached to them (Giacconi et al., 1962). The capabilities of these early X-ray detectors were limited and detections consisted mostly of strongly emitting galactic binary systems such as Sco X-1 (Holt et al., 1969). Even with this low sensitivity Bowyer et al. (1970) was able to attribute three of the detections to the AGN sources 3C 273, NGC 5128 and M87. A further advance in X-ray astronomy came with the launch of the *Uhuru* satellite in 1970. The satellite had increased sensitivity and recorded a total 339 X-ray sources of which about a dozen were of AGN origin. This detection included ten Seyfert I galaxies and two blazar objects, a newly discovered class of AGN with extremely fast variability (Forman et al., 1978). The newly discovered X-ray observations, together with the previously detected radio and optical emission, made it clear that AGN dominate the extragalactic sky on multiple wavelength regimes. The X-ray detections also showed that high energy emission (above 1 keV) was not limited to a single class of AGN but rather a common property of these objects. The next advance in X-ray astronomy came with the launch of the *Einstein* observatory in 1978. This satellite utilized grazing incident mirrors, which gave it improved spatial localization and an angular resolution of about 5" (Giacconi et al., 1979). With this superior detection and localization powers it was able to image knots and hot spots in jet-like structures previously associated with radio emission, showing that the jet structures were also emitting over multiple wavelengths. One of the contributions of high energy emission detected in these extended jets has been adequately described by the IC scattering of both external and internal synchrotron

photons (see for e.g. Tavecchio et al., 2000, for an IC model of external photons from the Cosmic Microwave Background).

The first AGN detected in γ-rays was the quasar 3C 273 with the COS-B satellite in 1978 (Swanenburg et al., 1978). Few subsequent detections were made until the launch of the Energetic Gamma-Ray Experiment Telescope (EGRET) aboard the Compton Gamma-Ray Observatory (CGRO) in 1991. This satellite detected γ-rays from more than 60 AGN comprising mostly of blazars (see e.g. Shrader and Gehrels, 1995). It quickly became clear that this class of AGN dominated the sky at high energies, implying an additional property that would distinguish this class from other types of AGN. The latest γ-ray satellite observatory, the *Fermi* telescope, launched in 2008, contains the Large Area Telescope (LAT) which covers the 20 MeV to 3 TeV energy range (Atwood et al., 2013). Since its launch it has detected 6378 γ-ray sources of which approximately 55% have been classified as AGN (Acero et al., 2015). AGN have also been detected in the TeV energy range by Imaging Atmospheric Cherenkov Telescopes (IACTs). These ground based telescopes image the Cherenkov radiation produced by the shower of secondary particles created when these very high energy (100 GeV - 100 TeV) photons interact with the Earth's atmosphere. According to the TevCat catalogue[i] 69 AGN have been detected using IACT including 65 blazars and 4 FR I sources (Wakely and Horan, 2008). These telescopes have shown that AGN produce some of the most energetic photons in the universe.

2.2 Classes of AGN

As telescopes increase in sensitivity many AGN sources that were previously too faint to observe have been discovered. This, coupled with the large amount of data produced by survey studies over the last half a century, means that we have detected AGN with different emission characteristics. All AGN have some similar properties such as the high luminosity of the compact nucleus, some degree of time variability and emission over a range of wavelengths. However, many of these sources differ substantially in other areas like emission line features, high energy emission cut-off and radio morphologies (presence and structure of radio jets). In order to understand the different properties that AGN have, it is useful to divide them into different classes depending on their emission characteristics. The recognized classes of AGN at present include Seyfert galaxies, Radio galaxies, Quasars, Blazars and low luminosity AGN (Beckmann and Shrader, 2012).

One important parameter for classifying AGN in terms of radio emission through synchrotron radiation is given by the radio-loudness,

$$R^* = \log\left(\frac{f_{5\mathrm{GHz}}}{f_{\mathrm{B}}}\right), \tag{2.1}$$

where f_B and $f_{5\mathrm{GHz}}$ are the fluxes in the optical B and radio bands respectively. If $R^* > 1$ the AGN is referred to as radio-loud while if $R^* < 1$ the source is radio-quiet (Netzer, 2013;

[i]Obtained from http://tevcat.uchicago.edu/ as on 3 February 2017

Peterson, 1997). The radio emission in radio-loud AGN has, in general, been associated with the production of synchrotron radiation from non-thermal electrons spiralling in the magnetic field of a relativistic jet. In the case of radio-quiet AGN it is not that the source does not produce radio emission, but rather that the radio emission is below the specified limit. The source of the radio emission produced in these systems are still unclear. It may be due to synchrotron emission produced in a weak jet as is seen in certain Seyfert galaxies such as NGC4151 (Ulvestad et al., 2005a,b) or a completely separate mechanism in the accretion disc (Courvoisier, 2001).

2.2.1 Seyfert galaxies

Seyfert galaxies were the first sources classified as AGN, by Carl Seyfert in 1943. These galaxies differ from regular galaxies in optical images by their bright confined nuclei relative to normal galaxies. The spectra of these galaxies include bright emission lines in both the optical and X-ray regime (such as the H II lines) superimposed on the stellar spectra of the stars in the host galaxy. Seyfert galaxies make up the largest fraction of AGN in the local universe.

As mentioned, Seyfert galaxies can be divided into two types based on their emission spectra. In Seyfert I galaxies (broad line Seyfert galaxies) the spectra show both a narrow and a broad line component indicating the presence of two emission regions in these galaxies. On the other hand, Seyfert II galaxies only show the presence of the narrow line component suggesting that the broad line component is either absent or obscured by an absorbing medium. Quantitatively Seyfert I galaxies are galaxies in which the H II Balmer emission lines have larger equivalent widths than the forbidden lines such as [O III]. For Seyfert II galaxies (narrow line Seyfert galaxies) the equivalent widths are similar for both series (Khachikian and Weedman, 1974). This principle is illustrated in Figure 2.3, where IC 4329A and NGC 5135 are classified as Seyfert I and Seyfert II galaxies respectively. The equivalent widths measured for the broad line components are typically on the order of $1000 - 10\,000\ \mathrm{km\,s^{-1}}$, while the narrow line component has equivalent widths on the order of $100 - 1000\ \mathrm{km\,s^{-1}}$. The core luminosity of Seyfert II galaxies are generally less than Seyfert I galaxies.

Although Seyfert galaxies are catalogued according to type I and II the transition between the two is smooth and some galaxies are difficult to distinguish. In order to obtain a more precise classification, the two classes can be further divided into subclasses such as those discussed in Beckmann and Shrader (2012, p. 92). Seyfert galaxies are generally radio-quiet with their spectrum showing very little synchrotron radiation. No Doppler boosting is observed for Seyfert I galaxies with face on inclination, indicating the absence of a prominent relativistic jet. Exceptions to the rule do, however, exist such as NGC4151 (Ulvestad et al., 2005b).

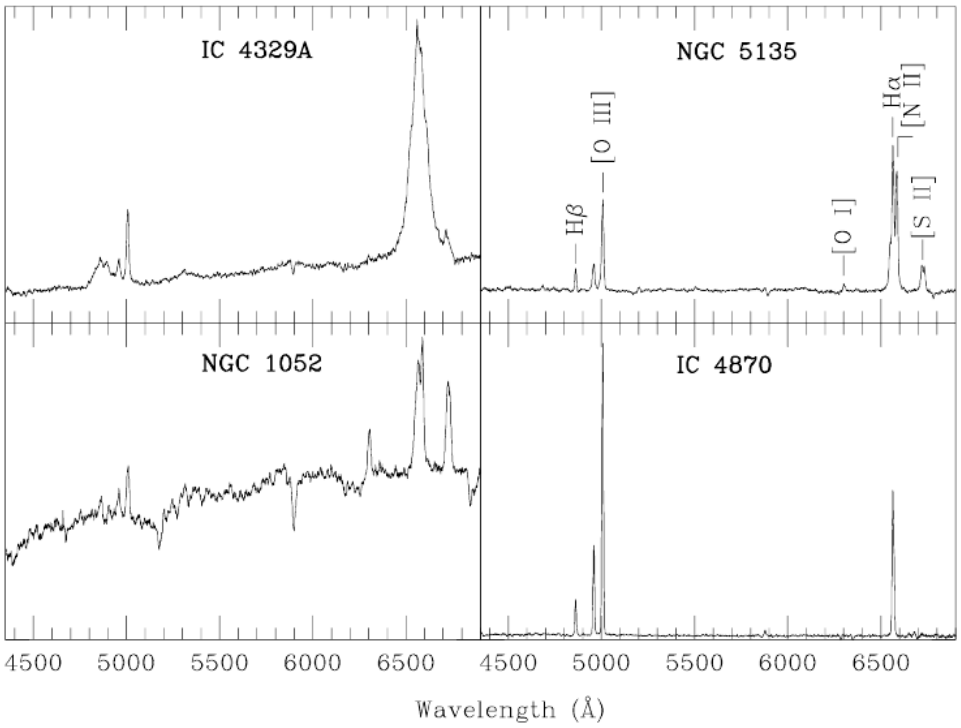

Figure 2.3: Example spectra from IC 4329A (Seyfert I), NGC 5135 (Seyfert II), NGC 1052 (LINER) and IC 4870 (Starburst galaxy), showing the relative difference in emission lines for radio-quiet AGN. Figure adopted from Véron-Cetty and Véron (2000).

2.2.2 Low-luminosity AGN/Low Ionization Nuclear Emission-line Regions (LINERS)

Low luminosity AGN have lower core luminosities than Seyfert galaxies but higher core luminosities than normal galaxies. The nuclei of these galaxies also show emission lines from low ionized gas with equivalent widths ranging between $200 - 400\ \mathrm{km\,s^{-1}}$. The spectra of these galaxies are similar to those of Seyfert II galaxies, however they include low ionization forbidden lines such as [O I] and [N II]. Low luminosity AGN may also host a thick accretion disc that is optically thin rather than a thin accretion disc, which is optically thick, as is the case for most of the other AGN classes (Véron-Cetty and Véron, 2000).

Due to the low luminosity of the nucleus in these galaxies it is often difficult to distinguish between emission lines produced in the core and other sources such as the H II regions of starburst galaxies (Véron-Cetty and Véron, 2000). One way to distinguish LINERS from starburst galaxies and other AGN was described by Baldwin et al. (1981). This paper showed that LINERS can be identified by comparing the equivalent widths of different emission lines. Figure 2.4 shows an example of a BPT (Baldwin, Phillips and Terlevich) diagram in which different relative line

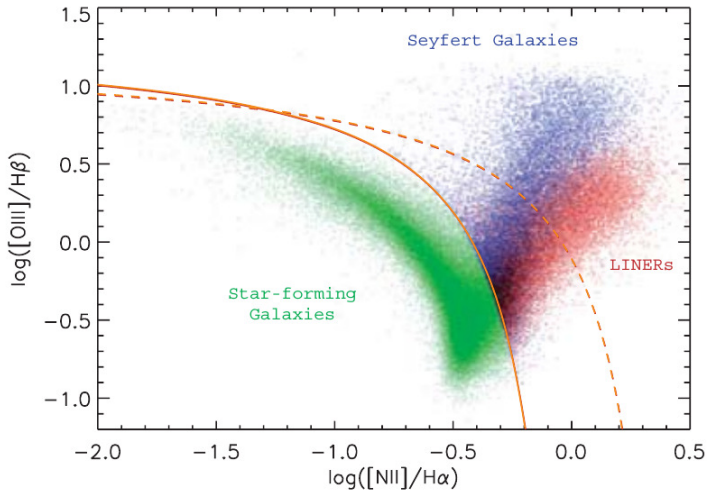

Figure 2.4: BPT diagrams showing the differences in relative line intensities of Seyfert, LINER and H II starburst galaxies. The division in each group is given by the solid lines. Figure adopted from Groves et al. (2006).

intensity ratios ([O III]/Hβ versus [N II]/Hα) are plotted. Regions in this diagram are shown for different types of galaxies.

2.2.3 Radio galaxies

Radio galaxies are radio-loud AGN characterized by bright radio jets originating from a compact radio source at the nucleus of the galaxy. These jets can stretch up to hundreds of kiloparsecs and may end in large radio lobes with hotspots. The optical spectra of these sources may appear similar to those observed in Seyfert galaxies and can similarly be divided into distinct types. Broad Line Radio Galaxies (BLRG) have spectra which show broad and narrow line emission line components similar to those observed in Seyfert I galaxies, while Narrow Line Radio Galaxies (NLRG) have spectra consisting only of a narrow line component like those observed in Seyfert II galaxies. A third class of radio galaxy, called Weak Line Radio Galaxies (WLRG), exists, which exhibit line spectra similar to those observed in LINERs (Lewis et al., 2003).

Radio galaxies can also be subdivided based on the morphology of their radio jets, the most common distinction being that introduced by Fanaroff and Riley (1974). Fanaroff-Riley class I (FR I) sources have low luminosity jets where the separation between the brightest luminosity regions is less than half the total size of the source. This means that on radio images the radio luminosity decreases with distance from the core (see Figure 2.5b). Fanaroff-Riley class II (FR II) sources show high luminosity jets in which the separation between the brightest luminosity components is more than half the size of the jet. For the FR II case the jets increase in brightness

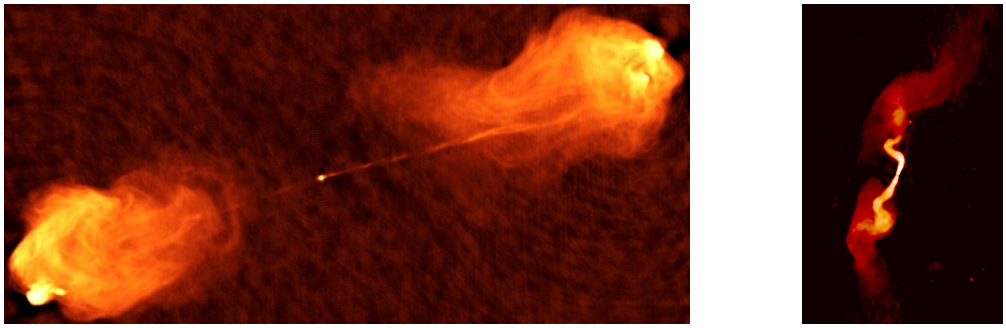

(a) (b)

Figure 2.5: (a) The FR II type radio galaxy Cyg A as imaged by the VLA at 5 GHz. (b) The FR I type radio galaxy 3c 31 as imaged by the VLA at 1.4 GHz. Figures adopted from the NRAO website: http://images.nrao.edu/ (retrieved on 07/11/2016).

further from the host galaxy (see Figure 2.5a). FR II type radio galaxies often end in lobe structures containing hot spots while FR I type galaxies may either end in faint plumes or radio lobes (Fanaroff and Riley, 1974). Overall the morphology of the radio jet has no correlation to the emission line class. This is consistent in the unified model of AGN which will be discussed in section 2.3.1.

Radio galaxies can have either one sided or double sided radio jets. This observed difference may not be due to intrinsic differences within the AGN but rather due to the relativistic motion of the emitting particles. To illustrate how this can occur consider an AGN producing two jets which propagate away from the core in opposite directions at relativistic velocities. This implies that the radiating particles within each jet will have a bulk velocity component directed opposite to each other. If the bulk velocity of the radiating particles in one jet has a large relativistic component directed towards the observer, the emission produced within the jet will be greatly enhanced by Doppler boosting (see Section 5.1.3 for a more quantitative discussion). The radiative particles in the second jet, however, will have a large component of the bulk velocity directed away from the observer, resulting in de-boosted observed emission. This will create a large difference between the relative intensities of the two jets. Observations of galaxies with one sided radio jets may be systems in which the inclination angle is such that the de-boosted emission of the second jet is too faint to detect. This model is supported by the difference in radio flux between the jets in two sided radio galaxies, as well as the presence of large scale radio structures on both sides of galaxies containing only one apparent radio jet. Using this model a good constraint can be obtained for the inclination of an AGN by determining the ratio of the relative brightness between the two jets (see e.g. section 2.3 in Böttcher et al., 2012).

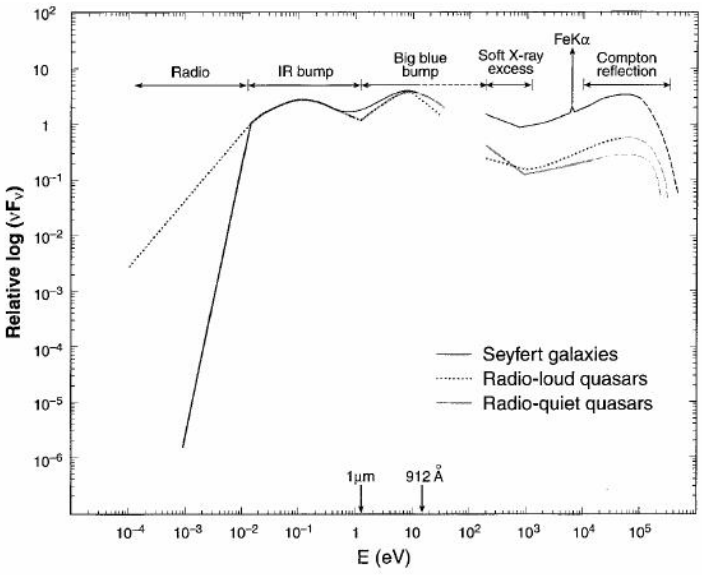

Figure 2.6: An example spectral energy distribution of two different classes of AGN. Figure adopted from Koratkar and Blaes (1999).

2.2.4 Quasars

Quasars or quasi stellar radio sources were first classified in the 1960s when radio surveys revealed radio sources with star like appearances. They are the most luminous AGN class and the optical spectra of these sources reveal strong broad emission lines at very large red shifts (Beckmann and Shrader, 2012). The emission lines are superimposed on a non-thermal emission spectrum at optical wavelengths. These objects are found at extremely large distances with the furthest detected object having a redshift of $z = 7.085$ (Mortlock et al., 2011). The starlike appearance of quasars is due to a so-called "blue bump" in its spectral energy distribution (SED, an example is shown if Figure 2.6). This component is caused by thermal emission, which peaks at frequencies between $10^{15} - 10^{16}$ Hz, from an accretion disc surrounding the central black hole of the host galaxy. The optical brightness of these sources tend to be highly variable.

Quasars have been detected as both radio-loud and radio-quiet AGN sources, however most of these sources are classified as radio-quiet. Radio-quiet quasars show emission spectra which are similar to Seyfert galaxies. In order to better distinguish between quasars and Seyfert galaxies an absolute magnitude limit has been introduced with quasars having $M_B < -23$ (Schmidt and Green, 1983). Radio-loud quasars make up about 10% of the quasar population (Beckmann and Shrader, 2012, p 113). These objects can be further divided into two groups, Flat Spectrum Radio Quasars (FSRQ) or Steep Radio Spectrum Quasars (SRSQ) referring to the slope of their SED in radio frequencies. FSRQs are also classified as part of the blazar class of AGN and will be discussed in the next section (Beckmann and Shrader, 2012).

2.2.5 Blazars

Blazars are AGN in which the observed emission is dominated by non-thermal emission produced in a relativistic jet pointed close to the line of sight of the observer. The highly relativistic bulk flow of the emitting particles in the jet produces Doppler boosted emission up to TeV energies. The radiation emitted by these sources covers a large part of the electromagnetic spectrum, from radio frequencies to very high energy (VHE) gamma-rays, and is characterized by two broad components. The lower energy component (radio to UV/X-ray emission) of the SED is produced by synchrotron radiation generated by non-thermal electrons within the relativistic jet. The high energy component (X-ray to VHE) on the other hand has been modelled with leptonic and hadronic emission models. In leptonic models the high energy emission is attributed to the IC scattering of photons from the accretion disc, torus, line emission regions and synchrotron emission (see e.g. Ghisellini, 2013, chapter 8 and references therein). The alternative hadronic models produce high energy emission through proton-γ-ray interaction, pair cascades, or proton synchrotron mechanisms (Böttcher et al., 2013). The Doppler boosted emission produced by these sources are also highly variable and can change by up to an order of a magnitude within intra-day timescales (see e.g. Carini et al., 1992).

Blazars can be divided into two subgroups based on their optical spectra. The first group, FSRQs, show similar spectra to quasars containing broad emission lines. The second class, called BL Lacs, has an almost featureless spectrum containing only weak emission lines (Beckmann and Shrader, 2012). The difference between FSRQs and BL Lacs results from the relative radiative power emitted from the accretion disc. FSRQs have radiative efficient accretion discs which leads to the photo-ionization of clouds surrounding the central engine, resulting in the production of strong emission line spectra. In BL Lacs the continuum emission dominates over the line spectra produced in the line emission regions implying the combination of a less radiative accretion disc and a strong non-thermal continuum (Urry and Padovani, 1995).

The BL Lac class of AGN can be further subdivided based on the position of their low energy peak emission in the galaxy rest frame. Low synchrotron peaked BL Lacs (LBL) exhibit low energy peaks ($\nu^{syn}_{\rm peak} < 10^{14}$ Hz), Intermediate synchrotron peak BL Lacs (IBL) have low energy emission which peaks between 10^{14} Hz $< \nu^{syn}_{\rm peak} < 10^{15}$ Hz, while High synchrotron peaked BL lacs (HBL) consist of BL lacs with low energy emission which peaks at $\nu^{syn}_{\rm peak} > 10^{15}$ Hz. A summary of the spectral properties of blazars is given in Abdo et al. (2010). Fossati et al. (1998) constructed SEDs for a sample of 126 blazars, with the SEDs averaged according to radio flux bins (see Figure 2.7). The authors were able to show that lower synchrotron peaked blazars are on average more luminous than high synchrotron peaked blazars. This result was explained as a difference in the intrinsic power of the AGN and the subsequent radiative cooling rates. LBLs posses the highest intrinsic power, producing a large number of seed photons, which can undergo IC scattering with the relativistic electrons within the jet. The large population of seed photons will lead to large radiative cooling rates. For the HBLs the central engine is less radiative, providing a smaller population of seed photons and thus lower cooling rates. The lower cooling

rates allow electrons within the jet to reach higher energies resulting in a higher peak spectrum. If FSRQs are included in this model they would have the highest population of seed photons resulting in high luminosity low peaked blazars (Ghisellini et al., 1998). This model is known as the blazar sequence.

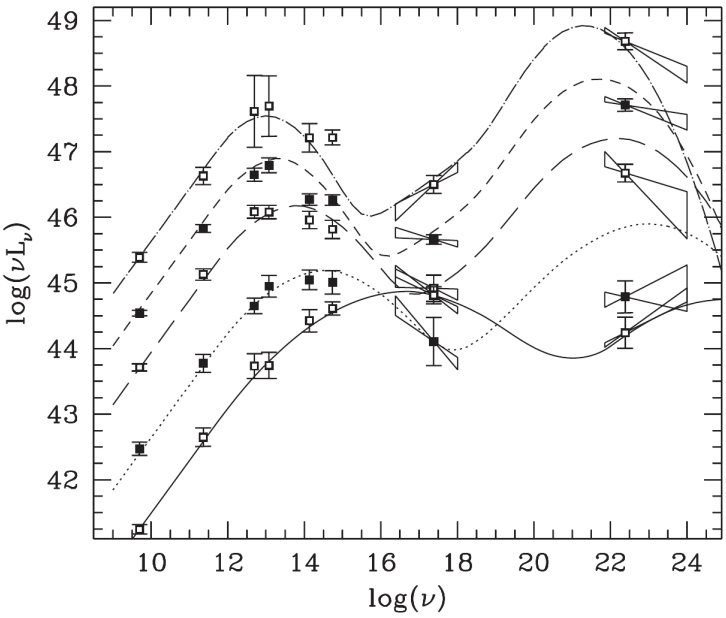

Figure 2.7: Average SED of a sample of blazars within radio flux bins. The curves show an analytical approximate fit for the emission. The figure illustrates that blazars with lower flux have higher synchrotron peaks, supporting the blazar sequence. Figure adopted from Fossati et al. (1998).

2.3 The AGN model

AGN have extreme power output, especially in the case of quasars which can reach luminosities above 10^{47} erg s^{-1}, about a million times that of the Milky Way. This, combined with the SED which indicates that the dominant emission is non-thermal, means that it cannot be generated by a population of stars in the nucleus of these galaxies. The idea that the central engine of AGN sources was a super-massive black hole (SMBH) surrounded by an accretion disc emerged in the 1960s (see e.g. Hoyle et al., 1964; Rees, 1984; Salpeter, 1964).

In the current model of AGN the power output is driven by the gravitational potential of a SMBH, with a mass in the order of $10^6 - 10^{10}$ $M_\odot$, at the centre of the galaxy (Urry and Padovani, 1995). This SMBH is actively accreting gas from the host galaxy and is surrounded by an accretion disc. In the accretion process viscous interactions between the plasma layers in

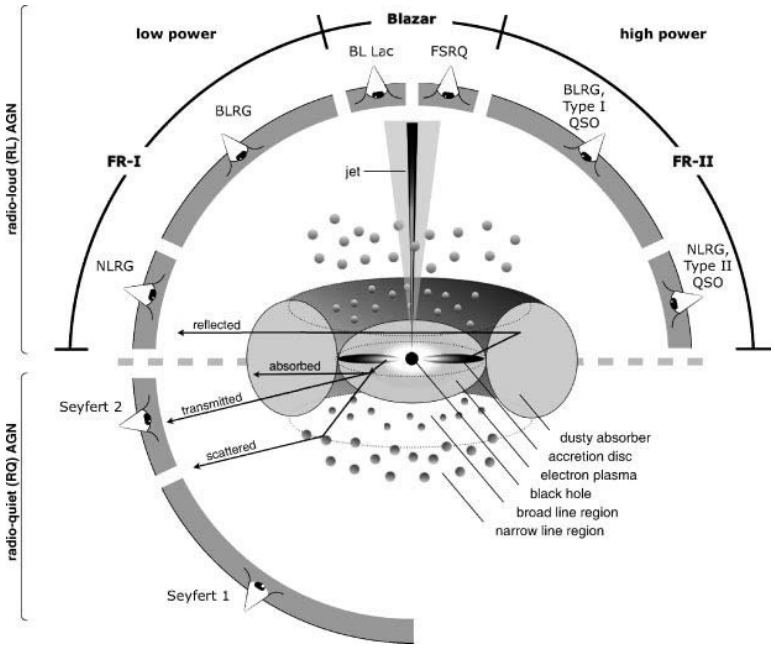

Figure 2.8: Diagram of the unification scheme of AGN dividing them based on radioloudness and inclination angle. Figure adopted from Beckmann and Shrader (2012) (figure 4.16).

the accretion disc converts the gravitational potential energy of the matter into thermal energy and radiation. An additional source of energy in the system can come from the Blanford-Znajek process (see section 2.4.1, Blandford and Znajek, 1977) which extracts rotational energy from the SMBH through general relativistic effects in the magnetic interactions present in the surrounding accretion disc. These magnetic interactions in the disc may also accelerate particles to relativistic velocities, ejecting them on opposite sides of the SMBH, perpendicular to the accretion disc. These ejected particles flow along the magnetic field lines to produce well collimated jets. Above and below the accretion disc there are additional emission regions in the form of ionized clouds of gas and dust, which orbit the central SMBH. These regions are divided into two components known as the broad line region (BLR) and the narrow line region (NLR, see Section 2.3.4, p. 22). Outside the accretion disc lies a dusty absorber or torus, which is thicker than the accretion disc and optically thick. Each of these components within the AGN will be discussed further in the later sections.

2.3.1 The unified model of AGN

AGN were initially classified according to their different emission attributes, however as more and more AGN were discovered the connections between the different types became clearer. This led to the fundamental question of whether the phenomenon of AGN can be explained by a unified

model rather than intrinsically different classes.

In the previous section (section 2.2) it was mentioned that Seyfert galaxies and radio-quiet quasars emit similar optical spectra and that the division of the two classes was based on an absolute magnitude limit. It was, therefore, not long before models were suggested to show that these sources have a common origin (see e.g. Penston et al., 1974; Weedman, 1973). Blandford and Rees (1978) proposed that radio-loud quasars and blazars, more specifically FSRQs, could be similar with the difference in the observed emission due to a change in the line of sight of the observer relative to the source. Attempts have also been made to unify radio-quiet and radio-loud AGN in terms of the alignment of a relativistic jet. It was, however, shown that this is not the case with the detection of weak jets in radio-quiet sources and the precise relation is still unknown (Ghisellini et al., 2004). Further models were able to build on these concepts to determine the precise relation between the classes and the current unified model is presented in Figure 2.8.

In the current model AGN are divided into the two main categories of, radio-loud and radio-quiet. Here radio-loud AGN refer to AGN which produce strong well collimated jets, while radio-quiet AGN produce either a weak or no jet structure. In each category a difference in the inclination angle of the system with respect to the line of sight of the observer will yield different emission characteristics and thus a different class of AGN. In the radio-quiet category LINERS, Seyfert I galaxies, Seyfert II galaxies and radio-quiet quasars all show emission line spectra. These line spectra are produced by the photo-ionization of gas clouds by the radiation produced in the accretion disc. The broad line components of the emission lines observed in some spectra are produced by the broad line region (BLR), which is a small region located close to the nucleus of the galaxy (within 1-100 pc). The narrow line components are produced by the narrow line region (NLR), which is a larger region that lies further out from the core. If the source is viewed face-on both the narrow line and broad line components would be observed and the resulting spectra would be that of either a Seyfert I galaxy or a radio-quiet quasar. If the source is oriented more edge-on, the dusty torus surrounding the nucleus obscures the emission of the broad line region resulting in the presence of only the narrow line component in the optical spectrum, such as observed in LINERs and Seyfert II galaxies.

The same inclination model applies to the radio-loud category of AGN. An edge-on source would only show the narrow line spectra resulting in a NLRG or WLRG. A more face-on inclination of the AGN would expose the BLR region resulting in a BLRG or radio-loud quasar spectrum. For radio-loud AGN with a nearly face-on line of sight the emission produced in the relativistic jet will be highly Doppler boosted, and the AGN would be classified as a blazar.

Subsequent differences in the intrinsic radiative power of the AGN also occur within the current model to explain the difference between the production of the Franaroff-Riley classes in radio galaxies, Seyfert I galaxies and radio-quiet quasars as well as Seyfert II galaxies and LINERs. This model has also been used to explain the difference between FSRQs and BL Lacs where FSRQs are explained as hosting FR II type jets, while BL Lacs host FR I type jets (Urry

and Padovani, 1995). A good summary of the unification of the different classes can be found in Antonucci (1993).

The unified model for AGN presented above is not complete and many questions, such as the mechanisms which produce the intrinsic differences between radio-load and radio-quiet AGN, remain. One study done by Laor (2000) suggests that this property may be linked to the mass of the SMBH in the centre of the galaxy. This author found that quasars with black hole masses $M_{BH} < 10^8 M_\odot$ are mostly radio-quiet while those with $M_{BH} > 10^9 M_\odot$ were radio-loud. Other studies of the radio luminosity of AGN as a function of the mass of the SMBH produced mixed results with some studies showing a direct proportionality while others found no relation. For example Franceschini et al. (1998) found that the luminosity scaled with the mass of the SMBH as $L \propto M_{BH}^{2.5}$. A later study by Ho (2002) found that the relation of radio luminosity to M_{BH} is much more complex and that the previous results only give the upper limit of the dependence. This suggests that there is some correlation between black hole masses and the production of relativistic jets in AGN. The production of relativistic jets have also been linked to the type of galaxy hosting the AGN with most radio-quiet AGN residing in spiral galaxies, whereas most radio-loud AGN are hosted by elliptical galaxies (Urry and Padovani, 1995).

2.3.2 Super-massive black holes

One of the basic properties of the SMBH at the centre of AGN is the presence of an event horizon. This is the radius at which the escape velocity of the SMBH becomes larger than the speed of light. Once matter which is accreting onto the SMBH has crossed this horizon it can no longer contribute to the observed emission of the source. We can define the event horizon in terms of the gravitational radius

$$r_g = \frac{GM_{BH}}{c^2}, \tag{2.2}$$

where G is the gravitational constant. For a non-rotating black hole the event horizon is given by the Schwarzschild radius $R_s = 2r_g$.

Close to the event horizon the gravity of the black hole is so large that space-time will be influenced by general relativistic effects (for an in depth review on general relativity see e.g. Misner et al., 1973). One effect that this will have on the emission produced close to the SMBH is gravitational red shifting,

$$\frac{\nu}{\nu_0} = 1 - \frac{GM_{BH}}{c^2 r}, \tag{2.3}$$

where ν_0 is the frequency of the emitted radiation, ν is the frequency of the received radiation and r is the distance from the black hole.

The small size of the event horizon, combined with the effect that no radiation is emitted by any processes that occur within this radius means that the SMBH at the centre of the AGN cannot be directly observed. Alternative, indirect means have to be employed in order to estimate properties such as the black hole mass. One such method is to use the observed timescale of variability to constrain the size of the emitting region. The size of the emitting region must be

smaller than the light crossing time of the variability (e.g. Böttcher et al., 2012), that is

$$r_e < \frac{c\Delta t}{1+z}, \tag{2.4}$$

where r_e is the radius of the emission region, c is the speed of light, Δt is the variability time scale and z is the redshift of the source. The time scale of the observed variability in AGN can stretch from minutes to years over all wavelengths (see e.g. Ackermann et al., 2016; Carini et al., 1992; Gupta et al., 2008). Considering the short scale variability that has been observed in AGN we can constrain the size of the central emission regions. For example if we consider the lower limit of hourly time scale variability for an AGN, we obtain that,

$$r_e \lesssim \frac{10^{14}}{1+z}\left(\frac{\Delta t}{1 \text{ hour}}\right) \text{ cm} \approx \frac{10^{-5}}{1+z}\left(\frac{\Delta t}{1 \text{ hour}}\right) \text{ pc}. \tag{2.5}$$

This implies that the source of the emission has to be a very compact region in the centre of the galaxy. If we assume that the size of the emitting region is of the same order as the Schwarzchild radius we can estimate the mass of the SMBH as,

$$M_{BH} = \frac{R_s c^2}{2G} \approx 10^8 \left(\frac{R_s}{10^{14} \text{ cm}}\right) M_\odot, \tag{2.6}$$

which is within the bounds previously stated.

A more accurate method to determine the black hole mass of the AGN indirectly, and subsequently constrain the size of the event horizon, is reverberation mapping. This technique involves the sampling of the continuum variability and emission line fluxes on time scales smaller than the light travel time between the central black hole and the broad line region. Cross-correlating these measurements can constrain the size of the broad line region and hence can be used to determine the orbiting velocity of the gas. Using these measurements one can estimate the mass of the central black hole by applying the virial theorem (Beckmann and Shrader, 2012).

2.3.3 Accretion disc

When gas, with angular momentum ℓ, accretes onto a SMBH, the gas will fall inwards until the centrifugal forces of the angular momentum balance out the gravitational force of the black hole. This results in an stationary equilibrium radius r_{circ},

$$r_{\text{circ}} = \frac{\ell^2}{GM_{BH}}. \tag{2.7}$$

At this equilibrium radius the velocity of the gas will be purely Keplarian with,

$$v_r = 0, \tag{2.8}$$

$$v_\phi = \sqrt{\frac{GM}{r}}, \tag{2.9}$$

where v_r and v_ϕ are the radial and rotational velocity components respectively. This motion will result in the formation of rotationally supported structures, such as an accretion disc and a torus, surrounding the central black hole. This section will follow the outline of the accretion process as discussed in Böttcher et al. (2012, pp. 81-89).

In the AGN model the thin accretion disc that surrounds the central SMBH stretches from the inner most stable orbit of the SMBH, which is of the order of $\sim 2r_g$, outwards to about 1 pc. In order for the gas in this configuration to fall inward and accrete onto the black hole the gas must lose some of its angular momentum. This loss in angular momentum is driven by viscosity within the accretion disc. The viscous forces within the gas in the disc will cause the inner gas to slow down and the outer regions to speed up resulting in a nett transfer of angular momentum outward in the radial direction. This in turn will cause some of the gas to spiral inward toward the black hole. For a thin accretion disc the molecular viscosity of the gas will be too low to have a significant effect on the angular momentum transfer and most of the interaction will occur due to turbulent viscosity produced by magneto-rotational instabilities within the disc.

The viscose interactions will also convert a fraction of the angular momentum into thermal energy. If the disc is radiatively efficient the excess energy can be radiated away quickly resulting in low thermal pressures within the disc. The low thermal pressure will allow the disc to remain thin with $H << r_{\rm acc}$ where H is the height of the disc and $r_{\rm acc}$ is the radius of the accretion disc. The luminosity of the disc as a result of the radiated energy can be given by (see e.g. Frank et al., 2002, for a detailed discussion),

$$L_{\rm acc} = \eta \dot{M} c^2, \tag{2.10}$$

where η is the efficiency with which the gravitational energy is converted into radiation and $\dot{M}$ is the rate at which mass accretion takes place. For gas of density ρ the mass accretion rate is given by,

$$\dot{M} = 2\pi r H \rho v_r. \tag{2.11}$$

The accretion disc emits radiation ranging from radio up to X-ray frequencies (see e.g. Haardt and Maraschi, 1993). This range of emission is due to the temperature difference within the accretion disc. At the outer boundaries the accretion disc will be cool resulting in low frequency thermal emission. As the matter spirals inwards it will heat up resulting in higher frequency emission. The emission produced by accretion discs are most prominent in the UV frequencies resulting in a "blue bump" in the SED of some AGN (see figure 2.6, Shields, 1978).

The rate at which matter accretes onto the SMBH is regulated by radiation pressure. The

friction in the accretion disc will transform some of the angular momentum into thermal energy which can be radiated away. This radiation will exert a pressure P on the surrounding material where the pressure gradient from the emission is given by,

$$\frac{dP}{dr} = \frac{-\sigma_T \rho}{m_p c} \frac{L}{4\pi r^2}. \tag{2.12}$$

Here σ_T is the Thompson cross-section of the free electrons in the accretion disc and m_p is the mass of a proton. If the resulting radiation pressure is larger than the gravity of the black hole the accreting material will be forced outward and the rate of accretion will decline. The luminosity needed to reach the equilibrium point between the radiation pressure and gravitational forces for spherical accretion is called the Eddington luminosity, which is given by

$$L_{\text{Edd}} = \frac{4\pi G M_{BH} m_p c}{\sigma_T}. \tag{2.13}$$

For a $10^8 M_\odot$ black hole the Eddington luminosity will reach $L_{\text{Edd}} \approx 10^{46}$ erg s^{-1}, which is of the order of the luminosity AGN emit.

An important parameter characterising the AGN luminosity is the Eddington ratio. This is the ratio of the bolometric luminosity of the AGN to the Eddington luminosity, given by,

$$\lambda_{\text{Edd}} = \frac{L_{\text{bol}}}{L_{\text{Edd}}}. \tag{2.14}$$

When $\lambda_{\text{Edd}} > 1$ the emission produced by the AGN cannot be generated by the accretion disc alone and additional mechanisms are required.

2.3.4 Line emission regions

One of the defining characteristics of many of the classes of AGN is the strong emission lines present in their spectrum. These emission lines can be composed of multiple components suggesting individual emission regions disconnected from one another. The emission lines observed in AGN are usually associated with temperatures on the order of 10^4 K (see e.g Osterbrock and Mathews, 1986). This suggests that the emission is produced through photo-ionization of the gas by the UV and X-ray emission produced in the accretion disc (Rees et al., 1989). As mentioned previously, observations have shown the existence of two line emission regions close to the centre of AGN, namely the BLR and the NLR.

The broad line component consists of broad emission lines most notably in the hydrogen Balmer series and have Doppler widths corresponding to 10^4 km s^{-1}. Reverberation mapping of these lines indicate that they are produced in non-uniform clouds close to the central engine. These clouds are in photo-ionization equilibrium with their surroundings meaning the rate of recombination within the gas is equal to the rate of ionization. The temperature and densities of these regions can be determined by measuring the relative intensities of emission lines from

different ionization states in the Balmer series. This method yields temperatures of 10^4 K with densities on the order of 10^9 cm^{-3} (Osterbrock and Mathews, 1986). A temperature on the order of 10^4 K, however, only corresponds to a line broadening of 10 km s^{-1}, which is much less than the measured widths. This indicates that these broad line clouds must have a large bulk orbital motion between $1\,000 - 10\,000$ km s^{-1} around the central engine. The motions of these clouds are dominated by the Keplarian orbital motion with a nett inward motion towards the black hole. The high orbital motions are also suggestive that this region orbits close to the central engine (Gaskell, 2009).

The narrow line components have smaller line widths on the order of 100 km s^{-1} and are most notable in the forbidden line series such as [C III] [O III], suggesting a diffuse gas as the source of emission (Osterbrock and Mathews, 1986). A lack of fast variability in the narrow emission lines indicate that they are produced in a much larger region of gas and dust. These lines are much more similar to galactic nebula than the broad emission lines produced in the broad line region. This region also produces its emission through photo-ionization of the X-ray continuum. The presence of the forbidden emission lines of atoms like oxygen and magnesium constrain the particle density to between $10^3 - 10^5$ cm^{-3} which is lower than in the BLR (Osterbrock and Mathews, 1986). The size of this region can stretch over hundreds of parsecs and is proportional to the luminosity of the [O III] emission line (Bennert et al., 2004). The morphology of these regions have been directly imaged in some Seyfert galaxies revealing collimated structures. This structure of the narrow line region may be due to the presence of the dusty torus collimating the photo-ionization (Kraemer et al., 2008).

2.3.5 The dusty torus

Observations of the different emission line spectra in AGN support the existence of an obscuring medium surrounding the accretion disc (see Figure 2.8). This structure is referred to as the torus. The evidence suggests that the torus consists of a thick doughnut-shaped region consisting of clumpy gas and dust (Elitzur and Shlosman, 2006). This structure is located just outside the accretion disc between 1-100 pc from the core (Netzer, 2013). The origin of this structure still remains a mystery. In the model proposed by Krolik and Begelman (1988) they explained the formation of the structure by accretion of molecular clouds from the host galaxy. However, several problems in this model were pointed out by Davies et al. (2006). Elitzur and Shlosman (2006) suggested a model in which the torus consists of wind driven outflows from the accretion disc.

The torus has a large column density on the order of 10^{25} cm^{-2}, which is high enough to absorb most of the emission produced in the nucleus. According to the unified model the dust in the torus absorbs the BLR emission when viewed from an edge-on inclination. For example, if the inclination is the only difference between the two types of Seyfert galaxies, then the BLR should still be present in Seyfert II galaxies. The emission produced within the BLR in Seyfert II galaxies may undergo Thompson scattering, allowing some of the emission to reach the observer.

The scattered emission will be linearly polarized due to this process. Measurements of linearly polarized spectra from Seyfert II galaxies have shown a broad line component, thus confirming the BLR in these galaxies are obscured (Antonucci and Miller, 1985; Miller and Goodrich, 1990; Tran et al., 1992).

Another observation which supports the existence of the torus structure is the presence of an infrared bump in the spectra of some AGN. The dust in the torus is generally at a lower temperature than that of the accretion disc, resulting in the production of emission at infrared rather than UV frequencies. This emission generates the additional bump that is illustrated in Figure 2.6.

2.4 Outflows and relativistic jets

Fast outflows have been detected in all classes of AGN as blueshifted absorption lines in their spectra (see e.g. Crenshaw et al., 1999, for Seyfert galaxies). Despite this common characteristic only certain classes of AGN have been consistently associated with the production of relativistic jets. It is thought that these jets consist of a highly collimated relativistic flow of plasma with a small opening angle, and transport vast amounts of energy away from the central engine to over hundreds of kiloparsec. The precise mechanisms responsible for the production of these jets in AGN are still unclear. In fact, we have a very limited understanding of the jet itself, including properties such as the composition (electron-positron or electron-ion) and how it remains collimated over such large distances. In addition, since emission is observed over the whole length of the jet, it implies particle acceleration, within the jet itself. One of the difficulties in studying the jets associated with AGN is the large length scales that have to be taken into account, which range from the production mechanisms in the order of the Schwarzchild radius of the SMBH up to the large scale morphology, which can stretch up to a megaparsec. In this section we will summarise our current understanding of the relativistic jets observed in AGN. The discussion will follow that of the in-depth analysis provided in Böttcher et al. (2012).

2.4.1 Powering outflows and jets

Outflows and jets similar to those observed in AGN have been detected in many galactic sources including protostars and microquasars. Among these sources an accretion disc is a common property, suggesting that this is a vital component in generating a collimated outflow. A five year radio/X-ray study of 3C 120, a Seyfert I galaxy, by Chatterjee et al. (2009) using data from the VLBA and RXTE instruments has shown an anti-correlation between X-ray and radio components. In this study, a decrease in the X-ray continuum was observed before the ejection of a bright radio component in the jet. Since the X-ray continuum in this source is produced by the accretion disc the result suggests an accretion disc-jet relation (Chatterjee et al., 2009).

Investigations into how matter from the accretion disc could be ejected to form a jet show that the kinetic energy of the infalling material would not be sufficient to power such an outflow, and

an additional mechanism is needed. One such mechanism involves the extraction of rotational energy from a rotating SMBH within its ergosphere. The ergosphere is a region just outside the event horizon of a rotating black hole in which the nett energy of an orbiting particle will be negative. This region extends from about twice the Schwarzchild radius in the plane of rotation to about one Schwarzchild radius at the poles (e.g. Schutz, 2009). Particles which enter and exit the ergosphere must have a positive energy, which implies that one can theoretically extract energy from a rotating black hole. This is known as the Penrose mechanism (Penrose, 1969). Consider the case if two particles enter the ergosphere with positive energies. Once inside the ergosphere they interact with one another in such a way that particle one transfers energy to particle two, resulting in a nett negative energy for particle one. This transfer in energy allows particle two to escape the ergosphere. However, since particle one now has a negative energy, the total energy of particle two (according to the law of conservation of energy) is more than the total energy of the two particles before they entered the ergosphere. As particle one falls into the event horizon it will transfer the negative energy to the black hole and, therefore, the total energy of the black hole will decrease (see e.g. Courvoisier, 2013, for a detailed discussion). The total energy that can be gained by this process is given by,

$$E = f_\epsilon(a) M_{BH} c^2 \tag{2.15}$$

where $f_\epsilon(a)$ is a function of the black hole spin a (see Böttcher et al., 2012, and references therein). For a SMBH of $10^8 M_\odot$ with $a \approx 1$, $f(a) = 0.29$, the maximum energy that can be extracted will be

$$E \approx 5 \times 10^{61} \left(\frac{M}{10^8 M_\odot} \right) \text{ erg}. \tag{2.16}$$

Since the typical luminosity of a quasar is of the order of 10^{47} erg s^{-1}, the rotational energy of the black hole can power the source for over ten million years. Wheeler (1970) applied the Penrose process to the AGN model and suggested that a star falling into the ergosphere of the SMBH could break apart, resulting in the ejection of high energy material. However, it was later shown that this process would not produce a significant fraction of energy gain compared to the original energy of the infalling star. The same result holds for infalling gas from the accretion disc (Wald, 1974b).

A new mechanism for extracting the rotational energy of a black hole was suggested in the same year by Wald (1974a). This model focused on the effects of general relativity on magnetic fields (within the ergosphere). Wald (1974a) showed that a uniform magnetic field aligned with the rotational axis of the SMBH will produce a quadrupole electric field. This quadrupole electric field means that the SMBH will act as a rotating conducting sphere which allows angular momentum to be transferred to charged particles. Blandford and Znajek (1977) investigated this effect for a SMBH in order to determine whether it could power the outflows of AGN. The results for a split monopole approximation showed that the SMBH will have a total

electromagnetic luminosity of,

$$L = \frac{2}{3c}\left(\frac{\psi(\mathrm{B})\Omega_h}{4\pi}\right)^2, \tag{2.17}$$

where $\psi(\mathrm{B})$ is the total magnetic flux through a hemisphere of the SMBH and

$$\Omega_h = \frac{a}{1+\sqrt{1-a^2}}\frac{c^3}{2GM_{BH}}. \tag{2.18}$$

If we consider the same rotating SMBH as in equation (2.15) this would result in,

$$L \approx 10^{49}\left(\frac{B}{10^3\mathrm{G}}\right)\left(\frac{M}{10^8 M_\odot}\right)\ \mathrm{erg\,s^{-1}}, \tag{2.19}$$

which is more than sufficient to power an AGN jet. This process is known as the Blandford-Znajek mechanism.

Three dimensional numerical simulations have provided additional support to the Blandford-Znajek process. Tchekhovskoy et al. (2011) successfully simulated a general relativistic hydrodynamical environment of a spinning black hole interacting with an accretion disc. The simulation showed that the interaction between the black hole and the magnetic field produced a magnetically arrested accretion disc with strong outflows. The energy of the particles in the generated outflow was found to be proportional to the spin of the black hole, with a spin parameter of $a = 0.99$ yielding an outflow of 140% the available accretion energy. This result can only be explained by angular momentum transfer from the black hole.

Applying this model to the production of AGN outflows the question must be asked, what mechanisms produce the magnetic fields close to the SMBH. Black holes have no internal magnetic field and therefore the magnetic field responsible for the transfer of energy has to be generated in the inner parts of the accretion disc. One possible mechanism for the production is the accretion disc dynamo effect. The process can produce strong magnetic fields within the disc itself but the field does not sufficiently exceed the disc thickness H and the nett magnetic field of the system due to this effect will be zero (Tout and Pringle, 1996). Another source may be the magnetic field generated by the interstellar medium (ISM). The average magnetic field in the ISM is on the order of ~ 6 μG for regions of density 10^3 cm^{-3}, (see e.g. Heiles and Troland, 2005), and scales with the particle density (n) on the order of $B \propto n^{0.65}$ (Crutcher, 2007). A problem with this approach, however, is the mechanism which would allow the accumulation of the magnetic field in the inner disc. This model has been investigated further by Beckwith et al. (2009); Spruit and Uzdensky (2005).

Observationally, the problem with the current magnetic launching model is the structure of the magnetic field. In order to accelerate plasma outwards along the axis of rotation a structured helical magnetic field is required, however radio observations of the core regions of the jet structure suggest turbulent magnetic fields with very low polarization ($< 5\%$). One possible solution to this problem may be that the core structure of the magnetic field is too small to be

resolved with the current generation of telescopes (Lister and Homan, 2005). The Blandford-Znajek model also does not explain how particles are accelerated up to high Lorentz factors or the collimation over the large length scales. These two processes could either occur very close to the central black hole or more gradually over longer distances.

Another aspect that has to be taken into consideration is the division between radio-loud and radio-quiet sources. If the production of jets is dependent on the Blandford-Znajek mechanism then the division in the radio-loudness of AGN should show a subsequent correlation in the black hole mass, spin or variations in the accretion disc's magnetic field. This is in accordance with the possible dependence of the radio-loudness on the black hole mass, discussed in section 2.3.1. Another model suggests that the difference may lie in the direction of rotation of the accretion disc with respect to the SMBH; radio-quiet AGN have accretion discs with prograde rotation while radio-loud galaxies have retrograde accretion discs. The retrograde rotation of the accretion disc allows for a rapid inflow region within the last stable orbit of the SMBH. This rapid inflow region in return generates a larger magnetic flux which leads to a more powerful outflow and the production of a jet (Garofalo et al., 2010; Reynolds et al., 2006). This model has been able to explain some of the population characteristics of AGN. For instance, while a prograde accretion disc can be stable over a long time period, a retrograde accretion disc will cause the spin of the SMBH to decrease at a large rate and, given enough time, the spin of the black hole will change such that the system becomes prograde. This property may be able to explain the observation that only about 10% of AGN are radio-loud. In addition, to form a retrograde accretion disc a large perturbation such as a galaxy merger is necessary. These types of events occurred more frequently at large cosmological distances which is in accordance with the distribution of radio-loud AGN.

The Blandford-Znajek mechanism provides an interesting explanation for the variability and flares observed in AGN outflows. Since the mass and spin of the central SMBH is unlikely to undergo any rapid changes, the variability in these outflows must be caused by a variation in the magnetic field. Magnetic field fluctuation within the accretion disc can be driven either by local changes in the magnetic field of the disc due to the dynamo effect or the collapse of the inner part of the accretion disc (Böttcher et al., 2012, and references therein).

2.4.2 Collimation

While the Blandford-Znajek process discussed in the previous section 2.4.1 can produce sufficient power and outflows, this does not imply the formation of a relativistic jet. In order to obtain a jet, the outflow must be collimated and accelerated to relativistic velocities. The relativistic jets observed in AGN remain collimated over distances more than 7 orders of magnitude larger than the initial production region. A good example of this is M87. Biretta et al. (2002) showed that the outflow generated by M87 has a large opening angle of $\approx 60^\circ$ within the inner 0.04 parsec ($\approx 100 r_g$) from the core. The outflow is then significantly collimated within a 1 parsec distance to an opening angle of $\approx 5^\circ$. This evidence suggests that the collimation process is not

due to the magnetic field close to the SMBH but rather a larger scale magnetic field structure that could be produced by the outer accretion disc.

There are several other factors which can help in the collimation of the jet. One limiting factor in the rate of jet expansion is the fact that the expansion of a fluid flow will cause an acceleration in the bulk flow of the fluid. This means that the jet cannot expand at a rate larger than one that would yield a fluid velocity faster than the speed of light. For a relativistic fluid this limits the opening angle of the jet to $\approx 1/\Gamma$. For a relativistic jet with an initial bulk Lorentz factor of $\Gamma = 10$ this limits the opening angle to 18°, which is still an order of magnitude larger than the opening angles measured in most AGN. Additional collimation factors may include the higher density Interstellar medium (ISM) and inter galactic medium (IGM), a disc wind driven from the accretion disc and a strong poloidal magnetic field generated within the rotating accretion disc (Böttcher et al., 2012, and references therein).

2.4.3 Particle acceleration, shocks and knots

The collimated plasma which forms the relativistic jet contains charged electrons that produce radiation through, for example, synchrotron and IC processes. As these particles propagate along the flow of the jet they will lose energy through these radiative processes as well as through adiabatic expansion. The time scales over which the electrons in AGN jets will radiate away a significant amount of their energy is on the order of a hundred years (see e.g. Böttcher et al., 2012, chapter 6 and references therein) which results in travel length scales far less than the observed hundreds of kiloparsec length scales over which these jets emit radiation. In order for emission to take place over these large distances there has to be additional sources of energy transfer to the electrons, in the form of particle acceleration, within the jet (see e.g. Böttcher et al., 2012, chapter 9).

One source of energy within these jets could be in the form of the magnetic fields. In the inner regions of the jet the energy transport may be dominated by the magnetic field energy or Poynting flux. This energy can be converted into particle acceleration through magnetic reconnection events. The exact details of this mechanism is still unclear as well as the length scale on which the jet would remain Poynting dominated (Lyubarsky, 2005).

If the jet is kinetically dominated the conversion of kinetic energy into the internal electron energy must take place to account for the radiated synchrotron emission. Since kinetically dominated jets are very stable (due to the high bulk motion) over larger distances they provide a good model for the outer regions of AGN (Blandford and Rees, 1974). Perturbations within such jets can lead to the formation of shocks, which would lead to the acceleration of particles that can provide emission within the jet.

The shock structures mentioned previously have been observed at very high resolution, sub-parsec scales, within the collimated jets as regions of higher luminosity and polarization (Pushkarev and Kovalev, 2008). These higher intensity regions can be stationary, move at apparent superluminal speeds down the jet away from the core or towards the core at slower

velocities (Lister and Homan, 2005). Figure 2.9 shows an example of the evolution of these structures on sub-parsec scales in the radio galaxy 3C 111. In order to generate a relativistic shock, however, the relative speed between the two regions separated by the shock must exceed the speed of sound in the medium. Figure 2.10 illustrates the current model for energy transport with relativistic jets in which the inner parsec scales are Poynting dominated, with a transition to kinetic domination at larger length scales (Marscher, 2005). The figure shows a shock region with higher density. As matter propagates through the shock, particles are accelerated to produce an emission region.

The superluminal components propagating down the jet can be generated by the ejection of relativistic blobs from close to the central engine. These blobs propagate down the jet leaving shock trails. The apparent superluminal velocities of emission components can be explained through the combined effects of geometry and the relativistic motion of the region (Rees, 1966). Figure 2.11 illustrates a blob propagating along the jet of an AGN with a velocity v at an inclination θ with respect to the line of sight to an observer O. The blob emits a photon at position A at time $t = 0$. This emitted photon arrives at the observer at a time,

$$t_1 = \frac{AO}{c}. \tag{2.20}$$

If the blob emits another photon at position B at time t_e, under the assumption that the source extends a small enough angular distribution in the sky such that $AO = BO + vt_e \cos\theta$, the second photon will arrive at the observer at the time,

$$t_2 = t_e + \frac{AO - vt_e \cos\theta}{c}. \tag{2.21}$$

The difference in the time of arrival of the two photons at the observer is be given by,

$$\begin{aligned} \Delta t &= t_2 - t_1 \\ &= t_e + \frac{AO - vt_e \cos\theta}{c} - \frac{AO}{c} \\ &= t_e \left(1 - \frac{v}{c} \cos\theta\right). \end{aligned} \tag{2.22}$$

During this time the projected displacement of the blob on the sky Δx will be,

$$\Delta x = vt_e \sin\theta. \tag{2.23}$$

Therefore the projected apparent velocity will be,

$$\begin{aligned} v_{\text{app}} &= \frac{\Delta x}{\Delta t} \\ &= \frac{v \sin\theta}{1 - \frac{v}{c} \cos\theta}. \end{aligned} \tag{2.24}$$

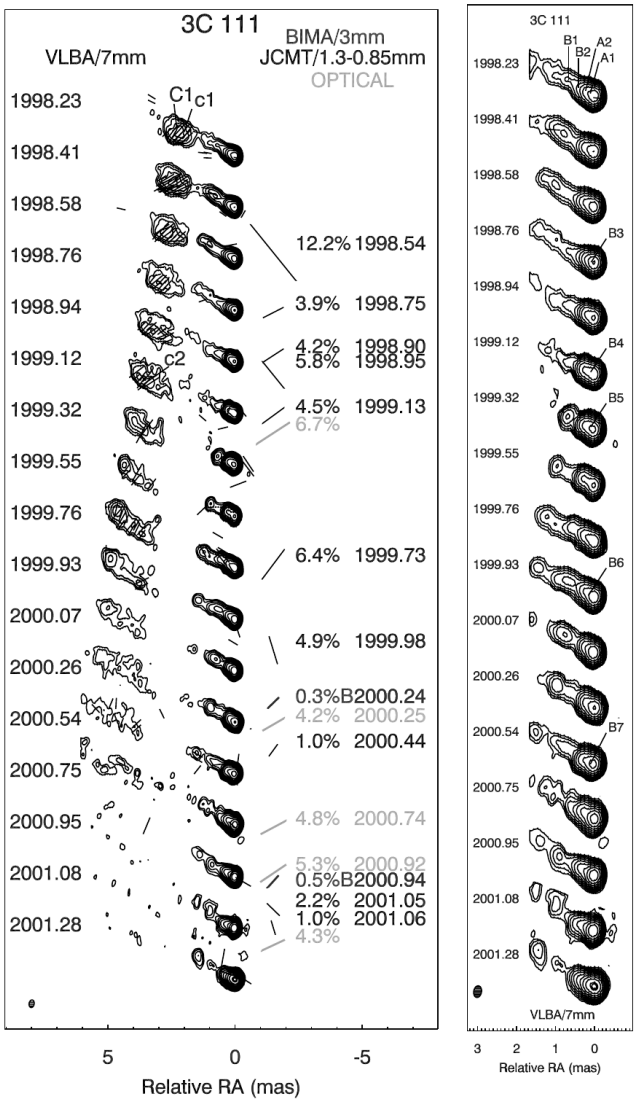

Figure 2.9: VLBA intensity maps of 3C 111 at 43 GHz illustrating the sub-parsec scale evolution of emission components. Figure adopted from Jorstad et al. (2005)

This function reaches a maximum value at an angle of,

$$\theta_{\max} = \cos^{-1}\left(\frac{v}{c}\right), \tag{2.25}$$

in which case,

$$v_{\rm app} = \frac{v}{\sqrt{1-\frac{v^2}{c^2}}} = \Gamma v. \tag{2.26}$$

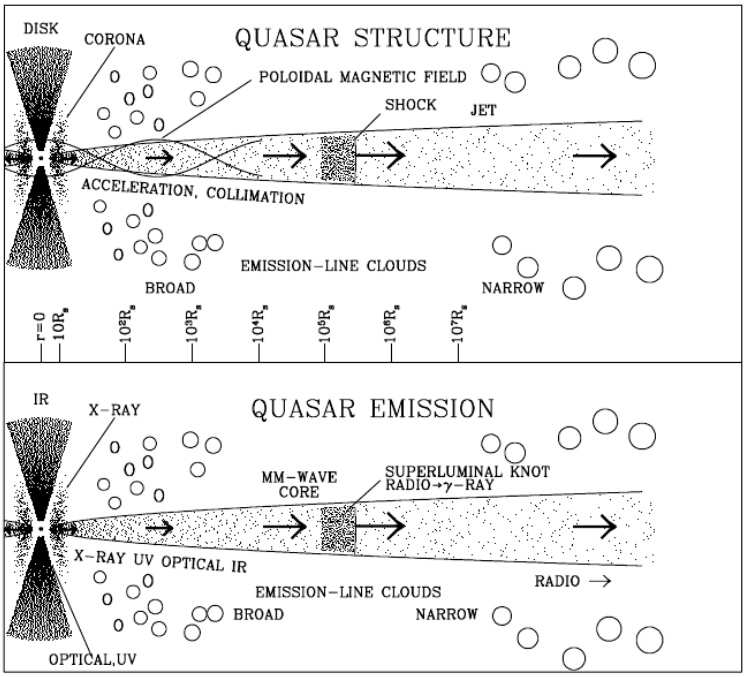

Figure 2.10: Diagram of the central structure of a radio-loud Quasar (top) and the associated emission regions (bottom), with darker shades indicting regions of higher intensity emission. Figure adopted from Marscher (2005).

where Γ is the Lorentz factor of the bulk flow. For relativistic motions $\Gamma \gg 1$, this can yield apparent motion faster than the speed of light.

2.4.4 The kiloparsec jet morphology

Multi-wavelength surveys of AGN jets have been carried out in order to study their kiloparsec morphology. On large scales the jet structures fall into the Fanaroff-Riley classification as discussed in section 2.3.1. High resolution imaging of these jets have revealed complex internal structures associated with them. Long term radio monitoring programs such as the MOJAVE (Monitoring of Jets in Active Galactic Nuclei with VLBA Experiments) at 15 Ghz (Kellermann et al., 2004; Lister et al., 2009) and RRFID (Radio Reference Frame Image Database) at 8 and 2 GHz (Piner et al., 2007) have studied the time dependent nature of the morphology of the jets. These studies have shown the presence of stationary as well as moving radio emission components in the jets. Some of the moving components showed apparent superluminal velocities up to $40c$. Additional time dependent structures such as jet bending and changes in the injection angle of the jet have also been noted (see e.g. Kellermann et al., 2004).

The large scale structures stretching over kiloparsec distances are divided into FR I and

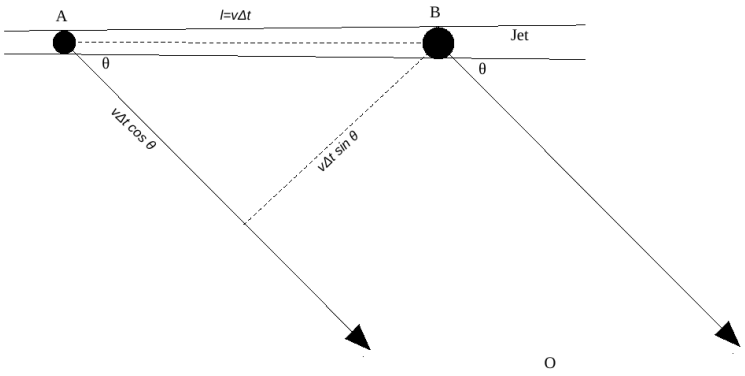

Figure 2.11: Diagram illustrating a blob propagating along a jet at relativistic velocity resulting in an apparent superluminal velocity.

FR II types depending on the total radio luminosity of the jets as well as the overall emission structure of the source. As mentioned previously FR I jets have the most prominent emission close to the central compact region and this deceases outward while the opposite is true for FR II sources. The luminosity division between FR I and FR II type jets are proportional to the radio as well as optical luminosity of the host galaxy, however, radio jets with luminosities $L_{\text{radio}} < 5 \times 10^{25}\text{WHz}^{-1}$ in the 1.4 GHz band are generally classified as FR I while those with luminosities higher than this are classified as FR II (Ledlow and Owen, 1996; Owen and White, 1991).

FR I type galaxies can be further divided by plume and lobe type morphologies. In plume type jet structures the jet usually becomes unstable causing it to meander. These jets often have ill-defined boundaries, with the emission steadily decreasing with distance from the core until it reaches below the observable limit. A lobed FR I has bright jets pushing outward from the core into an envelope structure. This envelope forms radio lobes at the edges of the jet. Radio observations of the spectral index distribution of the two types reveal that the lobe and plume type structures are not geometric effects due to a difference in viewing angle (see chapter 5, Böttcher et al., 2012). The plume jets have an increasing spectral index with distance from the core while for the lobed sources the spectral index deceases (Parma et al., 1996). FR II type galaxies only form lobe type structures, and the lobes contain hot spots and filaments in radio observation. The spectral index of these sources increase with distance from the core, which is opposite to the FR I lobed sources.

Not all jets are stable, and even though they may be collimated, they may suffer from bends and kinks. A jet bend occurs when the flow direction of the jet suddenly changes direction. These bends occur both on sub-parsec and larger distances from the cores. Because the bends that we observe are a combination of the projection of a three dimensional structure onto a two dimensional plane and relativistic effects, it is very difficult to determine the intrinsic change

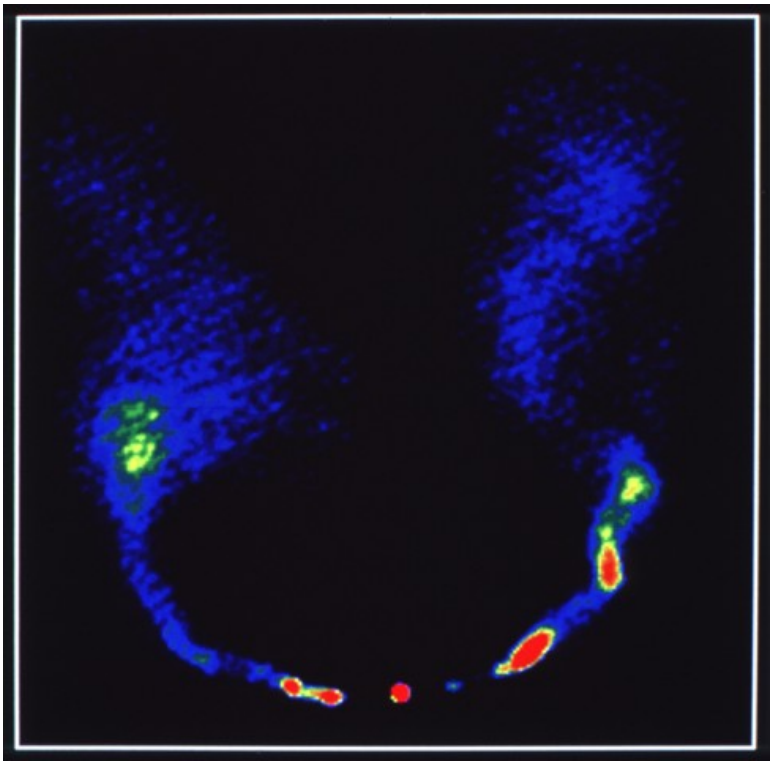

Figure 2.12: VLA image of 3c83.1 showing kiloparsec jet bending due to the ram pressure of intergalactic medium. Figures adopted from the NRAO website: http://images.nrao.edu/ (retrieved on 08/11/2016).

in the angle of the bend. A small change in the intrinsic angle of the jet may produce a large apparent bend in observations. This makes it hard to classify bends and determine their nature.

There are many reported cases of jets having sinusoidal bends on parsec scale distances. These sinusoidal patterns have been interpreted as helical structures within the jets (Denn et al., 2000; Hardee et al., 2005; Lobanov et al., 2003). Close to the core of the AGN, jet bending may be caused by Kelvin-Hemholtz instabilities, procession in the injection of material and magnetic kink type instabilities (see e.g. Hardee, 1979, for a theoretical analysis of the stability of cylindrical jet-like flows). On kiloparsec distances FR I type jets with two components on either side of the core, commonly have a U-shaped bend (see e.g. Figure 2.12). This bending is most likely caused by the relative motion between the nucleus and the inter galactic medium, which causes the ram pressure of the inter galactic material to deflect the large scale motion of the jet (see e.g. O'Dea and Owen, 1986).

To study the complex morphologies of the jets discussed above numerical fluid dynamic simulations can be constructed. In the next chapter the concepts of fluid dynamics and the numerical methods are summarized along with a review of the most important results which

have been obtained with these simulations.

Chapter 3

Numerical simulations of AGN jets

In the previous chapter the observational structures of AGN were discussed including the production, evolution and morphology of the relativistic jets observed in radio-loud sources. The long time scales on which these systems evolve, makes it difficult to obtain a complete understanding of their evolution through observations alone. Instead numerical methods have become a powerful tool to simulate AGN jets. This chapter will review numerically simulated relativistic jets in order to investigate their morphology and evolution. The numerical simulations are treated following a fluid dynamical approach. The study of fluid dynamics provides the governing equations for the macroscopic motion of a compressible medium. When this field of study is combined with that of thermodynamics one can provide a complete description of the properties of a fluid and determine possible future states of a system. This chapter is divided into two sections. The first section gives an overview of the numerical methods that can be used to create a simulation of relativistic jets, while the second section contains a discussion of previous simulation results and how they correlate to the observational data.

3.1 Fluid dynamics

Describing a relativistic AGN jet with fluid dynamics presents several challenges. AGN jets consists of very diffuse plasma (of which the exact composition is still unknown) moving at relativistic velocities within a magnetic field. In order to obtain an appropriate approximation when modelling a relativistic jet based upon a fluid dynamic approach, the assumptions presented by Blandford and Rees (1974) are normally applied. In this model it is assumed that the jets consist of a relativistic plasma containing magnetic fields. The density of the plasma propagating within the jet is very low, resulting in a collisional mean free path which can be larger than the typical radius of the jet. The static magnetic fields will, however, result in a small Larmor radius

(r_{L}) of the order of,

$$r_{\mathrm{L}} = 10^{-12}\gamma \left(\frac{\mathrm{B}}{1\ \mathrm{G}}\right)^{-1} \text{ parsec}, \tag{3.1}$$

for a relativistic proton with a Lorentz factor γ within a magnetic field of strength B (Ghisellini, 2013). Since the Larmor radius is much smaller than the typical radius of the jet, the plasma can be modelled by its fluid-like behaviour (Blandford and Rees, 1974).

The macroscopic motion of a fluid adheres to a set of conservation equations, describing the conservation of mass, momentum and energy. However, the complex nature of these governing equations do not allow for a single analytical solution of a relativistic jet environment to exist. In order to solve these equations and evolve the environment with time, numerical methods must be employed. An additional challenge in numerically simulating relativistic jets as a fluid is the large range of length scales that must be taken into account. In Chapter 2 it was mentioned that the mechanism responsible for launching the jet occurs in a regime on the order of $r_g \approx 10^{13}$ cm, while the large-scale structure of the jet can extend up to hundreds of kiloparsecs ($\sim 10^{23}$ cm). To create a numerical simulation which incorporates all of the processes that occur within AGN jets would require a numerical method with resolution comparable to the smallest length scale $\approx r_g$, and a domain covering the entire dimensions of the jet. Such simulations are too computational resource intensive to calculate with the current generation of computers. The continuous advance in computing technology and numerical algorithms, however, allows for the development of more accurate simulations incorporating more realistic environments, which can be used to study certain properties of AGN jets.

3.1.1 Fluid dynamic conservation equations

The fluid dynamic conservation equations are a set of non-linear, time dependant differential equations which are derived from the laws of conservation for matter, momentum and energy (Toro, 2009). These equations have the general form of,

$$\frac{\partial \mathbf{U}}{\partial t} + \nabla \cdot \mathsf{T}(\mathbf{U}) = \mathbf{S}(\mathbf{U}), \tag{3.2}$$

where $\mathbf{U}$ is a column vector consisting of conserved variables such as the mass density, the momentum and the energy of the fluid. $\mathsf{T}(\mathbf{U})$ is a tensor containing the flux vectors in the x, y and z directions, as a function of the conserved variables $\mathbf{U}$, and $\mathbf{S}(\mathbf{U})$ is a vector containing source terms, which are additional terms brought about by effects such as viscous and gravitational forces, as well as radiative cooling. This set of equations is known as the Navier-Stokes equations.

The constituents of equation (3.2) can take on different forms depending on the environment of the fluid. For example, in order to simulate the jet production mechanism close to the central SMBH accurately, the general relativistic effects of the large gravity as well as the relativistic effects of the fast moving plasma must be taken into account. In this case the constituents of the conservation equations (equation 3.2) would contain correction factors for the General

Relativistic Magneto Hydrodynamic (GRMHD) regime. An in depth review of GRMHD and the numerical simulations within this regime can be found in Font (2008). The constituents of equation (3.2) can be simplified if we only consider the morphology of the jet beyond a distance of $100r_g$. At this distance the general relativistic effects become negligible and only the relativistic motion of the fluid has to be taken into account. If we further assume that beyond this distance the dynamics of the jet is dominated by the kinetic energy of the fluid (i.e. the magnetic field has a negligible effect) the constituents of equation (3.2) are given by (see e.g. Mignone et al., 2007),

$$\mathbf{U} = \begin{bmatrix} \rho\Gamma \\ \rho\Gamma^2 h\mathbf{v} \\ \rho\Gamma^2 h - P \end{bmatrix}, \quad \mathsf{T}(\mathbf{U}) = \begin{bmatrix} \rho\Gamma\mathbf{v} \\ \rho\Gamma^2 h\mathbf{v}\mathbf{v} + P\mathbf{I} \\ \rho\Gamma^2 h\mathbf{v} \end{bmatrix}^T, \quad \mathbf{S}(\mathbf{U}) = 0, \tag{3.3}$$

where ρ is the proper density, P is the pressure, h is the specific enthalpy, Γ is the bulk flow Lorentz factor, $\mathbf{I}$ is a 3x3 unit matrix and $\mathbf{v}$ is the three velocity. The absence of source terms in equation (3.3) ($\mathbf{S}(\mathbf{U}) = 0$) implies the consideration of an ideal fluid with no viscosity. The set of conservation equations in this form is known as the Relativistic Hydrodynamic (RHD) regime of the Navier-Stokes equation.

3.1.2 The thermodynamics of a fluid

In order to completely describe a fluid a set of variables and relations are needed from which all the properties of the fluid can be calculated. This set of variables is referred to as the primitive variables and may include the pressure, the mass density, the velocity and the magnetic field within the fluid. The relation between primitive variables and additional fluid properties such as the energy and entropy are given by the laws of thermodynamics (e.g. Toro, 2009). The first law of thermodynamics relates the change in the internal energy of a system to the work done on or by the system and heat transfer,

$$\mathrm{d}e = \mathrm{d}q - p\mathrm{dv}, \tag{3.4}$$

where e represents the internal energy per unit mass, q is the heat per unit mass (specific heat, defined as energy transfer in the system), p is the pressure and $\mathrm{v} = (1/\rho)$ is the specific volume (Toro, 2009). The enthalpy per unit mass of a relativistic fluid is defined by,

$$h = c^2 + e + \frac{p}{\rho} = c^2 + \frac{p\gamma_{\mathrm{ad}}}{\rho(\gamma_{\mathrm{ad}} - 1)}, \tag{3.5}$$

where c is the speed of light.

From equation (3.4) we can define the change in specific heat in the system per unit temper-

ature T as the heat capacity C of the fluid, i.e.

$$C = \frac{\mathrm{d}q}{\mathrm{d}T} = \frac{\mathrm{d}e}{\mathrm{d}T} + p\frac{\mathrm{dv}}{\mathrm{d}T}. \tag{3.6}$$

From this one can derive the specific heat capacity at a constant pressure (C_p) and constant volume (C_v),

$$C_p = \left(\frac{\partial h}{\partial T}\right)_p, \tag{3.7}$$

$$C_\mathrm{v} = \left(\frac{\partial e}{\partial T}\right)_\mathrm{V}, \tag{3.8}$$

For an ideal gas in an adiabatic process (a process in which no heat transfer takes place) the relationship between the pressure and density of the fluid takes on a polytropic form,

$$p = K\rho^{\gamma_\mathrm{ad}}, \tag{3.9}$$

where K is a proportionality constant and $\gamma_\mathrm{ad} = C_p/C_\mathrm{v}$ is the ratio of the heat capacity at constant pressure to that at constant volume. From this result the equation of state relating the internal energy, pressure and density of the fluid can be derived as,

$$e = \frac{p}{\rho(\gamma_\mathrm{ad} - 1)}. \tag{3.10}$$

Another important property of a fluid is the velocity at which compression waves propagate through the system, called the speed of sound. The speed of sound in a relativistic fluid is expressed as (Böttcher et al., 2012, p91),

$$a_s^2 = c^2\gamma_\mathrm{ad}\frac{p}{h\rho}. \tag{3.11}$$

A useful quantity for expressing the velocities of objects travelling within a fluid is the Mach number. The Mach number defines the velocity in terms of the sound speed of the fluid,

$$M_s = \frac{v}{a_s}. \tag{3.12}$$

3.2 Numerical methods for fluid dynamics

In a fluid dynamic environment which is not in an equilibrium state the properties of the fluid discussed in the previous section will be time dependent. The dependence of these properties is governed by the fluid dynamic conservation equations discussed in section 3.1.1. These conservation equations (equation 3.2) can be solved numerically with various methods. Most of these methods involve the solution of an initial value problem, that is, a problem in which the

values of a set of primitive variables are specified at a time t_0. The change in these variables are calculated for a small time increment $\mathrm{d}t$, in order to determine what their values will be at a time $t_f = t_0 + \mathrm{d}t$.

In this section we will discuss the most commonly used numerical methods in the simulation of astrophysical environments, with the focus on simulating a relativistic jet. The section starts with an overview of the different discretization schemes. Upwind conservative Godunov schemes are then discussed in section 3.2.2, since these are the main numerical method used in PLUTO for evolving the conservation equations. In addition to this scheme the approximate Riemann solvers, necessary to advance the method with time, will be reviewed (section 3.2.3). For simplicity the derivations of numerical schemes in this discussion will focus on the adjective scalar equation, however the schemes can be extended for the use of the vector conservation equations. For an in-depth discussion on numerical methods in fluid dynamics the reader is referred to Toro (2009) and LeVeque et al. (2006).

3.2.1 Discretization schemes

For a distribution of variables in an environment the initial value problem cannot be evolved continuously over all space, and the spatial distribution of variables must instead be discretized. This discretization divides the spacial distribution function into finite values, which can take the form of points, cells or elements. The main discretization used for grid based fluid dynamic simulations are point (finite difference) and cell (finite volume) schemes.

The finite element discretization is mainly used in a different branch of numerical methods, referred to as smoothed particle hydrodynamics (SPH). In SPH methods the environment is not defined as a grid but rather as a number of finite elements containing fluid properties, called particles. These methods are robust and provide many attractive features such as dynamic resolution and spacial domains, and have been used to accurately simulate many astrophysical environments such as stellar winds (see e.g. Mohamed et al., 2012). There are however certain environments where these methods have disadvantages compared to grid based methods. The dynamic resolution of SPH based simulations is dependent on the density of particle elements in the environment which is unfavourable in environments with low density regions of interest. In these cases grid based methods provide better accuracy and are therefore better suited for simulating environments such as AGN jets. For this reason it was chosen to focus on grid based methods in this study, however the interested reader can find an introduction to SPH in Monaghan (1992).

The first grid based numerical astrophysical codes such as ZEUS (Stone and Norman, 1992a,b) and NIRVANA+ (Ziegler, 1998) employed point based finite difference schemes to simulated astrophysical environments. However it was later shown that these codes presented significant errors in some environments (see e.g. Falle, 2002). More recent fluid dynamic codes such as PLUTO have moved to a finite volume discretization and employ high resolution shock capturing schemes in order to obtain better accuracy when simulating environments containing

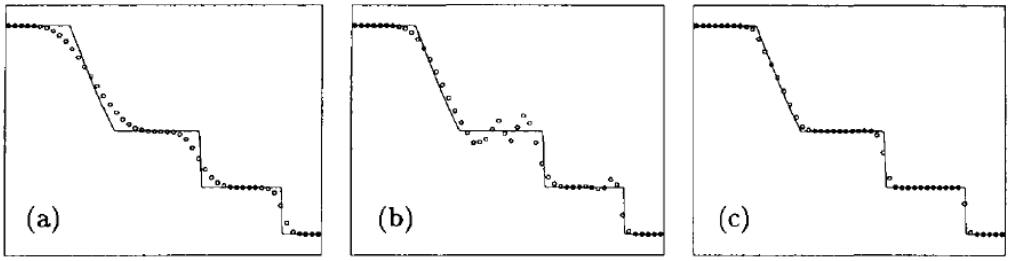

Figure 3.1: Comparison of different numerical solver solutions to the shock tube or Sod problem for a) a Godunov scheme showing a smeared discontinuity, b) a Lax-Wendorff style second-order scheme showing oscillations and c) a high resolution method with superbee limiter. In each diagram the solid line indicates the exact solution. Figure adopted from LeVeque et al. (2006), figure 1.1 p 2.

discontinuities (Mignone et al., 2010a).

The largest inaccuracies in fluid dynamic numerical methods occur where discontinuities such as shocks are formed within the medium. If these discontinuities are approximated as continuous functions they may either be smeared out or generate oscillations, affecting the structure of the discontinuities. Examples of these effects are shown in Figure 3.1 where different numerical schemes are applied to the shock tube problem (Sod, 1978).

The finite difference and finite volume schemes will be discussed in detail in the following subsections. The discussion will closely follow that given by Toro (2009).

3.2.1.1 Finite difference schemes

As previously mentioned the finite difference discretization divides the environment into a set of spatial points. Consider a conserved scalar $u(x,t)$ in a one dimensional environment with domain $0 \leq x \leq L$, adhering to a conservation equation of the form,

$$\frac{\partial u}{\partial t} + \frac{\partial f(u)}{\partial x} = 0, \tag{3.13}$$

where

$$f(u) = au(x,t), \tag{3.14}$$

and a is the wave propagation speed of the fluid. The initial value (IV) and boundary conditions (BC) of the scalar in the environment is given by,

$$\text{IV:} \quad u(x,0) = u_0(x), \tag{3.15}$$

$$\text{BC:} \quad \begin{array}{ll} u(0,t) & = u_{\text{left}}(t), \\ u(L,t) & = u_{\text{right}}(t), \end{array} \tag{3.16}$$

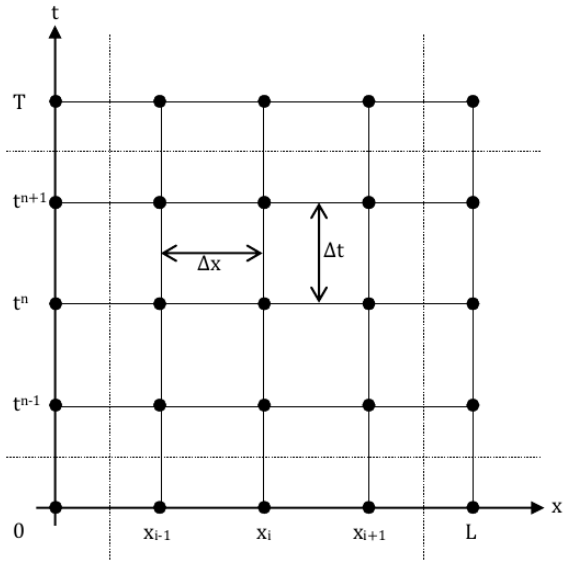

Figure 3.2: Illustration in one spatial (x) and time dimension (t) of a domain of length L containing N points with the finite difference discretization

where $u_0(x)$ is the initial value function of the environment at time $t = 0$, and $u_{\text{left}}(t)$ and $u_{\text{right}}(t)$ are the upper and lower boundary values, which are assumed to be known functions of time.

To apply the finite difference discretization we define N points on the domain $0 \leq x \leq L$ with separation,

$$\Delta x = \frac{L}{N-1}. \tag{3.17}$$

We also define,

$$x_i = i\Delta x,\ i = 0, ..., N-1 \tag{3.18}$$

where x_i denotes the position of the ith point (Figure 3.2).

In order to solve this initial boundary value problem (IBVP), $u(x,t)$ must be evolved with time from the initial value $u_0(x)$. This can be achieved by applying Taylor's theorem, which states that the value of a smooth function $g(y)$ at a position $y_2 = y_1 + \Delta y$ can be expressed as a series expansion,

$$g(y_2) = g(y_1) + \sum_k \frac{(\Delta y)^k}{k!} g^{(k)}(y_1), \tag{3.19}$$

where $g^{(k)}(y_1)$ denotes the kth derivative of $g(y)$ at y_1. The derivative $g^{(k)}(y_1)$ can be approximated in several ways. The first-order forward and reverse approximations to the first derivative can be written as,

$$g^{(1)}(y) = \frac{\mathrm{d}g(y)}{\mathrm{d}y} = \frac{g(y_2) - g(y_1)}{\Delta y} + O(\Delta y), \tag{3.20}$$

and

$$g^{(1)}(y) = \frac{\mathrm{d}g(y)}{\mathrm{d}y} = \frac{g(y_1) - g(y_0)}{\Delta y} + O(\Delta y), \tag{3.21}$$

respectively, where $y_0 = y_1 - \Delta y$, $y_2 = y_1 + \Delta y$ and $O(\Delta y)$ is the truncation error. If Δy is sufficiently small we find an accurate first-order approximation for the first derivative. A second-order accurate approximation of the derivative, called the centred approximation, can be made by combining the forward and reverse approximations as,

$$g^{(1)}(y) = \frac{\mathrm{d}g(y)}{\mathrm{d}y} = \frac{g(y_2) - g(y_0)}{2\Delta y} + O(\Delta y)^2. \tag{3.22}$$

In this discussion we will consider the reverse approximation.

If we assume that the scalar function, $u(x,t)$, defined in equation (3.13) is smooth with time we can apply Taylor's theorem at a position x_i during a time step $n = t_n/\Delta t$ to determine the value of the point at time step $n+1$,

$$u_i^{n+1} \approx u_i^n + \Delta t \frac{\partial u_i^n}{\partial t}, \tag{3.23}$$

where Δt is the time increment with which the equation will be evolved. Substituting equation (3.13) into this result we obtain,

$$u_i^{n+1} \approx u_i^n - a\Delta t \frac{\partial u_i^n}{\partial x}. \tag{3.24}$$

According to equation (3.21) we can rewrite the spatial derivative as,

$$\frac{\partial u_i^n}{\partial x} = \frac{u_i^n - u_{i-1}^n}{\Delta x} + O(\Delta x), \tag{3.25}$$

and substituting equation (3.25) into (3.24) results in,

$$u_i^{n+1} \approx u_i^n - c(u_i^n - u_{i-1}^n), \tag{3.26}$$

where $c = a\Delta t/\Delta x$ is known as the Courant-Friedrichs-Lewy (CFL) number and can be considered as the ratio of the wave propagation speed a to the grid speed $\Delta x/\Delta t$, which is defined by the discretization of the domain. Since $u_0(x_i)$ and $u_0(x_{i-1})$ are known in the initial boundary value problem we can use equation (3.26) to determine the value of $u(x, t_{n+1})$ in the environment. The forward and centred derivative approximations can be used to derive similar schemes, however, not all of the derivative approximations that are given result in stable solutions. In fact there are several conditions that have to be met for stability (see e.g. the discussion on von Neuman stability analysis in Toro, 2009, pp. 167-171). It can be shown that equation (3.26) only yields a stable solution if $0 \leq c \leq 1$, which limits the choice of discretization such that $a \leq \Delta x/\Delta t$ and, therefore, for a fixed grid limits the time steps to $\Delta t \leq \Delta x/a$.

The scheme presented in equation (3.26) is known as the first-order upwind finite difference

scheme, since the value of the upwind cell, the side from which information flows, $(i-1)$ is used to determine the next time step. It was first implemented by Courant, Isaacson and Rees (1952) and is therefore also referred to as the CIR scheme.

If a becomes negative, equation (3.26) will represent a downwind scheme and become unconditionally unstable. In such a case the upwind scheme is represented by,

$$u_i^{n+1} = u_i^n - c(u_{i+1}^n - u_i^n), \tag{3.27}$$

for $-1 \leq c \leq 0$. A generalized upwind scheme can be created by combining both equations (3.26) and (3.27) in the form,

$$u_i^{n+1} = u_i^n - c^+(u_i^n - u_{i-1}^n) - c^-(u_{i+1}^n - u_i^n), \tag{3.28}$$

where,

$$\begin{array}{l} c^+ = \frac{1}{2}\frac{\Delta t}{\Delta x}(a + |a|), \\ c^- = \frac{1}{2}\frac{\Delta t}{\Delta x}(a - |a|), \end{array}, \tag{3.29}$$

for $0 \leq |c| \leq 1$. This scheme holds for any hyperbolic linear partial differential equation and can thus be used to evolve the full fluid conservation equations (equation 3.2) with time.

3.2.1.2 Finite volume discretization

An alternative discretization scheme which can be used to solve equation (3.13) is the finite volume discretization. Consider again the IBVP given by equations (3.13) and (3.15). In this scheme the domain of length L is divided into a grid of M finite cells each with a uniform length given by,

$$\Delta x = x_{i+\frac{1}{2}} - x_{i-\frac{1}{2}} = \frac{L}{M}. \tag{3.30}$$

In this scheme i indicates the number of the cell, and $x_{i+\frac{1}{2}}$ and $x_{i-\frac{1}{2}}$ are the upper and lower boundaries of the ith cell. We define u_i^n according to a cell centred method, that is u_i^n is the average value of the conserved scalar within a cell and is positioned at the centre of the ith cell at a time t^n (Figure 3.3),

$$u_i^n = \frac{\int_{x_{i+\frac{1}{2}}}^{x_{i+\frac{1}{2}}} u(x, t^n)\mathrm{d}x}{\Delta x}, \tag{3.31}$$

where $u(x, t^n)$ is the value of the scalar at position x within the cell. This allows the value of the scalar to vary within each cell even though the average remains constant.

There are several methods to evolve the IBVP problem with finite volume schemes. The most common methods use interpolation between adjacent cell averages to determine the boundary conditions between cells. Using the boundary values between cells, the flux functions $(\partial f(u)/\partial x)$ can be solved and used to evolve equation (3.13). One example scheme in which this discretization is employed is the High Resolution Shock Capturing (HRSC) Godunov algorithms.

The HRSC schemes can be understood by dividing the scheme into three steps. First, the

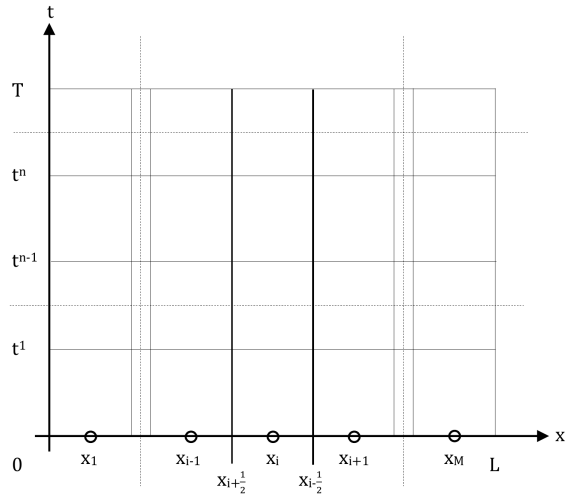

Figure 3.3: Illustration of a domain of length L with a finite volume discretization. Here x_i is the position at the centre of the ith cell where the averaged grid variables are defined. $x_{i+\frac{1}{2}}$ and $x_{i-\frac{1}{2}}$ denotes the upper and lower boundaries of the ith cell

flux functions are interpolated for the boundaries of each cell in the structured mesh. Second, a Riemann problem is solved between the boundaries. Third, the time is evolved by a small increment Δt. This method will be discussed further in the subsequent sections.

3.2.2 First-order Godunov upwind method

Godunov (1959) was the first to successfully extend the CIR scheme (discussed in section 3.2.1.1) to a conservative method in the form of

$$u_i^{n+1} = u_i^n + \frac{\Delta t}{\Delta x}\left[f_{i-\frac{1}{2}} - f_{i+\frac{1}{2}}\right], \tag{3.32}$$

where,

$$\begin{aligned} f_{i+\frac{1}{2}} &= f_{i+\frac{1}{2}}\left(u_{i-l_L}^n, ..., u_{i+l_R}^n\right), \\ f_{i-\frac{1}{2}} &= f_{i-\frac{1}{2}}\left(u_{i-l_L}^n, ..., u_{i+l_R}^n\right), \end{aligned} \tag{3.33}$$

are the numerical fluxes at the upper and lower cell boundaries respectively, and l_L and l_R are two non-negative integers[i]. The Godunov upwind method treats the environment as a piecewise constant distribution, shown in Figure 3.4. This implies that the value of the conserved scalar for each cell is constant and equal to the average value and that the cells are separated by a discontinuity, which gives rise to a Riemann problem on the boundary of each cell, of the form

[i]The numerical fluxes are an approximation of the physical flux

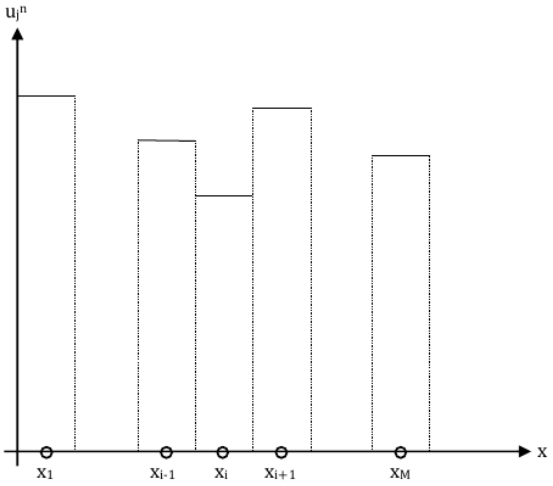

Figure 3.4: Assuming a constant distribution of variables in a cell forms a piecewise spatial distribution of the conserved scalar on the domain.

of,

$$\frac{\partial u}{\partial t} + \frac{\partial f(u)}{\partial x} = 0, \tag{3.34}$$

with the initial condition,

$$u(x,0) = u_0(x) = \begin{cases} u_i^n & \text{if } x < 0 \\ u_{i+1}^n & \text{if } x > 0 \end{cases}, \tag{3.35}$$

where $x = 0$ is the boundary of the cell. The problem is illustrated in Figure 3.5.

The Godunov scheme solves the value of the next time step u_i^{n+1} by solving the Riemann problem on both boundaries and taking the integral average of the two local solutions. This can be expressed as,

$$u_i^{n+1} = \frac{1}{\Delta x}\left[\int_0^{\frac{1}{2}\Delta x} u_{i-\frac{1}{2}}\left(\frac{x}{\Delta t}\right)\mathrm{d}x + \int_{-\frac{1}{2}\Delta x}^{0} u_{i+\frac{1}{2}}\left(\frac{x}{\Delta t}\right)\mathrm{d}x\right], \tag{3.36}$$

where $\Delta t = t^{n+1} - t^n$ is the time increment and the exact solution to the Riemann problem at the lower and upper boundaries of the cell are,

$$u_{i-\frac{1}{2}}\left(\frac{x}{t}\right) = \begin{cases} u_{i-1}^n & \text{if } x/t < a \\ u_i^n & \text{if } x/t > a \end{cases}, \tag{3.37}$$

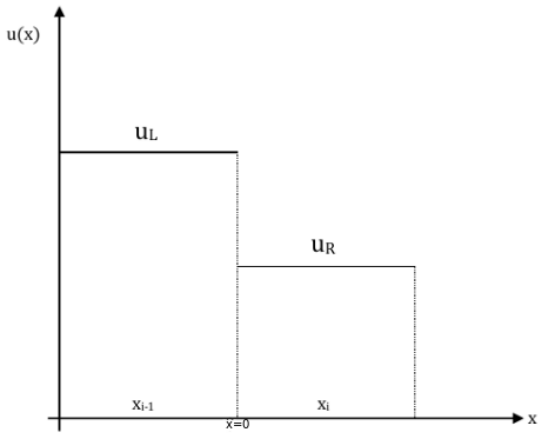

Figure 3.5: The Riemann problem at the lower boundary of the ith cell, where $u(x)$ is given as a piecewise constant function with a discontinuity at the cell boundary $x = 0$.

and

$$u_{i+\frac{1}{2}}\left(\frac{x}{t}\right) = \begin{cases} u_i^n & \text{if } x/t < a \\ u_{i+1}^n & \text{if } x/t > a \end{cases}, \tag{3.38}$$

In this expression x and t are defined locally in the cell (see Toro, 2009, chapter 4). Creating a combined solution $\widetilde{u}(x,t)$ to both Riemann problems (given by equations 3.37 and 3.38) we can rewrite equation (3.36) as,

$$u_i^{n+1} = \frac{1}{\Delta x}\int_{x_{i-\frac{1}{2}}}^{x_{i+\frac{1}{2}}} \widetilde{u}(x,\Delta t)\mathrm{d}x. \tag{3.39}$$

If we consider $\widetilde{u}(x,t)$ as an exact solution to equation (3.13) we can rewrite equation (3.39) in an integral form as,

$$u_i^{n+1} = \frac{1}{\Delta x}\left[\int_{x_{i-\frac{1}{2}}}^{x_{i+\frac{1}{2}}} \widetilde{u}(x,0)dx + \int_0^{\Delta t} f(\widetilde{u}(x_{i-\frac{1}{2}},t))\mathrm{d}t - \int_0^{\Delta t} f(\widetilde{u}(x_{i+\frac{1}{2}},t))\mathrm{d}t\right], \tag{3.40}$$

which leads to a general solution in the form of equation (3.32) with,

$$f_{i-\frac{1}{2}} = \frac{1}{\Delta t}\int_0^{\Delta t} f(\widetilde{u}(x_{i-\frac{1}{2}},t))\mathrm{d}t, \tag{3.41}$$

and

$$f_{i+\frac{1}{2}} = \frac{1}{\Delta t}\int_0^{\Delta t} f(\widetilde{u}(x_{i+\frac{1}{2}},t))\mathrm{d}t, \tag{3.42}$$

the flux functions of the lower and upper boundaries. The discussion above follows the solution for the scalar $u(x,t)$ in equation (3.13), however it can be applied to non-linear hyperbolic partial

differential equations, such as the conservation laws, in general. The Godunov method described above is a first-order scheme and a very high resolution is needed to obtain reasonable accuracy. Higher order extensions of the Godunov method do exist and the reader is referred to chapters 12, 14 and 16 of Toro (2009) for a detailed discussion.

3.2.3 Numerical Riemann solvers

In the Gonunov scheme a Riemann problem must be solved for each cell boundary in the domain, which is by far the most computationally intensive process in this method. Exact solutions to the Riemann problem do exist, however calculating these solutions are computationally expensive and, therefore, many numerical codes find approximations to the problem which yields faster results with reasonable accuracy. A complete discussion on Riemann problems and obtaining their exact solutions is given in chapter 4 of Toro (2009).

There are two types of approximate Riemann solvers: the first finds the approximate solution to the flux functions, while the second finds an approximation to the state of the problem and evaluates the flux functions at the approximated state. The second method is usually the least computationally intensive but this sacrifices the accuracy of the solution. This may lead to inaccurate (unphysical) solutions at regions with discontinuous flows. A large number of approximate Riemann solvers exist for both of the above mentioned types, each with different advantages. To create solutions containing the advantages of more than one solver hybrid methods have also been designed. In this study the discussion of the different approximate Riemann solvers will be limited to the two shock Riemann solver, the Harten, Lax van Leer (HLL) Riemann solver and the Lax-Friedrichs Rusanov flux solver. These solvers were identified as possible candidates for the numerical simulations designed in this work.

3.2.3.1 The two shock Riemann solver (TSRS)

The two shock Riemann solver is based on approximations to the exact solution of the state of the Riemann problem. As an example one exact solution to the pressure flux Riemann problem is given by,

$$f(p) \equiv f_L(p, \mathbf{W}_L) + f_R(p, \mathbf{W}_R) + \Delta v = 0, \tag{3.43}$$

where R and L represents the right and left hand side of the boundary of the cell and

$$\Delta v = v_R - v_L, \tag{3.44}$$

is the difference in the velocity of the fluid across the boundary. This solution shows that the pressure flux is zero over the discontinuity. The two shock solver assumes that the solution comprises of two non-linear shock waves with the approximation,

$$f(p) = (p - p_L)g_L(p) + (p - p_R)g_R(p) + v_R - v_L = 0, \tag{3.45}$$

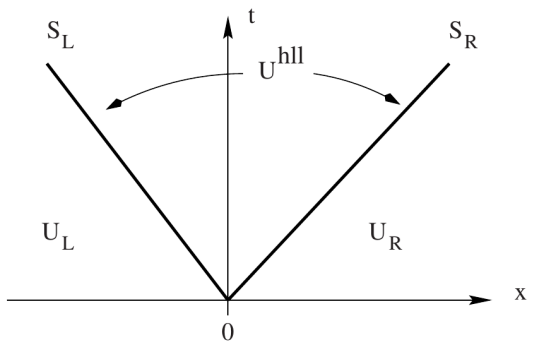

Figure 3.6: The HLL approximation to the Riemann problem at the boundary of a cell where U_L and U_R is the vector of the conserved properties of the fluid on either side of the boundary and $\mathbf{U^{hll}}$ is the approximate intermediate state. The three states are separated by two waves with velocity S_L and S_R. Figure adopted from Toro (2009) figure 10.3.

and

$$g_K(p) = \left[\frac{2}{(\gamma_{\rm ad}+1)\rho_K(p + \frac{\gamma_{\rm ad}-1}{\gamma_{\rm ad}+1}p_K)} \right]^{\frac{1}{2}}, \tag{3.46}$$

for $K = L$ or R. Based of the approximation for the pressure flux the exact solution to the Riemann problem can be obtained using shock relations. Since this approximation is applied to the exact solution this Riemann solver is very accurate, but computationally less expensive that the complete exact solution.

3.2.3.2 The Harten Lax van Leer Riemann solvers (HLL)

The HLL Riemann solver was first introduced in 1983 and constructs an approximate solution to the Riemann problem at the boundary consisting of three states separated by a two waves (Harten et al., 1983). The upper and lower states are given by the left and right boundary values of the Riemann problem, while an intermediate state is introduced between them. Figure 3.6 illustrates the three state solution. This approach obtains an approximation for the inter-cell flux $\mathbf{F}$ directly and then solves for $\mathbf{U}_i^{n+1}$. In order to obtain a solution in this configuration, estimates of the maximum signal speeds at the discontinuity between adjacent cells (S_R and S_L) is required. Davis (1988) and Einfeldt (1988) independently proposed different ways to calculate the wave speeds of the flux, which made the application of the HLL scheme possible. The resulting HLL Riemann solvers are very robust and efficient approximate solvers, used over a wide variety of applications.

The weakness of the HLL scheme is the assumption of the two wave configuration, which is only correct for a system of two hyperbolic conservation equations. This can result in in-

accurate resolution for features like contact surfaces and will cause them to appear smeared in the simulation instead of as sharp discontinuities. To improve the problem Einfeldt et al. (1991) proposed a modified version of the HLL Riemann solver know as the HLLM solver. The modifications include the change of the single intermediate state from a constant to a linear distribution. The distribution is controlled by parameters that determine the excessive dissipation of the intermediate waves.

A different solution to this problem was proposed by Toro et al. (1994) in the form of a three wave model containing four states. The solution consists of two states in the intermediate region of the Riemann problem, instead of the single state in the HLL solver. This scheme became known as the HLLC Riemann solver. Since its initial invention the solver has undergone several modifications to improve its accuracy (for example new methods for determining the wave speeds were proposed by Batten et al., 1997). For an complete review on the HLL family of Riemann solvers see e.g. Toro (2009), pp 315-336, and references therein.

As mentioned previously the HLL Riemann solver solves the flux functions in three states, which can be represented as,

$$\mathbf{F}^{hll}_{i+\frac{1}{2}} = \begin{cases} \mathbf{F}_L & \text{if } 0 \leq S_L, \\ \frac{S_R\mathbf{F}_L - S_L\mathbf{F}_R + S_L S_R(\mathbf{U}_R - \mathbf{U}_L)}{S_R - S_L} & \text{if } S_L \leq 0 \leq S_R, , \\ \mathbf{F}_R & \text{if } 0 \geq S_R \end{cases} \tag{3.47}$$

Here S_R and S_L are the wave speeds in the medium, $\mathbf{U}$ is the conserved vector given by equation (3.3) and the subscripts R and L denote the values on the right and left hand side of the boundary respectively. The wave speed can be calculated in various ways. Toro et al. (1994) proposed wave speeds based on pressure estimates of the intermediate state in the wave solution,

$$S_L = v_L - a_L q_L, \tag{3.48}$$

$$S_R = v_R + a_R q_R, \tag{3.49}$$

where v is the particle speed, a is the sound speed and q is given by

$$q_K = \begin{cases} 1 & \text{if } p_\star \leq p_K, \\ \left[1 + \frac{\gamma_{ad}+1}{2\gamma_{ad}} \frac{p_\star}{p_K - 1}\right]^{\frac{1}{2}} & \text{if } p_\star > p_K \end{cases}, \tag{3.50}$$

The wave speeds S_K is assigned distinguishing between shock waves with the true shock speed, and rarefaction waves, with the rarefaction speed. The variable $p_\star$ is an approximation to the pressure in the intermediate state. There are also several ways to approximate the pressure, for example, the Primitive Variable Riemann Solver (PVRS), given by,

$$p_{\text{pvrs}} = \frac{1}{2}(p_L + p_R) - \frac{1}{2}(v_R - v_L)\,\overline{\rho}\overline{a}, \tag{3.51}$$

where,

$$\begin{aligned} \overline{\rho} &= \tfrac{1}{2}\left(\rho_L + \rho_R\right), \\ \overline{a} &= \tfrac{1}{2}\left(a_L + a_R\right). \end{aligned} \tag{3.52}$$

For the HLLC Riemann solver containing a three wave solution, the solution to the flux function becomes,

$$\mathbf{F}^{hllc}_{i+\frac{1}{2}} = \begin{cases} \mathbf{F}_L & \text{if } 0 \le S_L, \\ \mathbf{F}_{\star L} & \text{if } S_L \le 0 \le S_\star, \\ \mathbf{F}_{\star R} & \text{if } S_\star \le 0 \le S_R, \\ \mathbf{F}_R & \text{if } 0 \ge S_R \end{cases}, \tag{3.53}$$

where $S_L \le S_R$ and,

$$\mathbf{F}_{\star K} = \frac{S_\star\left(S_K \mathbf{U}_K - \mathbf{F}_K\right) + S_K\left(p_K + \rho_L\left(S_K - v_K\right)\left(S_\star - v_K\right)\right)\mathbf{D}_\star}{S_K - S_\star}, \tag{3.54}$$

where $\mathbf{D}_\star = [0, 1, 0, 0, S_\star]$ and intermediate wave speed $S_\star$ can be calculated as,

$$S_\star = \frac{p_R - p_L + \rho_L v_L\left(S_L - v_L\right) - \rho_R v_R\left(S_R - v_R\right)}{\rho_L\left(S_L - v_L\right) - \rho_R\left(S_R - v_R\right)}. \tag{3.55}$$

The HLLC Riemann solver provides a method that is both accurate and time efficient and is one of the best approximate Riemann solver currently available.

3.2.3.3 The time variation diminishing Lax-Friedrichs Riemann solver (TVDLF)

The Lax-Friedrichs scheme was originally defined for a differencing scheme (Lax, 1954), however, it has been applied to many different problems. This includes using the scheme to derive an approximate Riemann solver. The adapted scheme provides solutions to the flux functions in the form of (Mignone et al., 2010a),

$$\mathbf{F}_{i+\frac{1}{2}} = \frac{1}{2}\left(\mathbf{F}^n_i + \mathbf{F}^n_{i+1}\right) + \frac{1}{2}|S_{\max}|\left(\mathbf{U}^n_i - \mathbf{U}^n_{i+1}\right), \tag{3.56}$$

and,

$$\mathbf{F}_{i-\frac{1}{2}} = \frac{1}{2}\left(\mathbf{F}^n_{i-1} + \mathbf{F}^n_i\right) + \frac{1}{2}|S_{\max}|\left(\mathbf{U}^n_{i-1} - \mathbf{U}^n_i\right), \tag{3.57}$$

where $S_{\max}$ is the maximum wave speed in the fluid that can be determined by the various techniques discussed for the HLL solver. The resulting flux functions can be directly substituted into equation (3.32) to determine the values of $\mathbf{U}^{n+1}_i$. This scheme provides a more stable solution than the previously discussed HLL solvers, however, it sacrifices accuracy.

3.2.4 Higher-order solvers

The solution provided by different numerical schemes can be characterized by four properties: consistency, stability, convergence and accuracy. The central bases of a good numerical scheme

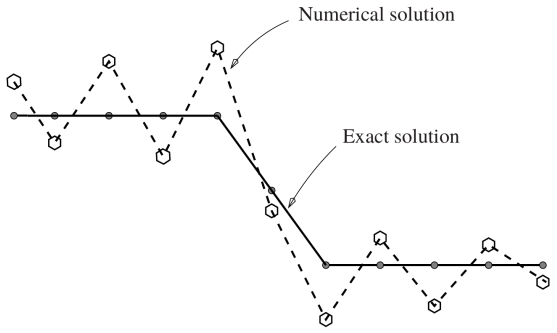

Figure 3.7: Oscillations introduced by numerical solvers, where the solid line indicates the exact solution and the dashed line indicates the numerical approximation. Figure adopted from Toro (2009) figure 13.11.

is achieving high-order accuracy without producing spontaneous (unphysical) oscillations. These unphysical oscillations are artefacts produced by numerical solvers in the vicinity of large gradients. This phenomenon is depicted in Figure 3.7, where the exact solution is denoted by the solid line and the numerical solution by the dashed line. Due to the presence of a large slope the points confining the slope are calculated with a slight error. This error propagates into the regions of constant values as oscillating waves. The production of these waves may become amplified as the time is evolved, as the values of the variables are updated with the oscillations. This will ultimately lead to an unphysical solution. The unphysical oscillations are characteristic of higher-order numerical schemes. In this section we will examine the measures that can be taken to extended numerical schemes to higher-orders to improve the accuracy of the solution, while limiting the occurrence of unphysical oscillations.

In order to extend the first-order Godunov scheme discussed in section 3.2.2, a non-linear method has to be constructed in the form of a Total Variation Diminishing (TVD) method. These TVD schemes are based on the premise that the variation in the approximated solution should not increase with time, which implies that these solutions are inherently convergent for scalar problems. One extension that can be applied to create such a method is the addition of artificial viscosity to the numerical solution (discussed in e.g. Richtmyer and Morton, 1967). Artificial viscosity can be introduced into numerical schemes in two ways. The first is by adding additional source terms to the conservation equations (equation 3.2) that are evolved with time. The second method introduces limiting algorithms in the numerical scheme, producing viscosity internal to the numerical scheme.

Van Leer (1977a,b, 1979) proposed a way of extending the accuracy of first-order numerical schemes by modifying the piecewise distribution of the cell averages. The simplest way to employ this is by replacing the constant state of the cell with a piecewise linear function. This can be

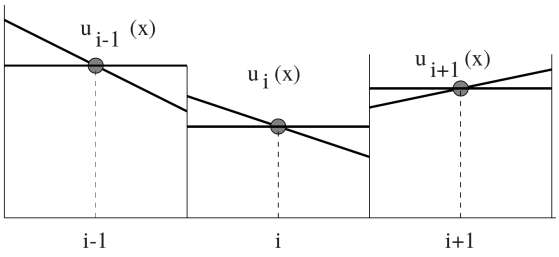

Figure 3.8: Diagram of the reconstructed Riemann problem for three consective cells. Figure adopted from Toro (2009) figure 13.6.

represented as,

$$u_i(x) = u_i^n + \frac{(x - x_i)}{\Delta x}\Delta i, \quad x \in [0, \Delta x], \tag{3.58}$$

where u_i^n is the cell average as defined in equation (3.31) and $\Delta i/\Delta x$ is the slope of the linear function. The term Δi can be calculated as,

$$\Delta i = \frac{1}{2}\left[(1+\omega)(u_i^n - u_{i-1}^n) + (1-\omega)(u_{i+1}^n - u_i^n)\right], \tag{3.59}$$

where $-1 \leq \omega \leq 1$ is a free parameter. If $\omega = 0$ the approximation is a centred difference approximation, determining the value of $u_i(x)$ based on both the adjacent cells. $\omega = 1$ and $\omega = -1$ gives the reverse and forward difference approximations respectively, determining $u_i(x)$ based on the lower or upper cell values. This reconstruction yields new boundary values for each cell,

$$u_i^L = u_i^n - \frac{1}{2}\Delta i, \tag{3.60}$$

and

$$u_i^R = u_i^n + \frac{1}{2}\Delta i, \tag{3.61}$$

where $x_i = \frac{1}{2}\Delta x$ is the centre coordinate of the cell. The reconstruction process leads to a new Generalized Riemann problem in which the wave solutions have curved paths in the x-t space, when the position of the wave is plotted with time. The exact initial value Riemann problem of the reconstructed linear functions become,

$$\begin{aligned} &\frac{\partial u}{\partial t} + \frac{\partial f(u)}{\partial x} = 0, \\ \text{IV:} \quad &u(x,0) = u_0(x) = \begin{cases} u_i(x) & \text{if } x < 0 \\ u_{i+1}(x) & \text{if } x > 0 \end{cases}. \end{aligned} \tag{3.62}$$

This reconstructed generalized Riemann problem is illustrated in Figure 3.8.

Ben-Artzi and Falcovitz (1984) are credited with the first study to develop a scheme which

evolved the environment based on the generalized Riemann problem, however this scheme is somewhat complex and resource intensive to implement. A good approximation to this problem can be achieved by using the previously discussed approximate solvers, considering constant boundary values as given by equations (3.60) and (3.61). This method of data reconstruction is known as the Monotone Upstream-centred Scheme for Conservation Laws (MUSCL) and is widely used in current numerical codes to provide higher-order accuracy. One extension of this scheme which constructs a second-order fully discrete scheme is the MUSCL-Hancock scheme. In this scheme the piecewise boundary values are reconstructed based on equations (3.60) and (3.61), and they are evolved with a time increment $\frac{1}{2}\Delta t$ as,

$$\begin{aligned} \bar{u}_i^L &= u_i^L - \frac{1}{2}\frac{\Delta t}{\Delta x}\left[f(u_i^L) - f(u_i^R)\right], \\ \bar{u}_i^R &= u_i^R - \frac{1}{2}\frac{\Delta t}{\Delta x}\left[f(u_i^L) - f(u_i^R)\right]. \end{aligned} \tag{3.63}$$

The evolved boundary values $\bar{u}_i^L$ and $\bar{u}_i^L$ are used to construct a Riemann problem,

$$\begin{aligned} &\frac{\partial u}{\partial t} + \frac{\partial f(u)}{\partial x} = 0, \\ \text{IV:}\quad &u(x,0) = u_0(x) = \begin{cases} \bar{u}_i^R \text{ if } x < 0 \\ \bar{u}_{i+1}^L \text{ if } x > 0 \end{cases}, \end{aligned} \tag{3.64}$$

which is solved using the first-order Godunov scheme discussed in section 3.2.2.

Another second-order extension to the first-order Godunov scheme, proposed by Colella (1985), is the piecewise linear method (PLM). In this scheme the flux function is approximated as,

$$f_{i+\frac{1}{2}}^{PLM} = \frac{1}{2}\left[f(u_{i+\frac{1}{2}}^{grp}(0,0)) + f(u_{i+\frac{1}{2}}^{grp}(0,\Delta t))\right]. \tag{3.65}$$

In this approximation $u_{i+\frac{1}{2}}^{grp}(0,0)$ is the solution to the Riemann problem (based on the linear reconstruction previously discussed for the MUSCL-Hancock scheme), after which the second term $u_{i+\frac{1}{2}}^{grp}(0,\Delta t))$ is found by characteristic tracing from the point $(0,\Delta t)$ to the reconstructed data $(0,0)$. In general the characteristic tracing can be expressed as,

$$u_{i+\frac{1}{2}}^{grp}(0,\Delta t) = u_k(\widehat{x}) \tag{3.66}$$

with,

$$\widehat{x} = \begin{cases} c\Delta x, & \text{if } a \le 0 \\ (1-c)\Delta x, & \text{if } a \ge 0 \end{cases}, \tag{3.67}$$

where k is either i or $i+1$ and $u_k(\widehat{x})$ is defined by equation (3.58).

The two higher-order extensions discussed above use linear piecewise reconstruction, however, higher order polynomial reconstruction have also been implemented in similar schemes (see e.g. Colella and Woodward, 1984, for a piecewise parabolic scheme).

3.3 Previous numerical simulation studies of AGN jets

Numerical simulations of AGN jets provide a powerful tool to study the theoretical models as outlined in the previous chapter. One example is the evolution of AGN. The lifespan of AGN is much longer than recorded history and, therefore, the study of the evolution of AGN over significant timescales are severely limited. Using numerical simulations of relativistic jets it is possible to evolve their environment with time, in order to study their evolution. Physical jets that have been reproduced experimentally within laboratories differ significantly from those associated with AGN due to the extreme unreproducible conditions, such as the highly relativistic bulk flow, found in these sources. This makes numerical simulations the best way to study relativistic jets. In this section a summary of selected results from previous studies of numerical simulations, and how they correspond to the observational data, are discussed.

As discussed in the previous chapter most AGN jets remain stable for hundreds of kiloparsec, orders of magnitude larger than their cross-section at launch. Despite the large scale stability of these sources, observations have revealed that many of them contain features such as kinks and bends (see Chapter 2.4.4) which indicate the development of smaller scale instabilities within the jets. This has led to the study of the jet stability over both short ($\sim$ 1 pc) and long ($\sim$ 1 kpc) length scales. The two most prominent types of instabilities which may occur within a kinetically dominated jet are Rayleigh-Taylor instabilities (acceleration of a less dense fluid into a more dense one) and Kelvin-Helmholtz instabilities (two fluids flowing past one another; Blandford and Rees, 1974). These instabilities have been the study of many numerical simulations, focussing on aspects such as their their production, which unstable modes grow the fastest and how the instabilities influence the jet morphology (see e.g. Zhao et al., 1992a,b). The discussion below is divided into two parts, the first dealing with simulations of the jet structure on parsec scales and the second with the kiloparsec morphology.

3.3.1 Parsec scale simulations

Parsec scale numerical simulations of relativistic jets have focussed on investigating the time dependent internal structure of the jet beam. In these simulations the jets are modelled as cylindrical beams of relativistic bulk flow in an unperturbed background medium. The individual emission components that have been observed within these jets, such as superluminal knots and shock fronts (see Figure 2.9), are modelled in the numerical simulations by perturbations in the injection parameters within the beam of the jet. In one study Agudo et al. (2001) showed that a series of emission components can be generated by a single perturbation in the flow of the beam. The injection of a perturbation propagating at apparent superluminal speed causes the development of trailing components of varying brightness as well as apparent propagation speed. The trailing components are formed by recollimation shocks that are produced by a pressure mismatch between the beam and the surrounding medium as the perturbation propagates along the jet. This result is illustrated in Figure 3.9 as a two dimensional colour map of the relative

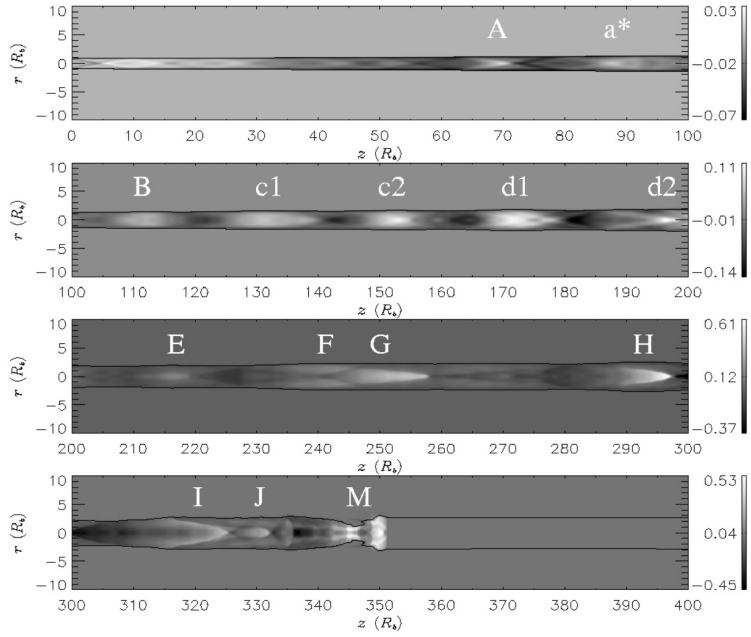

Figure 3.9: The production of trailing emission components by a single apparent superluminal perturbation propagating along a relativistic jet. Figure adopted from Agudo et al. (2001).

variation in the Lorentz factor with in the environment. Figure 3.10 shows a simulated emission map for such a perturbation with multiple emission components observed within the jet produced by the single perturbation. Later numerical simulations by Mimica et al. (2009) showed that this result holds for pressure matched as well as over-pressured beams. Observational results presented by, for example Britzen et al. (2010), support the production of these trailing shocks within AGN. Jorstad et al. (2005) showed observations of six AGN sources with emission components possibly produced by trailing shocks. These sources included 3C 111 shown in Figure 2.9.

Aloy et al. (2003) investigated the production of apparent superluminal emission components in a precessing jet. Their model included twofold precession induced by helical variations in the injection velocity of the beam. The resulting emission components did not form at the initial ejection site but rather at some distance along the beam and this was ascribed to the combination of the bulk motions, the viewing angle, and non-linear interactions between the perturbations and the jet structure. This result is shown in Figure 3.11 as a three dimensional rendering of the jet structure. Figure 3.11 also illustrates the difference in the structure of the component when viewed from the front and back sides. These superluminal components are different from trailing effects since they move at a higher apparent velocity.

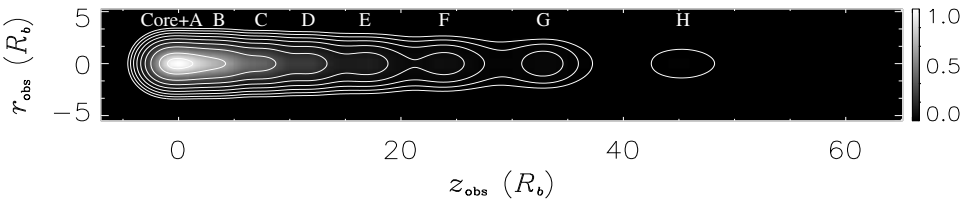

Figure 3.10: Simulated emission map for the components shown in Figure 3.9. Figure adopted from Agudo et al. (2001).

3.3.2 Kiloparsec scale simulations

Kiloparsec scale numerical simulations of AGN jets investigate the evolution of the entire jet structure in the IGM and how the interaction of the jet with the ambient medium determines the large scale morphology. The model commonly used in these simulations consist of an environment originally containing only ambient material, with the jet material injected at the start of the simulation from one of the boundaries.

Jet structure

In one of the first in depth studies of relativistic jets simulations, Martí et al. (1997) investigated how changes in environment parameters such as the Lorentz factor of the fluid inside the jet and the proper mass density ratio between the jet beam and ambient medium ($\eta = \rho_j/\rho_a$) affect the morphology of the relativistic hydrodynamic jet. These simulations were performed in a two dimensional environment and assumed that the jet was kinetically dominated with the magnetic field having a negligible effect on the morphology. The evolution of the jet in one of these simulations is presented in Figure 3.12 as a two dimensional colour map of the proper mass density in arbitrary units.

Martí et al. (1997) provides a discussion on the general structure of simulated relativistic jets, which is followed in this text. In Martí et al. (1997) the simulation environment initially consists of a uniform ambient medium. Jet material consisting of a fluid flowing at large Lorentz factors is injected into the ambient medium through one of the boundaries. The injected jet fluid forms a collimated beam of constrained jet medium moving at a high velocity. At the head of the injected jet material two shock fronts emerged separated by a contact discontinuity, referred to as the working surface. The outer shock front is a bow shock generated by the injection of material into the ambient medium and propagates outward creating a region of higher pressure shocked ambient medium. The inner shock front, called the reverse shock or Mach disk, decelerates the material in the beam transforming the kinetic energy of the jet medium into thermal energy.

The flow of the jet material is also deflected at the Mach disk, forming a backflow region or cocoon surrounding the beam of the jet. The cocoon region consists of a mixture of jet and ambient medium and becomes very turbulent. The turbulence in the cocoon is driven by effects such as Rayleigh-Taylor and Kelvin-Helmholtz instabilities. The Rayleigh-Taylor instabilities

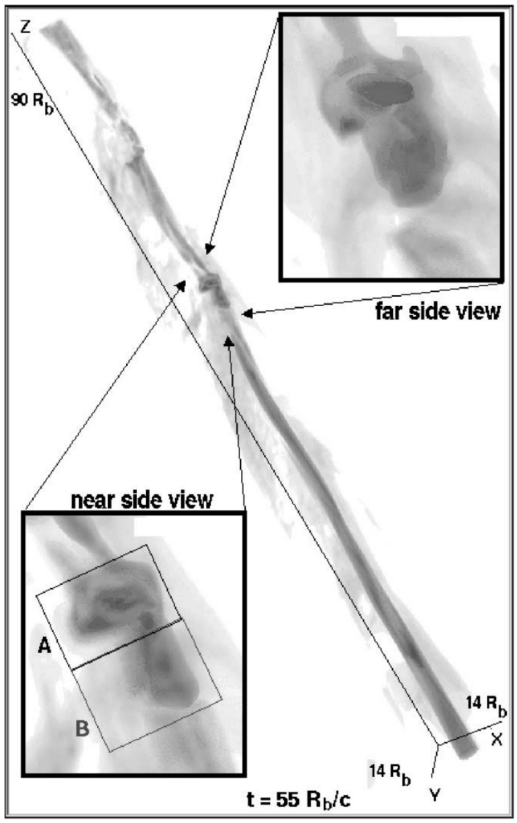

Figure 3.11: Three dimensional trace of a relativistic jet structure showing superluminal emission components produced by the precession of the injection velocity of the jet. Figure adopted from Aloy et al. (2003).

are caused by the higher pressure shocked ambient medium pushing into the cocoon, while the backward flow of this region generates Kelvin-Helmholtz instabilities. The cocoon region sheaths the jet beam preventing additional interaction between the jet beam and the ambient medium. This prevents the deceleration of jet material within the beam, however, the difference in flow direction between the beam and the cocoon can lead to the formation of Kelvin-Helmholtz modes in the jet beam.

While the structures discussed are generally present for most simulations, the detailed morphology of each structure changes based of the environment parameters. Figure 3.13 shows how different jet parameters influences the internal structure. One of the results that Martí et al. (1997) showed, was that an increase of the Lorentz factor results in an increase in the propagation efficiency of the jet, which in turn results in the production of a less turbulent cocoon. Scheck et al. (2002) extended the previous parameters studies of Scheck et al. (2002) to the effects of the plasma composition on the jet morphology, using two dimensional simulations. The results showed that the composition had an almost negligible effect on the large scale morphology of the

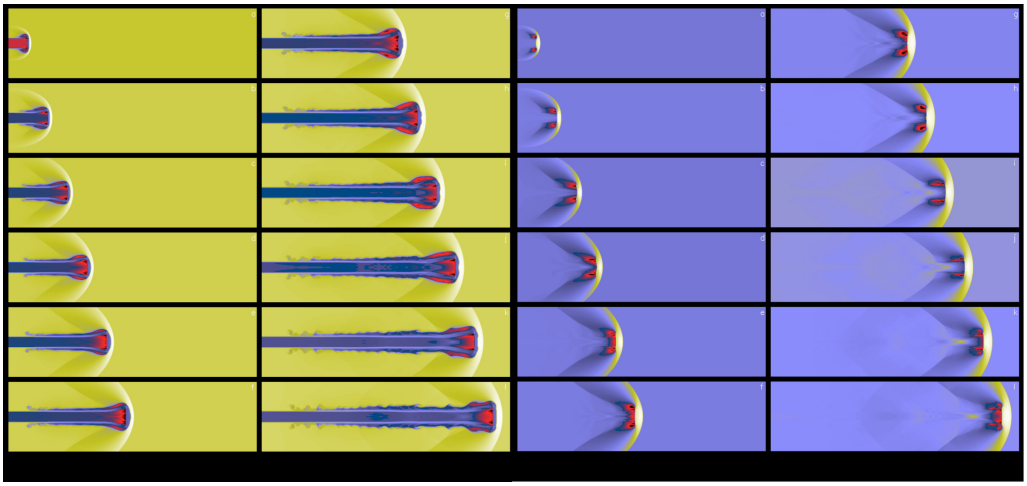

Figure 3.12: Two dimensional proper density (left) and pressure (right) plots showing the structure and evolution of a relativistic jet structure with parameters $\eta = 10^{-2}$, $\gamma_{ad} = \frac{44}{3}$, $\Gamma = 7.10$ and $M_b = 1.72$. Figure adopted from Martí et al. (1997).

jet.

Simulations of the relativistic jet beam presented by Aloy et al. (1999) found an additional sheath layer between the beam and external regions, which consists of a mixture of jet and ambient medium propagating in the direction of the jet at lower Lorentz factors. This layer is produced by the numerical viscosity added when implementing TVD numerical schemes (see Section 3.2.4). This numerical viscosity introduced by the approximate solvers to a certain extent mimics the real viscosity of the plasma in relativistic jets and the existence of a shear layer in AGN jets may explain some of the emission asymmetries that have been observed (see also Aloy et al., 2000).

More recently RMHD simulations of relativistic jets containing a dynamically important magnetic field have been developed to investigate the structure and evolution of magnetic fields in these environments. Most of these models are based on strong toroidal magnetic fields (see e.g. Komissarov, 1999). A comprehensive study on the effects of the magnetic field strength and topology on the morphology of relativistic jets was conducted by Leismann et al. (2005), using a two dimensional axis symmetric model. Their results showed that a toroidal magnetic field topology leads to the formation of nose cones at the front of the jet while poloidal configurations yield no such structure. The simulations produced jets containing two cavities[ii], an inner cavity consisting of material compressed by the magnetic field and an outer cavity which was inflated by the presence of the magnetic field (shown in Figure 3.14).

Overall numerical simulations have been able to shed light on how jets can remain collimated over such large distances. The development of instabilities within relativistic jets are damped by

[ii] An artefact produced by two dimensional simulations, see Section Two dimensions versus three dimensions.

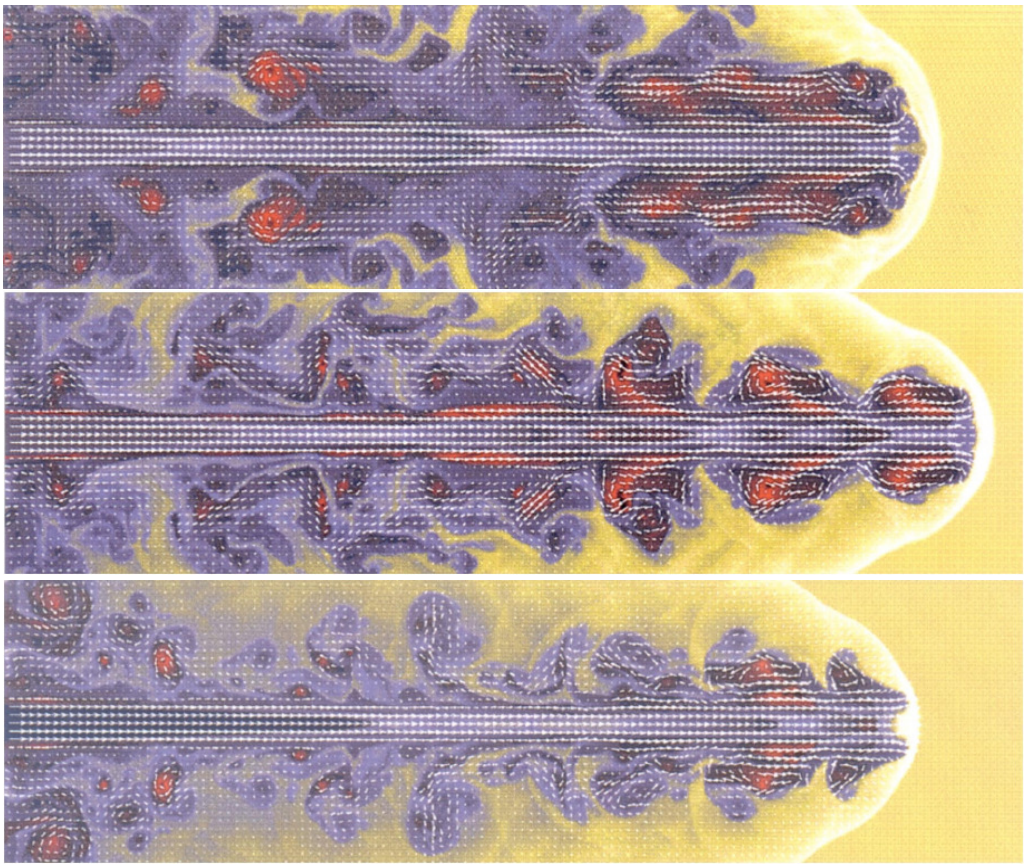

Figure 3.13: Two dimensional plots of proper rest mass density comparing the cocoon structure of a relativistic jet model for different Lorentz factors with $\eta = 10^{-2}$, $\gamma_{ad} = \frac{5}{3}$, $\Gamma = 2.29$ and $M_b = 6.0$ (top), $\eta = 10^{-2}$, $\gamma_{ad} = \frac{5}{3}$, $\Gamma = 7.10$ and $M_b = 6.0$ (middle) $\eta = 10^{-2}$, $\gamma_{ad} = \frac{5}{3}$, $\Gamma = 22.37$ and $M_b = 6.0$ (bottom). Figure adopted from Martí et al. (1997).

a number of factors including a large difference between the jet and the external medium density, the large Lorentz factor of the bulk flow, the shear layer which may develop around the beam flow and ordered magnetic fields.

Two dimensions versus three dimensions

In order to save computational resources many studies use two dimensional axis-symmetric environments to simulate relativistic jets. It has, however, been shown that there are significant differences in the morphology of full three dimensional simulations to that of axis-symmetric simulations. Mignone et al. (2010a) pointed out the production of an additional kink type instability in the beam of the jet in three dimensional RMHD models which were absent in the two dimensional case (see Figure 3.15). The coherent backflows (Aloy et al., 1999) and nose cone structures Leismann et al. (2005) found in axis-symmetric models was also not present in full

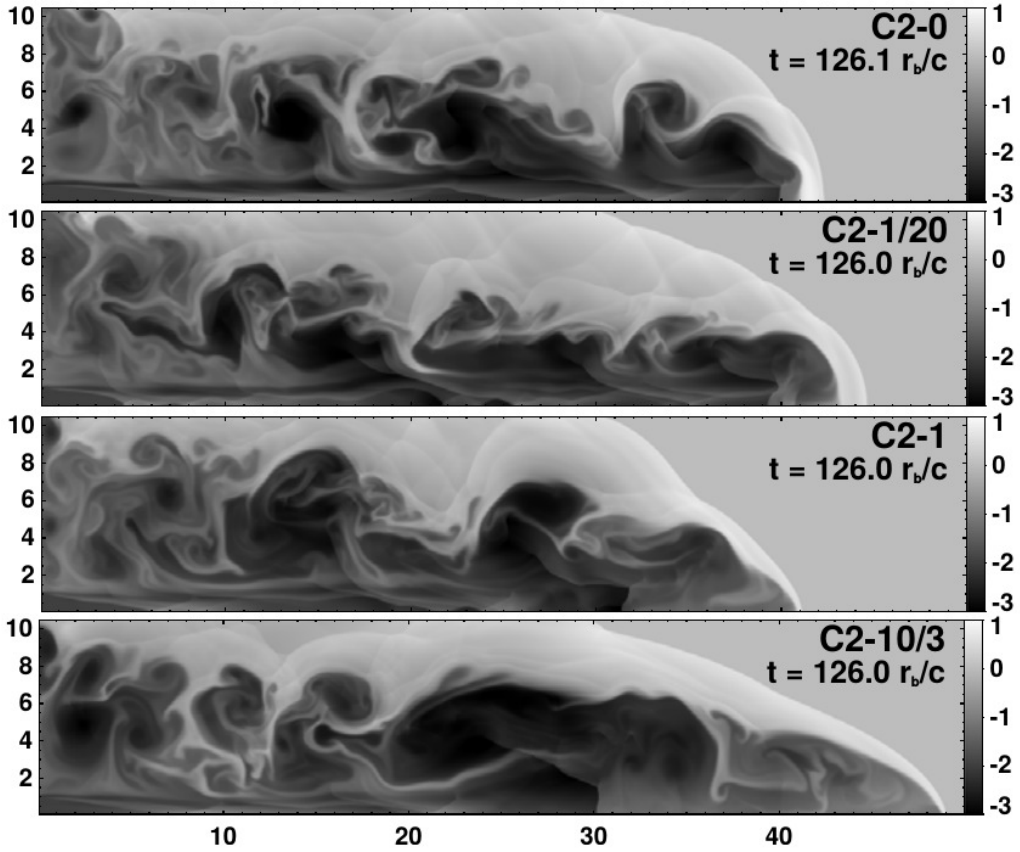

Figure 3.14: Logarithmic density plots of different magnetic models. Figure adopted from Leismann et al. (2005).

three dimensional simulations.

When comparing the instabilities of magnetized jets to those of non-magnetized ones in full three dimensional simulations, it is found that the magnetic field has a stabilizing effect on the short wavelength Kelvin-Helmholtz instabilities, however it introduces an additional resistive or kink type instability. If there is a small perturbation or bend in the jet the magnetic pressure, which is dependant on the azimuthal component of the magnetic field, increases on the concave side of the bend and decreases at the convex side. The difference in pressure allows the bend to grow and form a kink structure. The kink structures observed in simulations may be the cause of the observed helical bends discussed in section 2.4.4 (p. 33). McKinney and Blandford (2009) showed that kink instabilities may not significantly disrupt the production and initial flow of the jet, while Mignone et al. (2010a) showed that kink instabilities may shape the morphology of the jet but not significantly disrupt the flow of the jet material.

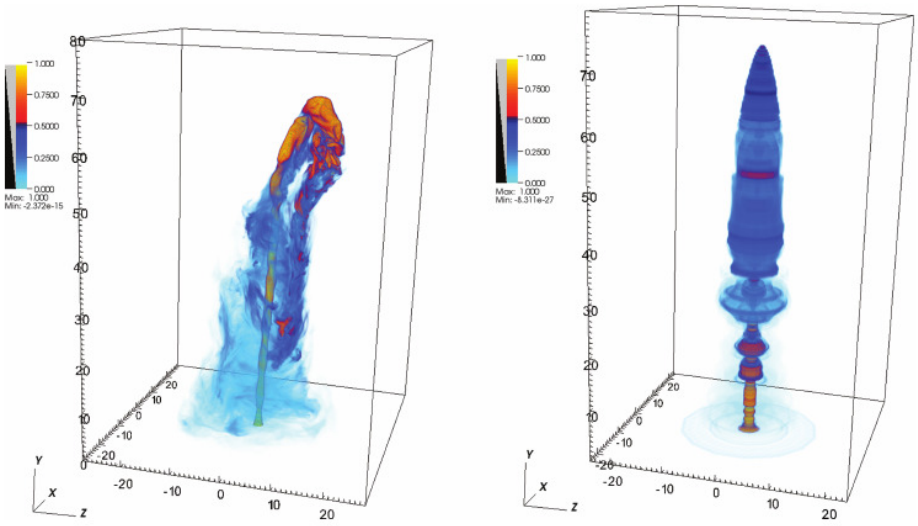

Figure 3.15: Volumetric rendering of the trace of simulated relativistic jets showing the comparison between a full three dimensional model (left) and a two dimensional axis-symmetric simulation (right). Figure adopted from Mignone et al. (2010a).

Fanaroff-Riley dichotomy

Kiloparsec scale numerical simulation can be used to investigate the elements responsible for producing the different Fanaroff-Riley classes. In order to investigate these structures relativistic jet simulations have to span a large enough time span in order for sufficient deceleration of the propagation speed to take place. As an example, the simulations run by Scheck et al. (2002) showed evolution time scales of up to 6.6×10^6 years. The result from this numerical long term simulation was that the propagation of the jet head can be divided into two distinct regions. On shorter time scales the jet head propagated at a constant velocity of $\approx 0.2c$ (similar to the propagation velocity derived by Martí et al., 1997), however, at large evolutionary time scales the velocity decelerated to $0.05c$ due to the degradation of the bulk flow caused by the expansion of the beam and internal shocks. The results of these simulations were able to recreate some of the observed properties of FR II type jets that included inflated lobe structures, hot spots, re-collimation shocks and deceleration along the beam of the jet. Leismann et al. (2004) achieved similar results for magnetized jet models with an exception for models containing a high magnetization parameter, in which case the dynamics of the propagation becomes dominated by the high density nose cone that was produced in the axis symmetric models.

The current model explaining the dynamics of FR I type radio jets suggests that they are generated by a decelerating beam flow. Perucho and Martí (2007) created a numerical simulation of the FR I source 3C 31 based on the study by Laing and Bridle (2002). In addition to the deceleration of the beam flow consistent with an FR I source the simulation, stretching over 10^6 years, showed the presence of re-collimation shocks due to an over pressured beam and the

evolution of a self-similar bow shock, which propagated at a quasi-constant speed. Perucho and Martí (2007) noted that the re-collimation shocks in a light jet trigger non-linear perturbations that can lead to the mixing of external medium with the jet beam. This entrainment of mass from the ambient medium in the beam of the jet is the most probable cause for the deceleration of the beam. The results presented in this study were also consistent with x-ray observations of FR I sources (see e.g. Croston et al., 2007; Kraft et al., 2003). There are, however, several mechanisms which can promote the process of ambient mass entrainment. Rossi et al. (2008) suggested that shear instabilities may be the main mechanism for entrainment. In this mechanism, the jet to ambient density ratio plays a crucial role with larger deceleration occurring in light jets. The time scale of the simulation presented is, however, too short to investigate the complete evolution of the system.

The occurrence of "HYbrid MOrphology Radio Sources" (HYMORS), galaxies in which one jet appears as an FR II, while the other jet component is FR I like (see e.g. Gopal-Krishna and Wiita, 2000), suggests that the FR dichotomy is also influenced by external variations in the ambient medium. Meliani et al. (2008) simulated the case where the jet encounters a sudden jump in ambient medium density at some distance from the injection site and was able to show that this resulted in the deceleration of the beam. The environment was simulated for a range of Lorentz factors between $\Gamma = 10 - 20$ and the authors suggest that it is possible for an FR II type source to change to an FR I type if a large enough change in density occurs within the IGM. The occurrence of this mechanism, however, relies on the presence of a jump in ambient densities where the outer region is more dense than the inner region, which may be a very uncommon occurrence. One scenario which can lead to such a jump in the ambient medium is the interaction between companion galaxies as shown by Evans et al. (2008).

The results of the numerical simulations discussed above provide good support for the observational data reviewed in Chapter 2. They show that numerical methods can be employed to simulate the complex dynamics which governs the jets associated with AGN. The simulations have shed light on the instabilities which occur in jet systems and how, despite these, they remain stable over large distances. They have also been able to reproduce stationary as well as superluminal emission regions and investigate their origin. Many uncertainties in the AGN jet model that can be investigated with numerical simulations still remain, however, and in this study we will focus on the synchrotron emission produced by the large scale morphology of the jet. By investigating the morphology of regions such as hot spots in the radio lobes of FR II type jets, how these structures evolve and how they relate to the radio variability, these sources can be better understood. The set-up of the numerical simulations used in this study will be discussed in the following chapter.

Chapter 4

Set-up and testing of relativistic jet model

To investigate time dependent structures and instabilities in the morphology of relativistic jets and how these structures influence the synchrotron emission that is produced by such sources, a fluid dynamic simulation was designed and run on several computers. In this chapter the software, numerical algorithms and model set-up for the jet simulations will be discussed in detail. The strengths and weaknesses of this method will also be evaluated.

4.1 PLUTO hydrodynamic code

A numerical fluid dynamic simulation of a relativistic jet can be created with numerical software, which employs a numerical scheme such as those discussed in Chapter 3 to evolve an environment consisting of fluid dynamic quantities with time on a computational domain. The software updates the values of each point or cell in a mesh grid with a set of time increments until a final pre-determined time step is reached. For the purposes of this project the opensource numerical software PLUTO (*ver* 4.0 and 4.2) was used to construct and evolve the relativistic jet environment. This software was designed by Mignone et al. (2007) and has been rigorously tested by these authors to ensure that the numerical schemes are implemented correctly. Previous studies implementing the PLUTO software has included the simulation of relativistic jets, showing results which are consistent to those of other grid based hydrodynamic codes (Mignone et al., 2010b).

The PLUTO software is a grid based hydrodynamic code which uses High Resolution Shock Capturing (HRSC) schemes to evolve the fluid dynamic environment. The environment of the simulation is defined as flow quantities on a structured spatial mesh grid enclosed by a set of boundary or ghost shells, which implement time dependent boundary conditions. The software evolves the flow quantities of the grid with time according to the fluid dynamical conservation laws

Table 4.1: List of PLUTO dependencies showing seperate columbs for static and AMR grid structures as well as serial and parallel configurations.

Dependency	Static Grid		Adaptive Grid	
	serial	parallel	serial	parallel
Python (*ver* > 2.0)	yes	yes	yes	yes
C compiler	yes	yes	yes	yes
C++ compiler	no	no	yes	yes
Fortran compiler	no	no	yes	yes
GNU make	yes	yes	yes	yes
MPI library	no	yes	no	yes
Chombo library (*ver* 3.2)	no	no	yes	yes
HDF5 library (*ver* 1.6 or 1.8)	opt	opt	yes	yes
PNG library	opt	opt	no	no

in the form of equation (3.2). PLUTO was designed for astrophysical simulations and employs numerical schemes that are designed for supersonic flows containing contact discontinuities. The software is able to simulate environments using either a static or Adaptive Mesh Refinement (AMR) grid structure. When the AMR is implemented the grid structure is dynamically refined during the runtime of the simulation. The refinement allows the cells in the mesh grid to be subdivided in regions where there are large gradients, such as shock fronts, generating higher resolution at these regions of interest. Regions with flat gradients (such as a uniform medium) remain undivided with a lower resolution. AMR, therefore, allows the numerical method to solve less cells while still achieving the same equivalent resolution as a static grid. The advantages of AMR include less computationally expensive simulations and smaller data sizes. The PLUTO software is designed on a modular base, with which the user can select the desired physics module and numerical scheme depending on the objective of the simulation. The main physics modules include; classical hydrodynamics (HD), ideal magnetohydrodynamics (MHD), special relativistic hydrodynamics (RHD) and special relativistic magnetohydrodynamics (RMHD).

The PLUTO software is written in the C++ language with a set-up executable utilizing Python. The code requires minimal pre-installed software with a list of the dependencies for the PLUTO code given in Table 4.1. Simulations created with the PLUTO software are parallelizable with the parallelization handled internally in the source code through the message passing interface (MPI) library. Scalability tests of PLUTO, run by the authors of the software on the *BlueGene* machine, show an almost ideal linear trend (Mignone et al., 2010b), as illustrated in Figure 4.1. These features make the code very attractive for designing and running large scale astrophysical simulations.

The software implementation of the HRSC scheme is based on a reconstruct, solve and average approach which can be separated into three main steps. First, a piecewise polynomial is reconstructed in each cell on the grid using piecewise monotonic interpolation. The interpolation method follows that discussed in Section 3.2.4 (p. 50) to yield a second order approximation.

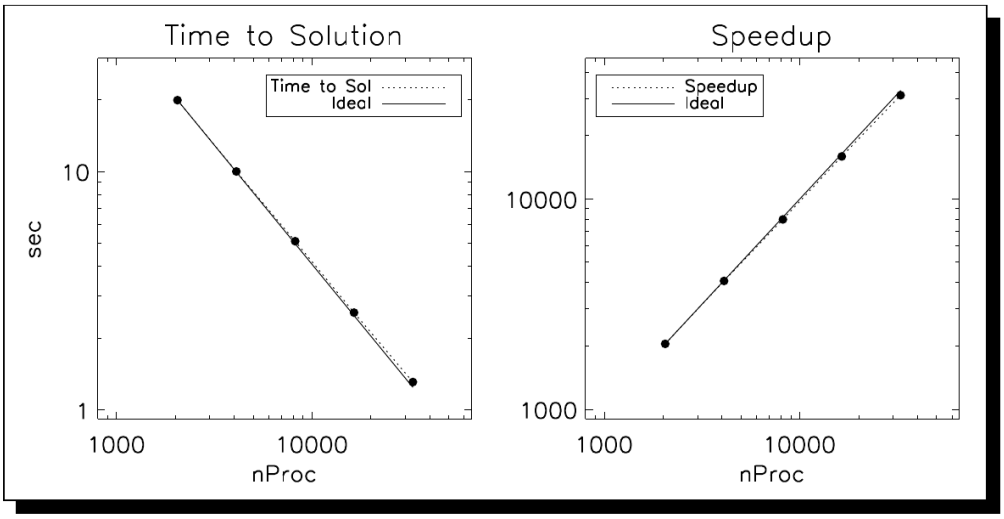

Figure 4.1: The scaling of the time to solve versus the number of processes (left) and the speed-up factor per process (right) of the PLUTO code running a periodic 512^3 computational grid problem. The solid line indicates the ideal scaling while the dotted line shows a fit of the average points. Figure adopted from (Mignone et al., 2010b).

Second, the Riemann problem discussed in Chapter 3 is then solved for each boundary in the computational grid. Finally, the values of fluid quantities in each cell are evolved with time. The code follows this strategy independent of the physics module which is applied and only the constituents of equation (3.3) change based on the applied module. The physics module therefore only provides the algorithm which will be evolved in the simulation.

The reconstruction of the piecewise polynomial $P(x)$ approximates the values of a vector $\mathbf{V}$, containing a set of primitive flow quantities, such that,

$$\begin{aligned} \lim_{x\to x_L} P(x) &= \mathbf{V}_L, \\ \lim_{x\to x_R} P(x) &= \mathbf{V}_R, \end{aligned} \tag{4.1}$$

on the left and right boundaries respectively. The reconstruction algorithms that are available in PLUTO depend on the physics module which is applied. In general the user can choose between a flat, linear, parabolic, third-order convex ENO (essentially non-oscillatory) and the fifth-order WENO (weighted essentially non-oscillatory) scheme reconstruction.

Once the boundary conditions for each cell have been established the Riemann problem can be solved. The PLUTO code also contains several Riemann solvers which can be implemented in the solution depending on the physics module which is used. The most diffusive and robust solver that is available is the Time Variation Diminishing Lax-Friedrichs (TVDLF) scheme (see Chapter 3). The HLL family of solvers are also available with the original two wave solver, the three wave HLLC solver (Toro et al., 1994) as well as the five state HLLD solver (Miyoshi and

Kusano, 2005). The HLL solvers provide attractive features such as computational efficiency, high accuracy and enforced physical constraints such as positive pressure and velocities smaller than the speed of light in the RHD physics module. The linearised Roe Riemann solver is also available and is more accurate than the HLL solvers, however, this solver can only be applied in the HD and MHD modules. Another Riemann solver only available in the HD module is the Advective Upstream Splitting Method (AUSM). This Riemann solver employs a flux splitting scheme, splitting the solution into convective and pressure terms, which are associated with linear and non-linear differential systems respectively. The most accurate solver that can be implemented is the two shock solver, which is based on the approximation of the exact state solution to the Riemann problem. This solver determines the solution to the Rankine-Hugoniot jump conditions in order to determine the flux (see e.g. Toro, 2009, chapter 9). This solver is, however, very resource intensive, which limits its use.

The time evolution step in PLUTO can be advanced via two main methods, fully discrete zone-edge extrapolated and semi-discrete methods. The zone-edged extrapolated methods use mid-point time quadrature to obtain second-order accuracy. The schemes take on the general form of,

$$\mathbf{U}_i^{n+1} = \mathbf{U}^n - \sum_d \frac{\Delta t}{\Delta V^d} \left(A_+^d \mathbf{F}_+^{d,n+\frac{1}{2}} - A_-^d \mathbf{F}_-^{d,n+\frac{1}{2}} \right) + \mathbf{S}, \tag{4.2}$$

where d is the direction, V is the volume of the cell in a direction, A is the surface area of the boundary and $\mathbf{F}_\pm^{n+\frac{1}{2}}$ is the flux estimates obtained from solving the Riemann problem,

$$R(\mathbf{V}_{+,L}^{n+\frac{1}{2}}, \mathbf{V}_{+,R}^{n+\frac{1}{2}}). \tag{4.3}$$

This time stepping algorithm combined with liner reconstruction yields the MUSCL-Hancock scheme discussed in Section 3.2.4 (Toro, 2009; Van Leer, 1974). If the eigenvalues and eigenvectors are known upwind limiting may be applied and yields the piecewise parabolic scheme of Colella and Woodward (1984), also known as characteristic tracing (see Section 3.2.4).

The semi-discrete time evolution methods consider the spatial discretization separately from the temporal evolution that is continuous with time. These schemes include the Runga-Kutta methods (Gottlieb and Shu, 1998). The second-order Runga-Kutta method can be given as,

$$\begin{aligned} U^\star &= U^n + \Delta t L^n, \\ U^{n+1} &= \frac{1}{2}(U^n + U^\star + \Delta t L^\star), \end{aligned} \tag{4.4}$$

where,

$$L^n = \sum_d \frac{\Delta t}{\Delta V^d} \left(A_+^d \mathbf{F}_+^{d,n} - A_-^d \mathbf{F}_-^{d,n} \right) + \mathbf{S}. \tag{4.5}$$

The time step Δt used to evolve the environment in these schemes are calculated dynamically

in PLUTO for each step as,

$$\Delta t = C_a \min_d \left(\frac{\Delta x^d_{\min}}{|S_{\max}|} \right) \tag{4.6}$$

where C_a is the CFL number specified in the environment set-up $x_{\min}$ is the smallest cell length and $S_{\max}$ in the maximum signal speed.

The PLUTO code provides the user with many options to select the numerical method which is best suited for the environment that needs to be simulated. The procedure for setting up and implementing these options in a simulation will be discussed in the next section.

4.2 PLUTO simulation set-up and design

The files needed to compile a simulation is generated semi-autonomously using PLUTO by running the `setup.py` script, located in the main PLUTO directory, within the simulation directory. The `setup.py` script contains several user prompts regarding the simulation set-up and generates 5 template files which define the simulation. These files are; the simulation header file (`definitions.h`), the initialization file (`pluto.ini`), the configuration file (`init.c`), the makefile (`makefile`) and the system configuration file (`sysconf.out`). An example of each of the files listed above is found in Appendix A.1.

The templates generated by `setup.py` is edited by the user to create the desired numerical simulation. These files control the predefined numerical scheme (such as the combination of reconstruction, Riemann solver and time stepping algorithms), the initial environment, the mesh grid structure and the write out of data files (write out interval and format). Additional alterations to any functionality of the PLUTO software can be made by altering the PLUTO source files. One alteration to the source files which was made for this study was the `userdefined_output.c` file, which controls the variables which are calculated for each cell during runtime of the simulation as well as how these variables are written out. The format and functionality of the template files will be discussed in further detail in the following sub-sections.

The system configuration file

The system configuration file (`sysconf.out`) contains all the information of the current computer system that the PLUTO simulation is set up on. It serves no purpose during the runtime of the simulation, but can be used by the user as a log of the system state for a simulation run, as well as by visualization software to provide additional information about the simulation. An example of this file is shown in Appendix A.1.1

The makefile

The `makefile` sets instructions concerning the compilation of the simulation files to produce an executable file, `pluto`. The instructions contained within this file include the selected compiler,

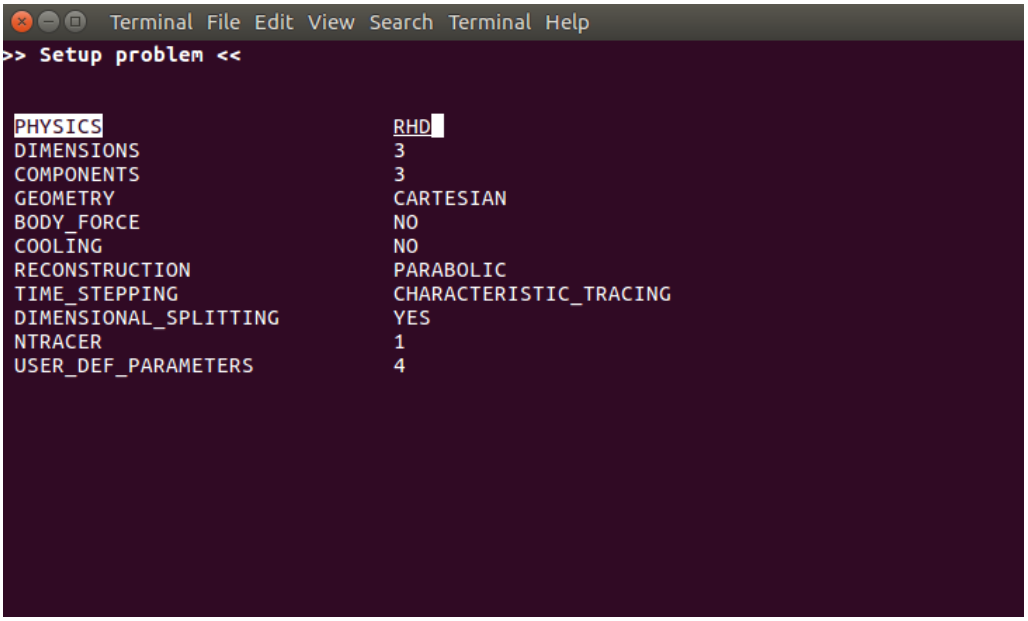

Figure 4.2: Screen shot of the setup.py user interface that can be used to generate the definitions.h file.

additional compiler flags, parallelization and additional libraries (for example the Hierarchical Data Format library, hdf5) that will be used. Running the `make` command with this file will generate the executable simulation file. An example of this file is shown in Appendix A.1.2

The header file

The header file (`definition.h`) contains information regarding the numerical scheme, which is used to evolve the simulation. It is automatically generated by running the `setup.py` PYTHON script from the simulation directory and setting the user prompts, however, the file can also be manually edited with a text editor. Figure 4.2 displays a screen shot of the `setup.py` user prompt listing some of the options that is specified in the header file. An example of the full header file is shown in Appendix A.1.3 and the options listed will be discussed.

The setup script allows one to set the form of the conservation equation that will be evolved by selecting the physics module (regime) that must be applied to the simulation. The user can also include body force source terms in either a vector or a potential form, as well as additional source terms for radiative cooling. In addition to the conservation laws a number of passive scalars can be defined that obey the advection equation (equation 3.13) which is evolved in the simulation. These scalars can be used as a trace of the distribution of a fluid medium within the environment.

In order to define the numerical scheme that is used the reconstruction order (as discussed

in section 4.1) as well as the time stepping algorithm is set. The scheme can also make use of dimensional splitting, in which the multidimensional equations are solved by a sequence of one dimensional problems. The set of one dimensional problems are less intensive to solve compared to solving all the flux vectors simultaneously for each direction, however, it can generate errors leading to inaccurate solutions.

The geometry of the mesh grid can be set up as either Cartesian, cylindrical, polar or spherical. The spatial dimensions of the environment as well as the number of vector components are also specified. This allows the user to define, for example, the velocity in four vector form with the number of components set to four. This option is useful when compiling so called two and a half dimensional simulations where the grid is only specified in two spatial dimensions but vectors, such as the magnetic field, assigned to the grid have components in all three spatial dimensions. This set-up is commonly used in two dimensional axis-symmetric models.

The header file allows users to define input parameters which can be called from the initialization file. Defining parameters in this file instead of "hard coding" values is beneficial, since they can be accessed from anywhere within the code during runtime. This also has the advantage that the values of these parameters can be reset without recompiling the problem.

Depending on the physics module that is selected during the set up, additional options such as the equation of state, divergence control (magnetic fields) and artificial viscosity can be specified. The availability of these options are dependent on the numerical set-up that is chosen. This discussion will be limited to the options available for the RHD module as this is the main module used in this study. For the RHD module the equation of state and entropy switch options are available. The user can specify the equation of state as either the ideal, isothermal or Taub-Matthews equation. The entropy switch option adds an additional conservation equation for the entropy of the system, which takes on the form of a passive scalar equation. Using the entropy switch allows the simulation to determine the pressure from the conservation of entropy instead of the energy density. This entropy conservation method ensures positive pressure, however it does not ensure the conservation of energy in the environment. The entropy switch can either be set to NO (uses energy density to determine pressure), SELECTIVE (the pressure is calculated from the conservation of entropy in the proximity of shock fronts), ALWAYS (uses entropy conservation to determine the pressure everywhere on the grid) and CHOMBO_REGRID (this method can be used with AMR to ensure conservation of entropy).

Some options in the header file cannot be set during the set-up prompt and require the user to edit the definitions.h file after set up. An example of a commonly used option is the flux limiter. Flux limiters provide an additional mechanism for limiting the gradients of the solutions between cell boundaries. This produces a dissipative effect at discontinuities which damps unphysical waves and introduces a form of numerical viscosity. The PLUTO code provides several flux limiting functions namely; FLAT, MINMOD, VANALBADA, OSPRE, VANLEER, UMIST, MC and DEFAULT. For a discussion on flux limiters the reader is referred to Toro (2009, chapter 13). Additional options which can be set in the header file are listed in Table 4.2 along with their

Table 4.2: Additional simulation options that can be edited in the header file.

Parameter	Options	Discription
INITIAL_SMOOTHING	YES/NO	Enables sub-sampling in cells to create smooth profiles for sharp boundaries not aligned with the grid
WARNING_MESSAGES	YES/NO	Print warning messages when a numerical error or inconsistency occur during runtime
PRINT_TO_FILE	YES/NO	Write output to log file
INTERNAL_BOUNDARY	YES/NO	Allows the user to set up boundaries inside the computational domain
SHOCK_FLATTENING	NO/ONED/MULTID	This option provides additional dissipation in the proximity of shocks fronts. The ONED option progressively reduces the spatial slopes of shocks using one-dimensional shock recognition. The MULTID option reverts the flux limiter used in reconstruction to the most diffusive form and computes fluxes using the HLL Riemann solver in the proximity of a shock front.
CHAR_LIMITING	YES/NO	Performs reconstruction on a set of characteristic variables rather than the primitive set. This reduces unphysical oscillations and improves the quality of the solution.

options and descriptions.

The runtime initialization file

The runtime initialization file or (pluto.ini) contains the runtime information necessary for the time evolution of the conservation equation in the environment. The file is split into blocks with each block containing information relating to a certain aspect of the simulation. Each block is specified by a header in square brackets and the order of the blocks does not matter. The parameters in the initialization file can be changed for different simulation runs without recompiling the problem. An example of the file is given in Appendix A.1.4.

The first block in the example file is the grid block and specifies the mesh grid set-up of the simulation. In a static grid set-up the block defines the size and resolution of the domain, while for an adaptive grid the block defines the base grid that is refined. The properties are defined separately for each dimension, X1-grid referred to as the x dimension, X2-grid referred to as the y dimension and X3-grid referred to as the z dimension. If a simulation is run in less than three dimensions the ignored direction should contain only one grid cell.

The next block, the CHOMBO refinement block, contains the additional grid parameters used in the refinement of the base grid when implementing AMR. These include the number of levels for refinement, the ratio between levels and the conditions for refinement.

The time block specifies the time evolution parameters of the simulation. In this block the user can set the properties of the CFL number (see section 3.2.1.1), the initial time increment dt and the time step (in simulation time units) at which the simulation is complete.

The solver block defines the Riemann solver which is implemented in the solution as discussed in section 4.1.

The boundary block specifies the boundary conditions on the edges of the domain. The boundaries of the domain consists of ghost cells on the edges of the mesh grid with known functions for the primitive fluid dynamic variables. The user can select a number of boundary conditions namely, outflow, reflective, axis symmetric, equatorial symmetric, periodic, shearing box or user defined. When the user defined option is selected the user can define the function for the boundary conditions in the UserDefBoundary() function in the initial conditions file (init.c). The boundary conditions are defined separately for each boundary and all boundary conditions should be defined regardless of the dimensions of the simulation.

The static output and CHOMBO output blocks controls the type of output files for the static and AMR grids respectively. The output files are written at certain time intervals that can be controlled separately for each output format.

Finally the parameters block allows the user to set the values of the user defined parameters, which are defined in the header file. These values can be accessed from anywhere within the code during runtime.

The problem configuration file

The problem configuration or (init.c) file provides a set of functions which control some of the properties and variables within the environment of the simulation. This includes functions for assigning the initial conditions of the environment, assigning background magnetic fields, defining specific boundary conditions and gravitational fields. The default functions used by PLUTO are listed in Table 4.3, however, users are free to define additional functions that can be implemented in the existing code. An example of this file for the initial jet test problem is shown is Appendix 4.3. In the example file a uniform background medium is defined in the Init() function and the jet is injected by defining a nozzle on the lower z boundary in the UserDefBoundary() function. Two additional function are defined in the file, the first of which (CalcJetParam()) calculates the primitive variables for the injected jet fluid, while the second (Profile()) controls the profile of the nozzle to ensure a smooth transition between the jet and background medium.

4.3 PLUTO software installation

The PLUTO code is freely available for download at `http://plutocode.ph.unito.it/` (Mignone et al., 2010b). The software was set up on 3 machines at the UFS. The first machine consisted of an Intel Core i5-2400 CPU with 8 Gb of memory (hereafter referred to as the i5 machine). The second machine consisted of an Intel Xeon(R) CPU E5-2640 v4 @ 2.40GHz 40 CPU with 64

Table 4.3: Functions used to define flow quantities of the simulated environment

Function	Discription
Init()	Sets the initial conditions and values of the flow quantities as a function of the spatial coordinates.
UserDefBoundary()	Allows the user to set the boundary conditions at the edges as well as define internal boundaries. This function requires the USERDEF option in the pluto.ini initialization file.
Analysis()	Computes additional data during runtime, which can be written to a file for further analysis during post-processing. For example, the total energy of the environment can be computed and stored in order to check energy conservation.
BodyForceVector()	Sets the function for vector acceleration within the environment.
BodyForcePotential()	Sets the function for applying a potential field to the environment, e.g. gravity.
BackgroundField()	Used to define a force-free background magnetic field.

Gb of memory (hereafter referred to as the Xeon machine). Finally the software was run on the University of the Free State High Performance Cluster (HPC) consisting of 17 nodes containing 48 cores with 64GB memory per node and an additional 8 nodes containing 64 cores with 128GB memory per node. The required dependencies for the static grid were installed on all three machines with the required dependencies for the AMR only installed on the HPC to test the AMR functionality.

To verify that the code was running correctly with no missing dependencies the Shock tube and Kelvin-Helmholtz test problems that are included with the code were run on all three machines. The results obtained for all machines were compared to each other and were found to be consistent. The relativistic shock tube problem was set up to be identical to problem 4.1 of Mignone et al. (2005), with the initial conditions,

$$(\rho,\ v_x,\ p) = \begin{cases} (10,\ 0,\ \frac{40}{5}) & \text{for } x < 5, \\ (1,\ 0,\ \frac{2}{3} \times 10^{-6}) & \text{for } x \geq 5. \end{cases} \tag{4.7}$$

The results obtained were consistent with those shown in figure 4, Mignone et al. (2005). An example of the results for the shock tube problem run on the Xeon machine is plotted in Figure 4.4. In order visualize the generated data additional visualization tools were installed on the i5 and Xeon machines. These tools consisted of the PYPLUTO library that is included with PLUTO, which is used for two-dimensional plots of the environment, and PARAVIEW, used to generate three dimensional renderings.

Figure 4.3: The University of the Free State High Performance Cluster.

4.4 The relativistic jet environment

In order to simulate a relativistic AGN jet a numerical model was designed and compiled using the PLUTO software. It was assumed that the distance of the simulated relativistic jet was far enough away from the central SMBH that it had transitioned into the kinetically dominated regime, with the magnetic field having a negligible effect on the dynamics of the jet (the magnetic energy density is assumed to be less than 10^{-3} that of the kinetic energy density in the environment). The RHD physics module therefore provides an accurate approximation of the environment and was used. The simulations were performed using a three dimensional Cartesian computational domain. A Cartesian grid was specifically selected since it simplifies the calculations of the emission during post-processing and a three dimensional model was used since it has previously been shown that two dimensional axis symmetric models do not reproduce all of the instabilities observed in full three dimensional simulations (see section 3.3.2).

The fluid model for the environment was set up as follows. A uniform density background medium was assigned to the mesh grid at a time $t = 0$, with no velocity. Arbitrary units were used in the designed model to avoid unnecessary truncation errors, which would occur when working with the small density numbers in cgs units. Subsequently all other units such as pressure and energy were also defined arbitrarily, the only exception being the velocity, which is defined in units of c to correctly apply relativistic effects. The use of arbitrary units is a common practise in numerical simulations and has been adopted by most studies of relativistic jet simulations including that of Martí et al. (1997). These arbitrary units can be scaled after computation to represent realistic values for AGN jet sources.

In order to simulate the production of a jet, a relativistic medium was injected through a

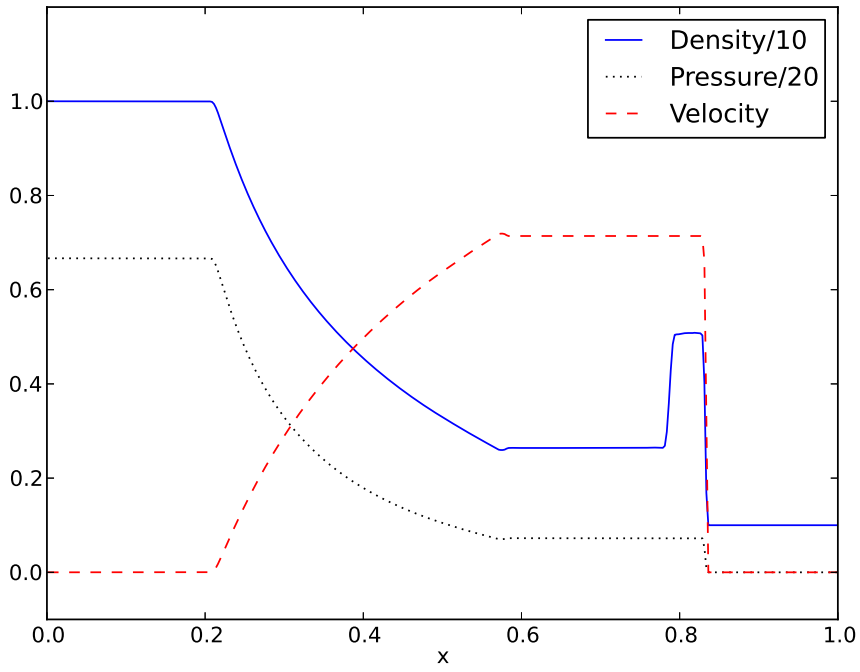

Figure 4.4: Relativistic shock tube problem at $t = 0.4$ run with $CFL = 0.8$. The initial conditions are set up identical to those of problem 4.1 Mignone et al. (2005).

nozzle, defined as a circular region at the centre of the $z = 0$ boundary. The jet medium was injected continuously, perpendicular to the $z = 0$ boundary, with a velocity component in the z direction. The density of the injected material was less than that of the ambient medium ($\rho_b/\rho_{am} < 1$). At the nozzle a pressure equilibrium between the jet and ambient medium was set up in order to prevent the unnecessary expansion or contraction of the jet at the injection site. The nozzle was defined with a steep profile to produce a smooth transition between the jet and ambient medium. The profile was calculated as,

$$\mathbf{U} = \begin{cases} \frac{\mathbf{U_j}}{\cosh(r^7)} & \text{for } r < 1 \\ \mathbf{U_a} & \text{for } r > 1 \end{cases}, \tag{4.8}$$

where $\mathbf{U_j}$ and $\mathbf{U_a}$ are the fluid dynamic variables for the jet and ambient medium respectively and r is the distance from the centre of the nozzle. Figure 4.5 shows a plot of this profile.

The boundaries of the grid, except for the $z = 0$ boundary, were assigned an outflow condition, such that,

$$\frac{\partial \mathbf{U}}{\partial n} = 0, \tag{4.9}$$

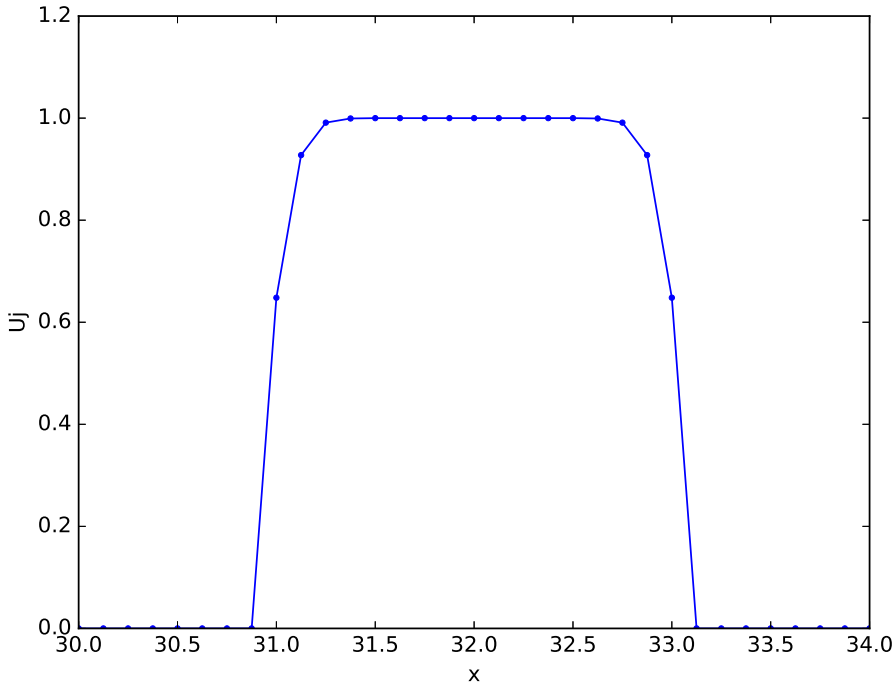

Figure 4.5: A one dimensional plot (at 8 points per unit length) of the profile applied to the injected jet medium at the nozzle to ensure a smooth transition between mediums. The nozzle is located at the centre of the $z = 0$ boundary, at $x = 32$.

where n represents the direction normal to the boundary. In addition to the jet nozzle, the $z = 0$ boundary was set to be reflective such that,

$$U(x, y, z) = U(x, y, -z) \tag{4.10}$$

with an exception to the z component of the velocity,

$$v_z(x, y, z) = -v_z(x, y, -z). \tag{4.11}$$

This condition was set to simulate the presence of the galaxy and a counter jet on the opposite side of the central engine.

The procedure for creating and running jet simulations using PLUTO was as follows. First each problem was designed on the i5 machine. During this design phase the compatibility of the combination of numerical algorithms was tested along with the checks to ensure that the problem was compilable. A low resolution simulation (1 point per unit length) was then run as a check to ensure that the problem would run. Second the problem was compiled and run on either the

Xeon machine or the HPC with increased resolution. Finally the data that was generated was transferred back to the i5 and Xeon machines for visualization. The following sections show and discuss the results of the fluid dynamic simulations run for this project.

4.4.1 Test simulations

The first step in creating a relativistic AGN jet simulation was the set up of an initial configuration in order to test various aspects of the simulation. Using the test simulation, the resource intensiveness of the simulation was tested along with the combination of numerical schemes, the convergence of the solution, and the correlation of the solution to the morphology found in previous studies.

The Cartesian grid for the initial test simulations consisted of a static mesh grid with a volume of 64^3 units. The unit length of the grid was scaled such that the radius of the relativistic beam injected into the environment would span 1 unit. Working under the assumption that the radius of the jet would be on the order of ~ 1 parsec the entire domain would span ~ 64 parsec, which would be relatively limited to study the large scale evolution and morphology of the relativistic jet. The smaller grid set-up, however, allowed for less computationally intensive test simulations.

Reconstruction and time evolution

Before a simulation of the jet model was be carried out, the possible numerical schemes which could be implemented were identified. The fully discrete zone-edge extrapolated time stepping methods were tested, since these methods provided second-order numerical schemes. Based on this time evolution two numerical schemes were set up, the MUSCL-Hancock scheme and Piecewise Parabolic Method (PPM, see Chapter 3). The schemes were first tested with the one dimensional shock tube problem discussed in Section 4.3. For both schemes the HLLC Riemann solver was implemented. A plot of the density is shown in Figure 4.6. Both schemes produced well behaved solutions, however, we note that the PPM resolves discontinuities better while the MUSCL-Hancock scheme provides a smoother solution at the discontinuities.

Having obtained well behaved solutions for the shock tube problem using both schemes, they were tested with the three dimensional jet model. These simulations were implemented with an HLLC hybrid solver, which uses the HLLC Riemann solver as the main solver with the more diffusive HLL solver implemented at shock boundaries. In this hybrid solver the HLLC solver provides high accuracy, but at the shock boundaries the more diffusive HLL solver is less likely to produce unphysical oscillations and ensures more stability at discontinuities. The shock detection and implementation of the hybrid solver configuration is handled internally by the PLUTO code. Dimensional splitting was implemented for both schemes in order to minimize the computational resources required. A CFL number of 0.8 was used in the simulations to ensure the stability of the solution, while limiting computational intensiveness. The computational resolution of the grid was set to 8 points per unit length.

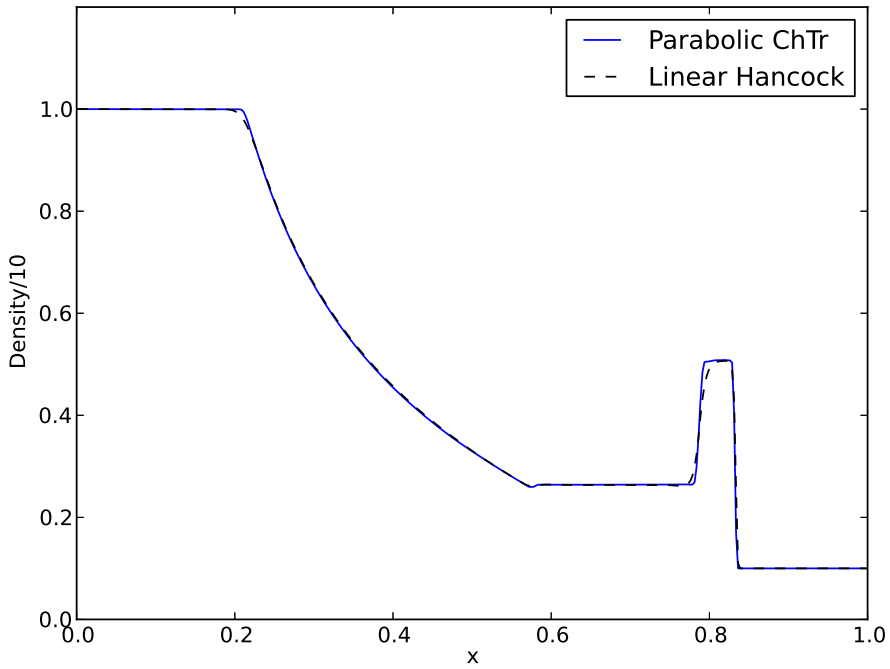

Figure 4.6: Comparison between the MUSCL-Hancock and PPM numerical solutions for the density of the relativistic shock tube problem at $t = 0.4$ run with $CFL = 0.8$.

The initial parameters for the environment were set with the ambient medium having a proper density $\rho = 10$, while the jet medium was injected with a proper density of $\rho = 0.1$ and a Lorentz factor of $\Gamma = 10$. The jet to ambient medium proper density ratio was therefore $\eta = 10^{-2}$. The density ratio and Lorentz factor were chosen similar to that of case **A** by Rossi et al. (2008), so that a comparison to those results could be made. The Mach number ($M_s = 3.0$) was also chosen based on the previous study. The pressure of the fluid was calculated using the ideal equation of state (equation 3.11) as $p = 7.90 \times 10^{-3}$. A complete list of the fluid quantities used is given in Table 4.4. The simulations were run until the injected jet material reached the edge of the computational domain.

Two dimensional proper density slices of the $x-z$ plane through the origin were constructed of the simulations to study the results (Figure 4.7). Comparing these results to those of Martí et al. (1997) the large scale regions of the jets were identified. All of the regions discussed previously, namely the beam, cocoon, bow shock, were present in both configurations, however, the internal structures of the regions differed significantly For the two schemes. The PPM scheme produced a turbulent cocoon region, which causes a large variation in cocoon thickness along the beam, while the linear Hancock scheme yielded a smooth cocoon structure showing no instabilities.

Table 4.4: Parameters used in the set up of the initial conditions of the test jet problem.

Parameter		Value (arbitrary units)
Lorentz factor	Γ	10
Velocity	v	$0.995c$
Density ratio	η	10^{-2}
Jet density	ρ_b	0.1
Ambient density	ρ_{am}	10
Mach number	M_b	3.0
Adiabatic index	γ_{ad}	5/3
Pressure	p	7.90×10^{-3}

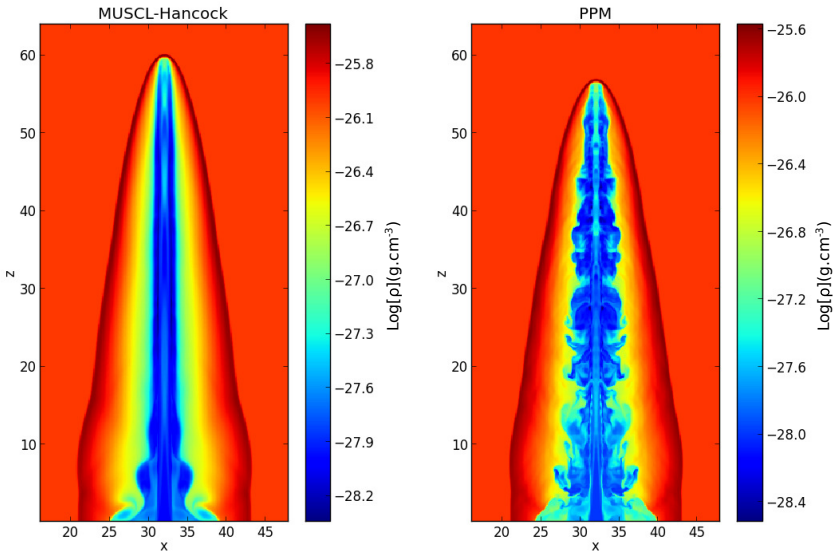

Figure 4.7: Two dimensional slices through the $x - z$ plane comparing the MUSCL-Hancock scheme (right) and the PPM scheme (left), at a time step of 90 units. The colour of the figure is scaled according to the logarithm of the proper density.

Comparing these results to similar simulations presented by Martí et al. (1997) and Rossi et al. (2008) it is noted that in both studies the cocoon region shows turbulence. The turbulence in the cocoon structure of the PPM model is similar to that of models **C2** and **C3** presented in Martí et al. (1997), however, the morphology of the jet head differs. The study of Rossi et al. (2008) shows a continuous cocoon with smaller scale turbulence than the results presented here. This difference in cocoon structure may be due to the perturbations that were injected into the beam in the model of Rossi et al. (2008). The results show that the MUSCL-Hancock scheme does not fully resolve the small scale turbulence that occurs within these systems at lower resolutions.

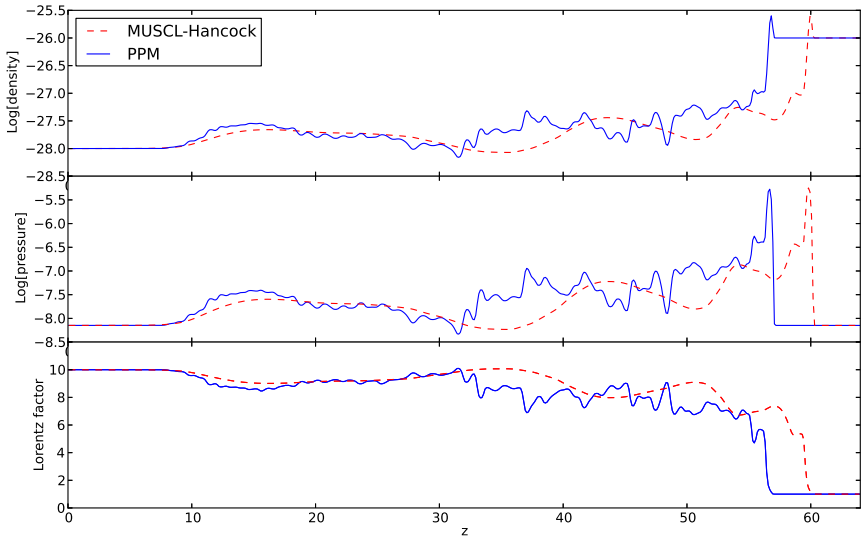

Figure 4.8: One dimensional plots comparing the fluid quantities, density (top), pressure (middle) and the Lorentz factor (bottom), along the centre of the injected jet beam for the MUSCL-Hancock and PPM numerical schemes at a time step of 90 units.

The density, pressure and velocity distribution along the centre of the beam (Figure 4.8) shows that the beams in both configurations are initially stable up to 8 unit lengths. Beyond ~ 8 unit lengths the PPM configuration exhibits short length scale perturbations which are not found in the MUSCL-Hancock scheme. These perturbations may be caused by the turbulence within the cocoon region acting on the jet beam. The perturbations grow larger with distance along the z-axis resulting in different beam structures. The perturbations in the beam lead to a deceleration of the bulk velocity at 30 length units from the injection site, which in turn results in a shorter propagation distance of the working surface in the PPM scheme when compared to the MUSCL-Hancock scheme.

Based on these results the PPM scheme with parabolic reconstruction of the boundary values between cells and characteristic tracing temporal evolution provided the solution which is most consistent with previous studies. This scheme was, therefore, implemented in all further models.

Jet profile

To determine the effects of the jet profile on the results, two simulations were run with the PPM scheme, as discussed above, and identical parameters (Table 4.4). One simulation implemented the jet profile (equation (4.12), while the second was configured with a discontinuous transition

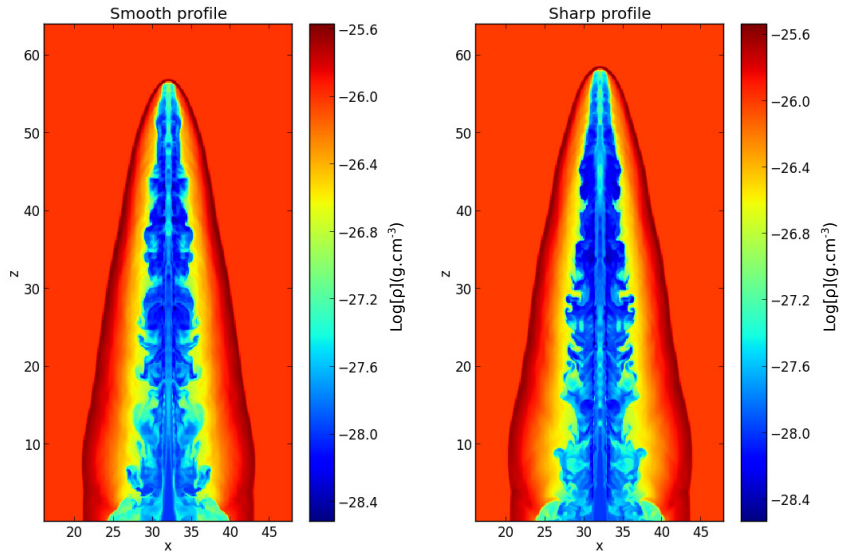

Figure 4.9: Two dimensional slices through the $x-z$ plane of the smoothed profiled jet problem (left) and the sharp transition jet problem (right), at a time step of 90 units. The colour of the figure is scaled according to the logarithm of the proper density.

of fluid variables between the jet and ambient medium at $r = 1$,

$$\mathbf{U} = \begin{cases} \mathbf{U_j} & \text{for } r < 1 \\ \mathbf{U_a} & \text{for } r > 1 \end{cases}. \tag{4.12}$$

Two dimensional slices of the proper density for both models are shown in Figure 4.9. The results show a differences in the small scale structure of the cocoon and beam regions, while the bow shock and jet head show similar morphologies. The density distribution along the centre of the beam (Figure 4.10) shows the difference in the beam structure with the sharp transition causing oscillating shock fronts to form in the beam at a distance of 12 length units. The oscillations transition into a perturbed beam structure at 22 length units which is similar in the beam structure of the profiled jet. The sharp transition model also had a larger propagation distance at the same numerical time step.

Riemann solvers

Several test simulations were also run for different Riemann solvers. The RHD physics module can be used in conjunction with four of the available Riemann solvers, namely, the TVDLF, HLL, HLLC and two shock solvers, which were all tested. The second configuration, employing the HLLC Riemann solver became unstable, generating negative pressure and energy, before the

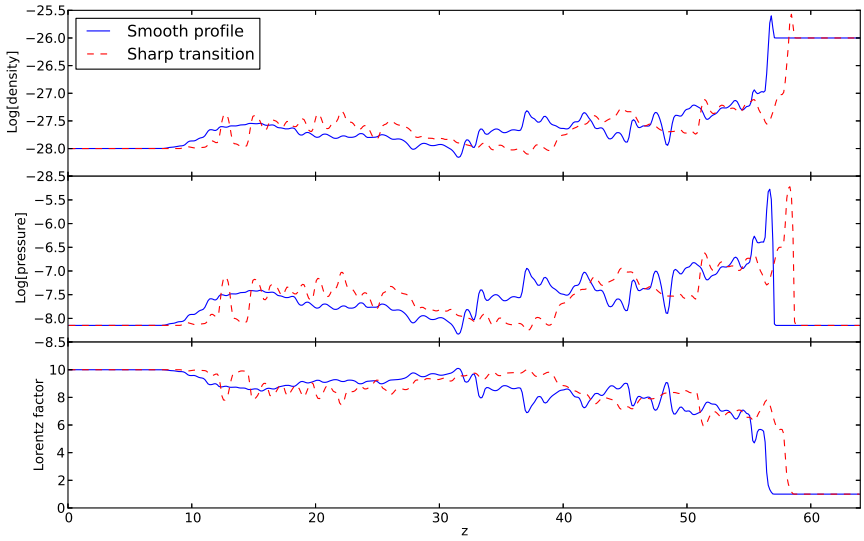

Figure 4.10: One dimensional plots comparing the fluid quantities, density (top), pressure (middle) and the Lorentz factor (bottom), along the centre of the injected jet beam for different beam profiles.

working surface reached the upper boundary of the simulation, and was discarded. To solve this problem the hybrid solver, previously discussed, was implemented. All of the test simulations were constructed and run with the PPM scheme and the same initial environment as the previous tests (Table 4.4).

Two dimensional slices of the proper density distribution of the three remaining simulations are plotted in Figure 4.11. All three simulations produced jet environments with similar large scale structures as discussed in Section 3.3.2. The most notable difference between the solution of the three solvers is the varying degree of turbulence in the cocoon region. The TVDLF solution produces a smooth cocoon with no turbulence. This may be caused by the diffusive nature of the solver not resolving the small scale instabilities that are present in the other solutions. The HLLC hybrid and two shock solutions both show turbulent cocoons but have different internal structure. The hybrid HLLC solution has a symmetric cocoon while that of the two shock solver shows clear asymmetries. Asymmetric cocoon and beam structure have been produced by previous studies of three dimensional simulations such as Rossi et al. (2008). From this we conclude that the two shock Riemann solver provides the more accurate solution.

Plotting the density distribution along the centre of the beam (Figure 4.12) it is clear that the large scale variation in beam density follows the same trend in all three simulations. Similar to the cocoon regions the smaller scale variations in density differs from one Riemann solver to the next. Finally we note from these results that the propagation of the jet head also varies for

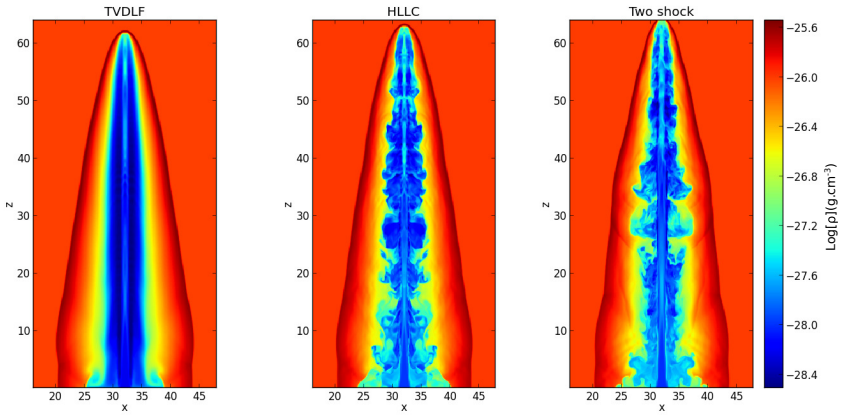

Figure 4.11: Two dimensional slices through the $x - z$ plane of the simulations run with the TVDLF solver (left), HLLC hybrid solver (middle) and the two shock solver (right), at a time step of 100 units. The colour of the figure is scaled according to the logarithm of the proper density.

the solvers with the more accurate solvers resulting in a larger propagation distance at the same time step.

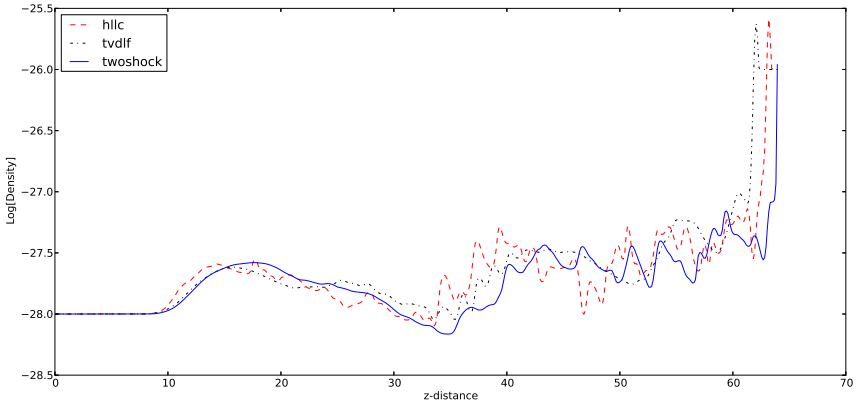

Figure 4.12: One dimensional plots of the proper density along the centre of the injected jet medium in the z-axis. The density is plotted for a comparison between the TVDLF, HLLC hybrid and Two shock Riemann solvers at a time step of 90 units.

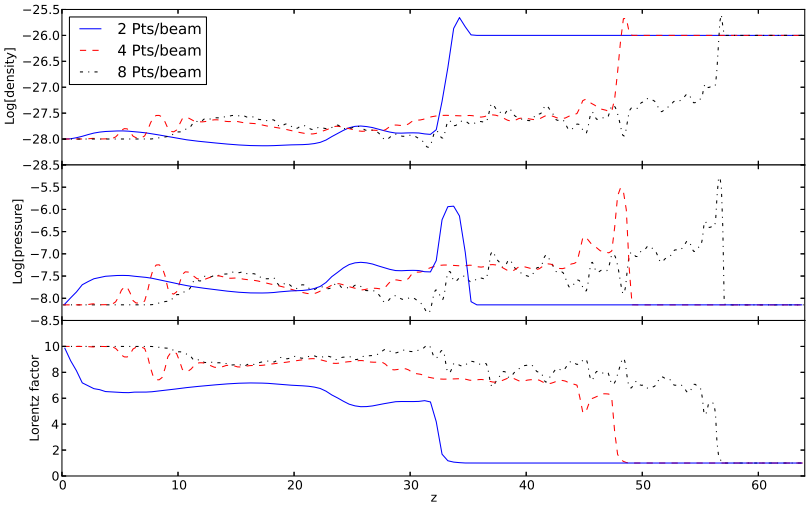

Figure 4.13: One dimensional plots at resolutions of 2, 4 and 8 cells per unit length comparing the fluid quantities, density (top), pressure (middle) and the Lorentz factor (bottom), along the centre of the injected jet beam at $t = 90$.

Resolution convergence

In order to determine whether the previous solutions are well behaved the resolution dependence of the solutions were tested. If the solutions are well behaved then the solution will converge at higher resolution to yield a solution that is not dependent on the resolution of the problem, but only on the physical conditions of the environment. It is therefore important when studying the morphology of the solution that the problem has converged and that an increase in resolution will not significantly alter the structure of the solution. The convergence tests were done starting at a resolution of 2 computational cell per unit length. The resolution was doubled until the solutions reached 8 computational cells per unit length. A further increase of resolution was considered, however the resulting computational intensiveness proved too expensive for the current resources.

Figure 4.13 shows the density of the beam along the z-axis for the hybrid HLLC configuration at different resolutions. From this result it is clear that problem is still resolution dependent and the structure of the jet beam changes as the resolution increases. The most notable change in beam structure is the increase in propagation distance as the resolution increases. The results indicate that higher resolution simulation are needed to fully study all the structures of AGN jets. This is consistent with the results obtained by Mignone et al. (2010a) for RMHD jets. The resolution tests for all three Riemann solvers previously discussed showed similar results.

Table 4.5: Parameters used in the set up of the initial conditions of the lower density test jet problem.

Parameter		Value (arbitrary units)
Lorentz factor	Γ	10
Velocity	v	$0.995c$
Density ratio	η	10^{-3}
Jet density	ρ_b	0.1
Ambient density	ρ_{am}	10
Mach number	M_b	7.8
Adiabatic index	γ_{ad}	5/3
Pressure	P	1×10^{-3}

Variation of the jet parameters

The effects of altering the jet parameters as discussed in Martí et al. (1997) were tested by configuring a problem with a lower density ratio ($\eta = 10^{-3}$) and a higher Mach number ($M_b = 7.8$) than the previous tests. This simulation was run to test whether a change in the jet parameters resulted in the same effects noted by the study of Martí et al. (1997) (e.g. change in propagation efficiency of the jet head). The simulation was run with the same PPM scheme as the previous problems and the hybrid HLLC Riemann solver, since this provided the most stable solutions. The environment parameters for this solution are shown in Table 4.5.

A two dimensional slice of the density distribution of this simulation is shown in Figure 4.14 at a time step of $t = 200$. The lower density ratio resulted in in a decrease in the propagation velocity of the jet head by nearly a factor of two (previous parameters crossed the computational domain just after $t = 100$), even though the injection velocity remained unchanged. This is due to the decreased momentum flux of the jet medium relative to the density of the ambient medium and, therefore, it takes a larger amount of time to inject the same momentum into the environment. The slower propagation speed also resulted in a larger cocoon diameter with smaller turbulent structures. The extended cocoon is also asymmetric similar to the two shock solver in the previous simulations. This occurs due to the instabilities having a larger time to develop in this simulation when compared to the previous tests.

Strong re-collimation shocks are present in the beam of the jet, shown as large oscillations in the density of the beam between ~ 5 and ~ 50 units in Figure 4.15. The re-collimation shocks showed a larger amplitude and shorter wavelengths when compared to the higher density model. These re-collimation shocks dominate the beam up to 40 unit lengths from the injection site, at which point the beam transitions into a turbulent regime. The slower propagation velocity and larger cocoon diameter are consistent with the results shown in Martí et al. (1997).

The resolution convergence of this problem was tested, calculating the simulation at a resolution of 2, 4 and 8 points per unit length and the density along the z-axis is plotted in Figure 4.15. This shows that the problem has a similar resolution dependence to that of the previous tests. In

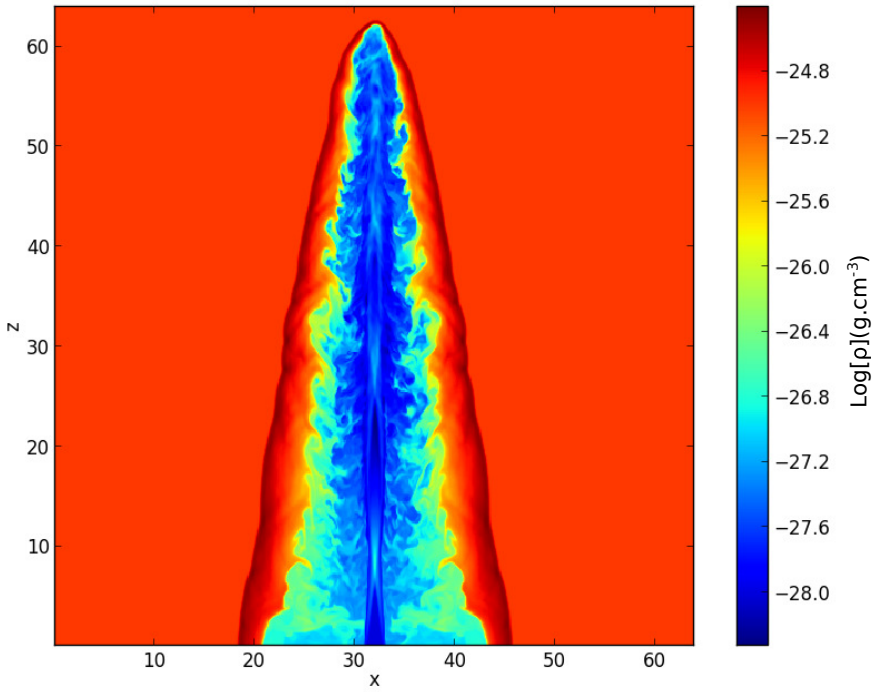

Figure 4.14: Two dimensional slice through the $x - z$ plane of the lower density ratio simulation at a time step of 200 units. The colour of the figure is scaled according to the logarithm of the proper density (see digital appendix Figure 4.14 for a three dimensional rendering of the trace).

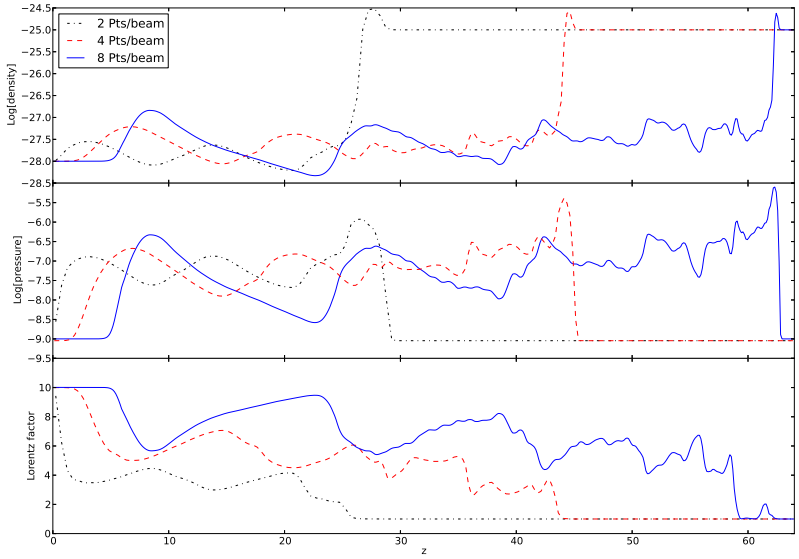

Figure 4.15: One dimensional plots at resolutions of 2, 4 and 8 cells per unit length comparing the fluid quantities, density (top), pressure (middle) and the Lorentz factor (bottom), along the centre of the injected jet beam at $t = 200$.

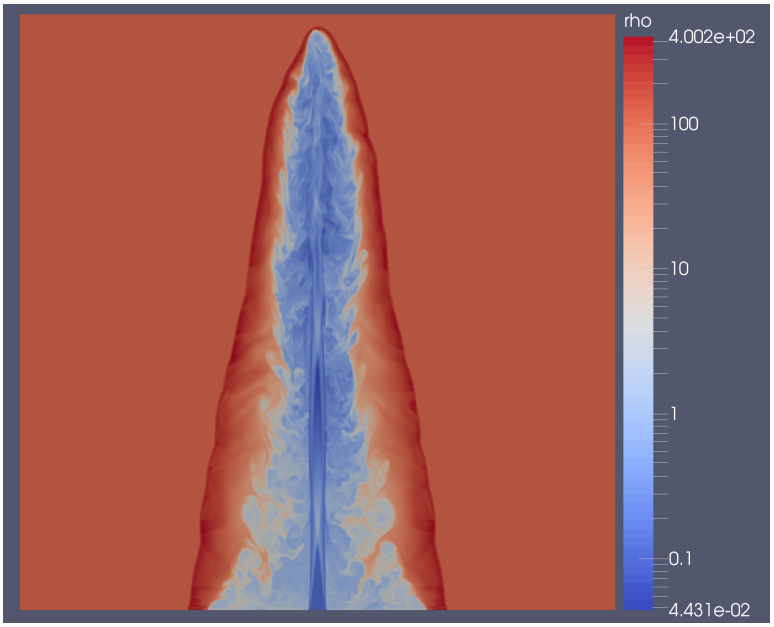

Figure 4.16: Two dimensional slice of the proper density through the $x - z$ plane of the AMR simulation at a time step of 200 units. Density scale is given in arbitrary units.

addition AMR was also tested with an equivalent resolution of 16 points per unit length. Figure 4.16 shows a two dimensional plot of the proper density distribution of the AMR simulation. The results were consistent with that of the static grid.

Table 4.6: Parameters used in the set up of the final relativistic jet problem.

Parameter		Value (arbitrary units)
Lorentz factor	Γ	10
Velocity	v	$0.995c$
Density ratio	η	10^{-5}
Jet density	ρ_b	0.1
Ambient density	ρ_{am}	10000
Mach number	M_b	7.8
Adiabatic index	γ_{ad}	5/3
Pressure	P	0.001

4.4.2 Final simulation model

A final model was set up considering the tests discussed in the previous section and the specific aims of the project, namely to investigate the generation of time dependent structures within relativistic jets and how these structures translate to the observed synchrotron emission. The time dependent structures that are studied in this project are a result of the instabilities which form in the jet and are not due to the injection of perturbations at the nozzle. A constant, steady state injection model was therefore considered in this model.

To study these instabilities a larger computational domain, with dimensions $64 \times 64 \times 128$ units, was considered in the final model. The increase in the spatial and time domains allow the instabilities to grow larger and disrupt the flow of the beam forming time dependent variations (see e.g. Zhao et al., 1992a,b). If the initial injection radius of the relativistic jet is of the order of $r_j \approx 1$ parsec then the entire domain would cover 128 parsec. This length scale is a factor of a thousand smaller than the largest relativistic jet structures observed in AGN however it is large enough to investigate some of the large scale instabilities that may form.

The injected jet material was kept at a constant flow of Lorentz factor 10 however the density ratio was significantly decreased to $\eta = 10^{-5}$ in order to promote the production of instabilities. The final parameters for the simulation are listed in Table 4.6. The simulation was run using the HLLC solver configuration as discussed in the previous section.

Convergence testing was again done for this problem at resolutions of 2, 4 and 8 cells per unit length. The test simulations was run for a small time period and compared in order to determine how well the solution converges. A comparison between the resolutions of 4 and 8 points per unit length are shown in Figure 4.17. These results show that an increase in the resolution of the problem from 4 to 8 points per unit length resulted in only a small decrease in the propagation distance, which is different to the previous conversion tests. Plotting a cross-section of the cocoon (Figure 4.17) shows a similar structure with a slightly larger diameter at 8 points per unit length. This result is consistent with the smaller propagation distance of the jet head. The higher resolution problem shows more turbulent structure however the general structure of both

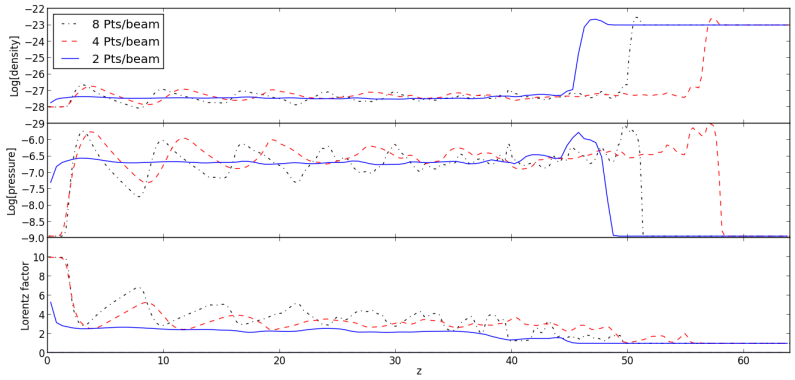

Figure 4.17: One dimensional plots at resolutions of 2, 4 and 8 cells per unit length comparing the fluid quantities (from top to bottom), proper density along the centre of the injected jet beam, proper density cross-section through the x-axis at $z = 16$ units, the pressure and the Lorentz factor along the centre of the injected jet beam at a time step $t = 2000$.

simulations are similar. These results show that the final problem is converging and a further increase in resolution will cause in a negligible change in the results.

Since the convergence tests shows that both 4 and 8 points per unit length produce similar results the simulation was run at the lower resolution, to make the simulation (and subsequent emission modelling) less computationally intensive. The two dimensional slices of the proper density, pressure and velocity magnitude at the final time step ($t = 5100$) are shown in Figure 4.18 and the one dimensional plots through the centre of the beam in Figure 4.19.

The simulation shows the presence of all the previously discussed regions, with the cocoon showing similar small scale turbulence. The structure of the cocoon (Figure 4.18) is divided into an inner region consisting of low density material and an outer, higher density, stationary region, that is generated by the mixing of ambient and cocoon material. The inner cocoon reaches its maximum diameter at a distance of 80 length units and shows a strong asymmetric structure. The beam of the jet is well collimated and stable up to 40 length units. At larger distances the presence of growing perturbations to lead to a small deflection in the propagation direction at 60 length units. Beyond 80 units the centre of the jet is no longer a stable beam of material. Instead the top of the jet consists of smaller high bulk velocity regions propagating towards the head of the jet.

The propagation of the beam at equal time intervals is shown as one dimensional plots of the proper density along the center of the beam in Figure 4.20. The propagation velocity of the jet head decelerates with time with the largest deceleration occurring between the time steps of 4100 and 5100. This occurs due to the breakup of the beam at these large distances. When the jet starts to propagate the beam shows recurring re-collimation shocks. However, once the

working surface moves beyond 40 units the beam becomes more turbulent showing less ordered structure.

In order to transform the results shown in this section to synchrotron emission estimates, radiative transport equations must be applied. This was achieved through developing post-processing software, that calculates two dimensional intensity maps of the estimated synchrotron emission to show regions of higher intensity as well as variability. The post-processing code that was written to calculate these maps will be discussed in the next chapter.

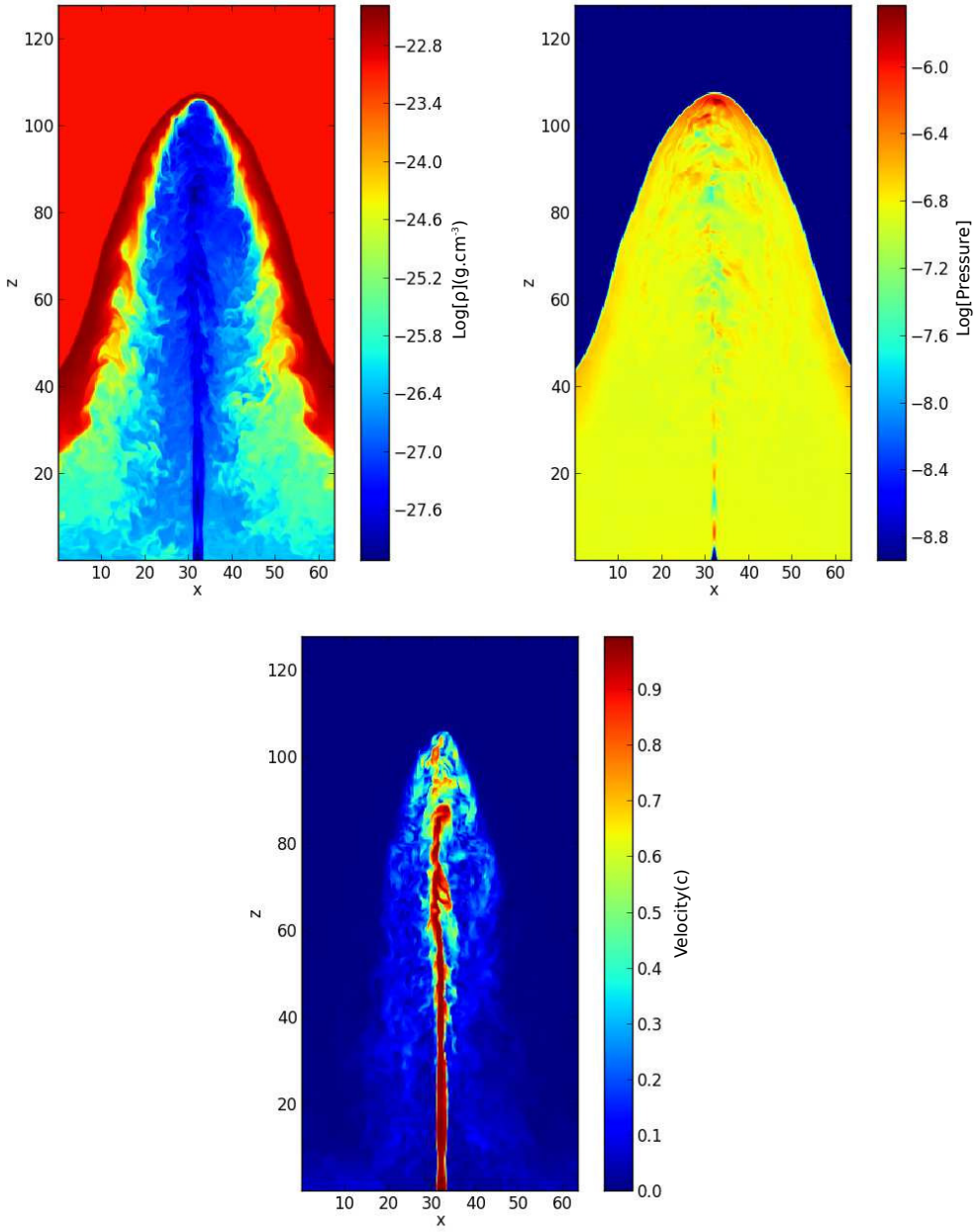

Figure 4.18: Two dimensional slices through the origin in the $x - z$ plane showing the proper mass density distribution (top left), the pressure (top right) and the magnitude of the velocity (bottom) in units of c at a time of 5100 units (see Digital appendix Figure 4.18 for an animation of the simulation).

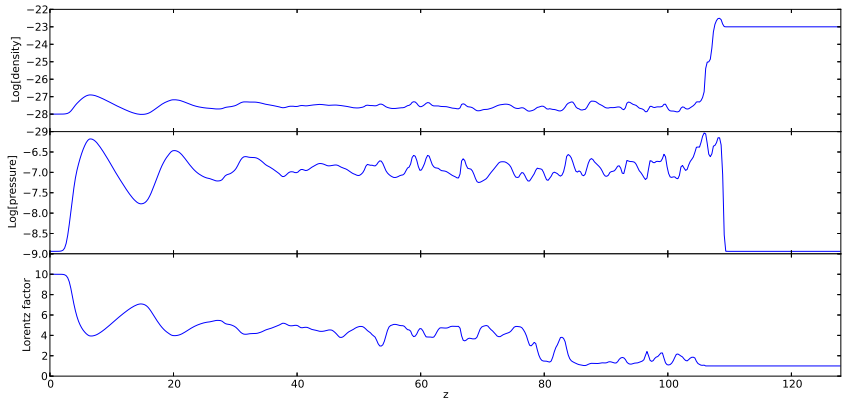

Figure 4.19: One dimensional plots of the fluid quantities, density (top), pressure (middle) and the Lorentz factor (bottom), along the centre of the injected jet beam at $t = 5100$.

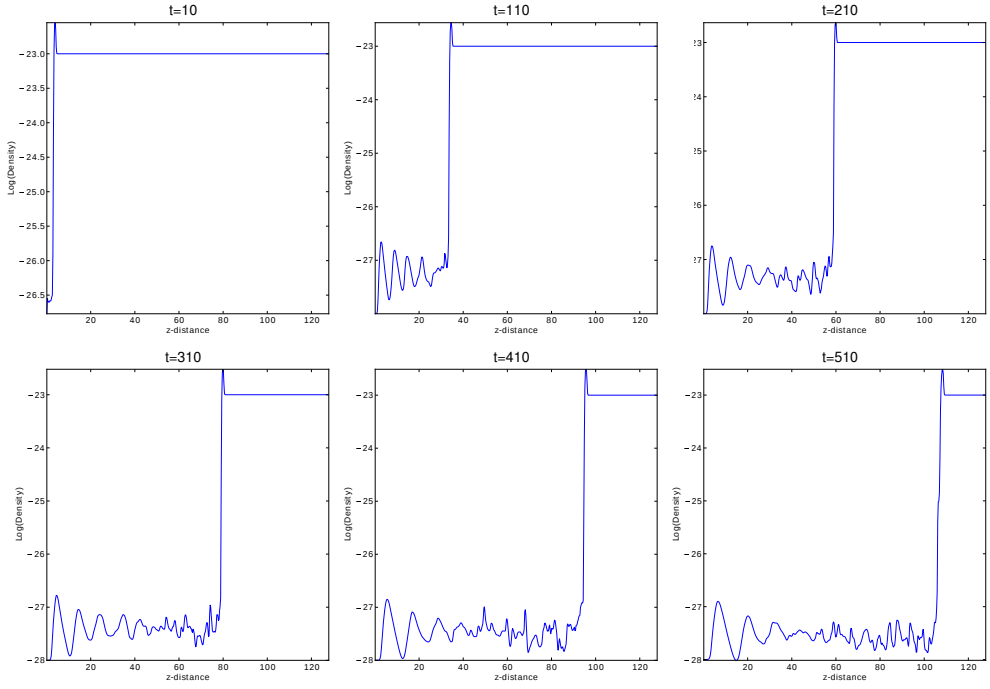

Figure 4.20: One dimensional plots of the proper density along the centre of the injected jet medium in the z-axis at sequential time steps.

Chapter 5

Modelling synchrotron emission of PLUTO simulations

When observing AGN with telescopes we do not directly measure the density, pressure or energy distributions of these sources but rather the emission spectrum that they produce. This spectrum is a combination of many different processes and regions within these sources, which makes modelling all of the observed features very challenging. A large part of the multi-wavelength spectrum observed from AGN is a non-thermal continuum produced by processes such as synchrotron radiation and Inverse Compton scattering within a relativistic jet. In this chapter I investigated how the different fluid dynamic structures that were formed in the numerical simulations discussed in the previous chapter can be used to model the synchrotron emission regions observed within AGN jets.

The fluid dynamic simulations run and discussed in the previous chapter only calculate the fluid properties such as the mass density and energy distributions of the environment. To determine the emission that these simulated environments produce, and compare them to observational data, a radiative transfer model must be applied. In this chapter I discuss the radiative transfer model I implemented and applied to the simulations as a post-processing code. The code is designed to provide an approximation of the synchrotron emission produced in the $10^9 - 10^{14}$ Hz frequency range for these sources, by applying the δ-approximated synchrotron method (which is discussed in Section 5.1.4).

The chapter is divided into three sections. In the first section the synchrotron transfer equations, used in the model, are derived. The second section explains the implementation of these equations in the post-processing code. In the final section I present the results from these simulations and discuss their implications.

5.1 Emission model

The general discussion on radiative processes presented in this section follows that of Rybicki and Lightman (1979). The δ-approximation model implemented for the synchrotron transfer equations is derived and discussed in detail by Böttcher et al. (2012) and Dermer and Menon (2009).

5.1.1 Basic definitions

In order to determine the energy output from an astrophysical source we measure the energy from photons we receive at earth. Since one can only measure the photons that have propagated along the line-of-sight of the observer a useful way to define the energy we receive is called the radiative flux F. This quantity is defined as the measure of the energy E we receive per unit area $\mathrm{d}A$ per time unit $\mathrm{d}t$,

$$F = \frac{\mathrm{d}E}{\mathrm{d}A\mathrm{d}t} \quad [\mathrm{erg\,cm^{-2}s^{-1}}], \tag{5.1}$$

The radiative flux includes the energy emitted over the entire electromagnetic spectrum. In order to provide a measure of the flux at certain frequencies we define the specific flux F_ν,

$$F_\nu = \frac{\mathrm{d}F}{\mathrm{d}\nu} = \frac{\mathrm{d}E}{\mathrm{d}A\mathrm{d}t\mathrm{d}\nu} \quad [\mathrm{erg\,cm^{-2}s^{-1}Hz^{-1}}], \tag{5.2}$$

which is the radiative flux per unit frequency ν. If the source is extended in the sky the flux measurement will include photons from all solid angles. The measurement of flux per solid angle $\mathrm{d}\Omega$ is defined as the intensity I. To obtain the flux from the intensity, the intensity is integrated over the solid angle taking into account the angle of the incident photons with respect to the surface θ,

$$F_\nu = \int I_\nu \cos\theta \mathrm{d}\Omega, \tag{5.3}$$

where I_ν is the specific intensity, which is the intensity per unit frequency ν, given by,

$$I_\nu = \frac{\mathrm{d}E}{\mathrm{d}A\mathrm{d}t\mathrm{d}\nu\, d\Omega} \quad [\mathrm{erg\,cm^{-2}s^{-1}Hz^{-1}ster^{-1}}], \tag{5.4}$$

The total luminosity of a source is found by integrating the flux over the surface area of the emitting source,

$$\begin{aligned} L_\nu &= \frac{\mathrm{d}E}{\mathrm{d}t\mathrm{d}\nu} \\ &= \int_0^{\mathrm{d}} F_\nu \mathrm{d}A \\ &= 4\pi d^2 F_\nu \quad [\mathrm{erg\,s^{-1}}], \end{aligned} \tag{5.5}$$

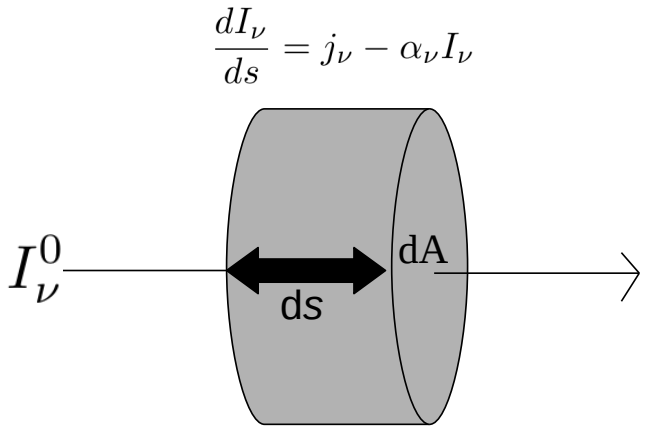

Figure 5.1: Change in intensity per unit length as emission propagates through a medium

where d is the distance to the source. The specific radiation energy density u_ν of a source is defined as the radiated energy per volume $\mathrm{d}V$ per solid angle per unit frequency,

$$u_\nu(\Omega) = \frac{\mathrm{d}E}{\mathrm{d}V \mathrm{d}\nu \ \mathrm{d}\Omega}. \tag{5.6}$$

The volume unit $\mathrm{d}V$ can be expressed as,

$$\mathrm{d}V = \mathrm{d}A\mathrm{d}s = \mathrm{d}A c \mathrm{d}t, \tag{5.7}$$

where $\mathrm{d}s = c\mathrm{d}t$ is the unit length of the volume increment and the energy density is thus related to the intensity as,

$$u_\nu = \frac{I_\nu}{c}. \tag{5.8}$$

5.1.2 Radiative Transfer

The specific intensity of radiation passing through a medium along a path towards an observer will not remain constant. Emission may be absorbed or scattered in different directions as it travels through the medium or new photons can be added to the radiation through the emission of atoms along the path (Figure 5.1). In order to determine the intensity of a source at any distance the radiation must be integrated along the path the photons travel using radiative transfer equations.

The emission of new photons per unit frequency per volume increment along the travel path is calculated as the specific emission coefficient j_ν, defined as,

$$j_\nu = \frac{\mathrm{d}E}{\mathrm{d}V \mathrm{d}\Omega \mathrm{d}t \mathrm{d}\nu} \quad [\mathrm{erg\ cm^{-3} Hz^{-1} s^{-1} sr^{-1}}]. \tag{5.9}$$

If this emission occurs over a distance ds then the total change in the specific intensity will be,

$$\mathrm{d}I_\nu = j_\nu \mathrm{d}s. \tag{5.10}$$

The specific absorption coefficient α_ν in turn is defined as the fraction of intensity lost due to scattering and absorption along a distance ds. The change in intensity along this distance due to absorption can then be expressed as,

$$\mathrm{d}I_\nu = -\alpha_\nu I_\nu \mathrm{d}s, \tag{5.11}$$

where the decrease in intensity due to absorption is proportional to the initial intensity of the medium.

The transfer equations are often represented in terms of the optical depth of the medium τ_ν, which is defined as,

$$\tau_\nu = \int_0^l \alpha_\nu(s)\mathrm{d}s, \tag{5.12}$$

where l is the column length of the medium. If we integrate equation (5.11) and substitute in the optical depth (equation 5.12), we obtain,

$$I_\nu(\tau_\nu) = I_\nu^0 e^{-\tau_\nu}. \tag{5.13}$$

If $\tau_\nu \geq 1$ this will result in a large decerease in the initial instensity and the medium is considered as optically thick. In an optically thin medium, $\tau_\nu < 1$, the intensity will only decease a small amount and final intensity will be close to the original intensity.

For a medium which is both emitting and absorbing radiation, equations (5.10) and (5.11) can be combined into the transfer equation,

$$\frac{\mathrm{d}I_\nu}{\mathrm{d}s} = j_\nu - \alpha_\nu I_\nu. \tag{5.14}$$

Expressing equation (5.14) in terms of the optical depth gives,

$$\frac{\mathrm{d}I_\nu}{\mathrm{d}\tau_\nu} = S_\nu - I_\nu, \tag{5.15}$$

where $S_\nu \equiv j_\nu/\alpha_\nu$. Integrating this expression provides the formal solution to the transfer equations,

$$I_\nu(\tau_\nu) = I_\nu^0 e^{-\tau_\nu} + \int_0^{\tau_\nu} e^{\tau'_\nu - \tau_\nu} S_\nu(\tau'_\nu)\mathrm{d}\tau'_\nu. \tag{5.16}$$

5.1.3 Lorentz transformations

Since the bulk motion of AGN jets are relativistic, Lorentz transformations between the emitted and received frames must be taken into account. According to special relativity when a pulse of

light is emitted at a time $t = 0$ at the origins of two reference frames (K and K') that move with a constant relative velocity with respect to each other the resulting light path in both reference frames must adhere to,

$$x^2 + y^2 + z^2 - (ct)^2 = 0 \tag{5.17}$$
$$x'^2 + y'^2 + z'^2 - (ct')^2 = 0, \tag{5.18}$$

where the unprimed coordinates are with respect to the reference frame K and the primed with respect to K'. In order to compare the coordinates of one reference frame to that of another, relationships can be derived between the primed and unprimed coordinates. These relations are known as the Lorentz transformations. If the relative motion between the reference frames (v) is in the x-direction the resulting Lorentz transformations are given by,

$$x' = \Gamma(x - vt) \tag{5.19}$$
$$y' = y \tag{5.20}$$
$$z' = z \tag{5.21}$$
$$t' = \Gamma\left(t - \frac{v}{c^2}x\right), \tag{5.22}$$

where

$$\Gamma = \frac{1}{\sqrt{1 - (v/c)^2}}, \tag{5.23}$$

is the Lorentz factor between the frames of reference[i]. This result has the implication that the measurement of the properties of a source change based on the reference frame from which the measurement takes place. Consider the plasma in a relativistic jet moving at velocities close to the speed of light. Applying the above transformations to the co-moving reference frame of the plasma, the relationship between the time interval measured in a stationary galactic reference frame (K) and the co-moving frame of the plasma (K') is given by,

$$\begin{aligned} \Delta t &= t_2 - t_1 \\ &= \Gamma\left(t'_2 + \frac{v}{c^2}x'\right) - \Gamma\left(t'_1 + \frac{v}{c^2}x'\right) \\ &= \Gamma(t'_2 - t'_1) \\ &= \Gamma(\Delta t'), \end{aligned} \tag{5.24}$$

If the relative motion of the reference frames are at an angle θ with respect to the x-axis the difference in the time of arrival between two photons emitted in the jet is given by equation (2.22). In this equation the emitted and arrival times are defined in terms of the stationary galactic frame. In order to obtain the relationship between the measured interval in the galactic

[i]Here the convention is followed that Γ refers to the Lorentz factor associated with the bulk motion, while γ will be used in the following section to refer to the Lorentz factor of individual particles.

frame and the interval in the co-moving frame of the plasma t'_e the Lorentz transformation (equation 5.24) must be applied, giving,

$$\begin{aligned}\Delta t &= \Gamma t'_e \left(1 - \frac{v}{c}\cos\theta\right) \\ &= \delta^{-1} t'_e,\end{aligned} \tag{5.25}$$

where

$$\delta = \frac{1}{\Gamma\left(1 - \frac{v}{c}\cos\theta\right)}, \tag{5.26}$$

is known as the Doppler factor. The frequency of the received photons are also effected by this transformation,

$$\nu = \frac{1}{t} = \delta\nu'. \tag{5.27}$$

Similar transformations can be derived for properties such as the measured energy E and solid angle $d\Omega$, where for example,

$$E = h\nu = \delta E' \tag{5.28}$$

and

$$\mathrm{d}\Omega = \mathrm{d}\mu\mathrm{d}\phi = \delta^{-2}\mathrm{d}\Omega', \tag{5.29}$$

in which $\mathrm{d}\mu = \mathrm{d}(\cos\theta) = \delta^{-2}\mathrm{d}\mu'$ and $\mathrm{d}\phi = \mathrm{d}\phi'$ (Rybicki and Lightman, 1979, chapter 4).

The transformation of intensity measured from a source can be derived from the previous relations as,

$$I_\nu = \frac{\mathrm{d}E}{\mathrm{d}A\mathrm{d}t\mathrm{d}\nu\ \mathrm{d}\Omega} = \frac{\mathrm{d}(\delta E')}{\mathrm{d}A'(\delta^{-1}\mathrm{d}t')(\delta\mathrm{d}\nu')\ (\delta^{-2}\mathrm{d}\Omega')} = \delta^3\frac{\mathrm{d}E'}{\mathrm{d}A'\mathrm{d}t'\mathrm{d}\nu'\ \mathrm{d}\Omega'} = \delta^3 I'_{\nu'} \tag{5.30}$$

Similarly the transformation of the absorption and emission coefficients in the transfer equations are given by (Rybicki and Lightman, 1979, pp. 146-147),

$$j_\nu = \frac{\mathrm{d}I}{\mathrm{d}s} = \frac{\delta^3 I'_{\nu'}}{\delta\mathrm{d}s'} = \delta^2 j'_{\nu'} \tag{5.31}$$

$$\alpha_\nu = \delta^{-1}\alpha'_{\nu'}, \tag{5.32}$$

and the relativistic transfer equation for the observed intensity change is given by,

$$\frac{\mathrm{d}I_\nu}{\mathrm{d}s} = \delta^2 j'_{\nu'} - \delta^{-1}\alpha'_{\nu'} I_\nu. \tag{5.33}$$

5.1.4 Synchrotron radiation

As discussed previously (see Chapter 2) the continuum emission from AGN contains radiation from non-thermal processes. The non-thermal emission produces two "bumps" in the spectral energy distributions of AGN. At lower energies the emission is primarily due to electron syn-

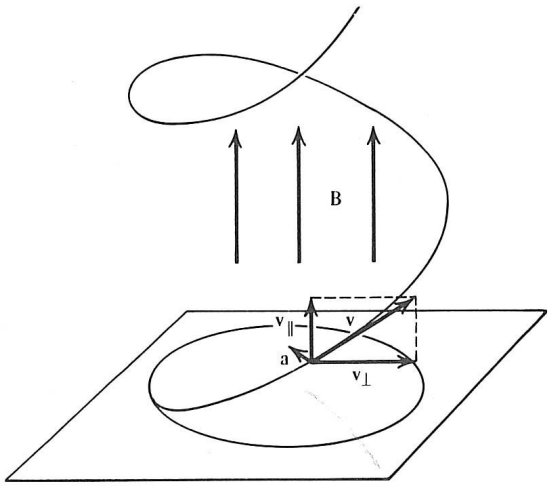

Figure 5.2: Charged particle following a helical trajectory along a uniform magnetic field. Figure adopted from Rybicki and Lightman (1979) figure 6.1.

chrotron radiation, while the higher energy component can be produced by leptonic or hadronic processes. In the leptonic model the emission is due to inverse Compton scattering of low energy photons off high energy electrons. Hadronic models suggest that the high energy component may be due to photohadronic interactions or proton synchrotron emission. The focus of this study is to reproduce the emission in the low energy component and, therefore, the production of electron synchrotron radiation will be discussed in detail.

Charged particles moving in a magnetic field will be accelerated and thus produce electromagnetic radiation. Since the particles moving in an AGN jet are relativistic the resultant emission is in the form of synchrotron radiation. The motion of the charged particles will follow a helical trajectory along a magnetic field (Figure 5.2) with a gyration frequency given by,

$$\omega_B = \frac{qB}{\gamma mc}, \tag{5.34}$$

where B is the magnetic field strength, q is the charge of the particle, γ is its Lorentz factor and m is its mass. The power of the emission radiated by a single particle in such a magnetic field can be determined by the Larmor equation,

$$P = \frac{2q^2}{3c^3}\gamma^4|a|^2, \tag{5.35}$$

where P is the power of the emission from the particle and a is the magnitude of the acceleration.

For a particle spiralling in a magnetic field the acceleration can be expressed as,

$$\begin{aligned} a &= \frac{q}{\gamma mc}\mathbf{v}\times\mathbf{B} \\ &= \omega_{\mathrm{B}} v_{\perp}, \end{aligned} \tag{5.36}$$

where the acceleration is perpendicular to the magnetic field. For an isotropic distribution of particle velocities the average perpendicular velocity component with respect to the magnetic field will be given by

$$\begin{aligned} \langle v_{\perp}^2 \rangle &= \frac{\int v^2 \sin^2\alpha \mathrm{d}\Omega}{4\pi} \\ &= \frac{2v^2}{3}, \end{aligned} \tag{5.37}$$

where α is the angle between the particle velocity and the magnetic field. Therefore, the pitch averaged total power radiated over all frequencies by a single charged particle is given by,

$$\begin{aligned} P &= \left(\frac{2}{3}\right)^2 \left(\frac{q^2}{mc^2}\right)^2 \gamma^2 B^2 \frac{v^2}{c} \\ &= \frac{32\pi}{9}\left(\frac{q^2}{mc^2}\right)^2 U_B \beta^2 c \gamma^2 \\ &= \frac{4}{3}\sigma_T c \beta^2 \gamma^2 U_B, \end{aligned} \tag{5.38}$$

where $\beta = v/c$, $\sigma_T = \frac{8\pi}{3}(\frac{q^2}{mc^2})^2$ is the Thompson cross section and $U_B = B^2/8\pi$ is the magnetic energy density.

The total power emitted through synchrotron radiation by a charged particle is spread of a range of frequencies ν such that,

$$P = \int_0^{\infty} P_{\nu}(\nu) d\nu, \tag{5.39}$$

where P_{ν} is the power radiated per frequency. The full expression for the power emitted per frequency, $P_{\nu}(\gamma, \alpha)$, has been derived as (Rybicki and Lightman, 1979),

$$P_{\nu} = \frac{\sqrt{3} q^3 B \sin\alpha}{mc^2} F\left(\frac{\nu}{\nu_{\alpha}}\right), \tag{5.40}$$

where,

$$F(x) \equiv x \int_x^{\infty} K_{5/3}(\zeta) \mathrm{d}\zeta, \tag{5.41}$$

where $K_{5/3}(\zeta)$ is the modified Bessel function of the second type, and ν_{α} is,

$$\nu_{\alpha} = \frac{3qB\sin\alpha}{4\pi mc}\gamma^2. \tag{5.42}$$

In the case of an isotropic distribution of radiating particles the expression can be integrated

over all angles α (Böttcher et al., 2012; Crusius and Schlickeiser, 1986),

$$P_\nu = \frac{\sqrt{3}q^3 B \sin\alpha}{2mc^2}\frac{v}{v_c}\left[W_{0,\frac{4}{3}}\left(\frac{v}{v_c}\right)W_{0,\frac{1}{3}}\left(\frac{v}{v_c}\right) - W_{\frac{1}{2},\frac{5}{6}}\left(\frac{v}{v_c}\right)W_{\frac{-1}{2},\frac{5}{6}}\left(\frac{v}{v_c}\right)\right], \tag{5.43}$$

where $W\left(\frac{v}{v_c}\right)$ is the Whittaker functions and,

$$\nu_c = \frac{3qB}{4\pi mc}\gamma^2, \tag{5.44}$$

is defined as a critical frequency.

If the emission is assumed to originate from a distribution of electrons, $n(\gamma)$, then the total power emitted from these electrons (averaged over pitch angle) is given by,

$$P_\nu = \int P_\nu(\gamma) n(\gamma) \mathrm{d}\gamma. \tag{5.45}$$

Calculating the full analytical expression for the synchrotron emission coefficients for each cell in the fluid dynamic environment will result in a very computational resource intensive code. To simplify the calculation the emission coefficient can be approximated, with reasonable accuracy, assuming that the charged particles only radiate at the critical frequency. This approximation takes on the form of a δ-function for the power spectrum (see equation 5.38),

$$P_\nu^{\mathrm{sy},\delta} = \frac{32\pi}{9}\left(\frac{q^2}{mc^2}\right)^2 U_B \beta^2 c\gamma^2 \delta(\nu - \nu_c), \tag{5.46}$$

where,

$$\nu_c = \nu_0 \gamma^2, \tag{5.47}$$

and

$$\nu_0 = \frac{3qB}{4\pi mc}. \tag{5.48}$$

To determine the emission coefficients of a medium the power radiated is integrated over the spectrum of all radiating particles, such that,

$$j_\nu = \frac{1}{4\pi}\int_1^\infty P_\nu(\gamma) n(\gamma) \mathrm{d}\gamma. \tag{5.49}$$

Here $n(\gamma)$ denotes the particle distribution function as the number of particles per unit volume with Lorentz factor γ, such that,

$$n = \int_0^\infty n(\gamma)\mathrm{d}\gamma, \tag{5.50}$$

where n is the particle density.

In this approximation it will be assumed that the particle distribution is in the form of a

single power-law distribution given by,

$$n(\gamma) = n_0 \gamma^{-p}, \tag{5.51}$$

where n_0 is a normalization factor and p in the particle index.

Substituting equation (5.46) into (5.49) and integrating yields,

$$\begin{aligned} j_\nu &= \frac{1}{4\pi} \int_1^\infty \frac{32\pi}{9} \left(\frac{q^2}{mc^2}\right)^2 U_B \beta^2 c \gamma^2 \delta(\nu - \nu_c) n(\gamma) \mathrm{d}\gamma, \\ &= \frac{4}{9} \left(\frac{q^2}{mc^2}\right)^2 u_B \beta^2 c \nu^{\frac{1}{2}} \nu_0^{-\frac{3}{2}} n\left(\sqrt{\frac{\nu}{\nu_0}}\right). \end{aligned} \tag{5.52}$$

The absorption coefficient for the medium can be derived in a similar fashion. Rybicki and Lightman (1979, p 189) derives the expression for the absorption coefficient as (see also Böttcher et al., 2012, p 48),

$$\alpha_\nu^\delta = -\frac{p+2}{8\pi m \nu^2} \int_1^\infty P_\nu(\gamma) \frac{n(\gamma)}{\gamma} \mathrm{d}\gamma. \tag{5.53}$$

Once again substituting equation (5.46) into this expression and integrating yields,

$$\begin{aligned} \alpha_\nu^\delta &= -\frac{p+2}{8\pi m \nu^2} \int_1^\infty \frac{32\pi}{9} \left(\frac{q^2}{mc^2}\right)^2 U_B \beta^2 c \gamma^2 \delta(\nu - \nu_c) \frac{n(\gamma)}{\gamma} \mathrm{d}\gamma, \\ &= \frac{2}{9} \left(\frac{p+2}{m\nu^2}\right) \left(\frac{q^2}{mc^2}\right)^2 U_B \beta^2 c \nu_0^{-1} n\left(\sqrt{\frac{\nu}{\nu_0}}\right). \end{aligned} \tag{5.54}$$

Equations (5.52) and (5.54) can be substituted into the relativistic transfer equation (equation 5.33) in order to determine the change in intensity along a line-of-sight in the simulation. The δ-approximation provides reasonable accuracy for the synchrotron radiation, Figure 5.3 shows a comparison of the approximated emissivity to the exact solution for a particle index of $p = 2.5$. The ratio of the emissivity (over all frequencies) of the exact solution and the δ-approximation can be determined as (Dermer and Menon, 2009, pp. 129-130),

$$\rho_\delta = \frac{j^{syn}}{j_\delta^{syn}} = 6a(p) \left(\frac{3}{2}\right)^{(p+1)/2}, \tag{5.55}$$

where

$$a(p) = \frac{2^{(p-1)/2} \sqrt{3} \Gamma[\frac{3p-1}{12}] \Gamma[\frac{3p+19}{12}] \Gamma[\frac{p-5}{4}]}{8\sqrt{\pi}(p+1)\Gamma[\frac{p+7}{4}]}, \tag{5.56}$$

is a function of the particle-index and Γ is the gamma function[ii]. In this study $p = 1.8$ was used as the particle index which results in $\rho_\delta = 1.237$.

[ii] No relation to the bulk Lorentz factor.

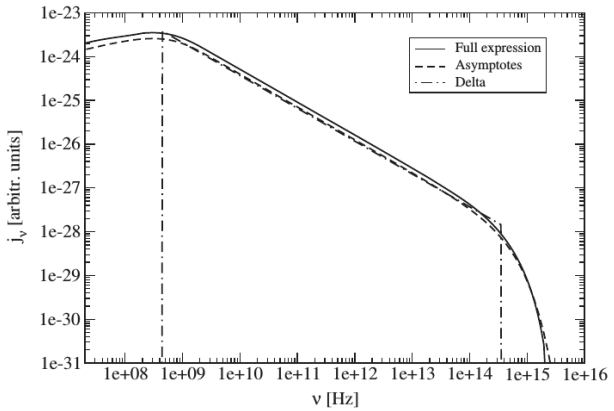

Figure 5.3: Comparison of the exact expression and δ-approximation of the synchrotron spectrum calculated with energy cutoffs $\gamma_1 = 10$ and $\gamma_2 = 10^4$ for a particle-index $p = 2.5$ and magnetic field strength $B = 1$ G. Figure adopted from Böttcher et al. (2012), figure 3.2.

5.2 Post-processing code

To produce two dimensional intensity maps of the three dimensional fluid environment, the emission and absorption coefficients of each cell must be integrated along the line-of-sight of the observer. To calculate the maps within the runtime of the PLUTO simulation would add an additional layer of complexity and computational intensiveness to the simulation. An additional disadvantage to calculating the maps during runtime is that the simulation must be rerun in order to alter the emission parameters. It was therefore decided to create a post-processing code to produce the intensity maps.

The post-processing code that was created for this study focussed on investigating the variation in the emission during the evolution of the jet rather than on quantitative flux estimates. The main aim of the code was to study the production of individual emission components such as hotspots in the cocoon of the simulations. The code was designed as a script in the PYTHON language specifically for the PLUTO data structure. It requires PYTHON version 2.7 or later and the PYPLUTO library that is included with the PLUTO software. The script must be run from within the simulation directory and can be used with double or single precision binary files as input for the calculations. The simulation that is used must be constructed with a uniform Cartesian mesh grid.

When the script is run the number of data frames, the time steps, the numerical time scale and the average time increment is displayed. The user is prompted for a polar (θ) and an azimuth angle (ϕ) that is used to define the line-of-sight, the observed frequency of the intensity map, as well as the data file which should be used as input. If a value of -1 is entered for the data

```
[vdwesthuizenip@localhost RHDVH]$ python See3.2.py
#####################################################################
 Synchrotron emission estimates for PLUTO data
Version 3.1
 ###################################################################################
------------TIME INFORMATION--------------
nlast = 544
time  = 5439.998
dt    = 0.1003454
Nstep = 54288
-----------------------------------------
Enter the angle phi: 1e-10
Enter the theta angle: 0.3491
Frequency for intensity map: 15e9
Frame number for estimate calculations: 510
Reading Data file : /home/vdwesthuizenip/PLUTO/RHDVH2/RHDVH/data.0510.flt
Grid size: (256,256,512)
Image size;
(272, 256.0)
Calculating intensity map for frame 510
writing file imapl0_63.0_0.0.flt
Execution time: 845.932785988 s
```

Figure 5.4: Screen shot of the post-processing code.

file, intensity maps will be calculated for each available data file in the directory. All of the integration steps are logged so the user can monitor the calculation. A screen shot of the user interface is shown in Figure 5.4. The full code is given in Appendix B.

5.2.1 Absorbtion and emission coefficients

The first step to produce intensity maps was to calculate the emission and absorption coefficients for each cell within the three dimensional grid of the fluid dynamic simulation. The model assumed that the fluid within each cell in the environment is a plasma containing electrons and protons. Within the plasma, electrons were considered as the main source of synchrotron emission and consisted of a population of electrons with a power law particle distribution (given by equation 5.51).

The normalization factor of the power law distribution was considered dependent on the fluid properties (energy and number density) of the cell. This dependence was based on the model presented by Gomez et al. (1995), in which it is assumed that the entire population of electrons in each cell is in the power-law distribution such that,

$$n = \int_{e_{min}}^{e_{max}} n_0 e^{-p} \mathrm{d}e, \tag{5.57}$$

with a total energy density,

$$e = \int_{e_{min}}^{e_{max}} e n_0 e^{-p} \mathrm{d}e. \tag{5.58}$$

This results in the results in a normalization factor of,

$$n_0 = \left(\frac{e(p-2)}{1-C_E^{2-p}}\right)^{p-1}\left(\frac{1-C_E^{1-p}}{n(p-1)}\right)^{p-2}, \tag{5.59}$$

assuming that the jet is composed of a 1:1 ratio of electrons and protons with,

$$n = \frac{\rho}{m_p}, \tag{5.60}$$

where m_p the mass of a proton, p is the particle-index and C_E is the ratio of the maximum and minimum energies of the electron contributing to the emission. For our initial estimates we chose $p = 1.8$ and $C_E = 10^3$.

Using the power-law particle distribution the absorption and emission coefficients were calculated according to equations (5.52) and (5.54). It was assumed that the jet medium contained a turbulent magnetic field which is large enough to produce synchrotron emission but small enough to be dynamically negligible. The magnetic field energy density is assumed to be an equipartition fraction of the internal energy density calculated as,

$$U_B = \epsilon_B e. \tag{5.61}$$

A value of $\epsilon_B = 10^{-3}$ was chosen based on results of Böttcher and Dermer (2010).

The normalization factor along with the components of the emission and absorption coefficients that are independent of frequency were determine for each cell during the runtime of the PLUTO simulation. This was done to save on computational resources as these values must be calculated for each cell and it is much more efficient to do this during runtime when all of the variables are already loaded into memory. A three dimensional trace plot of the frequency independent component of the emissivity is shown in Figure 5.5. The frequency component is dependent on the user input and is applied in the post processing code. The frequency component specified by the user is corrected to the co-moving frame of each fluid cell. After the full expressions for the emission and absorption coefficients were calculated they were transformed from the co-moving frame into the observer frame before numerically integrating the coefficients to determine the observed intensity.

5.2.2 Two dimensional image

In order to calculate the intensity maps a two dimensional image must be constructed. The image is defined by a plane that passes through the centre of the three dimensional fluid environment. The plane is oriented such that the line-of-sight is orthogonal to the plane. The line-of-sight is determined by the polar and azimuth angles that are given by the user. The azimuth angle defines the angle of the line-of-sight in the xy-plane relative to the x-axis, while the polar angle is defined relative to the z-axis. A polar angle of $\theta = 0°$ results in the observer viewing the jet

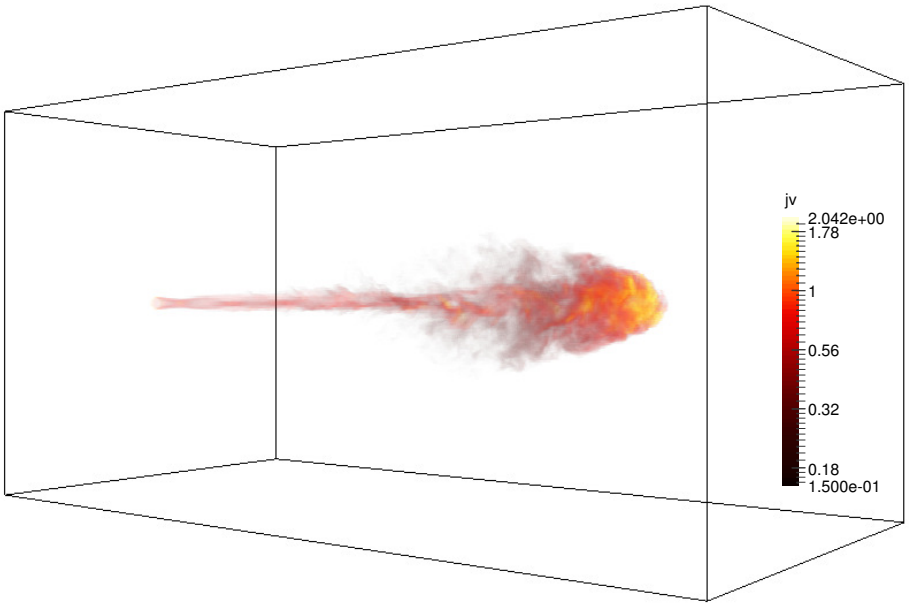

Figure 5.5: Three dimensional rendering of the trace of the jet medium. The colour scale shows the frequency independent component of the emission coefficient (see digital appendix Figure 5.3 for an animation of the evolution of the emission coefficients).

face-on with respect to the relativistic jet, while $\theta = 90°$ results in an edge-on view. Figure 5.6 illustrates the defined line-of-sight (O) relative to the polar (θ) and azimuth angles (ϕ).

The line-of-sight is defined by the vector,

$$\bar{n} = (\sin\theta\cos\phi,\ \ \sin\theta\sin\phi,\ \ \cos\theta), \tag{5.62}$$

which also gives the normal to the image plane. The image plane consists of a number of pixels with unit lengths equal to the cell length of the environment. The coordinates of each pixel on the image plane is defined by a pair of unit vectors $(I\hat{M}x, I\hat{M}y)$ that form an orthogonal basis, defined in terms of the three dimensional Cartesian grid as,

$$I\hat{M}x = (\cos\phi\cos\theta\,\hat{x},\ \ \sin\phi\cos\theta\,\hat{y},\ \ -\sin\theta\,\hat{z}) \tag{5.63}$$

$$I\hat{M}y = (-\sin\phi\,\hat{x},\ \ \cos\phi\,\hat{y},\ \ 0\,\hat{z}). \tag{5.64}$$

The dimensions of the image are dynamically resized based on the viewing angle of the observer and are determined by the length of a line running through the three dimensional grid along the basis vectors of the image plane through the centre of the plane. Due to the way the image plane

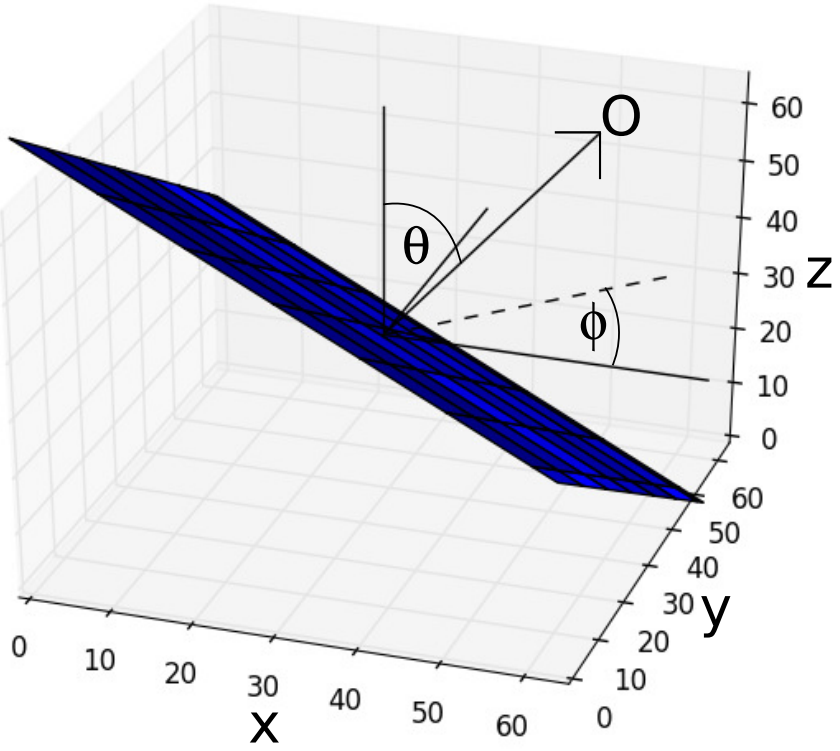

Figure 5.6: Two dimensional plane defined in the three dimensional fluid environment with line-of-sight (O) defined with polar angle $\theta = 45°$ and azimuth angle $\phi = 45°$.

is defined some pixels on the plane may not lie within the three dimensional fluid environment. In such a case the value of the pixel is set to zero. For example, if the dimensions of the fluid environment is given by $V(x, y, z) = (64, 64, 64)$ an image computed at $\theta = 0°$, $\phi = 0°$ will have dimensions of,

$$V(IMx) = V \cdot \hat{IMx} = (64, 64, 64) \cdot (1, 0, 0) = 64 \tag{5.65}$$

$$V(IMy) = V \cdot \hat{IMy} = (64, 64, 64) \cdot (0, 1, 0) = 64, \tag{5.66}$$

where $V(IMx)$ and $V(IMy)$ are the dimensions of the image plane in the IMx and IMy directions respectively. An angle of $\theta = 45°$, $\phi = 0°$ results in an image with dimensions,

$$V(IMx) = V \cdot \hat{IMx} = (64, 64, 64) \cdot (\frac{1}{\sqrt{2}}, 0, -\frac{1}{\sqrt{2}}) = 91 \tag{5.67}$$

$$V(IMy) = V \cdot \hat{IMy} = (64, 64, 64) \cdot (0, 1, 0) = 64. \tag{5.68}$$

5.2.3 Numerical integration

The emission and absorption coefficients are numerically integrated along the normal at each pixel on the two dimensional image in order to obtain an intensity map. For the integration it is assumed that the source extends over a small enough angle in the sky so that the emission from different regions within the environment follow parallel light paths towards the observer.

A closed Newton-Cotes formula is used to integrate the intensity function with,

$$\int_a^b f(x)\mathrm{d}x = \sum_{i=0}^{N} \Delta l_i f(x_i) \tag{5.69}$$

where $f(x) = \mathrm{d}I/\mathrm{d}s$ is given by equation (5.33), a and b are the points at which the line-of-sight enters and exits the three dimensional grid respectively, N is the total number of points between a and b and δl_i is the observed distance between adjacent points. The values of a and b are determined by the intersection points of the line-of-sight with the three dimensional environment. The observed distance between points will differ from the grid distance between points, defined in the co-moving frame of the fluid, due to relativistic effects, such that,

$$\Delta l_i = \delta_i \Delta h. \tag{5.70}$$

where h is the distance between the adjacent points along the line-of-sight, given by,

$$\Delta h = x_i - x_{i-1} = \sqrt{(\Delta x \sin\theta\cos\phi)^2 + (\Delta y \sin\theta \sin\phi)^2 + (\Delta z \cos\theta)^2}, \tag{5.71}$$

where Δx, Δy and Δz are the cell lengths of the three dimensional grid in the respective directions. For a grid with dimensions $\Delta x = \Delta y = \Delta z$, $x_i - x_{i-1} = 1$.

This integration scheme does not take into account the travel time of the radiation through the three dimensional environment. The light crossing time of each cell in the simulation is determined by,

$$t_c = \frac{\Delta h}{c}, \tag{5.72}$$

if $\Delta h = 1$, $t_c = 1$ unit. The light crossing time through a single cell is short when compared to the evolution of the final simulation which spans 5100 units. This has the implication that the structure of compact emission regions within the jet will not be significantly effected, however, measuring properties such as the apparent velocity of moving components will yield inaccurate results.

After the intensity map arrays have been calculated they are saved as NumPy binary files with the naming convention IMAP[FRAME][THETA][PHI].NPY. The resulting intensity maps are given in arbitrary units since the fluid properties are defined in these units.

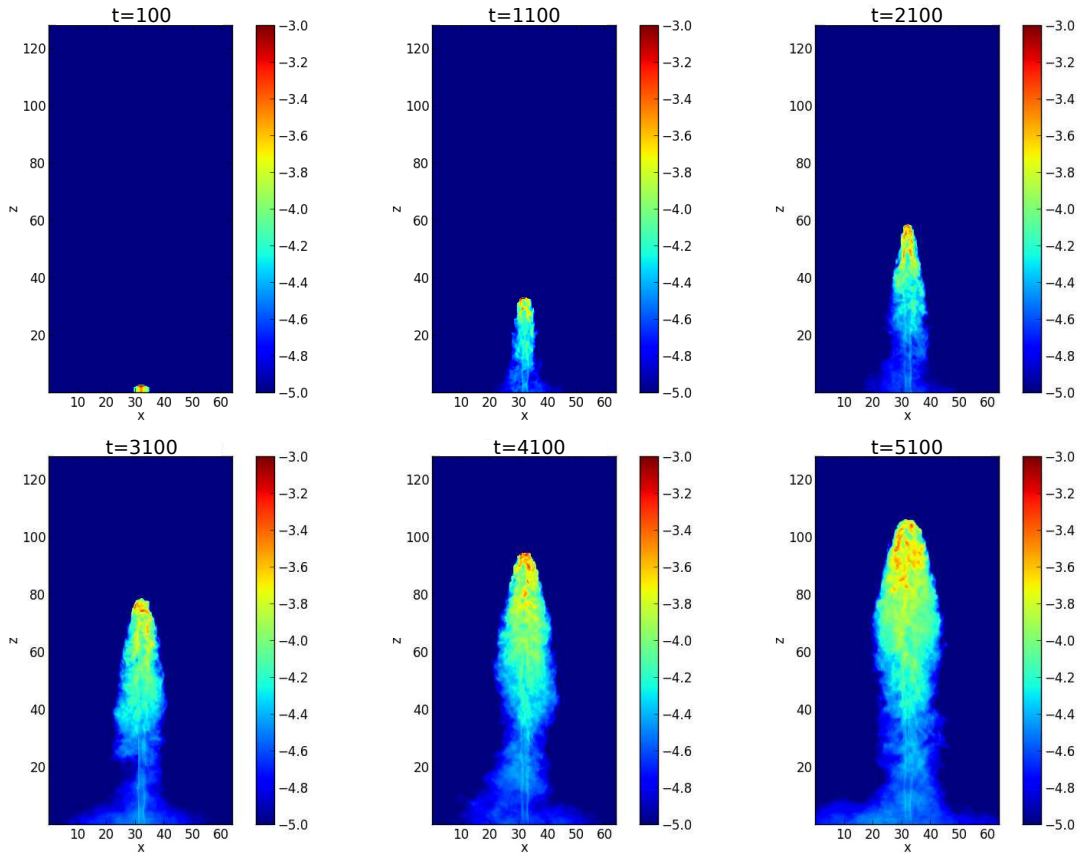

Figure 5.7: Two dimensional intensity maps calculated for a line-of-sight of $\theta = 90°$, $\phi = 0°$. The intensity maps are plotted for different time steps from 100 to 5100, with equal intervals.

5.3 Results

The post-processing code was applied to the final hydrodynamic simulation (see Section 4.4.2, p 88) and intensity maps were calculated at different time steps, polar and azimuth angles. The intensity maps were calculated for emission at a frequency of 15 GHz, similar to the MOJAVE observational survey (Lister and Homan, 2005).

5.3.1 Evolution and morphology

The evolution of the jet is shown in Figure 5.7, as intensity maps calculated for an edge-on viewing angle with $\theta = 90°$ and $\phi = 0°$, at different time steps from $t = 100$ to $t = 5100$ with equal intervals of $t = 1000$. The initial frame shows the injection of the relativistic jet material into the ambient medium producing a region of higher intensity. The propagation of the higher intensity region into the environment is consistent with that of the jet head shown in Chapter 4

(see Figure 4.20, p 92).

The general structure of the intensity maps shows a faint beam with a bright extended cocoon. The intensity of the relativistic beam varies in brightens with distance in both the x and z directions. The beam intensity is the brightest at the boundary between the beam and cocoon, with the intensity decreasing towards the centre. This edge brightening is produced by a thin sheath layer which forms due to the interaction of the jet and ambient medium.

The intensity of the relativistic jet is dominated by the cocoon region with the brightest emission close to the working surface of the jet. This result is consistent with the conversion of kinetic energy to internal energy at the working surface. The diameter of the cocoon increases with time as more material is injected. The entrainment of ambient medium, with low energy density, in the cocoon causes a sharp decrease in the intensity as the cocoon medium propagates downwards. This decrease in intensity gives the cocoon a lobe-like shape in the intensity maps.

The cocoon emission is not uniform but shows filaments of higher intensity emission caused by turbulence. To investigate the emission from the asymmetric structure of the cocoon, the intensity maps were also calculated for different values of ϕ. The results are shown in Figure 5.8. The intensity maps show that the structure of the emission filaments vary depending on the viewing angle, however, there are no drastic change in the overall intensity. This is consistent with the fluid dynamic results which show only small scale asymmetric structures at this time step.

The jet structure of the simulated emission maps resembles that of FR II type AGN with a faint beam close to the injection site and a bright lobe-like cocoon structure containing hot spots of emission that are time dependent. Figure 5.9 compares the simulated intensity map to a VLA image of the FR II source 3C 223. The simulated intensity map shows similar large scale cocoon structure to 3C 223, with the highest intensity region located close to the head of the jet.

5.3.2 Doppler Boosting

One of the principles in the unified model of AGN (discussed in Chapter 2) is that the type of AGN is in part dependent on the inclination angle of the observer relative to the jet. This effect is caused by the Doppler boosting of emission due to the relativistic velocity of the jet plasma. To investigate how the emission structures in the simulated intensity maps are influenced by Doppler boosting, intensity maps were calculated and plotted at different polar angles ranging from $\theta = 0°$ to $\theta = 90°$, shown in Figure 5.10.

The results show that changing the polar angle of the observation from an edge-on ($\theta = 90°$) to a nearly face-on system ($\theta = 0°$) causes the intensity of the relativistic beam to brighten significantly, while the intensity of the cocoon remains unchanged. This causes an over all increase in the intensity for lower polar angles, with the maximum intensity of the face-on observing angle ~ 3 orders of magnitude larger than that of the edge-on system. At low polar angles ($\theta = 10° - 20°$) the beam is the dominant emission region and the internal structure of the beam, which was obscured by the cocoon at high polar angles, can be clearly observed. For

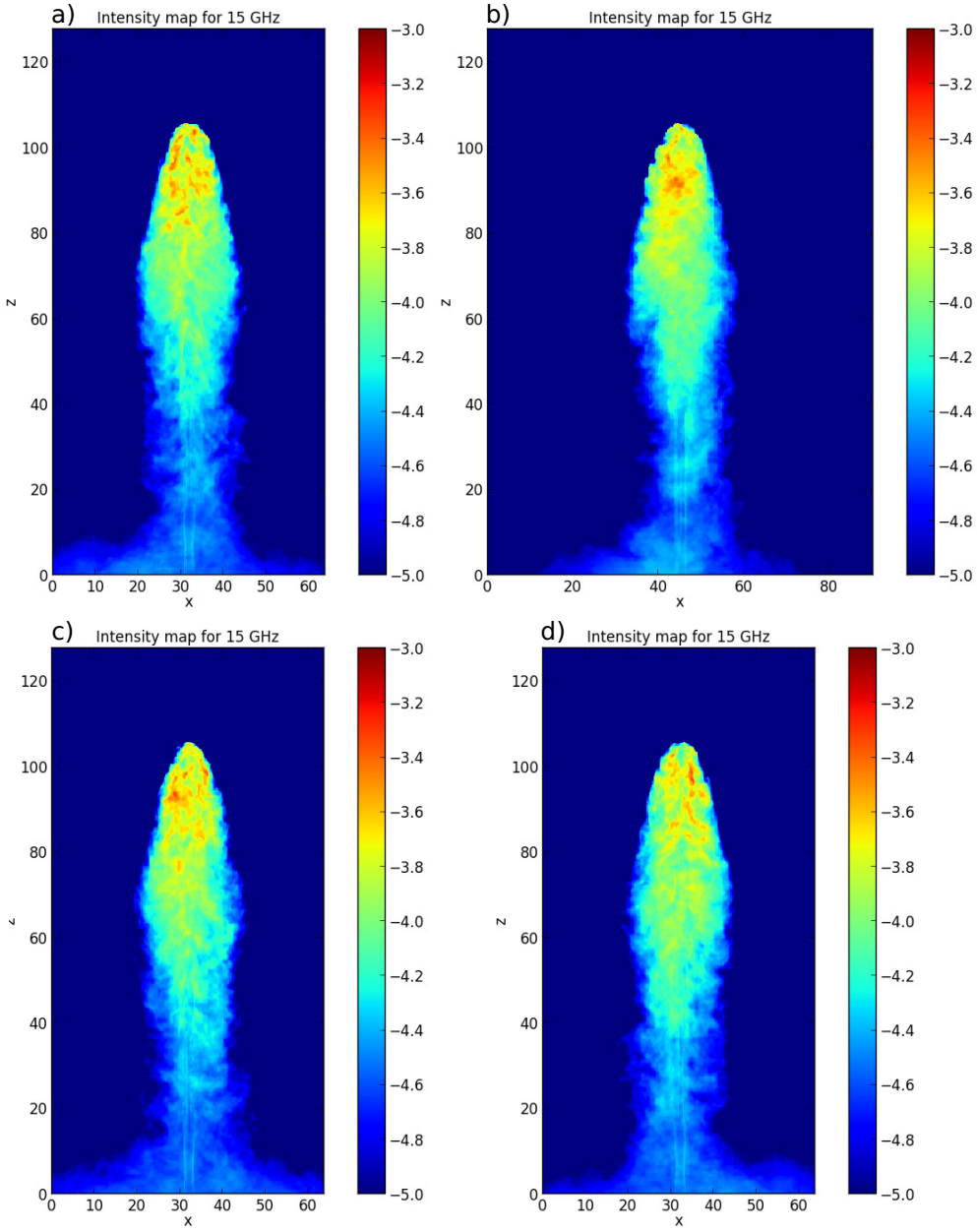

Figure 5.8: Intensity maps calculated at the time step $t = 5100$ for an edge-on system $\theta = 90^\circ$ at different azimuth angles a) $\phi = 0^\circ$, b) $\phi = 45^\circ$, c) $\phi = 90^\circ$, d) $\phi = 180^\circ$.

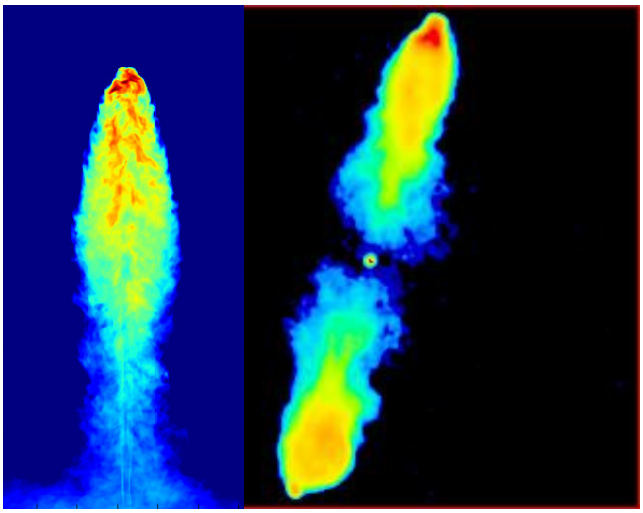

Figure 5.9: Simulated intensity map of a relativistic jet at $t = 5410$ (left). VLA image at 1477 MHz of 3C 223, image adopted from the 3CRR atlas http://www.jb.man.ac.uk/atlas/object/3C223.html (right, retrieved on 20/01/2017).

a completely face-on system ($\theta = 0°$) the emission is concentrated in a circular region near the centre of the beam, with the highest intensity region corresponding to the relativistic beam. The surrounding extended emission is produced by the cocoon.

The beam structure does not show a uniform intensity, but a clumpy structure with individual emission components (most clearly illustrated at a polar angle of $\theta = 30°$). Close to the injection site the re-collimation shocks discussed in Chapter 4 produces a small increase in brightness with symmetric distribution across the beam. At intermediate distances from the injection site, in the turbulent regime of the beam, the emission no longer exhibits a symmetric structure but appears deflected with small components breaking off from the main beam. At large distances where the beam has broken apart multiple, irregularly shaped emission regions are observed. An additional effect of the Doppler boosting observed in the results is that the edge brightening of the beam disappears as the polar angle is reduced. This confirms that the edge brightening is due to the sheath layer which has a lower Lorentz factor than the beam of the jet and subsequently is less Doppler boosted at low polar angles.

The resultant Doppler boosting shown in the intensity maps are consistent with observational studies, where FR II radio galaxies with a high polar angle produce symmetric radio structures that are dominated by radio lobes, while low polar angle galaxies show asymmetric radio structures on either side of the galaxy with one component dominated by a relativistic beam and the other only by diffuse lobe emission. The effects of Doppler boosting on a galaxy with two symmetric radio jets are illustrated by constructing a composite image of two simulated intensity

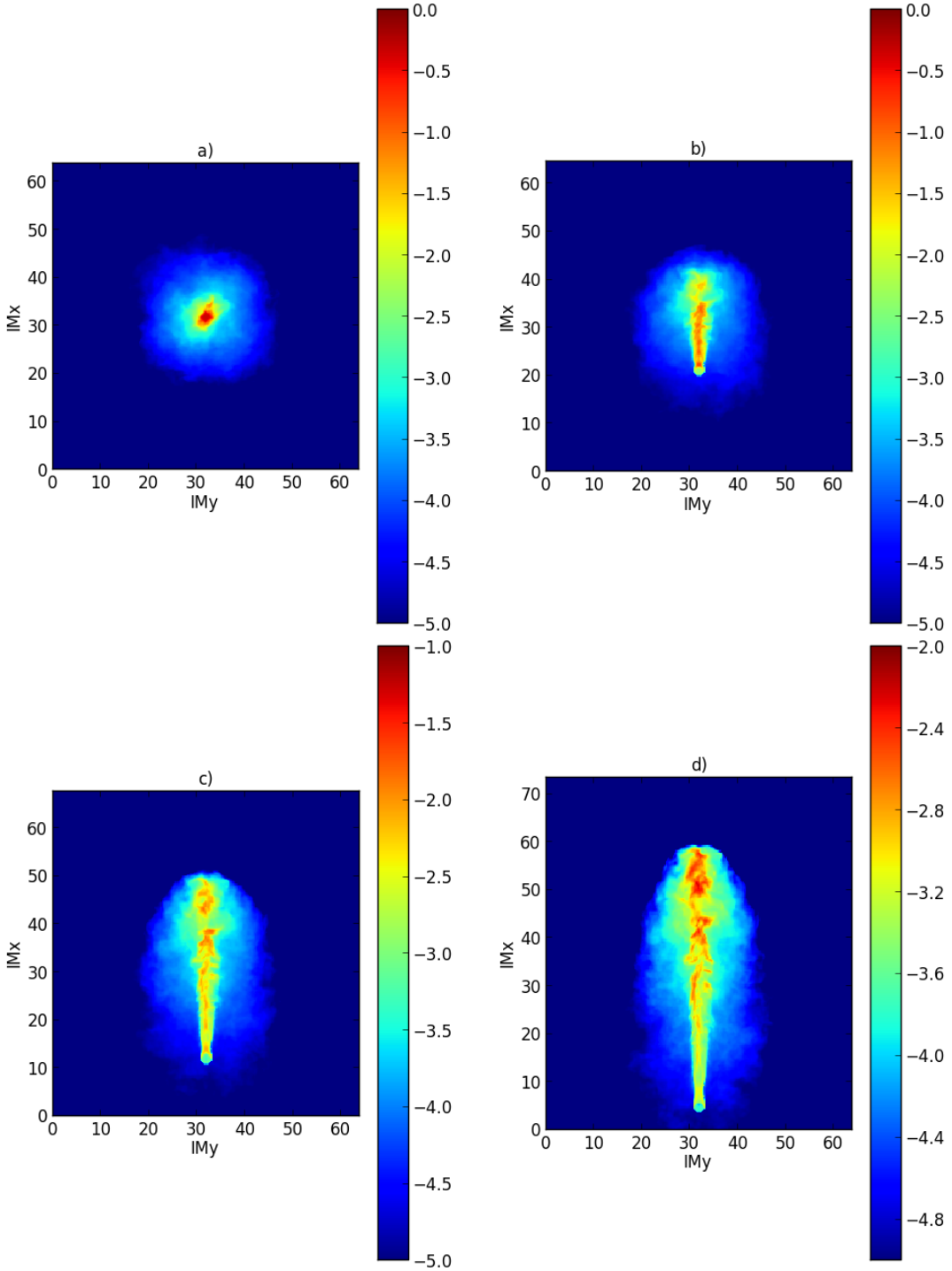

Figure 5.10: Intensity maps calculated at the time step $t = 5100$ for different polar angles at an azimuth angle of $\phi = 0°$ a) $\theta = 0°$, b) $\theta = 10°$, c) $\theta = 20°$, d) $\theta = 30°$, e) $\theta = 60°$, f) $\theta = 90°$.

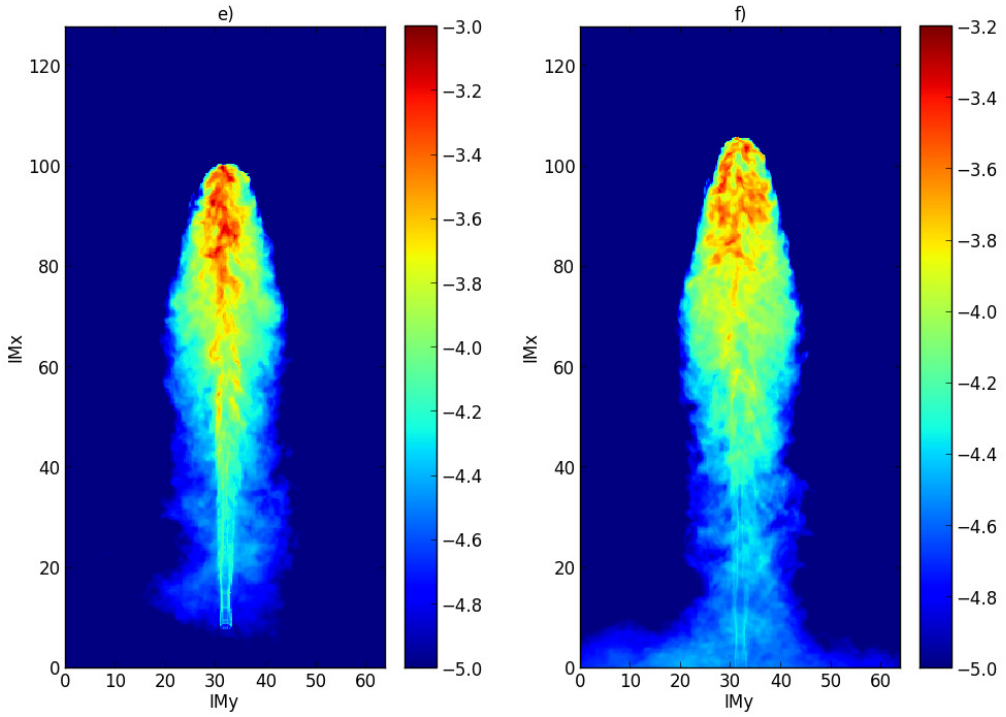

Figure 5.10: Continued.

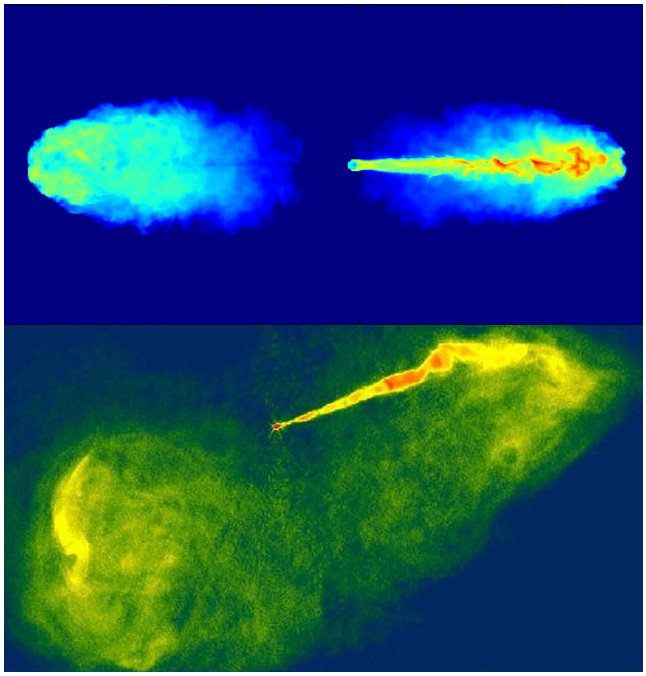

Figure 5.11: Simulated intensity map for a source containing symmetric bilateral jets with a polar angle $\theta = 30°$ with respect to the observer (top). VLA image of M87 at 1477 MHz, a giant eliptical galaxy producing a relativistic jet. Image source: ESA/Hubble https://www.spacetelescope.org/images/opo9943b/ (bottom, retrieved on 12/12/2016).

maps, calculated for polar angles of $\theta = 30°$ and $\theta = 210°$ (shown in the top panel of Figure 5.11). This figure also compares the simulated effects produced by the post-processing code to those observed in M87 with a similar inclination ($i \leq 25$, Heinz and Begelman, 1997). Once again a similar large scale morphology is observed, with a prominent relativistic jet visible on the side which is Doppler boosted towards the observer. On the opposite side only the emission from the cocoon region is visible.

5.3.3 Time dependent variability

To investigate the time dependence of emission structures within the jet beam, intensity maps were calculated at smaller time intervals between $t = 5090$ and $t = 5140$, at $\theta = 15°$ and $\phi = 0°$ (Figure 5.12). The results show the presence of both stationary and time dependent emission regions in the jet. The stationary components are formed in the stable region of the beam by recollimation shocks, while the time dependent structures form where the beam of the jet becomes unstable and breaks apart. The position of a moving component is marked in Figure 5.12 versus

that of a stationary component close to the injection site.

Due to the large time difference between the write out of data files in the fluid dynamic simulation when compared to the bulk motion of the jet medium, it is not possible to determine whether the change in the top emission region is the result of a single component propagation through the jet or multiple emission components. This combined with the neglect of light travel time in the post-processing code make determining the apparent velocity highly inaccurate. However, it can be stated that if this change in emission is due to a single component its apparent motion would be much less than the speed of light.

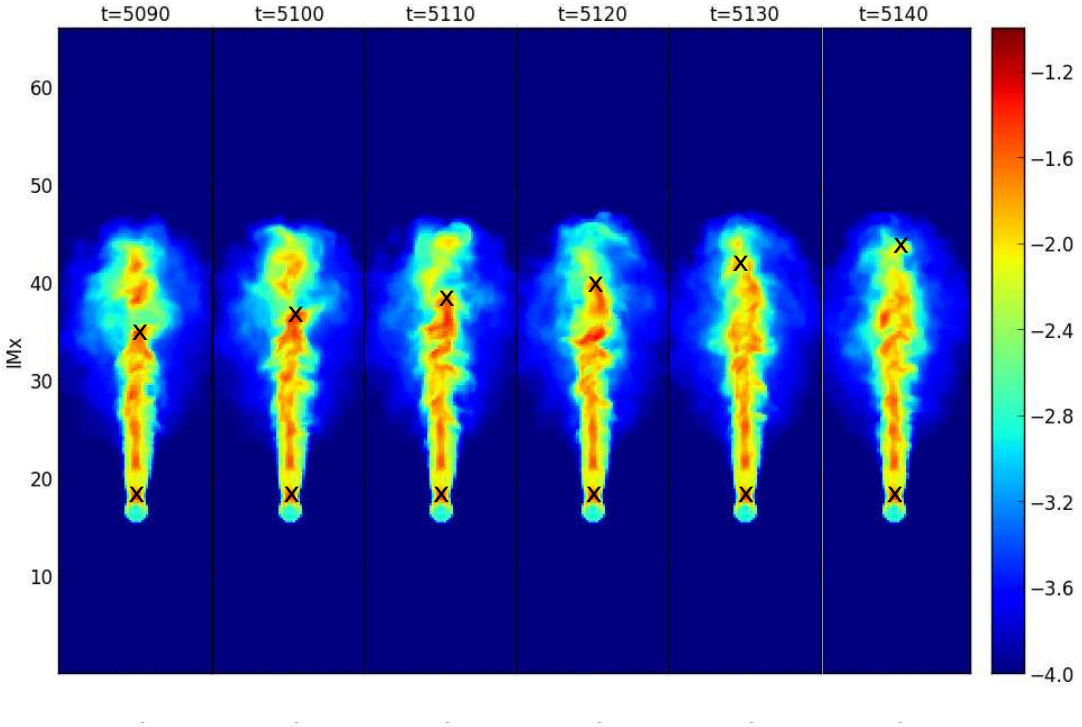

Figure 5.12: Two dimensional intensity maps calculated for a line-of-sight of $\theta = 15°$, $\phi = 0°$. The intensity maps are plotted for consecutive time steps from 5090 to 5140, with equal time intervals $\Delta t = 10$.

By integrating the intensity over the entire map relative light curves can be constructed of the evolution of the system. These light curves show the variation in the total intensity of the system rather than specific emission regions. The results are not fully accurate (e.g. the neglect of light travel time), however it provides a good measure of whether the instabilities that formed in the simulated jet can produce variability without the injection additional perturbations. The results are shown in figure (Figure 5.13).

For a face-on system ($\theta = 0°$, $\phi = 0°$) the relative flux increases at a high rate initially but slows down at later time steps with a clear break in the curve. The initial increase in flux is due to an increase in the beam length (which is the dominant emission component in the face-on source) as the jet propagates through the medium. After the beam reaches a certain length (≈ 80 units) it becomes unstable and breaks apart, the length of the beam cannot increase past this point and the rate at which the flux increases slows down. For an edge-on source the relative flux shows a steady increase. In this case the dominant emission component is the cocoon, which increases with a steady rate as more jet material is injected.

To investigate the scale of short term variability within the light curve a running mean curve was constructed. Each point on the running mean consisted of the mean of the 25 points before and after the current time step,

$$\bar{y}_i = \frac{\sum_{j=i-25}^{25} y_j}{50}. \tag{5.73}$$

The difference in percentage of the relative light curve to the mean curve was calculated in order to determine the small scale variation in flux. The variation light curves show small variability for both lines-of-sight, with the percentage variability decreasing as the flux increases. The face-on source produces a lower percentage variation than that of the edge-on source, however, the relative flux of this source is much higher and, therefore, the magnitude of these variations are larger. Overall these light curves show that variability can be produced through the fluid dynamic instabilities which are generated within AGN jets without the need for a perturbation in the injection rate. The amplitude of the variations remain similar throughout the simulation, while the overall flux increases, which results in a decline of the percentage variation. No large scale flares were observed in the light curves suggesting that a perturbation in the injection parameters is necessary to produce the flares which have been associated with observed data (see digital appendix for additional animations illustrating the evolution of intensity maps).

The results shown in this chapter are consistent with the fluid dynamic properties shown in Chapter 4. The relevance of these results to observational studies reviewed in Chapter 2 will be discussed in the next chapter along with the shortcomings of the model and how it can be improved in future studies.

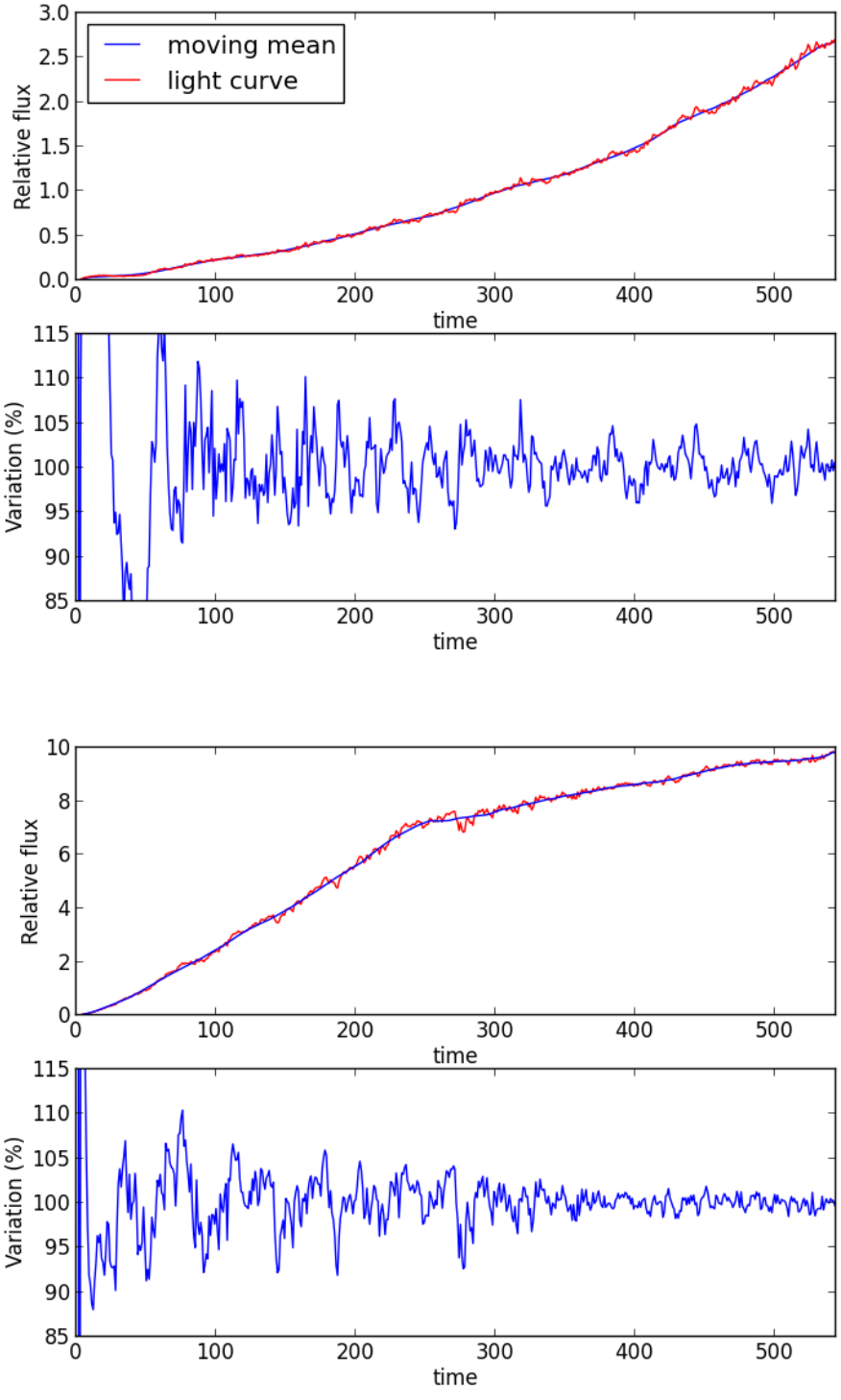

Figure 5.13: Relative light curves for lines-of-sight $\theta = 90°$, $\phi = 0°$ (top) and $\theta = 0°$, $\phi = 0°$ (bottom) showing the evolution of flux for the simulations. The top plots show the relative flux for each intensity map as well as for a moving mean of 50 frames. The bottom plots contains the percentage variation in flux with respect to the moving mean.

Chapter 6

Discussion and conclusion

Numerical fluid dynamic simulations are a powerful tool to investigate the physical environments that occur within relativistic jet structures associated with radio loud AGN. These simulations can be combined with emission models to produce simulated data sets that can be compared to observed data in order to explain some of the unique characteristics of these AGN. Studies of fluid dynamic simulations have been able to reproduce the large scale structure of these jets as well as the smaller internal structures such as apparent superluminal emission regions. The studies have led to a better understanding of the dynamics of relativistic jets which have not been reproducible through physical experiments.

Despite the advances which have been made by studying fluid dynamic simulations several challenges still remain. Fluid dynamic simulations are only an approximation to the macroscopic dynamics of a relativistic plasma jet as they do not simulate the microscopic interaction of charged particles within the plasma. It is important that these simulations be continuously improved and evolved as the available computing power increases and we are better able to simulate these sources.

6.1 Fluid dynamic simulations

In this study a fluid dynamic model of a relativistic jet was created and implemented in a numerical simulation, in order to study the production of instabilities, the large scale morphology and the deceleration of the beam in these jets. An idealistic model was implemented with the absence of source term such as viscosity, gravity, resistivity and the effects of radiative cooling. The numerical simulation was run with the PLUTO relativistic hydrodynamic code.

The various numerical schemes that are available in the PLUTO software were rigorously tested in order to find the best solution, which is accurate, stable and computationally affordable. The solutions were evaluated by comparing the morphology of the environment to the results shown in previous studies from various authors. Based on these tests the piecewise parabolic

method was implemented with the HLLC hybrid solver in the final simulation. In the initial tests the problems showed little resolution convergence at resolutions lower than 8 points per beam width, however adjusting the injection parameters of the beam to a lower density and higher Mach number improved the convergence significantly. The injection of lower density material in the beam resulted in a lower momentum flux, which in turn resulted in a slower propagation velocity of the bow shock and jet head, a shorter length scale for beam deceleration and increase in turbulence. Based on these tests and the aim to study beam deceleration and instabilities, a small density ratio between the jet and ambient medium was chosen for the final simulation.

The final fluid dynamic simulation presented in this study was able to reproduce a large scale morphology consistent to that of a relativistic jet. The jet structure consisted of a relativistic beam with a high Lorentz factor bulk motion, a working surface at the interface between the beam and ambient medium, a downflow around the beam which formed a cocoon region and a bow shock surrounding the entire structure. The structures of these regions were consistent with that of previous studies.

The cocoon showed turbulent asymmetric structures, while the beam of the jet was initially well collimated and stable at small distances from the injection site. Turbulent fluid dynamic instabilities (such as Kelvin-Helmholtz instabilities) in the beam, however increased with distance from the injection site causing fragmentation of the relativistic beam. The fragmentation produced regions of larger bulk velocity propagating through a turbulent medium. When the high bulk velocity regions reached the working surface they produced additional perturbations in the cocoon. This resulted in the production of time dependent variations in the jet similar to some components which have been observed in observational data.

When comparing this simulation to AGN jets the largest inconsistency of this model is the small length scale of the computational domain. The domain covers 128 pc where AGN jets are three orders of magnitude larger. Since the simulation in this study has been able to reproduce a relativistic jet, future simulations can be undertaken with increased computational resources and therefore a larger domain in order to simulate larger length and time scales. Such simulations can be used to investigate the evolution of the morphology shown in this study, for example, at what point does the propagation velocity of the jet head become negligible and how does this affect the structure of the relativistic beam and cocoon regions. Additional configurations that must be tested in future models are the addition of radiative cooling, gravity and magnetic fields in order to move the model closer to that of a real AGN jet.

6.2 Emission modelling

A post-processing emission code was created and used to calculate two dimensional intensity maps of the three dimensional fluid environment. The intensity maps provided an estimate for the synchrotron emission produced within each cell using a δ-approximation model. To calculate the intensity it was assumed that all of the emission was produced by relativistic electrons within

the jet. The relativistic electrons were assumed to have a single power-law energy distribution throughout the jet with the normalization of the distribution depending on the energy and mass density of the fluid.

The code takes into account relativistic effects with respect to the viewing angle of the observer and the intensity is calculated with respect to the stationary reference frame of the host galaxy. The code does not to take into account the light travel time and cosmological correction of the emission which makes calculating the apparent velocities of moving components within the jet inaccurate.

The results obtained for the emission estimates were consistent with what was expected from the fluid dynamic simulations. The large scale structure of the intensity maps closely resembled those of FR II type radio galaxies and showed the significance of Doppler boosting in the synchrotron emission at different polar angles. At the high polar angles of an edge-on system the intensity maps emphasized the cocoon region, while for small polar angles of nearly face on sources the beam of the jet dominates the intensity maps. These results were consistent with observational studies and a good overall comparison between the structures produced through simulated emission maps and observations are shown in Figure 5.11.

In Figure 5.11 it is shown that in both the simulated and true intensity maps the jet propagating towards the observer is brighter than the surrounding cocoon with the cocoon region having the highest intensity at the head of the jet. The simulated map shows individual compact emission regions at large distances from the injection site that appear as filaments. Finally the counter jet in both cases are not visible but a diffuse cocoon region can be seen on the opposite side of the radio galaxy. The asymmetric structure of M87 differs significantly from the simulated jet, which may be due to additional effects such as the movement of the galaxy through the IGM.

The intensity maps showed that intricate, time dependent, small scale structure was present in both the cocoon an the beam regions. The time dependent nature of these structure resulted in the production of short term variability in total intensity light curves. It was also shown that at low inclinations the beam produces both stationary and propagating emission components.

6.3 Conclusions and future work

In this study a fluid dynamic simulation was successfully implemented and used to reproduce the large scale emission structure of AGN jets. The fluid dynamic simulation was run using the PLUTO software while the emission estimates were calculated by a post-processing code that was written for this study and included the Lorentz transformations for a variation in the viewing angle. The results, discussed above, were able to reproduce most of the large scale characteristics of AGN jets and met the aims of the project as previously stated (Chapter 1). It was shown that the large scale emission morphology resembled that of observations of FR II type radio galaxies and that the simulated intensity maps reproduced the effects of Doppler boosting observed in different types of AGN with a specific comparison to the jet structure of M87. The

results obtained at different viewing angles are in line with the current unified model of AGN. The results produced edge brightened beams for nearly edge on sources which is due to a sheath layer of lower bulk motion at the interface between the beam and the cocoon region.

Time dependent emission structures were produced in both the cocoon and beam of the jet. The cocoon showed asymmetric filaments and hot spots, while, at low inclinations, the beam produced both stationary and moving emission components. Such time dependent structures have been observed in many AGN sources. Overall the simulation showed that that some of the time dependent structures which have been associated with AGN jets are produced by fluid dynamic instabilities which form in the jet environment itself rather than a variation in injection parameters. These time dependent components caused a variation in the total intensity of the jet with time, however, it did not produce the large flares that have been observed in AGN sources. This is consistent with the model that the production of these flares is linked to a perturbation in the injection parameters of the jet.

Although the simulated intensity maps that were produced have a similar structure to those of AGN jets there are still several improvements which can be made. In the simulation it was assumed that the synchrotron radiation was produced by electrons in a single power-law distribution while, in real AGN jets, the particle distribution constantly changes due to radiative cooling and particle acceleration at shocks. A better solution to this model is to assume that only a fraction of the electrons in the plasma are in the power law distribution. This faction may be treated as a conserved scalar in the simulation with additional source terms for radiative cooling and shock acceleration. This would allow a larger variation in synchrotron emission emphasizing the emission in shocked regions which can be used to more accurately reproduce emission components moving along the jet. In addition the current model does not allow for the measurement of change in the particle-index along the jet which can be used to better distinguish between the production of FR I and FR II type jets.

The time of arrival and cosmic corrections must also be included to ensure that the calculated intensity maps are a true reflection AGN jets. In order to fully compare the simulated intensity maps to that of radio telescopes, additional corrections have to be applied to take into account the instrumental limitations of the telescopes such the resolution and sensitivity. Progress has been made to include time of arrival effects in the post-processing code by optimizing data file size and computational efficiency, however, the completion is also left for future studies. The emission code can also be expanded to include the power-law fraction discussed above as well as cosmological correction to the intensity maps. An additional aim for the future of this project is to include approximations to the high energy emission spectrum in order to investigate the correlation of multi-wavelength emission in relativistic jets. This can also be used to study the location of high energy emission within these jets.

For the fluid dynamic simulation future studies will include investigate the effects of an ordered magnetic field, gravity, viscosity and perturbations in the injection of the fluid on the morphology of the solution in an attempt to reproduce structures such as kink instabilities. Since

the solution to the final simulation of a relativistic jet presented in this study showed promising results more computational resources can be invested in future simulations to increase the size of the computational domain and evolution time.

The project was able to reproduce the general structure of AGN jets and serves as a good base for further studies to improve upon the presented simulations and investigate more complex processes in depth such as the formation and propagation of knots inside the jet beam, and the relation between the total flux and injection parameters. Studying these models can lead to a better understanding of AGN jets, the conditions in which they are formed and the relationship between the various sub-classes of these sources that exists. Many other source have also been associated with the production of similar jet structures (e.g. microquasars and γ-ray bursts) and the tools that have been developed in this study can be adopted to model these sources.

Bibliography

Abdo, A. A., Ackermann, M., Agudo, I., Ajello, M., Aller, H. D., Aller, M. F., Angelakis, E., Arkharov, A. A., Axelsson, M., Bach, U., and et al. (2010). The Spectral Energy Distribution of Fermi Bright Blazars. *Astrophys. J.*, 716:30–70.

Acero, F., , and et al. (2015). Fermi Large Area Telescope Third Source Catalog. *Astrophys. J. Suppl.*, 218:23.

Ackermann, M., Anantua, R., Asano, K., Baldini, L., Barbiellini, G., Bastieri, D., Becerra Gonzalez, J., Bellazzini, R., Bissaldi, E., Blandford, R. D., Bloom, E. D., Bonino, R., Bottacini, E., Bruel, P., Buehler, R., Caliandro, G. A., Cameron, R. A., Caragiulo, M., Caraveo, P. A., Cavazzuti, E., Cecchi, C., Cheung, C. C., Chiang, J., Chiaro, G., Ciprini, S., Cohen-Tanugi, J., Costanza, F., Cutini, S., D'Ammando, F., de Palma, F., Desiante, R., Digel, S. W., Di Lalla, N., Di Mauro, M., Di Venere, L., Drell, P. S., Favuzzi, C., Fegan, S. J., Ferrara, E. C., Fukazawa, Y., Funk, S., Fusco, P., Gargano, F., Gasparrini, D., Giglietto, N., Giordano, F., Giroletti, M., Grenier, I. A., Guillemot, L., Guiriec, S., Hayashida, M., Hays, E., Horan, D., Jóhannesson, G., Kensei, S., Kocevski, D., Kuss, M., La Mura, G., Larsson, S., Latronico, L., Li, J., Longo, F., Loparco, F., Lott, B., Lovellette, M. N., Lubrano, P., Madejski, G. M., Magill, J. D., Maldera, S., Manfreda, A., Mayer, M., Mazziotta, M. N., Michelson, P. F., Mirabal, N., Mizuno, T., Monzani, M. E., Morselli, A., Moskalenko, I. V., Nalewajko, K., Negro, M., Nuss, E., Ohsugi, T., Orlando, E., Paneque, D., Perkins, J. S., Pesce-Rollins, M., Piron, F., Pivato, G., Porter, T. A., Principe, G., Rando, R., Razzano, M., Razzaque, S., Reimer, A., Scargle, J. D., Sgrò, C., Sikora, M., Simone, D., Siskind, E. J., Spada, F., Spinelli, P., Stawarz, L., Thayer, J. B., Thompson, D. J., Torres, D. F., Troja, E., Uchiyama, Y., Yuan, Y., and Zimmer, S. (2016). Minute-timescale ¿100 MeV gamma-Ray Variability during the Giant Outburst of Quasar 3C 279 Observed by Fermi-LAT in 2015 June. *Astrophys. J. Lett.*, 824:L20.

Agudo, I., Gómez, J.-L., Martí, J.-M., Ibáñez, J.-M., Marscher, A. P., Alberdi, A., Aloy, M.-A., and Hardee, P. E. (2001). Jet Stability and the Generation of Superluminal and Stationary Components. *Astrophys. J. Lett.*, 549:L183–L186.

Alfvén, H. and Herlofson, N. (1950). Cosmic Radiation and Radio Stars. *Physical Review*, 78:616–616.

Aloy, M.-A., Gómez, J.-L., Ibáñez, J.-M., Martí, J.-M., and Müller, E. (2000). Radio Emission from Three-dimensional Relativistic Hydrodynamic Jets: Observational Evidence of Jet Stratification. *Astrophys. J. Lett.*, 528:L85–L88.

Aloy, M. A., Ibáñez, J. M., Martí, J. M., Gómez, J.-L., and Müller, E. (1999). High-Resolution Three-dimensional Simulations of Relativistic Jets. *Astrophys. J. Lett.*, 523:L125–L128.

Aloy, M.-Á., Martí, J.-M., Gómez, J.-L., Agudo, I., Müller, E., and Ibáñez, J.-M. (2003). Three-dimensional Simulations of Relativistic Precessing Jets Probing the Structure of Superluminal Sources. *Astrophys. J. Lett.*, 585:L109–L112.

Antonucci, R. (1993). Unified models for active galactic nuclei and quasars. *Annual Review of Astron. and Astrophys.*, 31:473–521.

Antonucci, R. R. J. and Miller, J. S. (1985). Spectropolarimetry and the nature of NGC 1068. *Astrophys. J.*, 297:621–632.

Atwood, W., Albert, A., Baldini, L., Tinivella, M., Bregeon, J., Pesce-Rollins, M., Sgrò, C., Bruel, P., Charles, E., Drlica-Wagner, A., Franckowiak, A., Jogler, T., Rochester, L., Usher, T., Wood, M., Cohen-Tanugi, J., and S. Zimmer for the Fermi-LAT Collaboration (2013). Pass 8: Toward the Full Realization of the Fermi-LAT Scientific Potential. *ArXiv e-prints*.

Baade, W. and Minkowski, R. (1954). Identification of the Radio Sources in Cassiopeia, Cygnus A, and Puppis A. *Astrophys. J.*, 119:206.

Baldwin, J. A., Phillips, M. M., and Terlevich, R. (1981). Classification parameters for the emission-line spectra of extragalactic objects. *Publications of the ASP*, 93:5–19.

Batten, P., Clarke, N., Lambert, C., and Causon, D. M. (1997). On the choice of wavespeeds for the hllc riemann solver. *SIAM Journal on Scientific Computing*, 18(6):1553–1570.

Beckmann, V. and Shrader, C. (2012). *Active Galactic Nuclei*. Physics textbook. Wiley, Weinheim, Germany.

Beckwith, K., Hawley, J. F., and Krolik, J. H. (2009). Transport of Large-Scale Poloidal Flux in Black Hole Accretion. *Astrophys. J.*, 707:428–445.

Ben-Artzi, M. and Falcovitz, J. (1984). A second-order Godunov-type scheme for compressible fluid dynamics. *Journal of Computational Physics*, 55:1–32.

Bennert, N., Falcke, H., Shchekinov, Y., and Wilson, A. S. (2004). Comparing AGN broad and narrow line regions. In Storchi-Bergmann, T., Ho, L. C., and Schmitt, H. R., editors, *The Interplay Among Black Holes, Stars and ISM in Galactic Nuclei*, volume 222 of *IAU Symposium*, pages 307–308.

Biretta, J. A., Junor, W., and Livio, M. (2002). Evidence for initial jet formation by an accretion disk in the radio galaxy M87. *New Astron. Rev.*, 46:239–245.

Blandford, R. D. and Rees, M. J. (1974). A 'twin-exhaust' model for double radio sources. *Mon. Not. R. Astron. Soc.*, 169:395–415.

Blandford, R. D. and Rees, M. J. (1978). Some comments on radiation mechanisms in Lacertids. In Wolfe, A. M., editor, *BL Lac Objects*, pages 328–341.

Blandford, R. D. and Znajek, R. L. (1977). Electromagnetic extraction of energy from Kerr black holes. *Mon. Not. R. Astron. Soc.*, 179:433–456.

Böttcher, M. and Dermer, C. D. (2010). Timing Signatures of the Internal-Shock Model for Blazars. *Astrophys. J.*, 711:445–460.

Böttcher, M., Harris, D., and Krawczynski, H. (2012). *Relativistic Jets from Active Galactic Nuclei*. Wiley, Weinheim, Germany.

Böttcher, M., Reimer, A., Sweeney, K., and Prakash, A. (2013). Leptonic and Hadronic Modeling of Fermi-detected Blazars. *Astrophys. J.*, 768:54.

Bowyer, C. S., Lampton, M., Mack, J., and de Mendonca, F. (1970). Detection of X-Ray Emission from 3c 273 and NGC 5128. *Astrophys. J. Lett.*, 161:L1.

Britzen, S., Kudryavtseva, N. A., Witzel, A., Campbell, R. M., Ros, E., Karouzos, M., Mehta, A., Aller, M. F., Aller, H. D., Beckert, T., and Zensus, J. A. (2010). The kinematics in the pc-scale jets of AGN. The case of S5 1803+784. *Astronomy and Astrophysics*, 511:A57.

Carilli, C. L., Perley, R. A., Dreher, J. W., and Leahy, J. P. (1991). Multifrequency radio observations of Cygnus A - Spectral aging in powerful radio galaxies. *Astrophys. J.*, 383:554–573.

Carini, M. T., Miller, H. R., Noble, J. C., and Goodrich, B. D. (1992). The timescales of the optical variability of blazars. III - OJ 287 and BL Lacertae. *Astron. J.*, 104:15–27.

Carroll, B. and Ostlie, D. (2013). *Introduction to Modern Astrophysics, An: Pearson New International Edition*. Pearson Education Limited.

Chatterjee, R., Marscher, A. P., Jorstad, S. G., Olmstead, A. R., McHardy, I. M., Aller, M. F., Aller, H. D., Lähteenmäki, A., Tornikoski, M., Hovatta, T., Marshall, K., Miller, H. R., Ryle, W. T., Chicka, B., Benker, A. J., Bottorff, M. C., Brokofsky, D., Campbell, J. S., Chonis, T. S., Gaskell, C. M., Gaynullina, E. R., Grankin, K. N., Hedrick, C. H., Ibrahimov, M. A., Klimek, E. S., Kruse, A. K., Masatoshi, S., Miller, T. R., Pan, H.-J., Petersen, E. A., Peterson, B. W., Shen, Z., Strel'nikov, D. V., Tao, J., Watkins, A. E., and Wheeler, K. (2009). Disk-Jet Connection in the Radio Galaxy 3C 120. *Astrophys. J.*, 704:1689–1703.

Colella, P. (1985). A direct eulerian muscl scheme for gas dynamics. *SIAM Journal on Scientific and Statistical Computing*, 6:104–117.

Colella, P. and Woodward, P. R. (1984). The Piecewise Parabolic Method (PPM) for Gas-Dynamical Simulations. *Journal of Computational Physics*, 54:174–201.

Courvoisier, T. J.-L. (2001). What May We Learn from Multi-Wavelength Observations of Active Galactic Nuclei. In Setti, G. and Swings, J.-P., editors, *Quasars, AGNs and Related Research Across 2000. Conference on the occasion of L. Woltjer's 70th birthday*, page 155.

Courvoisier, T. J.-L. (2013). *High Energy Astrophysics*.

Crenshaw, D. M., Kraemer, S. B., Boggess, A., Maran, S. P., Mushotzky, R. F., and Wu, C.-C. (1999). Intrinsic Absorption Lines in Seyfert 1 Galaxies. I. Ultraviolet Spectra from the Hubble Space Telescope. *Astrophys. J.*, 516:750–768.

Croston, J. H., Kraft, R. P., and Hardcastle, M. J. (2007). Shock Heating in the Nearby Radio Galaxy NGC 3801. *Astrophys. J.*, 660:191–199.

Crusius, A. and Schlickeiser, R. (1986). Synchrotron radiation in random magnetic fields. *Astronomy and Astrophysics*, 164:L16–L18.

Crutcher, R. M. (2007). Magnetic fields in the non-masing ISM. In Chapman, J. M. and Baan, W. A., editors, *Astrophysical Masers and their Environments*, volume 242 of *IAU Symposium*, pages 47–54.

Curtis, H., Campbell, W., Moore, J., Wilson, R., and Wright, W. (1918). *Studies of the Nebulae: Made at the Lick Observatory, University of California, at Mount Hamilton, California, and Santiago, Chile.* Number v. 13 in Publications of the Lick Observatory of the University of California. University of California Press.

Davies, R. I., Thomas, J., Genzel, R., Müller Sánchez, F., Tacconi, L. J., Sternberg, A., Eisenhauer, F., Abuter, R., Saglia, R., and Bender, R. (2006). The Star-forming Torus and Stellar Dynamical Black Hole Mass in the Seyfert 1 Nucleus of NGC 3227. *Astrophys. J.*, 646:754–773.

Davis, S. F. (1988). Simplified second-order godunov-type methods. *SIAM Journal on Scientific and Statistical Computing*, 9(3):445–473.

Denn, G. R., Mutel, R. L., and Marscher, A. P. (2000). Very Long Baseline Polarimetry of BL Lacertae. *Astrophys. J. Suppl.*, 129:61–92.

Dermer, C. and Menon, G. (2009). *High Energy Radiation from Black Holes: Gamma Rays, Cosmic Rays, and Neutrinos.* Princeton Series in Astrophysics. Princeton University Press.

Einfeldt, B. (1988). On Godunov type methods for the Euler equations with a general equation of state. *SIAM J. Numer. Anal.*, 25(2):294318.

Einfeldt, B., Munz, C., Roe, P., and Sjgreen, B. (1991). On godunov-type methods near low densities. *Journal of Computational Physics*, 92(2):273 – 295.

Elitzur, M. and Shlosman, I. (2006). The AGN-obscuring Torus: The End of the "Doughnut" Paradigm? *Astrophys. J. Lett.*, 648:L101–L104.

Evans, D. A., Fong, W.-F., Hardcastle, M. J., Kraft, R. P., Lee, J. C., Worrall, D. M., Birkinshaw, M., Croston, J. H., and Muxlow, T. W. B. (2008). A Radio through X-Ray Study of the Jet/Companion-Galaxy Interaction in 3C 321. *Astrophys. J.*, 675:1057–1066.

Falle, S. A. E. G. (2002). Rarefaction Shocks, Shock Errors, and Low Order of Accuracy in ZEUS. *Astrophys. J. Lett.*, 577:L123–L126.

Fanaroff, B. L. and Riley, J. M. (1974). The morphology of extragalactic radio sources of high and low luminosity. *Mon. Not. R. Astron. Soc.*, 167:31P–36P.

Font, J. A. (2008). Numerical Hydrodynamics and Magnetohydrodynamics in General Relativity. *Living Reviews in Relativity*, 11:7.

Forman, W., Jones, C., Cominsky, L., Julien, P., Murray, S., Peters, G., Tananbaum, H., and Giacconi, R. (1978). The fourth Uhuru catalog of X-ray sources. *Astrophys. J. Suppl.*, 38:357–412.

Fossati, G., Maraschi, L., Celotti, A., Comastri, A., and Ghisellini, G. (1998). A unifying view of the spectral energy distributions of blazars. *Mon. Not. R. Astron. Soc.*, 299:433–448.

Franceschini, A., Vercellone, S., and Fabian, A. C. (1998). Supermassive Black Holes in Early-Type Galaxies: Relationship with Radio Emission and Constraints on the Black Hole Mass Function. *Mon. Not. R. Astron. Soc.*, 297:817–824.

Frank, J., King, A., and Raine, D. J. (2002). *Accretion Power in Astrophysics: Third Edition.*

Garofalo, D., Evans, D. A., and Sambruna, R. M. (2010). The evolution of radio-loud active galactic nuclei as a function of black hole spin. *Mon. Not. R. Astron. Soc.*, 406:975–986.

Gaskell, C. M. (2009). What broad emission lines tell us about how active galactic nuclei work. *New Astron. Rev.*, 53:140–148.

Ghisellini, G., editor (2013). *Radiative Processes in High Energy Astrophysics*, volume 873 of *Lecture Notes in Physics, Berlin Springer Verlag.*

Ghisellini, G., Celotti, A., Fossati, G., Maraschi, L., and Comastri, A. (1998). A theoretical unifying scheme for gamma-ray bright blazars. *Mon. Not. R. Astron. Soc.*, 301:451–468.

Ghisellini, G., Haardt, F., and Matt, G. (2004). Aborted jets and the X-ray emission of radio-quiet AGNs. *Astronomy and Astrophysics*, 413:535–545.

Giacconi, R., Branduardi, G., Briel, U., Epstein, A., Fabricant, D., Feigelson, E., Forman, W., Gorenstein, P., Grindlay, J., Gursky, H., Harnden, F. R., Henry, J. P., Jones, C., Kellogg, E., Koch, D., Murray, S., Schreier, E., Seward, F., Tananbaum, H., Topka, K., Van Speybroeck, L., Holt, S. S., Becker, R. H., Boldt, E. A., Serlemitsos, P. J., Clark, G., Canizares, C., Markert, T., Novick, R., Helfand, D., and Long, K. (1979). The Einstein /HEAO 2/ X-ray Observatory. *Astrophys. J.*, 230:540–550.

Giacconi, R., Gursky, H., Paolini, F. R., and Rossi, B. B. (1962). Evidence for x Rays From Sources Outside the Solar System. *Physical Review Letters*, 9:439–443.

Godunov, S. K. (1959). A difference method for numerical calculation of discontinuous solutions of the equations of hydrodynamics. *Matematicheskii Sbornik*, 89(3):271–306.

Gomez, J. L., Marti, J. M. A., Marscher, A. P., Ibanez, J. M. A., and Marcaide, J. M. (1995). Parsec-Scale Synchrotron Emission from Hydrodynamic Relativistic Jets in Active Galactic Nuclei. *Astrophys. J. Lett.*, 449:L19.

Gopal-Krishna and Wiita, P. J. (2000). Extragalactic radio sources with hybrid morphology: implications for the Fanaroff-Riley dichotomy. *Astronomy and Astrophysics*, 363:507–516.

Gottlieb, S. and Shu, C.-W. (1998). Total variation diminishing runge-kutta schemes. *Mathematics of computation of the American Mathematical Society*, 67(221):73–85.

Groves, B. A., Heckman, T. M., and Kauffmann, G. (2006). Emission-line diagnostics of low-metallicity active galactic nuclei. *Mon. Not. R. Astron. Soc.*, 371:1559–1569.

Gupta, A. C., Fan, J. H., Bai, J. M., and Wagner, S. J. (2008). Optical Intra-Day Variability in Blazars. *Astron. J.*, 135:1384–1394.

Haardt, F. and Maraschi, L. (1993). X-ray spectra from two-phase accretion disks. *Astrophys. J.*, 413:507–517.

Hardee, P. E. (1979). On the configuration and propagation of jets in extragalactic radio sources. *Astrophys. J.*, 234:47–55.

Hardee, P. E., Walker, R. C., and Gómez, J. L. (2005). Modeling the 3C 120 Radio Jet from 1 to 30 Milliarcseconds. *Astrophys. J.*, 620:646–664.

Harten, A., Lax, P. D., and van Leer, B. (1983). On upstream differencing and godunov-type schemes for hyperbolic conservation laws. *SIAM Review*, 25(1):35–61.

Heiles, C. and Troland, T. H. (2005). The Millennium Arecibo 21 Centimeter Absorption-Line Survey. IV. Statistics of Magnetic Field, Column Density, and Turbulence. *Astrophys. J.*, 624:773–793.

Heinz, S. and Begelman, M. C. (1997). Analysis of the Synchrotron Emission from the M87 Jet. *Astrophys. J.*, 490:653–663.

Ho, L. C. (2002). On the Relationship between Radio Emission and Black Hole Mass in Galactic Nuclei. *Astrophys. J.*, 564:120–132.

Holt, S. S., Boldt, E. A., and Serlemitsos, P. J. (1969). Search for Line Structure in the X-Ray Spectrum of SCO X-1. *Astrophys. J. Lett.*, 158:L155.

Hoyle, F., Fowler, W. A., Burbidge, G. R., and Burbidge, E. M. (1964). On Relativistic Astrophysics. *Astrophys. J.*, 139:909.

Hubble, E. P. (1926). Extragalactic nebulae. *Astrophys. J.*, 64:321369.

Jansky, K. G. (1933). Radio Waves from Outside the Solar System. *Nature*, 132:66.

Jorstad, S. G., Marscher, A. P., Lister, M. L., Stirling, A. M., Cawthorne, T. V., Gear, W. K., Gómez, J. L., Stevens, J. A., Smith, P. S., Forster, J. R., and Robson, E. I. (2005). Polarimetric Observations of 15 Active Galactic Nuclei at High Frequencies: Jet Kinematics from Bimonthly Monitoring with the Very Long Baseline Array. *Astronomical Journal*, 130:1418–1465.

Kellermann, K. I., Lister, M. L., Homan, D. C., Vermeulen, R. C., Cohen, M. H., Ros, E., Kadler, M., Zensus, J. A., and Kovalev, Y. Y. (2004). Sub-Milliarcsecond Imaging of Quasars and Active Galactic Nuclei. III. Kinematics of Parsec-scale Radio Jets. *Astrophys. J.*, 609:539–563.

Khachikian, E. Y. and Weedman, D. W. (1974). An atlas of Seyfert galaxies. *Astrophys. J.*, 192:581–589.

Komissarov, S. S. (1999). Numerical simulations of relativistic magnetized jets. *Mon. Not. R. Astron. Soc.*, 308:1069–1076.

Koratkar, A. and Blaes, O. (1999). The Ultraviolet and Optical Continuum Emission in Active Galactic Nuclei: The Status of Accretion Disks. *Publications of the ASP*, 111:1–30.

Kraemer, S. B., Schmitt, H. R., and Crenshaw, D. M. (2008). Probing the Ionization Structure of the Narrow-Line Region in the Seyfert 1 Galaxy NGC 4151. *Astrophys. J.*, 679:1128–1143.

Kraft, R. P., Vázquez, S. E., Forman, W. R., Jones, C., Murray, S. S., Hardcastle, M. J., Worrall, D. M., and Churazov, E. (2003). X-Ray Emission from the Hot Interstellar Medium and Southwest Radio Lobe of the Nearby Radio Galaxy Centaurus A. *Astrophys. J.*, 592:129–146.

Krolik, J. H. and Begelman, M. C. (1988). Molecular tori in Seyfert galaxies - Feeding the monster and hiding it. *Astrophys. J.*, 329:702–711.

Laing, R. A. and Bridle, A. H. (2002). Dynamical models for jet deceleration in the radio galaxy 3C 31. *Mon. Not. R. Astron. Soc.*, 336:1161–1180.

Laor, A. (2000). On Black Hole Masses and Radio Loudness in Active Galactic Nuclei. *Astrophys. J. Lett.*, 543:L111–L114.

Lax, P. D. (1954). Weak solutions of nonlinear hyperbolic equations and their numerical computation. *Communications on Pure and Applied Mathematics*, 7(1):159–193.

Ledlow, M. J. and Owen, F. N. (1996). 20 CM VLA Survey of Abell Clusters of Galaxies. VI. Radio/Optical Luminosity Functions. *Astron. J.*, 112:9.

Leismann, T., Aloy, M.-A., and Müller, E. (2004). Mhd simulations of relativistic jets. *Astrophysics and Space Science*, 293(1):157–163.

Leismann, T., Antón, L., Aloy, M. A., Müller, E., Martí, J. M., Miralles, J. A., and Ibáñez, J. M. (2005). Relativistic MHD simulations of extragalactic jets. *Astronomy and Astrophysics*, 436:503–526.

LeVeque, R., Steiner, O., Gautschy, A., Mihalas, D., Dorfi, E., and Müller, E. (2006). *Computational Methods for Astrophysical Fluid Flow: Saas-Fee Advanced Course 27. Lecture Notes 1997 Swiss Society for Astrophysics and Astronomy.* Saas-Fee Advanced Course. Springer Berlin Heidelberg.

Lewis, K. T., Eracleous, M., and Sambruna, R. M. (2003). Emission-Line Diagnostics of the Central Engines of Weak-Line Radio Galaxies. *Astrophys. J.*, 593:115–126.

Lister, M. L., Cohen, M. H., Homan, D. C., Kadler, M., Kellermann, K. I., Kovalev, Y. Y., Ros, E., Savolainen, T., and Zensus, J. A. (2009). MOJAVE: Monitoring of Jets in Active Galactic Nuclei with VLBA Experiments. VI. Kinematics Analysis of a Complete Sample of Blazar Jets. *Astron. J.*, 138:1874–1892.

Lister, M. L. and Homan, D. C. (2005). MOJAVE: Monitoring of Jets in Active Galactic Nuclei with VLBA Experiments. I. First-Epoch 15 GHz Linear Polarization Images. *Astron. J.*, 130:1389–1417.

Lobanov, A., Hardee, P., and Eilek, J. (2003). Internal structure and dynamics of the kiloparsec-scale jet in M87. *New Astron. Rev.*, 47:629–632.

Lyubarsky, Y. E. (2005). On the relativistic magnetic reconnection. *Mon. Not. R. Astron. Soc.*, 358:113–119.

Marscher, A. P. (2005). The Relationship between Radio and Higher-Frequency Emission in Active Galactic Nuclei. *Mem. Societa Astronomica Italiana*, 76:13.

Martí, J. M., Müller, E., Font, J. A., Ibáñez, J. M. Z., and Marquina, A. (1997). Morphology and Dynamics of Relativistic Jets. *Astrophys. J.*, 479:151–163.

McKinney, J. C. and Blandford, R. D. (2009). Stability of relativistic jets from rotating, accreting black holes via fully three-dimensional magnetohydrodynamic simulations. *Mon. Not. R. Astron. Soc.*, 394:L126–L130.

Meliani, Z., Keppens, R., and Giacomazzo, B. (2008). Faranoff-Riley type I jet deceleration at density discontinuities. Relativistic hydrodynamics with a realistic equation of state. *Astronomy and Astrophysics*, 491:321–337.

Mignone, A., Bodo, G., Massaglia, S., Matsakos, T., Tesileanu, O., Zanni, C., and Ferrari, A. (2007). PLUTO: A Numerical Code for Computational Astrophysics. *Astrophys. J. Suppl.*, 170:228–242.

Mignone, A., Plewa, T., and Bodo, G. (2005). The Piecewise Parabolic Method for Multidimensional Relativistic Fluid Dynamics. *Astrophys. J. Suppl.*, 160:199–219.

Mignone, A., Rossi, P., Bodo, G., Ferrari, A., and Massaglia, S. (2010a). High-resolution 3D relativistic MHD simulations of jets. *Mon. Not. R. Astron. Soc.*, 402:7–12.

Mignone, A., Tzeferacos, P., Zanni, C., Tesileanu, O., Matsakos, T., and Bodo, G. (2010b). PLUTO: A Code for Flows in Multiple Spatial Dimensions. Astrophysics Source Code Library.

Miller, J. S. and Goodrich, R. W. (1990). Spectropolarimetry of high-polarization Seyfert 2 galaxies and unified Seyfert theories. *Astrophys. J.*, 355:456–467.

Mimica, P., Aloy, M.-A., Agudo, I., Martí, J. M., Gómez, J. L., and Miralles, J. A. (2009). Spectral Evolution of Superluminal Components in Parsec-Scale Jets. *Astrophys. J.*, 696:1142–1163.

Misner, C., Thorne, K., and Wheeler, J. (1973). *Gravitation*. Number pt. 3 in Gravitation. W. H. Freeman, San Francisco, USA.

Miyoshi, T. and Kusano, K. (2005). A multi-state HLL approximate Riemann solver for ideal magnetohydrodynamics. *Journal of Computational Physics*, 208:315–344.

Mohamed, S., Mackey, J., and Langer, N. (2012). 3D simulations of Betelgeuse's bow shock. *Astronomy and Astrophysics*, 541:A1.

Monaghan, J. J. (1992). Smoothed particle hydrodynamics. *Annu. Rev. Astron. Astrophys.*, 30:543–574.

Mortlock, D. J., Warren, S. J., Venemans, B. P., Patel, M., Hewett, P. C., McMahon, R. G., Simpson, C., Theuns, T., Gonzáles-Solares, E. A., Adamson, A., Dye, S., Hambly, N. C., Hirst, P., Irwin, M. J., Kuiper, E., Lawrence, A., and Röttgering, H. J. A. (2011). A luminous quasar at a redshift of z = 7.085. *Nature*, 474:616–619.

Netzer, H. (2013). *The Physics and Evolution of Active Galactic Nuclei*. Cambridge University Press, Cambridge, UK.

Netzer, H. (2013). *The Physics and Evolution of Active Galactic Nuclei*.

O'Dea, C. P. and Owen, F. N. (1986). Multifrequency VLA observations of the prototypical narrow-angle tail radio source NGC 1265. *Astrophys. J.*, 301:841–859.

Osterbrock, D. E. and Mathews, W. G. (1986). Emission-line regions of active galaxies and QSOs. *Annual Review of Astron. and Astrophys.*, 24:171–203.

Owen, F. N. and White, R. A. (1991). Surface photometry of radio galaxies. II - Cluster sources. *Mon. Not. R. Astron. Soc.*, 249:164–171.

Parma, P., de Ruiter, H. R., Mack, K.-H., van Breugel, W., Dey, A., Fanti, R., and Klein, U. (1996). 1358+305: a giant radio galaxy at z=0.206. *Astronomy and Astrophysics*, 311:49–56.

Penrose, R. (1969). Gravitational Collapse: the Role of General Relativity. *Nuovo Cimento Rivista Serie*, 1.

Penston, M. V., Penston, M. J., Selmes, R. A., Becklin, E. E., and Neugebauer, G. (1974). Broadband optical and infrared observations of Seyfert galaxies. *Mon. Not. R. Astron. Soc.*, 169:357–393.

Perucho, M. and Martí, J. M. (2007). A numerical simulation of the evolution and fate of a Fanaroff-Riley type I jet. The case of 3C 31. *Mon. Not. R. Astron. Soc.*, 382:526–542.

Peterson, B. M. (1997). *An Introduction to Active Galactic Nuclei*.

Piner, B. G., Mahmud, M., Fey, A. L., and Gospodinova, K. (2007). Relativistic Jets in the Radio Reference Frame Image Database. I. Apparent Speeds from the First 5 Years of Data. *Astron. J.*, 133:2357–2388.

Pushkarev, A. and Kovalev, Y. (2008). Probing parsec scale jets in AGN with geodetic VLBI. In *The role of VLBI in the Golden Age for Radio Astronomy*, page 86.

Reber, G. (1944). Cosmic Static. *Astrophys. J.*, 100:279.

Rees, M. J. (1966). Appearance of Relativistically Expanding Radio Sources. *Nature*, 211:468–470.

Rees, M. J. (1984). Black Hole Models for Active Galactic Nuclei. *Annual Review of Astron. and Astrophys.*, 22:471–506.

Rees, M. J., Netzer, H., and Ferland, G. J. (1989). Small dense broad-line regions in active nuclei. *Astrophys. J.*, 347:640–655.

Reynolds, C. S., Garofalo, D., and Begelman, M. C. (2006). Trapping of Magnetic Flux by the Plunge Region of a Black Hole Accretion Disk. *Astrophys. J.*, 651:1023–1030.

Richtmyer, R. D. and Morton, K. W. (1967). *Difference methods for initial-value problems.*

Rossi, P., Mignone, A., Bodo, G., Massaglia, S., and Ferrari, A. (2008). Formation of dynamical structures in relativistic jets: the FRI case. *Astronomy and Astrophysics*, 488:795–806.

Rybicki, G. and Lightman, A. (1979). *Radiative Processes in Astrophysics.* A Wiley-Interscience publication. Wiley.

Sadun, A. C. and Morrison, P. (2002). Hercules a (3c 348): Phenomenology of an unusual active galactic nucleus. *The Astronomical Journal*, 123(5):2312.

Salpeter, E. E. (1964). Accretion of Interstellar Matter by Massive Objects. *Astrophys. J.*, 140:796–800.

Scheck, L., Aloy, M. A., Martí, J. M., Gómez, J. L., and Müller, E. (2002). Does the plasma composition affect the long-term evolution of relativistic jets? *Mon. Not. R. Astron. Soc.*, 331:615–634.

Schmidt, M. (1963). 3C 273 : A Star-Like Object with Large Red-Shift. *Nature*, 197:1040.

Schmidt, M. and Green, R. F. (1983). Quasar evolution derived from the Palomar bright quasar survey and other complete quasar surveys. *Astrophys. J.*, 269:352–374.

Schutz, B. (2009). *A First Course in General Relativity.* Cambridge University Press, Cambridge, United Kingdom.

Seyfert, C. K. (1943). Nuclear Emission in Spiral Nebulae. *Astrophys. J.*, 97:28.

Shields, G. A. (1978). Thermal continuum from acretion disks in quasars. *Nature*, 272:706–708.

Shrader, C. R. and Gehrels, N. (1995). Recent Results from the Compton Gamma Ray Observatory. *Publications of the Astronomical Society of the Pacific*, 107:606.

Sod, G. A. (1978). A survey of several finite difference methods for systems of nonlinear hyperbolic conservation laws. *Journal of Computational Physics*, 27(1):1 – 31.

Spruit, H. C. and Uzdensky, D. A. (2005). Magnetic Flux Captured by an Accretion Disk. *Astrophys. J.*, 629:960–968.

Stone, J. M. and Norman, M. L. (1992a). ZEUS-2D: A radiation magnetohydrodynamics code for astrophysical flows in two space dimensions. I - The hydrodynamic algorithms and tests. *Astrophys. J. Suppl.*, 80:753–790.

Stone, J. M. and Norman, M. L. (1992b). ZEUS-2D: A Radiation Magnetohydrodynamics Code for Astrophysical Flows in Two Space Dimensions. II. The Magnetohydrodynamic Algorithms and Tests. *Astrophys. J. Suppl.*, 80:791.

Swanenburg, B. N., Hermsen, W., Bennett, K., Bignami, G. F., Caraveo, P., Kanbach, G., Mayer-Hasselwander, H. A., Masnou, J. L., Paul, J. A., and Sacco, B. (1978). COS B observation of high-energy gamma radiation from 3C273. *Nature*, 275:298.

Tavecchio, F., Maraschi, L., Sambruna, R. M., and Urry, C. M. (2000). The X-Ray Jet of PKS 0637-752: Inverse Compton Radiation from the Cosmic Microwave Background? *Astrophys. J. Lett*, 544:L23–L26.

Tchekhovskoy, A., Narayan, R., and McKinney, J. C. (2011). Efficient generation of jets from magnetically arrested accretion on a rapidly spinning black hole. *Mon. Not. R. Astron. Soc.*, 418:L79–L83.

Toro, E. (2009). *Riemann Solvers and Numerical Methods for Fluid Dynamics: A Practical Introduction*. Springer Berlin Heidelberg.

Toro, E. F., Spruce, M., and Speares, W. (1994). Restoration of the contact surface in the hll-riemann solver. *Shock Waves*, 4(1):25–34.

Tout, C. A. and Pringle, J. E. (1996). Can a disc dynamo generate large-scale magnetic fields? *Mon. Not. R. Astron. Soc.*, 281:219–225.

Tran, H. D., Miller, J. S., and Kay, L. E. (1992). Detection of obscured broad-line regions in four Seyfert 2 galaxies. *Astrophys. J.*, 397:452–456.

Ulvestad, J. S., Antonucci, R. R. J., and Barvainis, R. (2005a). VLBA Imaging of Central Engines in Radio-Quiet Quasars. *Astrophys. J.*, 621:123–129.

Ulvestad, J. S., Wong, D. S., Taylor, G. B., Gallimore, J. F., and Mundell, C. G. (2005b). VLBA Identification of the Milliarcsecond Active Nucleus in the Seyfert Galaxy NGC 4151. *Astrophys. J.*, 130:936–944.

Urry, C. M. and Padovani, P. (1995). Unified Schemes for Radio-Loud Active Galactic Nuclei. *Publications of the ASP*, 107:803.

van Breugel, W. J. M. and Miley, G. K. (1977). Radio 'jets'. *Nature*, 265:315–318.

Van Leer, B. (1974). Towards the Ultimate Conservation Difference Scheme. II. Monotonicity and Conservation Combined in a Second-Order Scheme. *Journal of Computational Physics*, 14:361–370.

Van Leer, B. (1977a). Towards the ultimate conservative difference scheme. III - Upstream-centered finite-difference schemes for ideal compressible flow. IV - A new approach to numerical convection. *Journal of Computational Physics*, 23:263–299.

Van Leer, B. (1977b). Towards the Ultimate Conservative Difference Scheme. IV. A New Approach to Numerical Convection. *Journal of Computational Physics*, 23:276.

Van Leer, B. (1979). Towards the ultimate conservative difference scheme. V - A second-order sequel to Godunov's method. *Journal of Computational Physics*, 32:101–136.

Véron-Cetty, M. and Véron, P. (2000). The emission line spectrum of active galactic nuclei and the unifying scheme. *The Astronomy and Astrophysics Review*, 10(1):81–133.

Véron-Cetty, M. P. and Véron, P. (2000). The emission line spectrum of active galactic nuclei and the unifying scheme. *AAPR*, 10:81–133.

Waggett, P. C., Warner, P. J., and Baldwin, J. E. (1977). NGC 6251, a very large radio galaxy with an exceptional jet. *Mon. Not. R. Astron. Soc.*, 181:465–474.

Wakely, S. P. and Horan, D. (2008). TeVCat: An online catalog for Very High Energy Gamma-Ray Astronomy. *International Cosmic Ray Conference*, 3:1341–1344.

Wald, R. M. (1974a). Black hole in a uniform magnetic field. *Physical Review D*, 10:1680–1685.

Wald, R. M. (1974b). Energy Limits on the Penrose Process. *Astrophys. J.*, 191:231–234.

Weedman, D. W. (1973). A Photometric Study of Markarian Galaxies. *Astrophys. J.*, 183:29–40.

Woltjer, L. (1959). Emission Nuclei in Galaxies. *Astrophys. J.*, 130:38.

Zhao, J.-H., Burns, J. O., Hardee, P. E., and Norman, M. L. (1992a). Instabilities in astrophysical jets. I - Linear analysis of body and surface waves. *Astrophys. J.*, 387:69–82.

Zhao, J.-H., Burns, J. O., Norman, M. L., and Sulkanen, M. E. (1992b). Instabilities in astrophysical jets. II - Numerical simulations of slab jets. *Astrophys. J.*, 387:83–94.

Ziegler, U. (1998). NIRVANA $^{+}$: An adaptive mesh refinement code for gas dynamics and MHD. *Computer Physics Communications*, 109:111–134.

Appendix A

Appendix

A.1 Example files for PLUTO simulation

A.1.1 System configuration file

Example of the sysconf.out file generated by the PLUTO setup.py script for the UFS HPC.

```
USER           = vdwesthuizenip
WORKING_DIR    = /auto/home/mount/vdwesthuizenip/PLUTO4.2/PLUTO/TEST/twoshock
SYSTEM_NAME    = Linux
NODE_NAME      = ui
RELEASE        = 2.6.32-642.6.2.el6.x86_64
ARCH           = x86_64
BYTE_ORDER     = little
VERSION        = #1 SMP Tue Oct 25 15:06:33 CDT 2016
PLUTO_DIR      = /home/vdwesthuizenip/PLUTO4.2/PLUTO
PLUTO_VERSION  = "4.2"
C_COMPILER     = gcc
MPI_C_COMPILER =
```

A.1.2 Makefile

Example of the makefile generated for the initial test simulation on the UFS HPC using the mpicc compiler.

```
#############################################################################
#
#     Configuration file for mpicc (parallel)
#
#############################################################################

CC       = mpicc
CFLAGS   = -c -O3
LDFLAGS  = -lm

PARALLEL = TRUE
USE_HDF5 = FALSE
#############################################################################
USER           = vdwesthuizenip
# ************************************************************
#
#                   PLUTO 4.2  Makefile
#
# ************************************************************

pluto:                               # Default target

ARCH         = Linux.mpicc.defs
PLUTO_DIR    = /home/vdwesthuizenip/PLUTO4.2/PLUTO
SRC          = $(PLUTO_DIR)/Src
INCLUDE_DIRS = -I. -I$(SRC)
VPATH        = ./:$(SRC)/New:$(SRC):$(SRC)/Time_Stepping:$(SRC)/States

include $(PLUTO_DIR)/Config/$(ARCH)

# ------------------------------------------------------------
#         Set headers and object files
# ------------------------------------------------------------

OBJ = adv_flux.o arrays.o boundary.o check_states.o  \
      cmd_line_opt.o entropy_switch.o  \
```

```
      flag_shock.o flatten.o get_nghost.o   \
      init.o int_bound_reset.o input_data.o \
      mappers3D.o mean_mol_weight.o \
      parse_file.o plm_coeffs.o rbox.o \
      set_indexes.o set_geometry.o set_output.o \
      tools.o var_names.o

OBJ += bin_io.o colortable.o initialize.o jet_domain.o \
       main.o restart.o runtime_setup.o show_config.o  \
       set_image.o set_grid.o startup.o split_source.o \
       userdef_output.o write_data.o write_tab.o \
       write_img.o write_vtk.o

include $(SRC)/Math_Tools/makefile

# ------------------------------------------------------------
#  Define macros by adding -D<name> where <name> has been
#  set to TRUE in the system configuration file (.defs)
# ------------------------------------------------------------

ifeq ($(strip $(PARALLEL)), TRUE)
 CFLAGS += -I$(SRC)/Parallel -DPARALLEL
 include $(SRC)/Parallel/makefile
 ifeq ($(strip $(USE_ASYNC_IO)), TRUE)
  CFLAGS += -DUSE_ASYNC_IO
 endif
endif

ifeq ($(strip $(USE_HDF5)), TRUE)
 CFLAGS += -DUSE_HDF5
 OBJ    += hdf5_io.o
endif

ifeq ($($strip $(USE_PNG)), TRUE)
 CFLAGS += -DUSE_PNG
endif

-include local_make
```

```
# ------------------------------------------------------------
#   Additional_header_files_here   ! dont change this line
# ------------------------------------------------------------

HEADERS += ppm_coeffs.h

# ------------------------------------------------------------
#   Additional_object_files_here   ! dont change this line
# ------------------------------------------------------------

OBJ += ppm_states.o
OBJ += ppm_coeffs.o
OBJ += rk_step.o
OBJ += update_stage.o
OBJ += char_tracing.o
include $(SRC)/RHD/makefile
include $(SRC)/EOS/Taub/makefile

# ------------------------------------------------------------
#    PLUTO target rule
# ------------------------------------------------------------

pluto: $(OBJ)
        $(CC) $(OBJ) $(LDFLAGS) -o $@

# ------------------------------------------------------------
#                     Suffix rule
# ------------------------------------------------------------

.c.o:
        $(CC) $(CFLAGS) $(INCLUDE_DIRS) $<

clean:
        @rm -f  *.o
        @echo make clean: done

# ------------------------------------------------------------
#          Dependencies for object files
# ------------------------------------------------------------
```

```
$(OBJ):  $(HEADERS)
```

A.1.3 Header file

An example of the definitions.h header file for the test jet simulation is shown below.

```
#define  PHYSICS                 RHD
#define  DIMENSIONS              3
#define  COMPONENTS              3
#define  GEOMETRY                CARTESIAN
#define  BODY_FORCE              NO
#define  COOLING                 NO
#define  RECONSTRUCTION          PARABOLIC
#define  TIME_STEPPING           CHARACTERISTIC_TRACING
#define  DIMENSIONAL_SPLITTING   YES
#define  NTRACER                 1
#define  USER_DEF_PARAMETERS     4

/* -- physics dependent declarations -- */

#define  EOS                     TAUB
#define  ENTROPY_SWITCH          NO

/* -- user-defined parameters (labels) -- */

#define  MACH                    0
#define  RHO_a                   1
#define  RHO_j                   2
#define  LOR                     3

/* [Beg] user-defined constants (do not change this line) */

#define  UNIT_DENSITY            1.00e-27
#define  UNIT_LENGTH             1e13
#define  UNIT_VELOCITY           2.99792e10

/* [End] user-defined constants (do not change this line) */

/* -- supplementary constants (user editable) -- */

#define  INITIAL_SMOOTHING   YES
#define  WARNING_MESSAGES    YES
#define  PRINT_TO_FILE       YES
```

```
#define  INTERNAL_BOUNDARY   NO
#define  SHOCK_FLATTENING    MULTID
#define  CHAR_LIMITING       NO
#define  LIMITER             MINMOD_LIM
```

A.1.4 Initialization file

An example of the pluto.ini file for the test jet simulation is shown below.

```
[Grid]

X1-grid    1    0.0    512     u    64.0
X2-grid    1    0.0    512     u    64.0
X3-grid    1    0.0    512    u     64.0

[Chombo Refinement]

Levels           4
Ref_ratio        2 2 2 2 2
Regrid_interval  2 2 2 2
Refine_thresh    0.3
Tag_buffer_size  3
Block_factor     8
Max_grid_size    64
Fill_ratio       0.75

[Time]
CFL              0.8
CFL_max_var      1.2
tstop            100000.0
first_dt         0.5e-4

[Solver]

Solver         hllc

[Boundary]

X1-beg        outflow
X1-end        outflow
X2-beg        outflow
X2-end        outflow
X3-beg        userdef
X3-end        outflow

[Static Grid Output]
```

```
uservar    8 T VMAG Erho N0 vorty BMAG jv av
dbl        100.0  -1   single_file
flt        10.0  -1   single_file cgs
vtk        50.0  -1   single_file cgs
dbl.h5    -1.0  -1
flt.h5    -1.0  -1
tab       -1.0  -1
ppm        10.0  -1
png       -1.0  -1
log        1
analysis  -1.0  -1

[Chombo HDF5 output]

Checkpoint_interval  -1.0  0
Plot_interval         1.0  0

[Parameters]

MACH                 3.0
RHO_a                10.0
RHO_j                0.1
LOR                  10.0
```

A.1.5 Problem configuration

An example of the init.c file for the test jet simulation is shown below.

```
/*!
  \file
  \brief Contains basic functions for problem initialization.

  The init.c file collects most of the user-supplied functions useful
  for problem configuration.
  It is automatically searched for by the makefile.

  \author A. Mignone (mignone@ph.unito.it)
  \date   Sept 10, 2012
*/
/*
   ////////////////////////////////////////////////////////////////////
    */
#include "pluto.h"

static void CalcJetParam(); //declare function to calculate the jet
   parameters from user inputs
static double Profile(double r, int nv); //declare function adding a
   profile to the jet nozzle for a smooth transition
static double pj; //declare pressure variable
double g_gamma; //declare adiabatic index


/*
   ********************************************************************
    */
void Init (double *v, double x1, double x2, double x3)
/*!
 * The Init() function can be used to assign initial conditions as
 * as a function of spatial position.
 *
 * \param [out] v   a pointer to a vector of primitive variables
 * \param [in] x1   coordinate point in the 1st dimension
 * \param [in] x2   coordinate point in the 2nd dimension
 * \param [in] x3   coordinate point in the 3rdt dimension
 *
```

```
 * The meaning of x1, x2 and x3 depends on the geometry:
 * \f[ \begin{array}{cccl}
 *    x_1  & x_2    & x_3  & \mathrm{Geometry}     \\ \noalign{\
    medskip}
 *     \hline
 *    x    &   y    &  z   & \mathrm{Cartesian}    \\ \noalign{\
    medskip}
 *    R    &   z    &  -   & \mathrm{cylindrical}  \\ \noalign{\
    medskip}
 *    R    & \phi   &  z   & \mathrm{polar}        \\ \noalign{\
    medskip}
 *    r    & \theta & \phi & \mathrm{spherical}
 *    \end{array}
 *  \f]
 *
 * Variable names are accessed by means of an index v[nv], where
 * nv = RHO is density, nv = PRS is pressure, nv = (VX1, VX2, VX3)
    are
 * the three components of velocity, and so forth.
 *
 *********************************************************************
    */
{ double *vjet;

  g_gamma=5./3.; //Assign adiabatic index of an ideal fluid
  CalcJetParam(x1, x2, x3, vjet);           //function used to
     calculate equilibrium pressure

  v[RHO] = g_inputParam[RHO_a]; //Assigning ambient density from
     pluto.ini
  v[VX1] = 0.0;                  //Assigning velocity
  v[VX2] = 0.0;                  //Backgroud medium in rest
  v[VX3] = 0.0;                  //with regards to labratory frame
  v[PRS] = pj;                  //Assigning ambient pressure
  v[TRC] = 0.0;                  //Assigning 0 trace particles to
     ambient

}
```

```
/*
   ************************************************************************
    */
void Analysis (const Data *d, Grid *grid)
/*!
 *  Perform runtime data analysis.
 *
 * \param [in] d the PLUTO Data structure
 * \param [in] grid   pointer to array of Grid structures
 *
 ************************************************************************
     */
{
 // No additional runtime analysis was done
}
#if PHYSICS == MHD
/*
   ************************************************************************
    */
void BackgroundField (double x1, double x2, double x3, double *B0)
/*!
 * Define the component of a static, curl-free background
 * magnetic field.
 *
 * \param [in] x1  position in the 1st coordinate direction \f$x_1\f$
 * \param [in] x2  position in the 2nd coordinate direction \f$x_2\f$
 * \param [in] x3  position in the 3rd coordinate direction \f$x_3\f$
 * \param [out] B0 array containing the vector componens of the
    background
 *                 magnetic field
 ************************************************************************
     */
{
   B0[0] = 0.0;
   B0[1] = 0.0;
   B0[2] = 0.0;
}
#endif
```

```
/*
   *********************************************************************
    */
void UserDefBoundary (const Data *d, RBox *box, int side, Grid *grid)
/*!
 *  Assign user-defined boundary conditions.
 *
 * \param [in,out] d  pointer to the PLUTO data structure containing
 *                    cell-centered primitive quantities (d->Vc) and
 *                    staggered magnetic fields (d->Vs, when used) to
 *                    be filled.
 * \param [in] box    pointer to a RBox structure containing the
    lower
 *                    and upper indices of the ghost zone-centers/
    nodes
 *                    or edges at which data values should be
    assigned.
 * \param [in] side   specifies the boundary side where ghost zones
    need
 *                    to be filled. It can assume the following
 *                    pre-definite values: X1_BEG, X1_END,
 *                                         X2_BEG, X2_END,
 *                                         X3_BEG, X3_END.
 *                    The special value side == 0 is used to control
 *                    a region inside the computational domain.
 * \param [in] grid  pointer to an array of Grid structures.
 *
 *********************************************************************
    */
{ int   i, j, k, nv;
  double *x1, *x2, *x3;
  double ***bxs, ***bys, ***bzs;
  double prof, vjet[256], vout[NVAR], x1m, x2m, r;

  #ifdef STAGGERED_MHD
   D_EXPAND(bxs = d->Vs[BX1s];   ,
            bys = d->Vs[BX2s];   ,
            bzs = d->Vs[BX3s];)
  #endif
```

```
x1  = grid[IDIR].xgc;
x2  = grid[JDIR].xgc;
x3  = grid[KDIR].xgc;

if (side == 0) {     /* -- check solution inside domain -- */
  DOM_LOOP(k,j,i){};
}

 if (side == X3_BEG){  /* -- X3_BEG boundary -- */
  if (box->vpos == CENTER) {
    BOX_LOOP(box,k,j,i){
      CalcJetParam (x1[i], x2[j], x3[k], vjet); /* Jet Values */
      VAR_LOOP(nv) vout[nv] = d->Vc[nv][2*KBEG-k-1][j][i]; /*
          Ambient */
      vout[VX3] *= -1.0;
      #ifdef PSI_GLM
       vjet[PSI_GLM]  = d->Vc[PSI_GLM][KBEG][j][i] - d->Vc[BX2][
           KBEG][j][i];
       vout[PSI_GLM] *= -1.0;
      #endif
      x1m=x1[i] - 32;
      x2m=x2[j] - 32;
      r=sqrt(x1m*x1m+x2m*x2m);
      prof = (fabs(r) <= 1.0);
      VAR_LOOP(nv) d->Vc[nv][k][j][i] = vout[nv] - (vout[nv] - vjet
          [nv])*Profile(r,nv);
    }
  }else if (box->vpos == X1FACE){
    #ifdef STAGGERED_MHD
      x1 = grid[IDIR].xr;
     }
    #endif
  }else if (box->vpos == X2FACE){
    BOX_LOOP(box,k,j,i){  }
  }else if (box->vpos == X3FACE){
    BOX_LOOP(box,k,j,i){  }
  }
}
```

```
}
#if BODY_FORCE != NO
/*
   ********************************************************************
    */
void BodyForceVector(double *v, double *g, double x1, double x2,
   double x3)
/*!
 * Prescribe the acceleration vector as a function of the coordinates
 * and the vector of primitive variables *v.
 *
 * \param [in] v  pointer to a cell-centered vector of primitive
 *                variables
 * \param [out] g acceleration vector
 * \param [in] x1  position in the 1st coordinate direction \f$x_1\f$
 * \param [in] x2  position in the 2nd coordinate direction \f$x_2\f$
 * \param [in] x3  position in the 3rd coordinate direction \f$x_3\f$
 *
 *********************************************************************
     */
{
  g[IDIR] = 0.0;
  g[JDIR] = 0.0;
  g[KDIR] = 0.0;
}
/*
   ********************************************************************
    */
double BodyForcePotential(double x1, double x2, double x3)
/*!
 * Return the gravitational potential as function of the coordinates.
 *
 * \param [in] x1  position in the 1st coordinate direction \f$x_1\f$
 * \param [in] x2  position in the 2nd coordinate direction \f$x_2\f$
 * \param [in] x3  position in the 3rd coordinate direction \f$x_3\f$
 *
 * \return The body force potential \f$ \Phi(x_1,x_2,x_3) \f$.
 *
```

```
 *************************************************************************
     */
{
  return 0.0;
}
#endif



/* *************************************************************
   */
void CalcJetParam(double x1, double x2, double x3, double *vj)
/*Function to calculate parameters from userdefined variables in
 *  *pluto.ini file
 *   *
 *    *
 *     *
 *
    ************************************************************
     */
{
  double bm, b2_av, bphi, lor, a = 0.5;
  double r, x, scrh, mag_z, mag_phi, Cs;
  double bmagx, bmagy, bmagz, xm1, xm2;
  double b_z=0.0;

  xm1   = x1-32; //calculate x distance from origin
  xm2   = x2-32; //calculate y distance from origin
  r=sqrt(xm1*xm1+xm2*xm2);
  lor = g_inputParam[LOR]; //assign lorentz factor to variable
  if (fabs(r) < 1.e-9) r = 1.e-9;

  x = fabs(r/a);
  vj[RHO] = g_inputParam[RHO_j]; //assign beam density

  EXPAND(vj[VX1] = 0.0; ,
         vj[VX2] = 0.0; , /* assign 3-vel */
         vj[VX3] = sqrt(1.0 - 1.0/(lor*lor));)
```

```
  Cs = g_inputParam[MACH]/vj[VX3]; //calculate sound speed inverse
  pj    = vj[RHO]/(g_gamma*Cs*Cs - g_gamma/(g_gamma - 1.0)); //
      calculate thermal pressure
  scrh=MIN(x*x, 1.0);
  vj[PRS] = pj; //+ (bm*bm)*(1.0 - scrh);

  //if ((int)g_time%100<5 && g_time>800)
  //{
    //vj[RHO]=vj[RHO]*10.0;
    //Cs=g_gamma*pj/(vj[RHO]+g_gamma*pj/(g_gamma-1));
   //  vj[VX3]=g_inputParam[MACH]/Cs;
  //}
  //else
  //{
  //if (g_time>805 && g_time<807)
  //{
   //  vj[RHO]=vj[RHO]*10.0;
    //lor=lor*2.0;

/* -- set tracer value -- */

  #if NTRACER > 0
   vj[TRC] = 1.0;
  #endif

}

/* ********************************************** */
double Profile(double r, int nv)
/*
 *
 *
 *
 ********************************************** */
{
  int xn = 7;
  double r0 = 1;
```

```
    return 1.0/cosh(pow(r/r0,xn));

}
```

Appendix B

Sychrotron emission code

```
import pyPLUTO as pp
import numpy as np
import matplotlib
import math
import time

##############################################################################

def viewangle(phi, theta, imx, imy, sx, sy, sz):

  xp=sx/2+np.cos(theta)*np.cos(phi)*imx-np.sin(phi)*imy
  yp=sy/2+np.cos(theta)*np.sin(phi)*imx+np.cos(phi)*imy
  zp=sz/2-np.sin(theta)*imx

  nx=np.sin(theta)*np.cos(phi)
  ny=np.sin(theta)*np.sin(phi)
  nz=np.cos(theta)

  if nx >= 0:
    t0_x=(0.0-xp)/nx
    tm_x=(sx-xp)/nx
  else:
    t0_x=(sx-xp)/nx
    tm_x=(0.0-xp)/nx

  if ny >= 0:
```

```
    t0_y=(0.0-yp)/ny
    tm_y=(sy-yp)/ny
  else:
    t0_y=(sy-yp)/ny
    tm_y=(0.0-yp)/ny

  if nz >= 0:
    t0_z=(0.0-zp)/nz
    tm_z=(sz-zp)/nz
  else:
    t0_z=(sz-zp)/nz
    tm_z=(0.0-zp)/nz
  t0=np.array([t0_x, t0_y, t0_z])
  tf=np.array([tm_x, tm_y, tm_z])
  ti=min(abs(t0[0]), abs(t0[1]), abs(t0[2]))
  tm=min(abs(tm_x), abs(tm_y), abs(tm_z))

  for i in range(0,3):
    if ti==abs(t0[i]):
      tii=t0[i]
    if tm==abs(tf[i]):
      tmm=tf[i]


  #print(t0)
  pl=np.array([round(xp), round(yp), round(zp), round(tii), round(tmm
      )])
  return pl

##########################################################################################

def cells(phi, theta, pl, tc):

  xp=pl[0]
  yp=pl[1]
  zp=pl[2]
  t0=pl[3]

  xc=xp+tc*np.sin(theta)*np.cos(phi)
```

```
    yc=yp+tc*np.sin(theta)*np.sin(phi)
    zc=zp+tc*np.cos(theta)

    out=np.array([round(xc), round(yc), round(zc)])
    return out


##############################################################################

def gridsize(sx, sy, sz, phi, theta):

    tx1=int(sx/(np.cos(theta)*np.cos(phi)))
    tx2=int(sy/(np.cos(theta)*np.sin(phi)))
    tx3=int(sz/(-np.sin(theta)))

    max_imx=min(abs(tx1), abs(tx2), abs(tx3))

    ty1=sx/(-np.sin(phi))
    ty2=sy/(np.cos(phi))

    max_imy=min(abs(ty1), abs(ty2))

    print("Image size; ")
    print(max_imx, max_imy)
    return (int(max_imx),int( max_imy))
##############################################################################


print
    ('##############################################################################
      \n
Synchrotron emission estimates for PLUTO data \nVersion 3.1\n
    ##############################################################################')


nr=pp.nlast_info(datatype="float") #Reading simulation information
out=[] #Creating an array to store coordinates for integration

#User prompts
```

```
#dt=input("Enter datatype of input files: ") #User input for datatype
phi=float(input("Enter the angle phi: ")) #User input for the Azimuth
    angle
theta=float(input("Enter the theta angle: ")) #User input for the
    polar angle
mu=float(input("Frequency for intensity map: ")) #User input for the
    frequency of emission
fr=int(input("Frame number for estimate calculations: ")) #User input
    for frame number

#Avoid division by zero
if theta==0:
  theta=1e-40

j=0

if fr<0:
  for j in range(0,nr):
    #Loading dataframes
    start_time=time.time()
    D = pp.pload(j,datatype="float")

    #Removing unnecessary data to save memory
    del D.prs
    del D.rho
    del D.T
    del D.vorty

    #Determining the dimensions of the loaded data
    sx=len(D.x1)
    sy=len(D.x2)
    sz=len(D.x3)

    print("Grid size")
    print(sx)
    print(sy)
    print(sz)

    #Calculationg Bcos(theta) and Lorentz factor for each cell
```

```
D.Bcos=(D.vx1/2.998e10*np.sin(theta)*np.cos(phi)-D.vx2/2.998e10*
    np.sin(theta)*np.sin(phi)+D.vx3/2.998e10*np.cos(theta))
D.LOR=1/np.sqrt(1-D.VMAG*D.VMAG)

#Removing unnecessary data to save memory
del D.vx1
del D.vx2
del D.vx3

#Calculating emission and absorption coefficients
mup=D.LOR*(1-D.Bcos)*mu
D.jv0 = D.jv/mup**0.4
D.av0 = D.av/(mup**2.9)

#Applying relativistic correction
D.jrec=D.jv0/pow(D.LOR*(1-D.Bcos),3)
D.arec=D.av0
#Calculating the size of the image
gs=gridsize(sx,sy,sz,phi,theta)
D.Iv=np.zeros([gs[1],gs[0]])

#Calculating intensity maps
print("Calculating intensity map for frame " + str(fr))
log=open("see.log", 'a')
log.write("Calculating intensity map for theta={} and phi={}".
    format(theta,phi) +"\n
    ##########################################\n{:^12} {:^10} {:^24}
     {:^20}".format("IMx,IMy", "Time step", "x,y,z", "Intensity\n
    "))
for n in range((-gs[0]/2), (gs[0]/2)): #Step through x pixels of
    image frame
  for m in range((-gs[1]/2) ,(gs[1]/2)): #Step through y pixels
      of image frame
    pl=viewangle(phi, theta, n, m, sx, sy, sz) #Deteriming the
        position of image pixel in 3D grid environment
    for t in range(int(pl[3]), int(pl[4])): #Numerical
        integration of the emisivity along the normal
      out=cells(phi, theta, pl, t) #Determining the position of
          each integration point in 3d environment
```

```
            if 0 <= out[0] < sx and 0 <= out[1] < sy and 0 <= out[2] <
                sz:
              D.Iv[(m+gs[1]/2),(n+gs[0]/2)]=D.Iv[(m+gs[1]/2),(n+gs
                  [0]/2)]+D.jrec[int(out[0]),int(out[1]),int(out[2])]-D.
                  arec[int(out[0]),int(out[1]),int(out[2])]*D.Iv[(m+gs
                  [1]/2),(n+gs[0]/2)]

              log.write("{:^6},{:^6}{:^10}{:^8},{:^8},{:^8}{:^20}\n".
                  format((m+gs[1]/2),(n+gs[0]/2),(t+pl[3]),out[0],out
                  [1],out[2], D.Iv[(m+gs[1]/2),(n+gs[0]/2)]))
else:
  #Loading dataframes
  start_time=time.time()
  D = pp.pload(fr,datatype="float")
  j=fr
  #Removing unnecessary data to save memory
  del D.prs
  del D.rho
  del D.T
  del D.vorty

  #Determining the dimensions of the loaded data
  sx=len(D.x1)
  sy=len(D.x2)
  sz=len(D.x3)

  print("Grid size: ({0},{1},{2})".format(sx,sy,sz))
  #print(sx)
  #print(sy)
  #print(sz)

  #Calculationg Bcos(theta) and Lorentz factor for each cell
  D.Bcos=(D.vx1/2.998e10*np.sin(theta)*np.cos(phi)+D.vx2/2.998e10*np.
      sin(theta)*np.sin(phi)+D.vx3/2.998e10*np.cos(theta))
  D.LOR=1/np.sqrt(1-D.VMAG*D.VMAG)

  #Removing unnecessary data to save memory
  del D.vx1
  del D.vx2
```

```
del D.vx3

#Calculating emission and absorption coefficients
mup=D.LOR*(1-D.Bcos)*mu
D.jv0 = D.jv/mup**0.4
D.av0 = D.av/(mup**2.9)

#Applying relativistic correction
D.jrec=D.jv0/pow(D.LOR*(1-D.Bcos),3)
D.arec=D.av0
#Calculating the size of the image
gs=gridsize(sx,sy,sz,phi,theta)
D.Iv=np.zeros([gs[1],gs[0]])

#Calculating intensity maps
print("Calculating intensity map for frame " + str(fr))
log=open("see.log", 'a')
log.write("Calculating intensity map for theta={} and phi={}".
    format(theta,phi) +"\n##########################################\n
    {:^12} {:^10} {:^24} {:^20}".format("IMx,IMy", "Time step", "x,y
    ,z", "Intensity\n"))
for n in range((-gs[0]/2), (gs[0]/2)): #Step through x pixels of
    image frame
  for m in range((-gs[1]/2) ,(gs[1]/2)): #Step through y pixels of
      image frame
    pl=viewangle(phi, theta, n, m, sx, sy, sz) #Deteriming the
        position of image pixel in 3D grid environmen
    for t in range(int(pl[3]), int(pl[4])): #Numerical integration
        of the emisivity along the normal
      out=cells(phi, theta, pl, t) #Determining the position of
          each integration point in 3d environment
      if 0 <= out[0] < sx and 0 <= out[1] < sy and 0 <= out[2] < sz
          :
        D.Iv[(m+gs[1]/2),(n+gs[0]/2)]=D.Iv[(m+gs[1]/2),(n+gs[0]/2)
            ]+D.jrec[int(out[0]),int(out[1]),int(out[2])]-D.arec[int
            (out[0]),int(out[1]),int(out[2])]*D.Iv[(m+gs[1]/2),(n+gs
            [0]/2)]

        log.write("{:^6},{:^6}{:^10}{:^8},{:^8},{:^8}{:^20}\n".
```

```
                format((m+gs[1]/2),(n+gs[0]/2),(t-pl[3]),out[0],out[1],
                out[2], D.Iv[(m+gs[1]/2),(n+gs[0]/2)]))
        #else:
          #print("err")

log.close()
fname="imapl"+pp.get_nstepstr(j)+"_{1}_{2}".format(round(180/np.pi*
    theta),round(180/np.pi*phi)) +".npy"
#fname="imap"+pp.get_nstepstr(j)
print("writing file " + fname)
np.save(fname,D.Iv)
del D
print("Execution time: %s s" % (time.time() - start_time))

##########################################################################################
```

Appendix C

Conference contributions

The research done in this project has been presented at several conferences at both national and international levels and the contributions that have been submitted for peer review are as follows:

1. Van der Westhuizen, I.P., Van Soelen, B. and Meintjes P.J., Hydrodynamical Simulations of Relativistic Astrophysical Jets, *3rd Annual Conference on High Energy Astrophysics in Southern Africa (HEASA2015), Johannesburg, South Africa,* 18-20 June 2015, PoS(HEASA2015)017.

2. Van der Westhuizen, I.P., Van Soelen, B., Meintjes P.J., Riekert, S.J.P.K. and Beall, J.H. (2015), Numerical modelling of hydrodynamical astrophysical outflows: application using the PLUTO code, *Proceedings of South African Institute of Physics (SAIP2015), Port-Elizabeth, South Africa*, 28 June-3 July 2015, pp. 356-361.

3. Van der Westhuizen, I.P., Van Soelen, B. and Meintjes P.J., Emission modelling of numerical hydrodynamical simulations with application to active galactic nuclei, *Proceedings of South African Institute of Physics (SAIP2016), Cape Town, South Africa jets*, 4-8 July 2016, submitted.

4. Van der Westhuizen, I.P., Van Soelen, B. and Meintjes P.J., Simulating the synchrotron emission of AGN with grid based relativistic hydrodynamics, *28th IUPAP Conference on Computational Physics (CCP2016), Johannesburg, South Africa*, 10-14 July 2016, submitted.

5. Van der Westhuizen, I.P., Van Soelen, B. and Meintjes P.J., Modelling the Synchrotron Emission of AGN with Grid-Based Hydrodynamic Simulations. *4rd Annual Conference on High Energy Astrophysics in Southern Africa (HEASA2016), Cape Town, South Africa*, 25 - 26 August 2016, submitted

6. Van der Westhuizen, I.P., Van Soelen, B., Meintjes P.J. and Beall J.H., Hydrodynamics and instabilities of relativistic astrophysical jets in transient outflows in AGN and other accretion driven sources *Proceedings of Frontier Research in Astrophysics, Mondello, Italy*, 23-28 May 2016, submitted.

Numerical modelling of hydrodynamical astrophysical outflows: application using the PLUTO code

I P van der Westhuizen[1], B van Soelen[1], P J Meintjes[1], S J P K Riekert[2] and J H Beall[3]

[1]Department of Physics, University of the Free State, Bloemfontein, 9301, SA
[2]High Performance Cluster, University of the Free State, Bloemfontein, 9301, SA
[3] St. John's Collage, Annapolis, MD, 21401, USA

E-mail: VanDerWesthuizenIP@ufs.ac.za

Abstract. In order to gain a better understanding of how structures form and evolve in astrophysical outflows it is necessary to build a numerical model to simulate the motion of material in these environments. Due to the large length scales of astrophysical outflows compared to the Debye radius of the ejected particles, a fluid dynamical approach provides a suitable model for the large scale motion of the outflow. In this study a 3 dimensional relativistic fluid dynamical model was set up on a structured mesh with dimensions of 64x64x64 units. A uniform ambient medium was defined on the mesh grid and a nozzle of radius 1 was created on the initial z boundary to inject a jet with a Lorentz factor of 10. The opensource magnetohydrodynamical code PLUTO was used to evolve the numerical model with time. The PLUTO code uses high resolution shock capturing schemes to evolve the time dependent partial differential conservation equations on the structured mesh. This model led to the formation of a collimated relativistic beam surrounded by a cocoon of backflow material. Asymmetric turbulence was found, which caused instabilities in the central beam and led to the formation of shocks in the jet. These results are consistent with those seen in previous studies, which were used in order to validate the simulation.

1. Introduction

Observational studies have shown that many astrophysical sources produce collimated outflows of material. Some of these objects include radio loud Active Galactic Nuclei (AGN), accreting binary systems and Young Stellar Objects (YSO) [1]. High resolution imaging of sources such as radio loud AGN have revealed the presence of complex small scale structures in the outflows. These structures include radio blobs which are time dependent and propagate through the outflows at superluminal velocities [2]. The formation and propagation of these time dependent structures may be a cause of variability in sources containing relativistic outflows. The processes which cause the formation of such structures within the relativistic outflows are not well understood and they are often too complex for analytical analysis. In such cases numerical simulations provide a powerful analysis tool to investigate the formation and evolution of these outflows. In this study we focus on AGN jets and their properties, since their structures have been observed over a wide range of the electromagnetic spectrum.

AGN are some of the most energetic objects in the universe and emit large amounts of radiation over a wide range of the electromagnetic spectrum. The non-thermal emission received from radio loud AGN is dominated by the jet component emerging from the central engine [3]. The biggest challenge with creating a numerical model for such sources is the large range of length scales which have to be taken into consideration. This includes the effects of ion interactions in the plasma on atomic length scales as well as the large scale hydrodynamic motion of the plasma, which in the case of AGN jets, can stretch over kiloparsec scales. We can, however, simplify the problem by considering a relativistic jet that has to conserve charge neutrality, which causes the Debye radius of the electrons and protons in the jet to be negligible when compared with the jet radius. This allows us to create an appropriate model using purely relativistic magnetohydrodynamics [4].

In this paper a preliminary relativistic outflow model was created and evolved using the PLUTO opensource code. The initial model was developed to test the computational intensiveness of the simulations on the University of the Free State High Performance Cluster and to validate the base code before incorporating more complex effects into the model. In this paper section 2 will focus on the numerical methods used to create the relativistic outflow model as well as the setup of the simulation, section 3 will give the preliminary results and compare our simulation to previous studies. Finally section 4 contains a short conclusion.

2. Numerical method

The simulation of a relativistic hydrodynamical outflow is created by numerically solving the fluid dynamical conservation equations on a structured mesh grid. We implemented this using the PLUTO *ver.* 4.0 opensource code [5]. The basis of computational fluid dynamics, the PLUTO code and our simulation setup is discussed in the sections below.

2.1. Computational fluid dynamics

The motion of a relativistic fluid can be described by a set of partial differential equations, which are called the hydrodynamical conservation equations and has the following general form

$$\frac{\partial \vec{U}}{\partial t} + \nabla \cdot \vec{\vec{T}}(U) = \vec{\vec{S}}(U), \tag{1}$$

where $\vec{U}$ is a column vector consisting of the conserved variables, $\vec{\vec{T}}(U)$ is a tensor containing the flux vectors as a function of the conserved variables in every direction and $\vec{\vec{S}}(U)$ is a tensor containing the source terms, which are additional terms introduced by effects such as viscosity and gravitational forces [6].

For an ideal relativistic fluid with no magnetic field the variables in equation 1 are described by:

$$\vec{U} = \begin{bmatrix} \rho\Gamma \\ \rho\Gamma^2 h\mathbf{v} \\ \rho\Gamma^2 h - p \end{bmatrix}, \quad \vec{\vec{T}}(U) = \begin{bmatrix} \rho\Gamma\mathbf{v} \\ \rho\Gamma^2 h\mathbf{v}\mathbf{v} + p\mathbf{I} \\ \rho\Gamma^2 h\mathbf{v} \end{bmatrix}, \quad \vec{\vec{S}}(U) = 0, \tag{2}$$

where ρ is the density, p is the pressure, h is the entropy, Γ is the Lorentz factor, $\mathbf{I}$ is a 3x3 unit matrix and $\mathbf{v}$ is the velocity vector.

In order to completely describe a fluid we need an equation of state (EoS), which relates different quantities in the fluid to each other. The EoS may vary from one substance to another, therefore the choice of equation plays an important role in the simulation. For example, the caloric EoS which relates the internal energy to the pressure and density of an ideal fluid is given by

$$e = \frac{p}{\rho(\gamma_{ad} - 1)}, \tag{3}$$

where e is the internal energy of the fluid and $\gamma_{ad} = C_p/C_v$ is the adiabatic index [7]. A complete introduction to computational fluid dynamics is given in [6].

Based on previous studies we chose to characterize the relativistic hydrodynamical simulation based on 5 variables namely, the Lorentz factor Γ, the Mach number M_b, the jet to ambient density ratio η and the adiabatic index γ_{ad}. Using these variables we can recover quantities such as the pressure, the energy and the velocity of the fluid [7].

For example by combining equation (3) with the definition of the sound speed in a fluid ($C_s = \frac{v}{M_b}$) we can solve for the pressure as,

$$p = \frac{(\gamma_{ad} - 1)\rho C_s^2}{\gamma_{ad}(\gamma_{ad} - 1 - C_s^2)}. \tag{4}$$

Therefore, using the proper EoS, all of the properties of the fluid can be calculated.

2.2. PLUTO relativistic magnetohydrodynamics code

To evolve the fluid dynamical simulation the opensource modular relativistic magnetohydrodynamical code PLUTO *ver.* 4.0 was used.[1] The code was specifically designed for supersonic time-dependent flows containing discontinuities, which makes it ideal for the simulation of relativistic astrophysical outflows. PLUTO uses High Resolution Shock Capturing (HRSC) algorithms to solve the fluid dynamic conservation equations and evolve them with time. It contains different modules for hydrodynamic (HD), relativistic hydrodynamic (RHD), magnetohydrodynamic (MHD) and relativistic magnetohydrodynamic (RMHD) models, which allows the code to incorporate different effects based on the conditions of the simulation. The modular nature of the code also allows the addition of effects such as gravity, viscosity and radiative cooling to be incorporated in the calculations [5].

The PLUTO code integrates and evolves equation (1) using three computational steps. The first step is to use interpolation to construct boundary values for each cell on the structured mesh. The interpolation is done based on the centre averaged values that are assigned for each cell. It then solves a Riemann problem to determine the flux vectors across each cell boundary. Finally the code evolves equation (1) with time. The PLUTO code follows these three steps regardless of which physics module is used. The effects of the different physics modules are incorporated by a conversion in the variables of equation (1) before the computational steps [5].

2.3. Simulation setup

For testing and validation purposes a 3 dimensional numerical model of a relativistic hydrodynamical jet was constructed. For this model we considered a Cartesian static mesh grid of $64 \times 64 \times 64$ units. In this simulation arbitrary units were assigned to all variables to avoid truncation errors when working with the extremely large or small values that accompany *cgs* units. In this simulation 1 unit length corresponds to the radius of the jet nozzle at the initial inlet. An initial rest background medium was assigned to the mesh grid at $t = 0$ with a uniform density and pressure. A nozzle containing the jet material was set up on the $z = 0$ boundary. Only RHD was used in this simulation and therefore no magnetic field was assigned. A pressure matched model was set up with the pressure of the material recovered using equation (4). The density of the jet medium was normalized in arbitrary units such that $\Gamma\rho_{jet} = 1$. To validate the simulation we used parameters similar to those of previous studies such as [7] and [9]. These parameters are listed in table 1.

The boundary condition for the $z = 0$ boundary was set to reflective to simulate the production of two symmetric jets on either side of the central engine. All other boundary

[1] The code was implemented by [5] and is available at http://plutocode.ph.unito.it/.

Table 1. Variables used in the set up of the initial conditions for the preliminary RHD jet simulation.

Parameter		Value (arbitrary units)
Lorentz factor	Γ	10
Density ratio	η	10^{-3}
Jet density	ρ_b	0.1
Ambient density	ρ_{am}	100
Mach number	M_b	3.0
Adiabatic index	γ_{ad}	5/3

conditions were set to outflow so that the matter could escape freely. The simulation was run at a resolution of 8 points per unit length. A constant inflow of jet material with $\Gamma = 10$ in the positive z direction was used. The piecewise parabolic interpolation method was used to determine the boundary values of each cell. The Hartman Lax van Leer Riemann solver with contact discontinuity (HLLC) was used to solve the Riemann problem for this model, while the time stepping was done using characteristic tracing [8].

3. Results and Discussion

The proper density, pressure and proper velocity distributions produced by the simulation were visualized as two dimensional slices through the y-axis. Figure 1 shows these slices at three different time steps. From this visualization we can see that the structure of the jet consists mainly of 6 regions. The outer region consists of the uniform unperturbed ambient medium. A terminal bow shock is formed around the body of the jet, produced by the inflow of material that compresses the surrounding ambient medium. As the ambient medium passes through the bow wave its pressure increases forming a shocked region. The high pressure and density of this region causes a discontinuity to form at the surface between the shocked medium and the jet material. This is called the working surface. The speed at which the working surface propagates through the medium determines the propagation speed of the jet.

The centre of the jet consists of the high Lorentz factor ($\Gamma = 10$) material that is flowing through the nozzle into the computational domain. This region will be referred to as the relativistic beam of the jet. As the jet material propagates through the beam of the jet it will reach the working surface at the head of the jet. At this boundary the interaction between the jet and the high pressure ambient material causes the jet material to decelerate, converting the kinetic energy into internal energy. The collision between the lower density jet material and the higher density ambient medium also causes a backflow of material surrounding the beam of the jet. This backflow forms a region of low density material between the jet and the ambient medium which prevents the interaction of jet material with the high pressure ambient medium. This region (called the cocoon) assists in keeping the jet collimated over the propagation distance [9].

The turbulent interaction of material at the head of the jet causes vortices to form in the cocoon. These vortices in the cocoon are further amplified by the formation of Kelvin-Helmholtz instabilities at the surface between the cocoon and the higher pressure ambient medium. Periodic shock waves are also formed in the central beam of the jet. These shocks are generated by perturbations in the boundary between the beam of the jet and the surrounding cocoon, and are the result of a pressure difference between material in the beam and the cocoon along with

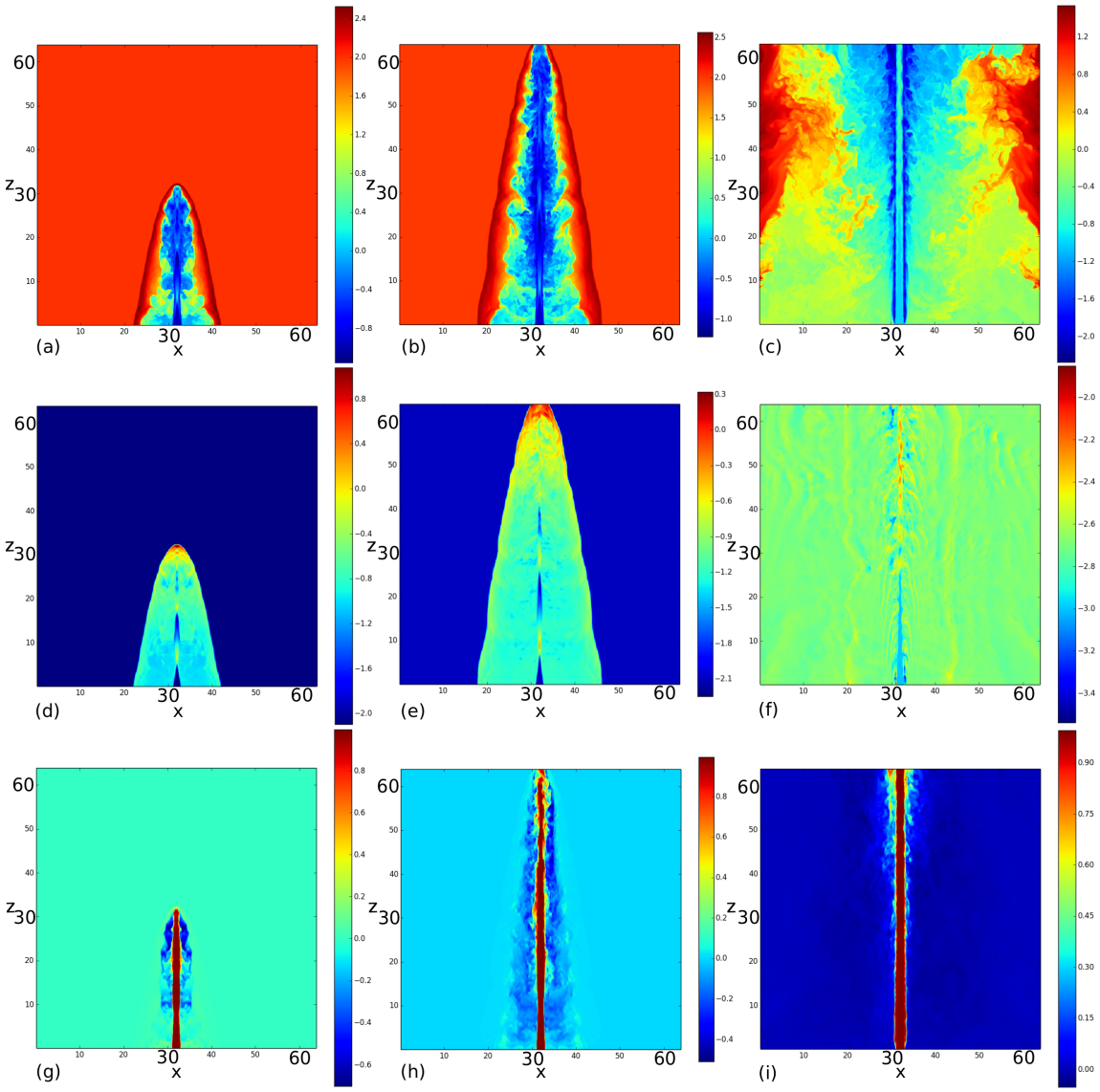

Figure 1. Two dimensional visualizations of the preliminary simulation through the y-axis of the jet, showing the proper density at (a) $t = 100$, (b) $t = 200$, (c) $t = 4300$; the pressure at (d) $t = 100$, (e) $t = 200$, (f) $t = 4300$, and the proper velocity component in the z direction at (g) $t = 100$, (h) $t = 200$, (I) $t = 4300$. Logarithmic scales are shown for the density and pressure plots in arbitrary units, while the velocity plots have a linear scaling in units of c.

the turbulence generated in the cocoon [7].

As the simulation evolves with time the cocoon of the jet expands outwards into the surrounding medium. The turbulence on the surface of the beam grows with time due to the interaction between the cocoon and jet material. This amplifies perturbations in the beam of the jet to form wavelike structures in the flow.

The simulation was run on the UFS HPC on 270 cores with a CPU time of 106098.27 h. This corresponded to 7384.7 units of simulation time. As seen in figure 1 the head of the jet leaves the computational domain at a time of 200 units, which allows for enough time for the formation of a stable jet. The real time necessary to complete the simulation amounted to 405.65 h. The

simulation used a total of 112.8 Gb of memory. Higher resolution of the simulation was sacrificed for a decrease in computational resources. Additional computing power will be necessary when more complex effects such as magnetic fields are included in the simulation.

4. Conclusion

A 3D simulation of a relativistic outflow was created and evolved over time. The simulation shows a collimated central beam with little deceleration surrounded by an outer cocoon. Asymmetric structures formed in the jet, which is in accordance with observations of AGN sources and previous studies. The results shown are comparable to those in [7] and [9]. Small scale differences in the asymmetric turbulence are present in our results when compared to [7]. We attribute these differences in the jet morphology to a difference in the chosen parameters, a difference in grid structure and the fact that the model in that study was based on an axis symmetric two dimensional jet.

More complex effects such as viscosity, magnetic fields and a variable flow can now be incorporated into our model. The next step in our study will be to incorporate variable injection of jet material to investigate the formation of structures corresponding to a non-uniform flow inside the beam of the jet as well as how these structures propagate with time. This fluid dynamical simulation is not limited to the AGN case but can also be adopted for a variety of astrophysical objects such as microquasars, YSO, and X-ray binaries.

Acknowledgments

Acknowledgement is given to the HPC unit at the University of the Free State for their assistance in the installation and set up of software used to run simulations on the UFS HPC.
The financial assistance of the National Research Foundation (NRF) towards this research is hereby acknowledged. Opinions expressed and conclusions arrived at, are those of the author and are not necessarily to be attributed to the NRF.
This work is based on the research supported in part by the National Research Foundation of South Africa for the grant 87919. Any opinion, finding and conclusion or recommendation expressed in this material is that of the authors and the NRF does not accept any liability in this regard.

References

[1] De Gouveia Dal Pino E M 2005 Astrophysical jets and outflows *AdSpR* Issue 5 **35** 908-924
[2] Ghisellini G, Padovani P, Celotti A and Maraschi L 1993 Relativistic bulk motion in active galactic nuclei *ApJ* **407** 65-82
[3] Böttcher M 2011 Modeling the spectral energy distributions and variability of blazars *2011 Fermi & Jansky: Our Evolving Understanding of AGN* (*preprint arXiv:1205.0539*)
[4] Begelman M C, Blandford R D and Rees M J 1984 Theory of extragalactic radio sources *Rev. Mod. Phys.* **56** 255-351
[5] Mignone A, Bodo G, Massaglia S, Matsakos T, Tesileanu O, Zanni C and Ferrari A 2007 PLUTO: a numerical code for computational astrophysics *ApJ* **170** 228-42
[6] Toro E F 2009 *Riemann Solvers and Numerical Methods for Fluid Dynamics: A Practical Introduction Third Edition* (Berlin: Springer) Chapter 1 pp 1-40
[7] Marti J M, Mller E, Font J A, Ibez J M and Marquina 1997 Morphology and dynamics of relativistic jets *ApJ* **479** 151-163
[8] Mignone A and Bodo G 2006 An HLLC Riemann solver for relativistic flows - II. Magnetohydrodynamics *MNRAS* **368** 1040-54
[9] Rossi P, Mignone A, Bodo G, Massaglia S and Ferrari A 2008 Formation of dynamical structures in relativistic jets: the FRI case *A&A* **488** 795-806

PROCEEDINGS OF SCIENCE

Hydrodynamical simulations of relativistic astrophysical jets

I.P. van der Westhuizen*, **B. van Soelen, P.J. Meintjes**
Department of Physics, University of the Free State, Bloemfontein, 9301, South Africa
E-mail: VanDerWesthuizenIP@ufs.ac.za, VanSoelenB@ufs.ac.za, MeintjPJ@ufs.ac.za

The continuous advance in computing technology enables the implementation of more complex analyses in numerical codes, which allows more realistic simulation of astrophysical processes. In this paper the opensource magnetohydrodynamical code PLUTO is used to create a numerical model for an ideal relativistic jet. The presence of relativistic jets have been found in a variety of astrophysical sources such as gamma-ray bursts and radio-loud active galactic nuclei. The PLUTO code includes numerical Riemann solvers which provide solutions to the fluid dynamical partial differential conservation equations on a structured mesh and allows us to evolve the environment with time. Our initial model consists of a 3-dimensional grid containing a uniform background medium. Relativistic material is injected into the grid from the $z = 0$ boundary. The simulation results show the formation of a jet-like structure containing a collimated relativistic central beam surrounded by an outer cocoon of backflow material. Large-scale turbulence was found in the cocoon of the jet which led to the formation of asymmetric structures. The results obtained in the simulation are consistent with those seen in previous studies of ideal relativistic jets and in future models we can now implement more complex effects such as gravity in order to create more realistic models.

3rd Annual Conference on High Energy Astrophysics in Southern Africa -HEASA2015,
18-20 June 2015
University of Johannesburg, Auckland Park, South Africa

*Speaker.

1. Introduction

The presence of relativistic jets has been found in a variety of sources ranging from Mpc scale jets observed in radio-loud Active Galactic Nuclei (AGN) to short-lived gamma-ray bursts. These jets consist of collimated flows of ejected plasma moving at relativistic speeds and carry large amounts of energy and momentum away from their hosts. Particle acceleration and the subsequent cooling inside relativistic jets, through processes such as synchrotron emission and inverse Compton scattering, make them prominent sources of multi-wavelength emission. High resolution radio mapping of AGN jets revealed complex internal structures such as radio knots and blobs propagating through the jet. The emission observed from these structures must have a direct correlation to the physical environment inside the jet and, therefore, understanding the morphology of relativistic jets is vital. Along with this, the mechanisms for energy transport, the formation, and the collimation of relativistic jets over larger distances are not yet fully understood and is still a topic of ongoing research [1].

Due to the complex nature of the processes that occur within relativistic fluids a purely analytical approach will not be able to produce a complete model for a relativistic jet, instead numerical analysis can provide a powerful tool to produce predictions from current theoretical models that one can compare with observational data. Numerical modelling enables the study of relativistic jet morphology by simulating the predicted environment to determine structural formation inside such a jet. Recent studies in this field focussed on jet instabilities, shock propagation in jets and the influence of magnetic fields on the dynamic structure of relativistic jets [2, 3, 4]. In this paper we present an ideal relativistic hydrodynamic jet simulation, which was created in order to test the capabilities of the magnetohydrodynamical code PLUTO for future projects. In Section 2 of this paper the PLUTO code will be discussed further. Section 3 contains the details of the hydrodynamical model while Section 4 will show the initial results that were obtained. Finally we will end with a short conclusion in Section 5.

2. The PLUTO code

PLUTO[1] is an opensource modular relativistic magnetohydrodynamical numerical code specifically designed for the simulation of supersonic time-dependent flows containing discontinuities. The code integrates a set of general conservation equations of the form

$$\frac{\partial \vec{U}}{\partial t} = -\nabla \cdot \vec{\vec{T}}(\vec{U}) + \vec{\vec{S}}(\vec{U}), \tag{2.1}$$

where $\vec{U}$ is a column vector consisting of conserved quantities, $\vec{\vec{T}}(\vec{U})$ is a tensor containing the flux vectors as a function of $\vec{U}$, and $\vec{\vec{S}}(\vec{U})$ is a tensor containing source terms that can be used to introduce effects such as viscosity and gravitational forces [5].

The current iteration of PLUTO supports four different physics modules namely hydrodynamics (HD), relativistic hydrodynamics (RHD), magnetohydrodynamics (MHD) and relativistic magnetohydrodynamics (RMHD) for computation in the different regimes. The different modules incorporate different regimes by changing the components of the conservation vector $\vec{U}$. In

[1] The code was implemented by [5] and is available at http://plutocode.ph.unito.it/.

the RHD module, which is used for this simulation, the constituents of equation (2.1) have the following form

$$\vec{U} = \begin{bmatrix} \rho\Gamma \\ \rho\Gamma^2 h\mathbf{v} \\ \rho\Gamma^2 h - P \end{bmatrix}, \quad \vec{\vec{T}}(\vec{U}) = \begin{bmatrix} \rho\Gamma\mathbf{v} \\ \rho\Gamma^2 h\mathbf{v}\mathbf{v} + P\mathbf{I} \\ \rho\Gamma^2 h\mathbf{v} \end{bmatrix}, \quad \vec{\vec{S}}(\vec{U}) = 0, \tag{2.2}$$

where ρ is the proper density, P is the pressure, h is the specific enthalpy, Γ is the Lorentz factor, $\mathbf{I}$ is a 3x3 unit matrix and $\mathbf{v}$ is the three velocity.

The numerical integration of the conservation equations in PLUTO is done using a High Resolution Shock Capturing (HRSC) algorithm with finite volume formalism [5]. This process follows three general steps: firstly the boundary values for each cell are interpolated based on assigned centre average values; A Riemann problem is then set up using the interpolated boundary values and solved using a numerical Riemann solver and finally the solution to the Riemann problem is evolved with time. For our simulations the HLLC Riemann solver was used together with piecewise parabolic interpolation.

3. Hydrodynamical model

For the initial model we considered a relativistic jet composed of an ideal fluid, that is a fluid which has zero viscosity and thus no internal friction. The fluid dynamical approach provides an appropriate model for simulating the morphology of relativistic jets even though the collisional mean free path of the particles in the jet is very large. This is because the Debye radius of the constituents are much smaller than the radius of the jet [6]. For simplicity, we considered the case where the jet is dominated by the kinetic energy of the ejected material and the magnetic field plays no dynamical role. This allows us to describe the motion of the jet using purely relativistic hydrodynamic conservation laws as described in Equations (2.1) and (2.2).

The model consisted of a 64x64x64 Cartesian mesh grid in which the unit length represents the radius of the injection nozzle. Arbitrary units were used for all quantities in the simulation since the very large or small values of cgs units would lead to additional numerical errors. A uniform stationary background medium was initially assigned to the mesh grid and a circular injection nozzle was created on the $z = 0$ boundary. The injection nozzle was used to inject a steady flow of jet material with a velocity directed along the z-axis. In order to simulate the production of bipolar jets a reflective boundary condition was used for the $z = 0$ boundary. All other boundary conditions were set to outflow, with a zero gradient across the boundary ($\frac{\partial q}{\partial n} = 0$, where q represents the conserved variables and n the direction orthogonal to the boundary), such that matter could escape freely.

Four variables were used in order to describe the model; the Lorentz factor Γ, the Mach number M_b, the jet to ambient density ratio η and the adiabatic index γ_{ad}. All other jet properties, such as the pressure, the energy and the velocity of the fluid, can be determined from the above mentioned variables [7]. For example the pressure of the system can be solved by combining the ideal caloric equation of state,

$$e = \frac{P}{\rho(\gamma_{ad} - 1)}, \tag{3.1}$$

Parameter		Value (arbitrary units)
Lorentz factor	Γ	10
Velocity	v	$0.995c$
Density ratio	η	10^{-3}
Jet density	ρ_b	0.1
Ambient density	ρ_{am}	100
Mach number	M_b	7.8
Adiabatic index	γ_{ad}	$5/3$
Pressure	P	0.001

Table 1: Parameters used in the set up of the initial conditions.

where e is the internal energy of the fluid, with the definition of the sound speed ($C_s = v/M_b$) in a fluid, yielding

$$P = \frac{(\gamma_{ad}-1)\rho C_s^2}{\gamma_{ad}(\gamma_{ad}-1-C_s^2)}. \tag{3.2}$$

The parameters used for the relativistic jet model are given in Table 1 along with the calculated primary quantities. These parameters were chosen to be similar to previous studies such as [4, 7, 8]. For our model the density of the injected material was normalized to $\rho = 1$ in the observer frame and hence a proper density of $\rho = 0.1$ was used in the co-moving reference frame. A uniform pressure was used between the background and jet material in accordance with the model presented in [6].

4. Results

The simulation described in the previous section was run with two different resolution configurations. For the first case a static resolution of 8 points per unit length was used. Adaptive Mesh Refinement (AMR) was used for the second case, amounting to an equivalent resolution of 16 points per unit length. The AMR dynamically changes the amount of computational cells on the mesh grid depending on the boundary values of adjacent cells in order decrease the computational intensiveness of the simulation. The AMR does this in a way that allows low resolution for regions with minimal activity and high resolution for active regions where more detail is necessary.

Figure 1 shows a 3-dimensional rendering of the injected material at $t = 150$ in arbitrary units for the static grid case. The figure shows a collimated central region, containing only injected material, propagating through the grid. This region is considered as the central beam of the jet model. The central beam of the jet is surrounded by an outer cocoon region containing diluted jet material mixing with the ambient medium.

In order to investigate the morphology of the jet model in detail, 2-dimensional slices through the origin were plotted of the proper density, the pressure and the velocity component in the z direction. The results at different time steps are displayed in Figures 2 and 3 for the static grid and AMR simulations respectively. The figures show that the injection of material at the base of the

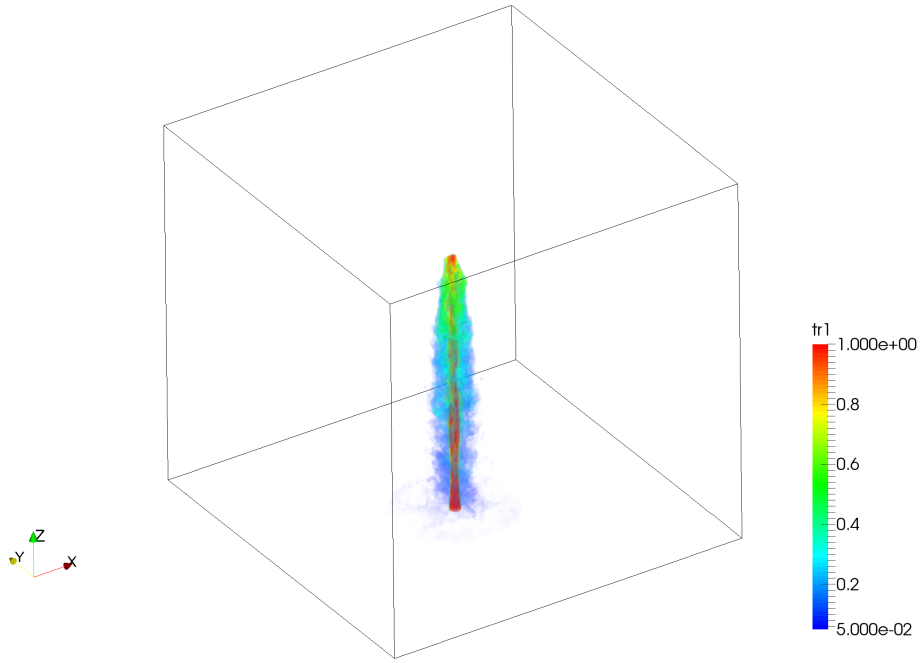

Figure 1: A 3-dimensional rendering showing the trace of the injected material at time t=150.

z-axis causes a terminal bow shock to form and propagate through the ambient medium. Initially this bow wave appears symmetric due to the uniform nature of the background medium. However, at later stages asymmetry develops as a result of the turbulence inside the cocoon of the jet. As the bow shock propagates through the background medium it compresses the material to form a region of higher pressure between the jet material and the bow wave.

At the front of the jet on the surface between the high density shocked background medium and the low density injected jet material a contact discontinuity, called the working surface, is formed [7]. At the working surface the interaction between the background medium and the jet material converts the kinetic energy of the injected material into internal energy. This interaction also drives a turbulent backflow of material around the central beam of the jet. The backflow material forms the cocoon layer between the shocked background medium and the central beam of the jet.The higher pressure of the shocked ambient medium and the cocoon helps to keep the central beam collimated throughout the simulation [9]. This pressure mismatch between the cocoon of the jet and the injected material also causes periodic shock waves to form inside the central beam of the jet. No large-scale instabilities formed inside the beam of the jet in either of the simulations and the injected material remains well collimated throughout the entire simulation, even at very large timescales such as $t = 4300$ when the working surface has left the computational domain. Our simulation showed little deceleration of the material in the central beam since the interaction of the injected material and the background medium is limited by the surrounding cocoon [7]. At larger timescales ($t = 4300$) a thin shear layer forms between the cocoon and the relativistic jet. This layer contains material moving in the positive z-direction at sub relativistic speeds $v \approx 0.30c$.

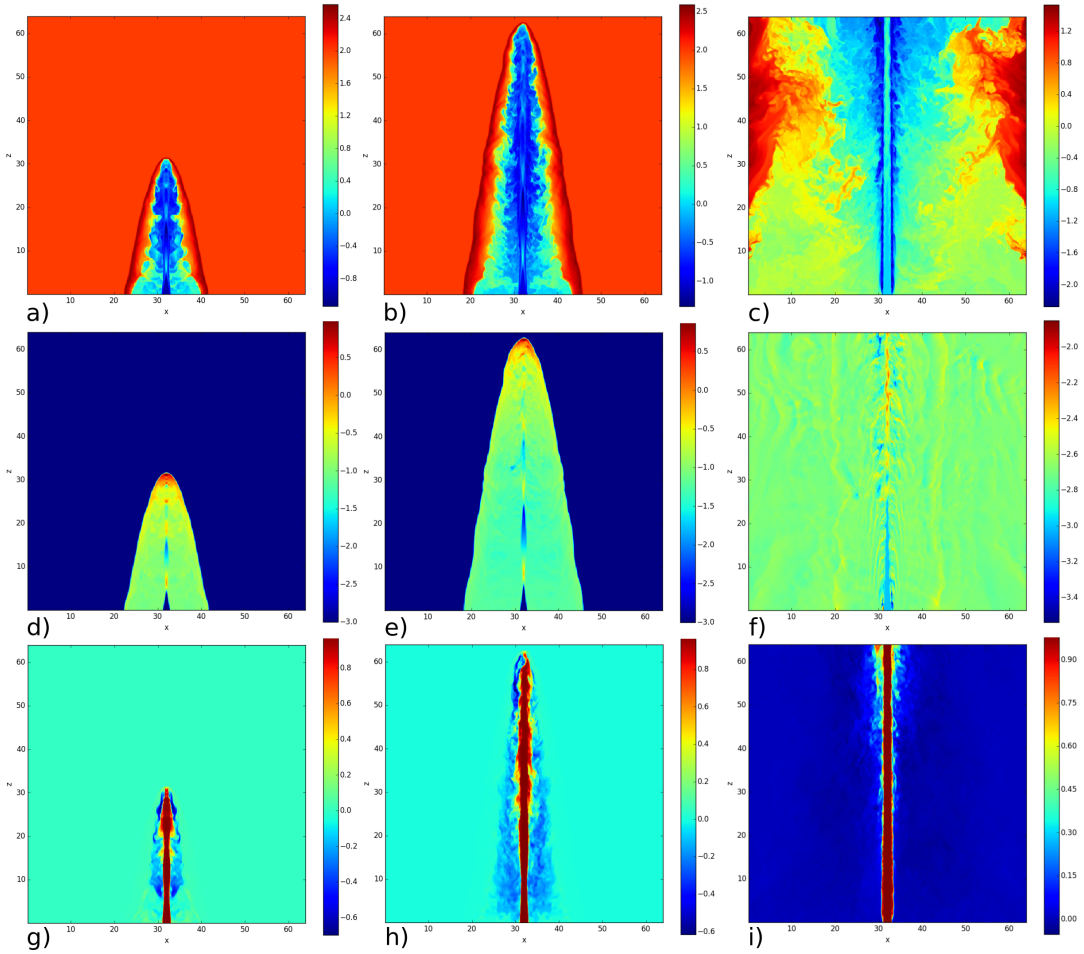

Figure 2: Two-dimensional slices of the static grid simulation, with 8 points per beam width resolution, showing the proper density at (a) $t = 100$, (b) $t = 200$, (c) $t = 4300$; the pressure at (d) $t = 100$, (e) $t = 200$, (f) $t = 4300$, and the proper velocity component in the z direction at (g) $t = 100$, (h) $t = 200$, (i) $t = 4300$. Logarithmic scales are shown for the density and pressure plots in arbitrary units, while the velocity plots have a linear scaling in units of c.

Comparing the results in Figure 2 to those of Figure 3 it was found that the AMR simulation yielded a similar morphology to that of the static grid. The AMR simulation however shows a difference in the asymmetry which we attribute to the higher equivalent resolution.

5. Discussion and conclusion

A 3-dimensional model for an ideal relativistic jet was set up and evolved with time using the PLUTO magnetohydrodynamical code. The results obtained from this simulation showed the formation of a relativistic collimated central beam with little deceleration surrounded by a cocoon of backflowing material caused by the interaction of injected material and the background medium at the working surface. The formation of these structures were consistent to the morphology shown by previous authors. Some minor differences were found when compared to the previous studies

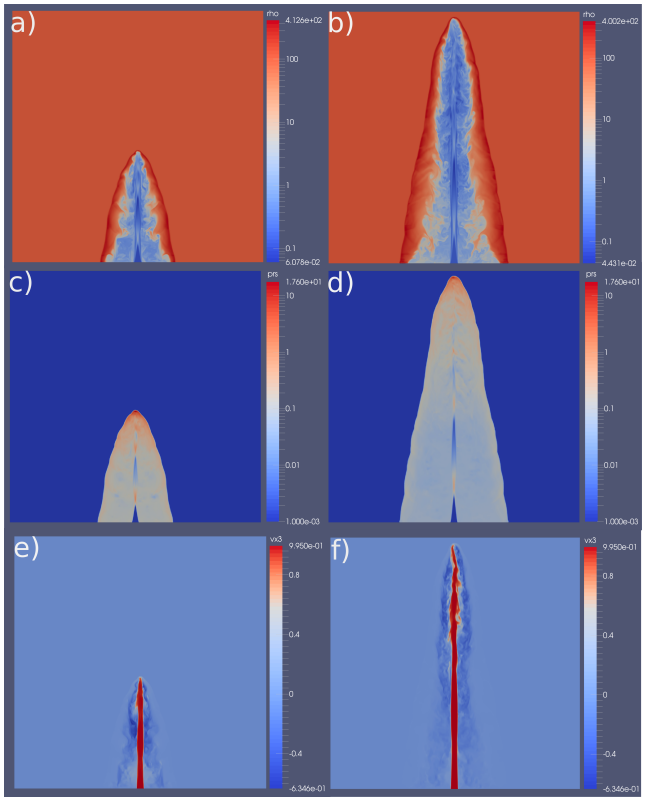

Figure 3: Two-dimensional slices of the AMR simulation, with a 16 points per beam width equivalent resolution, showing the proper density at (a) $t = 100$, (b) $t = 200$; the pressure at (c) $t = 100$, (d) $t = 200$, and the proper velocity component in the z direction at (e) $t = 100$, (f) $t = 200$. Logarithmic scales are shown for the density and pressure plots in arbitrary units, while the velocity plots have a linear scaling in units of c.

in the formation of asymmetric turbulence which we attribute to variations in the model setup that was used.

Our future aim is to incorporate more complex effects into this model, that would be present in real relativistic jets, such as gravity, viscosity and magnetic fields. We intend on constructing an emission model which can be used to compared simulated emission to observational data to investigate the effects of variable flow rates, blob production and collision, and a non-uniform background on the emission.

Acknowledgments

Acknowledgement is given to the High Performance Cluster (HPC) unit at the University of the Free State for their assistance in the installation and set up of software used to run simulations on the UFS HPC.

The financial assistance of the National Research Foundation (NRF) towards this research is hereby acknowledged. Opinions expressed and conclusions arrived at, are those of the author and are not necessarily to be attributed to the NRF.

This work is based on the research supported in part by the National Research Foundation of South Africa for the grant 87919. Any opinion, finding and conclusion or recommendation expressed in this material is that of the authors and the NRF does not accept any liability in this regard.

References

[1] Böttcher M, Harris D E and Krawczynski H, *Introduction and Historical Perspective; in Relativistic Jets from Active Galactic Nuclei (eds M. Böttcher, D. E. Harris and H. Krawczynski)*, Wiley-VCH Verlag GmbH & Co. KGaA, **chap 1, pp 1-16** Weinheim, Germany, 2012.

[2] Mignone A, Rossi P, Bodo G, Ferrari A, Massaglia S *High-resolution 3D relativistic MHD simulations of jets MNRAS* **402**, 7-12, 2010.

[3] Mimica P, Aloy M A, Müller E *Internal shocks in relativistic outflows: collisions of magnetized shells A& A* **466** 93-106, 2007.

[4] Rossi P, Mignone A, Bodo G, Massaglia S and Ferrari A *Formation of dynamical structures in relativistic jets: the FRI case A&A* **488** 795-806, 2008.

[5] Mignone A, Bodo G, Massaglia S, Matsakos T, Tesileanu O, Zanni C and Ferrari A *PLUTO: a numerical code for computational astrophysics ApJ* **170** 228-42, 2007.

[6] Blandford R D, Rees M F, *A twin-exhaust model for double radio sources*, *MNRAS* **169**, 395-415, 1974.

[7] Marti J M, Müller E, Font J A, Ibáñez J M and Marquina *Morphology and dynamics of relativistic jets ApJ* **479** 151-163, 1997.

[8] Aloy M A, Ibáñez J M, Marti J M, Gómez J L, and Müller E *High-resolution three-dimensional simulations of relativistic jets ApJ* **523**, 125-128, 1999.

[9] Begelman M C, Blandford R D and Rees M J *Theory of extragalactic radio sources Rev. Mod. Phys.* **56**, 255-351, 1984.

PROCEEDINGS OF SCIENCE

Hydrodynamics and instabilities of relativistic astrophysical jets in transient outflows in AGN and other accretion driven sources

I.P. van der Westhuizen*, **B. van Soelen, P.J. Meintjes**
Department of Physics, University of the Free State, 9301, RSA
vanderwesthuizenip@ufs.ac.za

J.H. Beall

St. John's College, Annapolis, MD, 21401, USA

Active galactic nuclei (AGN) show variability over both intra day and longer time scales. This characteristic has been the topic of many recent studies especially the investigation of correlation between multi-wavelength components. The variability can be investigated through numerical hydrodynamics. In this study an ideal relativistic hydrodynamic jet was simulated in order to investigate the instabilities which form in the jet as a source of variability in AGN. A synchrotron delta-approximation model was applied to the hydrodynamical environment in order to obtain an estimate of the intensity emitted at an example frequency of 15 GHz. This frequency was chosen such that the estimated intensity maps could be comparable to the MOJAVE survey. The tools used in such a hydrodynamic model can be applied to other transient sources such as X-ray binaries which have been shown to produce jet-like components.

Frontier Research in Astrophysics - II
23-28 May 2016
Mondello (Palermo), Italy

*Speaker.

1. Introduction

Radio observations of Active Galactic Nuclei (AGN) have shown that many of these sources produce extended radio emission associated with relativistic jet-like outflows. These radio jet-like structures consist of a narrow beam of material being ejected from the nucleus of the host galaxy, which can extend up to megaparsec scale distances. Radio loud AGN containing relativistic jets produce emission over a large range of the electromagnetic spectrum and the spectral energy distribution of such sources have a characteristic double bump structure. The emission in the lower bump is mainly produced through synchrotron radiation of relativistic electrons spiralling in the magnetic field of the jet, while the high energy component may be due to a mixture of inverse-Compton scattering of the synchrotron radiation, as well as external photons and hadronic processes [1].

The emission characteristics of AGN make them ideal targets for multi-wavelength studies. High resolution radio observations, conducted by the VLBI, revealed that relativistic jets have complex internal structures and long term radio monitoring programs such as the MOJAVE (15 Ghz frequency band) [2, 3] and RRFID (8 and 2 GHz bands) surveys [4] have been undertaken to study the time dependent nature of the morphology of the jets. These studies have shown the presence of stationary as well as superluminal emission components travelling at apparent velocities in the order of $15c$, time dependent jet bending and changes in the injection angle of the jet (see e.g. [3]).

To investigate the morphology and instabilities that form inside these jets the macroscopic flow of such systems can be modelled by fluid dynamics. The complex nature of such a dynamic environment means that we will not be able to obtain an analytical solution, instead we turn to numerical methods in order to create an appropriate model of the system. Previous studies in the field of numerically modelling relativistic jets have investigated jet instabilities, shock propagation in jets and the influence of magnetic fields on the dynamic structure of the system [5, 6, 7]. In order to compare a numeric fluid dynamical simulation to observational data we have to calculate the emission based on an emission model. This model calculates the radiation that would be produced in the environment based on physical properties such as the energy and particle density in the system (see e.g. [8]).

In this paper we present a numeric fluid dynamical simulation containing an ideal relativistic jet propagating through a uniform ambient medium. The simulation was designed and evolved with time using the grid based numerical hydrodynamical code PLUTO [9]. This simulation is done under the assumption that the energy in the jet is kinetically dominated with the magnetic field having negligible effects on the dynamic morphology of the jet. An emission model, in the form of a post-processing code, was applied to the simulation to generate approximate intensity maps of the synchrotron radiation produced by the environment. The synchrotron radiation was calculated at 15 GHz. This was done in order to compare the emission structures that have been observed in radio observations of the MOJAVE survey to those generated by the fluid dynamical simulation. Further details of the numeric fluid dynamical simulation are given in section 2 while the calculation of the intensity maps is discussed in section 3. Section 4 contains our results followed by a conclusion in section 5.

Parameter		Value (arbitrary units)
Lorentz factor	Γ	10
Velocity	v	$0.995c$
Density ratio	η	10^{-5}
Jet density	ρ_b	0.1
Ambient density	ρ_{am}	100
Mach number	M_b	7.8
Adiabatic index	γ_{ad}	$5/3$
Pressure	P	0.001

Table 1: Parameters used in the set up of the initial conditions.

2. Numeric fluid dynamical model

Grid based numeric fluid dynamical simulations consist of a set of defined cells in a mesh grid with assigned properties, such as density, velocity and energy, that adhere to the fluid dynamical conservation laws. The properties of each cell can be evolved with time according to a set of partial differential conservation equations in the form of,

$$\frac{\partial \vec{U}}{\partial t} = -\nabla \cdot \vec{\vec{T}}(\vec{U}) + \vec{\vec{S}}(\vec{U}), \tag{2.1}$$

where $\vec{U}$ is a vector containing the conserved properties, $\vec{\vec{T}}(\vec{U})$ is a tensor containing flux vectors calculated between adjacent cells, as a function of $\vec{U}$, and $\vec{\vec{S}}(\vec{U})$ comprises of source terms that account for effects such as gravity, the viscosity and resistivity of the fluid [10].

The numerical model presented in this paper was set up in the relativistic hydrodynamic (RHD) regime with no source terms to simulate the production of an ideal relativistic fluid jet with no viscosity. The components of equation (2.1) in the RHD regime can be given as,

$$\vec{U} = \begin{bmatrix} \rho\Gamma \\ \rho\Gamma^2 h\mathbf{v} \\ \rho\Gamma^2 h - P \end{bmatrix}, \quad \vec{\vec{T}}(\vec{U}) = \begin{bmatrix} \rho\Gamma\mathbf{v} \\ \rho\Gamma^2 h\mathbf{v}\mathbf{v} + P\mathbf{I} \\ \rho\Gamma^2 h\mathbf{v} \end{bmatrix}, \quad \vec{\vec{S}}(\vec{U}) = 0, \tag{2.2}$$

where ρ is the mass density in the co-moving frame, P is the pressure, h is the specific enthalpy, Γ is the bulk-flow Lorentz factor, $\mathbf{I}$ is a 3x3 unit matrix and $\mathbf{v}$ is the three velocity [9].

The simulation was set-up on a Cartesian mesh grid consisting of $64 \times 64 \times 128$ length units with a resolution of 4 points per unit length, resulting in $256 \times 256 \times 512$ computational cells. A uniform background medium was assigned to the grid with the initial z boundary set up to inject jet material through a nozzle of radius 1 into the environment. The less dense jet material was injected at a constant rate with a Lorentz factor $\Gamma = 10$. All other boundary conditions were set-up as outflow. The properties assigned to the ambient and jet material are listed in table 1. All units listed in table 1 are arbitrary except for the velocity which is given in units of the speed of light c in order to apply the Lorentz transformations correctly between adjacent cells in the simulation. A

pressure matched jet model was used for the simulation to ensure that the jet remained collimated at the injection site.

The numerical simulation was set-up and evolved with time using the open-source code PLUTO *ver*4.2 [9]. The code uses upwind high resolution shock capturing algorithms to solve the conservation equations and evolve them with time. The set-up used piecewise parabolic interpolation, to determine the flux functions between cells, the HLLC Riemann solver and characteristic time stepping to evolve the properties of each cell with time [11]. The simulation was run until the head of the jet material reached the edge of the computational domain.

3. Artificial intensity maps

To construct artificial synchrotron intensity maps of the three dimensional simulation we first determined the radiation that will be emitted and absorbed by each cell. This was done by calculating the synchrotron emission and absorption coefficients based on the properties of the cell. In order to produce two dimensional intensity plots of the synchrotron radiation in the jet, the coefficients can be used to calculate the change in intensity through each cell along a line of sight s. The change in intensity (in the co-moving reference frame) can be given as,

$$\frac{dI_\nu}{ds} = j_\nu^{sy} - \alpha_\nu^{sy} I_\nu, \tag{3.1}$$

where the superscript "*sy*" indicates that the coefficients are calculated for synchrotron radiation [12].

The emission coefficient produced by synchrotron radiation is calculated by integrating the power radiated by a single radiating particle, $P_\nu(\gamma)$, over the particle spectrum $n(\gamma)$ of the medium [12],

$$j_\nu^{sy} = \frac{1}{4\pi}\int n(\gamma) P_\nu(\gamma) \mathrm{d}\gamma. \tag{3.2}$$

Integrating the full expression for the radiative power of each cell in the computational domain can be very computationally intensive and to compensate for this the synchrotron radiative power was approximated using an analytical δ-function model [12]. The δ-function approximates the synchrotron power emitted by a particle of energy γ assuming that the particle only radiates at a critical frequency ν_c, given by,

$$\nu_c = \frac{3qB}{4\pi mc}\gamma^2. \tag{3.3}$$

The expression for the radiative power of the δ-function approximation is given by,

$$P_\nu(\gamma) = \frac{32\pi}{9}\left(\frac{q^2}{mc^2}\right)^2 u_B \beta^2 \gamma^2 \delta(\nu - \nu_c), \tag{3.4}$$

where q is the charge of the radiating particle, m is the mass of the radiating particle, c is the speed of light, u_B is the magnetic field energy density and ν is the frequency of emission in the co-moving frame [12].

In our calculation we assumed that the dominant radiative particles in the jet consisted of non-thermal electrons with a power-law particle distribution given by,

$$n(\gamma) = n_0 \gamma^{-p}, \tag{3.5}$$

where the normalization factor, n_0, is determined by [13]

$$n_0 = \left(\frac{e(p-2)}{1-C_E^{2-p}}\right)^{p-1}\left(\frac{1-C_E^{1-p}}{\frac{\rho}{m_p}(p-1)}\right)^{p-2}. \tag{3.6}$$

Here m_p is the mass of a proton, p is the power-law index, e is the internal energy density and C_E is the ratio of the maximum and minimum energies. For our initial estimates we chose $p = 1.8$ and $C_E = 10^3$. The internal energy density of the system can be calculated using the caloric equation of state [14],

$$e = \frac{P}{\rho(\gamma_{\text{ad}} - 1)}, \tag{3.7}$$

in which γ_{ad} is the adiabatic index of the fluid. The magnetic field energy density is assumed to be an equipartition fraction of the internal energy density calculated as,

$$u_B = \varepsilon_B e \tag{3.8}$$

where $\varepsilon_B = 10^{-3}$ was used based on values given by [15].

Combining the previous expressions (3.3-3.7) and integrating equation (3.2) we obtain an expression for the emissivity,

$$j_\nu^{sy} = \frac{4}{9}\left(\frac{q^2}{mc^2}\right)^2 u_B \nu^{\frac{1}{2}} \nu_0^{\frac{-3}{2}} n\left(\sqrt{\frac{\nu}{\nu_0}}\right), \tag{3.9}$$

where,

$$\nu_0 = \frac{3qB}{4\pi mc}. \tag{3.10}$$

A similar analysis was applied to the absorption coefficient, where the absorption coefficient was calculated as,

$$\alpha_\nu^{sy} = -\frac{1}{8\pi m\nu^2}\int P_\nu(\gamma)\gamma^2 \frac{\partial}{\partial\gamma}\left(\frac{n(\gamma)}{\gamma^2}\right)\mathrm{d}\gamma, \tag{3.11}$$

which leads to the expression,

$$\alpha_\nu^{sy} = \frac{2}{9}\frac{p+2}{m\nu^2}\left(\frac{q^2}{mc^2}\right)^2 u_B \nu_0^{-1} n\left(\sqrt{\frac{\nu}{\nu_0}}\right). \tag{3.12}$$

A detailed description of this derivation can be found in [12].

Before the coefficients are used to calculate the two dimensional intensity map, Lorentz transformations must be applied to move from the co-moving to the stationary reference frame of the galaxy. This effect is due to the relativistic velocity of the bulk flow in the simulation. The synchrotron coefficients of each cell transform as,

$$j_\nu^{sy} = \frac{j_{\nu'}^{sy\prime}}{(\Gamma[1-\beta\mu])^2}, \tag{3.13}$$

$$\alpha_\nu^{sy} = \alpha_{\nu'}^{sy\prime}(\Gamma[1-\beta\mu]) \tag{3.14}$$

where the primed terms indicate quantities calculated in the co-moving reference frame, the unprimed quantities are in the galactic stationary frame, and μ is the cosine of the angle between

the observer and the velocity of the fluid in the galactic stationary frame [12]. For our initial calculations additional effects such as the light travel time and the expansion of the universe were neglected.

The two dimensional intensity maps were computed using a post-processing code written in the Python programming language. In this code the user can arbitrarily set the line of sight s for integration as well as the frequency of the intensity maps in the stationary frame. The frequency set by the user in the stationary frame is transformed to the co-moving frame of each cell in the code before the coefficients are calculated. The intensity is then integrated along the set line of sight to create a two dimensional intensity map.

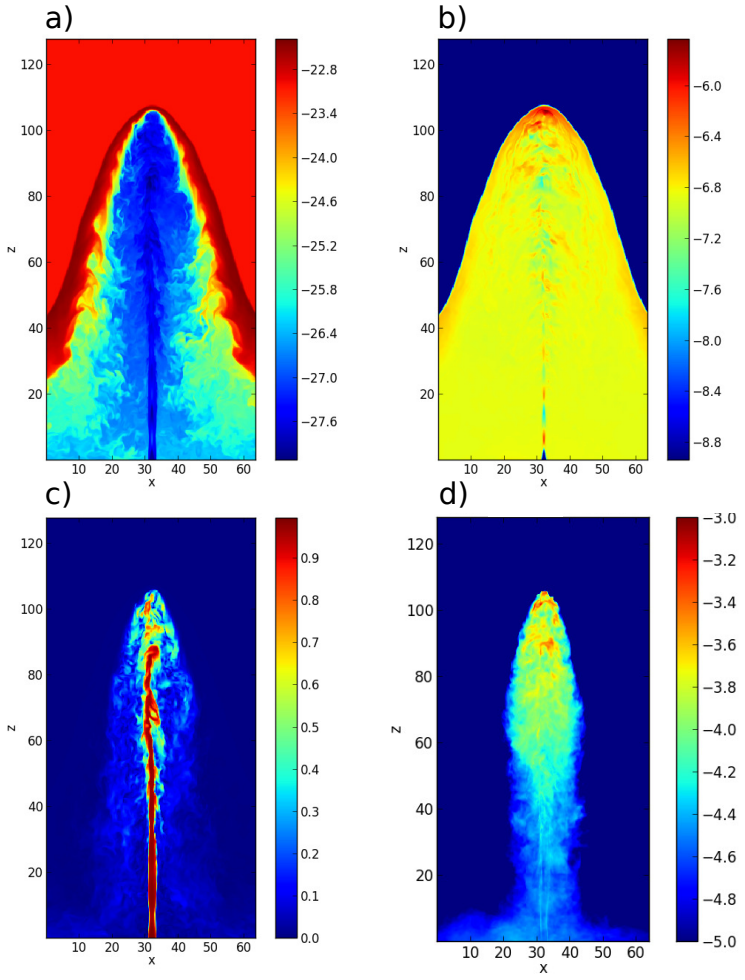

Figure 1: Visualization of the simulation results showing a) the density slice through the xz-plane of the jet b) the pressure slice through the xz-plane of the jet, c) the velocity magnitude slice through the xz-plane of the jet and d) the calculated intensity map at 15 GHz. Logarithmic scales are shown for the density and pressure plots in arbitrary units, while the velocity plots have a linear scaling in units of c. The intensity map is map is scaled as the logarithm of arbitrary units.

4. Results

The numerical simulation was run with the set-up and parameters as discussed in section 2. Figure 1 illustrates plots of xz-slices containing the density, pressure and velocity magnitude distributions for the environment, as well as the corresponding calculated intensity map, calculated at the 15 GHz frequency, for the same time step.

We note the formation of 5 distinct regions within these plots of the simulation. Firstly the outer uniform region consists of the background material initially assigned to the cells. As jet material is injected into the environment, at supersonic speeds through the nozzle on the initial z boundary, it compresses the background material and forms a terminal bow shock surrounding the body of the jet. This terminal bow shock propagates through the ambient medium forming a region of turbulent high pressure material. In the central region we obtain a relativistic beam of jet material. Close to the injection site this beam is very stable, highly collimated and shows little deceleration (as shown in figure 1(c)). Instabilities grow larger as the distance from the injection site increases creating bends in the beam at 40 length units and breaking apart the beam at a distance of 85 units.

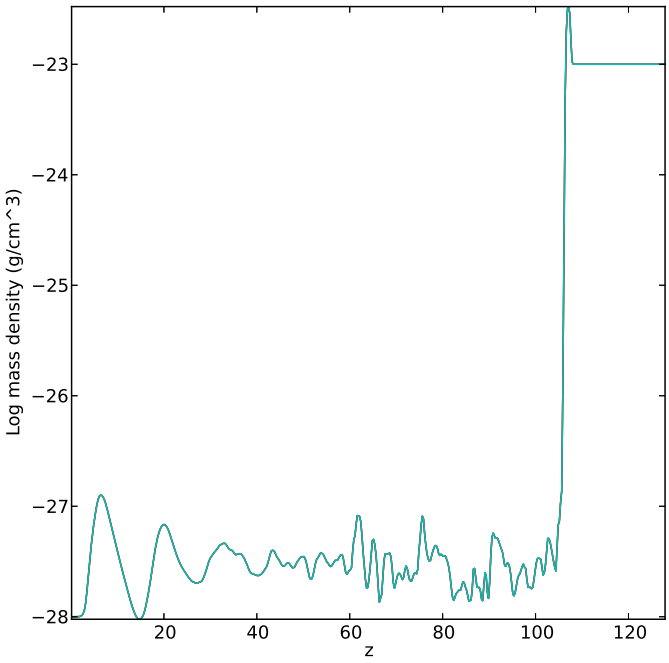

Figure 2: One dimensional plot of the density through the central beam.

At the head of the beam, the region between the jet and the high pressure shocked material forms a shock front, referred to as the working surface. At this surface the remaining kinetic energy of the injected jet medium is converted into internal energy which creates a hot spot of emission on the intensity map in figure 1(d). This interaction at the working surface also drives a backflow

of material, which forms a cocoon around the central beam and limits further interaction between the jet and background medium. This cocoon assists in the collimation of the beam and prevents further deceleration of the jet material [14].

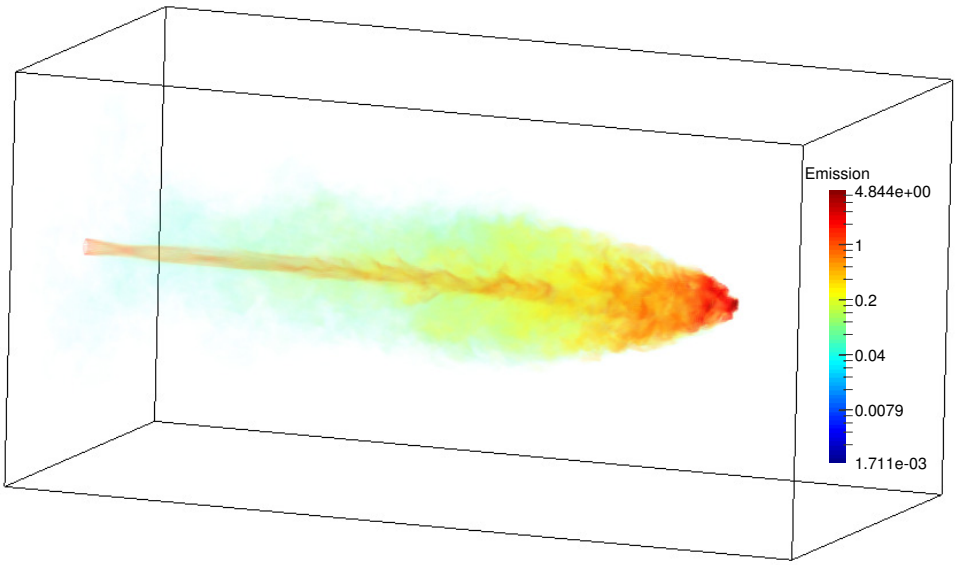

Figure 3: Three dimensional rendering of the emission coefficient of the jet material.

Plotting the density along the center of the beam in the z-direction (as shown in figure 2) we note the occurrence of harmonic oscillations in these properties close to the injection nozzle. These oscillations form stationary shock fronts in the beam, called re-collimation shocks, and are caused by the over-pressured shocked medium acting on the beam. This is also illustrated in figure 1(b). As the material propagates further from the injection site these shocks are damped and the beam becomes more unstable. At a distance of 40 length units the beam transitions from being re-collimation shock dominated to a turbulent regime. Figure 2 also shows the working surface at a distance of 105 units.

To determine what effect these structures have on the synchrotron radiation the emission and absorption coefficients were calculated according to equations (3.9) and (3.12) for a frequency of 15 GHz. This frequency was selected based on the MOJAVE survey such that the structures in the artificial intensity maps could be compared to observational data at a later stage. Figure 3 shows a 3 dimensional rendering of the trace of injected jet material with the colour indicating the emission coefficient.

This rendering shows that the emission close to the injection nozzle is dominated by the beam of the jet with the presence of faintly emitting material in the cocoon. As the distance from the injection site increases we note that the cocoon becomes the dominant emission region forming a lobe type structure at the head of the jet. Hotspots can be seen on the head of the cocoon due to the

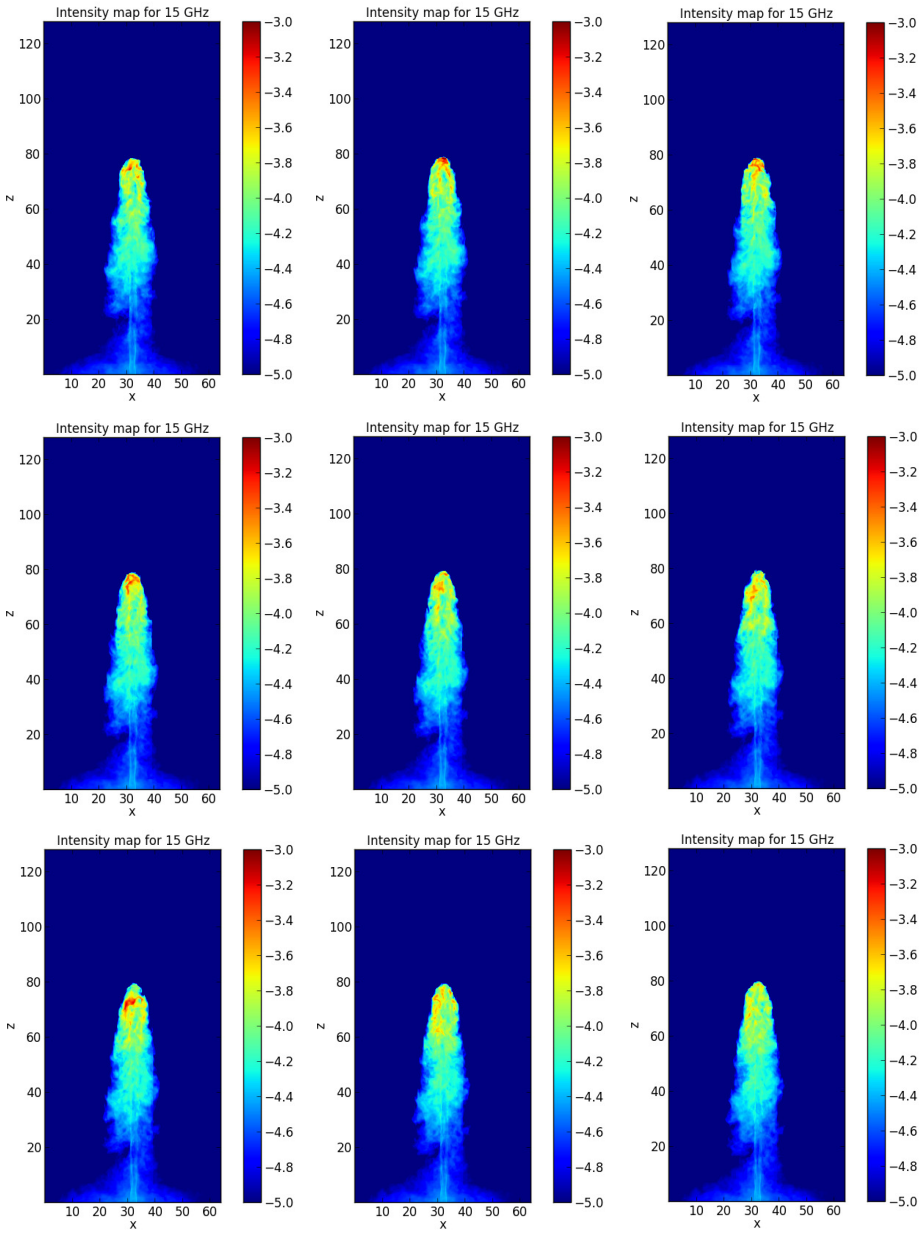

Figure 4: Intensity maps calculated at 15 GHz for sequential time steps

conversion of energy by the working surface.

To calculate intensity maps we considered a jet propagating perpendicular with respect to an observer. Figure 4 shows the variation in emission and hot spot regions in sequential time steps. These results show that even though a constant injection rate was applied to the jet material variability can occur in the intensity maps. This variability is attributed to the occurrence of turbulence in the beam at large distances from the injection nozzle.

5. Conclusion

In this paper we were able to recreate an ideal relativistic jet environment using the PLUTO hydrodynamic code. The results show the formation of a collimated relativistic beam with little deceleration surrounded by a cocoon region of backflowing material. These results are in accordance with previous studies such as [7, 14].

The results show that the internal structure of the beam is initially dominated by re-collimation shocks but transitions to a turbulent regime further from the injection site. Estimates of the synchrotron emission generated by such a jet has shown large scale similarities to FRII type radio galaxy structures with a relativistic beam, a lobe structures at the head of the jet as well as hot spots on the lobes.

In order to make an accurate quantitative comparison between the simulation results and observational data more complex effects must be taken into account. These include effects such as gravity and viscosity in the fluid dynamical simulations, the cosmological expansion, time of arrival effects as well as a change in the particle spectrum within the jet.

Simulations such as the one presented in this paper are not limited to sources such as AGN. Many other sources such as microquasars and γ-ray bursts (GRB) have been associated with the production of jets and the resulting synchrotron radiation.

Acknowledgments

Acknowledgement is given to the HPC unit at the University of the Free State for their assistance in the installation and set up of software used to run simulations on the UFS HPC.
The financial assistance of the National Research Foundation (NRF) towards this research is hereby acknowledged. Opinions expressed and conclusions arrived at, are those of the author and are not necessarily to be attributed to the NRF. This work is based on the research supported in part by the National Research Foundation of South Africa for the grant 87919. Any opinion, finding and conclusion or recommendation expressed in this material is that of the authors and the NRF does not accept any liability in this regard.

References

[1] M. Böttcher *Modeling the spectral energy distributions and variability of blazars*, *2011 Fermi & Jansky: Our Evolving Understanding of AGN* (preprint arXiv:1205.0539) 2011.

[2] M. L. Lister *et al. MOJAVE: Monitoring of jets in active galactic nuclei with VLBA experiments. V. Multi-epoch VLBA images*, *ApJ* **137** , 3718-3729, 2009.

[3] K.I. Kellermann, *et al. Sub-Milliarcsecond Imaging of Quasars and Active Galactic Nuclei. III. Kinematics of Parsec-scale Radio Jets*, *ApJ* **609**, 539-563, 2004.

[4] B. G. Piner, M. Mahmud, A. L. Fey, and K. Gospodinov *Relativistic jets in The Radio Reference Frame Image Database I: Apparent speeds from the first five years of data*, *ApJ* **133**, 2357-2388, 2007.

[5] A. Mignone, P. Rossi, G. Bodo, A. Ferrari, S. Massaglia *High-resolution 3D relativistic MHD simulations of jets*, *MNRAS* **402**, 7-12, 2010.

[6] P. Mimica, M. A. Aloy, E. Müller *Internal shocks in relativistic outflows: collisions of magnetized shells*, *A& A* **466** 93-106, 2007.

[7] P. Rossi, A. Mignone, G. Bodo, S. Massaglia and A. Ferrari *Formation of dynamical structures in relativistic jets: the FRI case*, *A&A* **488**, 795-806, 2008.

[8] P. Mimica, M. A. Aloy, I. Agudo, J. M. Marti, J. L. Gómez, J. A. Miralles *Spectral evolution of superluminal components in parsec-scale jets*, *ApJ* **696**, 1142-1163, 2009.

[9] A. Mignone, G. Bodo, S. Massaglia, T. Matsakos, O. Tesileanu, C. Zanni and A. Ferrari *PLUTO: a numerical code for computational astrophysics*, *ApJ* **170**, 228-42, 2007.

[10] E. F. Toro *Riemann Solvers and Numerical Methods for Fluid Dynamics: A Practical Introduction Third Edition*, Springer, Berlin, Chapter 1, pp 1-40, 2009.

[11] A. Mignone and G. Bodo *An HLLC Riemann solver for relativistic flows - II. Magnetohydrodynamics*, *MNRAS* **368**, 1040-1054, 2006.

[12] M. Böttcher, D. E. Harris and H. Krawczynski *Relativistic Jets from Active Galactic Nuclei*, Wiley-VCH Verlag GmbH & Co. KGaA, Weinheim, Germany, Chapter 3, pp 39-80, 2012.

[13] J. L. Gomez, J. M. Marti, A. P. Marscher, J. M. Ibáñez and J. M. Marcaide *Parsec-scale synchrotron emission from hydrodynamic relativistic jets in active galactic nuclei*, *ApJ* **449**, 19-21, 1995.

[14] J. M. Marti, E. Müller, J. A. Font, J. M. Ibáñez and Marquina *Morphology and dynamics of relativistic jets*, *ApJ* **479**, 151-163, 1997.

[15] M. Böttcher and C. Dermer *Timing signatures of the internal-shock model for blazars*, *ApJ* **711**, 445-460, 2010.

Emission modelling of numerical hydrodynamical simulations with application to active galactic nuclei jets

IP van der Westhuizen, B van Soelen and PJ Meintjes

Department of Physics, University of the Free State, Bloemfontein, 9301, SA

E-mail: vanderwesthuizenip@ufs.ac.za

Abstract. Active Galactic Nuclei, such as quasars and blazars, are highly variable over intra-day to year time scales. The regions that produce this variability have been the topic of many recent studies, especially in the investigation of correlation between multi-wavelength components from radio to gamma-rays. In this study a simulation is presented of an idealistic relativistic hydrodynamical jet propagating through a uniform background medium. This simulation is created with the use of the numerical code PLUTO ver 4.2 which uses high resolution shock capturing algorithms to evolve the fluid dynamic partial differential equations with time. In order to investigate possible causes of variable emission in the simulation a post processing emission code is developed to compute intensity maps of the hydrodynamic computational environment. The code is designed to model the synchrotron self-absorption spectrum in the radio regime for each cell. This emission is calculated using the emission and absorption coefficients, which are then integrated along a fixed line of sight to produce simulated intensity maps of the relativistic jet. Using the intensity maps we can investigate regions of variable emission as well as the respective time scales on which they occur. In this paper we present the initial results and intensity maps produced by the emission code as well as the planned future development of the project. The tools which are being developed for this hydrodynamic model can be applied to a range of other transient sources, such as X-ray and γ-ray binaries, to investigate the different emission components produced by such sources.

1. Introduction

Observational studies of jets from Active Galactic Nuclei (AGN) have revealed a complex system of both stationary and moving emission regions inside AGN sources [1]. These emission regions have been associated with shock fronts inside the relativistic jet and produce variability on both short, intra-day, as well as longer time-scales. AGN sources emit radiation over a wide range of the electromagnetic spectrum, from radio to gamma rays, with low energy region of the spectrum being dominated by synchrotron radiation produced by relativistic electrons inside the jet [2].

In order to investigate the production and propagation of shock fronts and other structures inside highly relativistic jets that may lead to the observed characteristics many studies have turned to numerical simulations using fluid dynamics to evolve jet-like environments with time [3]. Such simulations have revealed complex interaction between the relativistic jet material and the surrounding medium as well as the internal structure [4, 5]. The physical characteristics, such as the density, velocity and pressure, calculated by hydrodynamic simulations are, however, not directly related to the emission we receive from these sources. In order to produce emission

Table 1. Variables used in the set up of the initial conditions for the preliminary RHD jet simulation.

Parameter		Value (arbitrary units)
Lorentz factor	Γ	10
Density ratio	η	10^{-3}
Jet density	ρ_b	0.1
Ambient density	ρ_{am}	100
Mach number	M_b	3.0
Adiabatic index	γ_{ad}	5/3

maps from the numerical simulations, that are comparable to observational data, the emission mechanisms of such sources as well as the relativistic effects must be taken into account [2].

In this paper we present the results of ideal numerical hydrodynamic simulations of a relativistic jet evolved using the PLUTO opensource code. We also present intensity maps calculated by a radiative code which computes emission based on properties of each computational cell and integrates the calculated emission along a user defined line of sight. In section 2 we will discuss the numerical environment used to run the relativistic hydrodynamic (RHD) simulations, while section 3 will focus on the emission modelling of these simulations. Section 4 summarizes the current results followed by a conclusion in section 5.

2. Numerical simulation of relativistic outflows

A RHD simulation of an AGN jet can be achieved by setting up a fluid environment on a structured mesh grid. On this mesh grid each cell has specified quantities, such as density, pressure and velocity, to characterize the fluid and the environment can then be evolved with time by numerically solving the fluid dynamical conservation equations. In this study we considered an ideal relativistic outflow, with no viscosity, injected into a uniform medium. For this simulation the magnetic field was considered to be dynamically unimportant and we, therefore, chose a purely relativistic hydrodynamic solver. To calculate the internal energy density of the fluid the ideal caloric equation of state was used,

$$e = \frac{p}{\rho(\gamma_{ad} - 1)}, \tag{1}$$

where e is the internal energy of the fluid and $\gamma_{ad} = C_p/C_v$ is the adiabatic index [5].

The 3D environment of the simulation was set up on a Cartesian mesh grid consisting of $64 \times 64 \times 64$ length units. The units of the simulation was chosen as arbitrary to avoid large truncation errors, which may occur if the computed values are very small. Initially a uniform rest background medium was assigned to the grid, while a nozzle was defined on the $z = 0$ boundary to inject relativistic outflow material into the computational domain. The radius of the nozzle was set to 1 length unit and less dense jet material was injected at a steady rate with $\Gamma = 10$. The density of the injected material was normalized such that $\Gamma\rho_{jet} = 1$. For the environment we assumed a pressure matched (PM) model to collimate the outflow material. The pressure of the medium was chosen such that the injected material was supersonic. A complete list of the initial parameters for the simulation is given in table 1. The environment was evolved numerically with time using PLUTO *ver 4.2* Opensource code [6]. This grid base code is designed for supersonic flows containing contact discontinuities and uses high resolution shock capturing schemes. The code was set up to use piecewise parabolic interpolation along

with the HLLC Riemann solver [7] and characteristic trace time stepping. The simulation was run on the UFS high performance cluster (HPC) at a resolution of 8 points per unit length.

3. Post-processing emission modelling

In order to produce emission maps of the numerically simulated environment post-processing emission modelling code is being designed in the Python programming language. The code determines the synchrotron emission (j_v^{sy}) and absorption (α_v^{sy}) coefficients for each cell based on a delta-approximation model [8], given by

$$j_\nu^{sy} = \frac{4}{9}\left(\frac{q^2}{mc^2}\right)^2 u_B \nu^{\frac{1}{2}} \nu_0^{\frac{-3}{2}} n\left(\sqrt{\frac{\nu}{\nu_0}}\right), \tag{2}$$

$$\alpha_\nu^{sy} = \frac{2}{9}\frac{p+2}{m\nu^2}\left(\frac{q^2}{mc^2}\right)^2 u_B \nu_0^{-1} n\left(\sqrt{\frac{\nu}{\nu_0}}\right), \tag{3}$$

where,

$$\nu_0 = \frac{3qB}{4\pi mc} \tag{4}$$

Here q is the charge of the radiating particle (assumed to be electrons), m is the mass of the radiating particle, c is the speed of light, u_B is the magnetic field energy density, ν is the frequency in the co-moving frame and $n(\gamma)$ is the particle spectrum [2]. To calculate the coefficients it was assumed that the jet material had a power law particle distribution with spectral index $p = 2$. The magnetic field energy density was assumed to be proportional to the energy density of the fluid with,

$$u_b = \epsilon_B e \tag{5}$$

where $\epsilon_B = 10^{-3}$ is the B-field equipartition parameter based on [9].

Next the code transforms the coefficients from the co-moving frame to an observer frame with regards to the user defined angle as,

$$j_\nu^{sy} = \frac{j_\nu^{sy'}}{(\Gamma[1-\beta\cos(\psi)])^2}, \tag{6}$$

where j_ν^{sy} is the emission coefficient in the observer frame, $j_\nu^{sy'}$ is the emission coefficient in the co-moving frame, Γ is the Lorentz factor, β the magnitude of the velocity in units of c and $\cos(\psi)$ is the angle between the observer and the velocity of the fluid.

The post-processing code finally determines the change in intensity dI_ν for each cell following

$$\frac{dI_\nu}{ds} = j_\nu^{sy} - \alpha_\nu^{sy} I_\nu, \tag{7}$$

and integrates this change along a user defined line of sight to produce a 2D intensity map. This is illustrated in figure 1.

4. Results

The simulation was run until the head of the outflow crossed the computational domain. figure 2 displays 2D slices of the xz-plane at the origin, showing the density, pressure and velocity distributions. From these results we note that the outflow remains collimated and highly relativistic throughout the simulation similar to the simulations produced by [4, 5].

Figure 3 displays the calculate intensity maps for three different angles with regards to the propagation direction of the jet. The emission was calculate for a frequency of 12 GHz in the

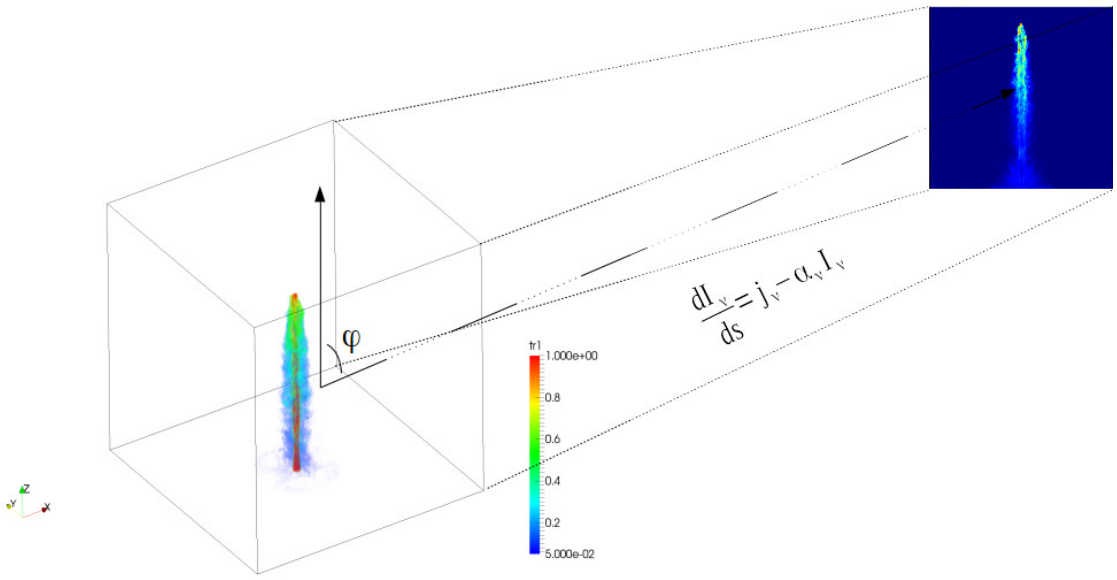

Figure 1. To obtain intensity maps of the emission produced inside a relativistic jet simulation, the 3D environment (in this image a rendering of the trace of jet material showing internal energy density) is projected onto a 2D image by integrating the change in intensity for each cell along a line of sight.

observer frame. In these figures we note that the bow wave structure seen in the density and pressure plots has negligible emission compared to the other structures of the jet. Both the cocoon and the relativistic beam of the jet are initially faint, but increases in brightness with an increase in the z direction closer to the head of the jet. The emission map is dominated by emission at the working surface as well as hotspot regions on the boundary of the relativistic beam. We also note the occurrence of individual asymmetric emission regions close to the head of the jet.

As the viewing angle, ψ, changes from edge on ($\psi = 90°$) to head-on ($\psi = 0°$) the maximum intensity increases due to Doppler boosting of the fluid moving toward the observer. For example the hotspot regions present in the edge on system are less prominent at a $\phi = -30°$. This indicates that these regions are located in the cocoon of the jet and are moving at lower velocities compared to the relativistic beam. For the head-on system we obtain a ring type structure with emission of an order of magnitude larger than the edge on system. The origin of the ring structure is still unknown and further investigation is required to rule out all numerical effects.

5. Discussion and conclusions

A 3D numerical simulation of a relativistic outflow was created and evolved with time using the PLUTO code. The simulation shows a collimated central beam with little deceleration surrounded by an outer cocoon. Intensity maps were computed for the simulation at 12 GHz with a delta approximated synchrotron model. The formation of individual asymmetric emission regions was shown for steady injection model. This suggests that bright emission components can form and propagate in AGN jets without the presence of perturbations in the injection of the outflow. Using these results we will be able to study the propagation of these emission regions further and compare the results to observational data such as [1]. The emission code is still under development with continuous testing and optimization. Future improvements include the addition of a high energy component through an inverse-Compton model, SED modelling, including time of arrival effects and flux calculations. Jet like outflows have been associated with

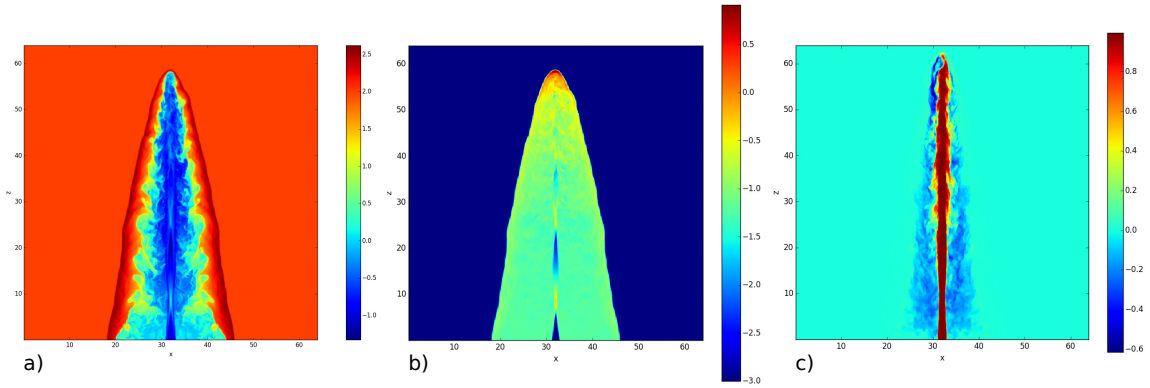

Figure 2. Two dimensional visualizations of the simulation through the xz-plane of the jet, showing a) the density, b) the pressure and c) the velocity component in the z direction. Logarithmic scales are shown for the density and pressure plots in arbitrary units, while the velocity plots have a linear scaling in units of c.

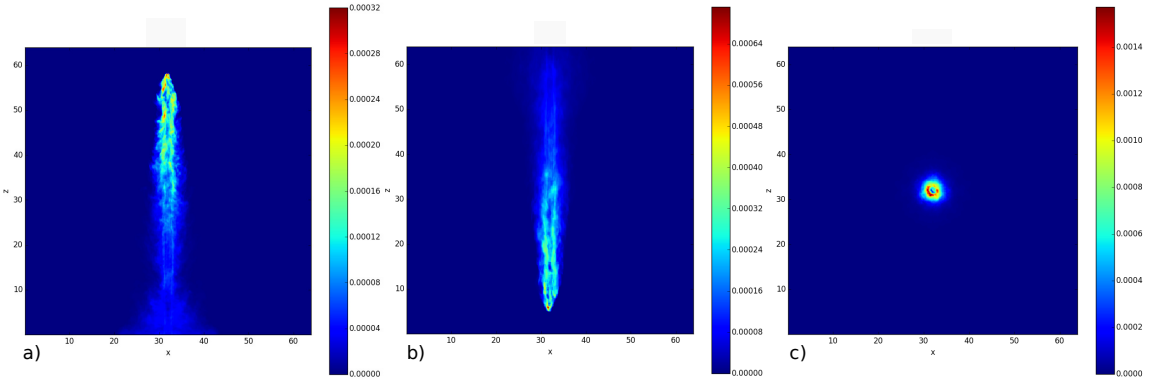

Figure 3. Intensity maps calculated at 12 GHz for different viewing angles a) $\psi = 90°$ b) $\psi = -30°$ c) $\psi = 0°$

many sources such as micro-quasars, young stellar objects (YSO), gamma-ray bursts (GRB's) and X-ray binaries. The code being developed for this project can be applied to these source in future studies.

References

[1] Lister M L, *et al.* 2009 MOJAVE: Monitoring of jets in active galactic nuclei with VLBA experiments. V. Multi-epoch VLBA images *ApJ* **137** 37183729

[2] Böttcher M 2011 Modeling the spectral energy distributions and variability of blazars *2011 Fermi & Jansky: Our Evolving Understanding of AGN* (*preprint arXiv:1205.0539*)

[3] Toro E F 2009 *Riemann Solvers and Numerical Methods for Fluid Dynamics: A Practical Introduction Third Edition* (Berlin: Springer) Chapter 1 pp 1-40

[4] Rossi P, Mignone A, Bodo G, Massaglia S and Ferrari A 2008 Formation of dynamical structures in relativistic jets: the FRI case *A&A* **488** 795-806

[5] Marti J M, Müller E, Font J A, Ibáñez J M and Marquina 1997 Morphology and dynamics of relativistic jets *ApJ* **479** 151-163

[6] Mignone A, Bodo G, Massaglia S, Matsakos T, Tesileanu O, Zanni C and Ferrari A 2007 PLUTO: a numerical code for computational astrophysics *ApJ* **170** 228-42

[7] Mignone A and Bodo G 2006 An HLLC Riemann solver for relativistic flows - II. Magnetohydrodynamics *MNRAS* **368** 1040-54
[8] Böttcher M, Harris D E and Krawczynski H, 2012 *Relativistic Jets from Active Galactic Nuclei*, Weinheim, Germany: Wiley-VCH Verlag GmbH & Co. KGaA Chapter 3 pp 39-80
[9] Böttcher M and Dermer C 2010 Timing signatures of the internal-shock model for blazars *ApJ* **711** 445-460

Simulating the synchrotron emission of AGN with grid based relativistic hydrodynamics

I P van der Westhuizen, B van Soelen and P J Meintjes
Department of Physics, University of the Free State, Bloemfontein, 9301, SA
E-mail: vanderwesthuizenip@ufs.ac.za

Abstract. Grid based numerical hydrodynamic codes have been used to simulate the evolution of a variety of astrophysical environments, ranging from stellar winds to accretion disks in binary systems. These simulations can be used as valuable tools to correlate the theoretical models and observational data. In this study a grid based relativistic hydrodynamic simulation is created, using the freely available numerical code PLUTO ver 4.2, to study possible causes of variability in AGN. The code uses shock-capturing Godunov-type methods to solve the fluid dynamic conservation equations on a structured mesh grid. To simulate the production of a jet similar to those observed in AGN a three dimensional static grid was created containing $256 \times 256 \times 512$ computational cells. A uniform background medium was assigned to this grid, while a nozzle was defined on the $z = 0$ boundary to inject a pressure matched relativistic jet, with $\Gamma = 10$ ($v = 0.995c$), into the medium. The simulation showed the formation of a central collimated relativistic beam along with a surrounding cocoon region. In addition, a post-processing emission modelling code is being developed, in order to determine the emission produced by the relativistic jet. The emission model utilizes the data produced by the hydrodynamic code to calculate intensity maps due to synchrotron self absorption. The emission code takes into account the effects produced by the relativistic motion of the emitting regions (excluding light travel time) which can lead to effects such as the Doppler boosting observed in blazars. Synchrotron based emission models can be applied to other astrophysical objects, such as X-ray binary systems, which means that the application of the emission code can be adapted to model a variety of astrophysical sources.

1. Introduction

Relativistic astrophysical jet-like outflows have been associated with many different sources such as Active Galactic Nuclei (AGN), microquasars and gamma-ray bursts (GRB). In the case of AGN the jets can stretch over Mpc scales, carrying large amounts of energy away from the central engine and producing radiation over a wide range of the electro-magnetic spectrum. The spectral energy distribution of AGN are characterized by a double hump structure consisting of a low energy and a high energy component. The emission in the low energy component is dominated by synchrotron emission from non-thermal electrons, while the high energy component has been modelled by a combination of inverse-Compton and hadronic processes, see for e.g. [1].

Many radio surveys have been undertaken to study the synchrotron emission produced in the relativistic jets and how this relates to their dynamic morphology. For example, the MOJAVE program has studied the movement of superluminal components in AGN as well as the change in ejection direction and precession, over year-long time periods [2].

There are, however, still many unanswered questions about the processes that occur in jets and how they relate to the received emission. Numerical fluid dynamics is a powerful tool to study these dynamic structures. The macroscopic motion of relativistic jets can be described as a fluid and it must, therefore, adhere to the set of partial differential equations which describes the laws of conservation of mass, energy and momentum. By solving the conservation equations numerically, and evolving them with time, we can evolve the jet morphology to future states. This is a good method for investigating the variable nature of relativistic jets.

In order to compare the evolution of structures that are obtained using numerical simulations to the observed variability, we need to determine the synchrotron emission from the physical characteristics of the jet, such as internal energy, magnetic field strength, pressure and density.

In this proceedings we present a numerical simulation of an ideal relativistic jet. In this model the magnetic field was assumed to be dynamically negligible compared to the kinetic energy of the particles. A detailed discussion of the numerical simulation is given in section 2 while the emission modelling follows in section 3. Section 4 contains our results followed by a conclusion in section 5.

2. Numerical models

In hydrodynamical simulations a numerical jet environment is constructed and evolved with time according to the conservation equations of fluid dynamics which can be expressed as

$$\frac{\partial \vec{U}}{\partial t} = -\nabla \cdot \vec{\vec{T}}(\vec{U}) + \vec{\vec{S}}(\vec{U}), \tag{1}$$

where $\vec{U}$ is a column vector consisting of conserved quantities, $\vec{\vec{T}}(\vec{U})$ is a tensor containing the flux vectors as a function of $\vec{U}$, and $\vec{\vec{S}}(\vec{U})$ is a tensor containing source terms that can be used to introduce effects such as viscosity and gravitational forces [3]. Since AGN jets are have a high bulk Lorentz factor it is necessary to perform the simulations in the relativistic hydrodynamic (RHD) regime. In this case, the constituents of equation (1) have the following form:

$$\vec{U} = \begin{bmatrix} \rho\Gamma \\ \rho\Gamma^2 h\mathbf{v} \\ \rho\Gamma^2 h - P \end{bmatrix}, \quad \vec{\vec{T}}(\vec{U}) = \begin{bmatrix} \rho\Gamma\mathbf{v} \\ \rho\Gamma^2 h\mathbf{v}\mathbf{v} + P\mathbf{I} \\ \rho\Gamma^2 h\mathbf{v} \end{bmatrix}, \quad \vec{\vec{S}}(\vec{U}) = 0, \tag{2}$$

where ρ is the proper density, P is the pressure, h is the specific enthalpy, Γ is the Lorentz factor, $\mathbf{I}$ is a 3x3 unit matrix and $\mathbf{v}$ is the three velocity[3].

All other fluid properties, such as the pressure and the internal energy, can be determined from the above mentioned variables [4]. For example, the pressure can be solved by combining the ideal caloric equation of state,

$$e = \frac{P}{\rho(\gamma_{\rm ad} - 1)}, \tag{3}$$

where e is the internal energy density of the fluid, with the definition of the sound speed ($C_s = v/M_b$, M_b representing the Mach number), yielding

$$P = \frac{(\gamma_{\rm ad} - 1)\rho C_s^2}{\gamma_{\rm ad}(\gamma_{\rm ad} - 1 - C_s^2)}. \tag{4}$$

The complex nature of this set of equations (equation 1) makes it impossible to find analytical solutions for these types of environments. We, therefore, need to numerically solve these equations. For this study the numerical hydrodynamical code PLUTO was used to evolve the numerical simulation. PLUTO is a open-source relativistic magnetohydrodynamical code which

Table 1. Parameters used in the set up of the initial conditions.

Parameter		Value (arbitrary units)
Lorentz factor	Γ	10
Velocity	v	$0.995c$
Density ratio	η	10^{-6}
Jet density	ρ_b	0.1
Ambient density	ρ_{am}	10000
Mach number	M_b	7.8
Adiabatic index	γ_{ad}	5/3
Pressure	P	0.001

uses high resolution shock capturing algorithms to solve the conservation equations and evolve them with time [5].

For our simulation we set up a three dimensional Cartesian mesh grid consisting of $256 \times 256 \times 512$ computational cells. The grid was initially assigned a uniform background medium at rest. A nozzle with a radius of 4 computational cells, was created on the $z = 0$ axis at the bottom of the simulation and jet material was injected into the environment at a constant rate. For this simulation the density of the injected jet was chosen to be less than the ambient density ($\eta = \frac{\rho_b}{\rho_{am}} = 10^{-6}$). The simulation was performed using arbitrary units in order to avoid numerical errors. A pressure matched model was used for the simulation in order to help collimate the jet. The parameters used for the simulation were based on previous papers such as [4, 6]. All parameters used in the simulation are listed in table 1.

The simulation was run using the HLLC Riemann solver, piecewise parabolic interpolation and characteristic tracing time stepping [7]. The environment was evolved until the bow shock created by the injection of jet material reached the edge of the computational domain.

3. Synchrotron emission

In order to compare the numerical simulations with the observed emission in radio frequencies we need to translate the three dimensional environment of physical parameters onto a two dimensional image plane. In order to do this we first calculate the synchrotron emission and absorption coefficients for each cell in the simulation, using a post-processing code. In this code we assumed that the electrons inside the jet consist of particles with a power-law energy distribution with the number density, $n(\gamma)$, given by,

$$n(\gamma) = n_0 \gamma^{-p}, \tag{5}$$

where the normalization factor, n_0, is determined by [8]

$$n_0 = \left(\frac{e(p-2)}{1 - C_E^{2-p}} \right)^{p-1} \left(\frac{1 - C_E^{1-p}}{\frac{\rho}{m_p}(p-1)} \right)^{p-2}. \tag{6}$$

Here m_p is the mass of a proton, p is the power-law index and C_E is the ratio of the maximum and minimum energies. For our initial estimates we chose $p = 1.8$ and $C_E = 10^3$. The magnetic field energy density is assumed to be an equipartition fraction of the internal energy density,

$$u_B = \epsilon_B e \tag{7}$$

where $\epsilon_B = 10^{-3}$ based on values fitted by [9].

An analytical delta-approximation model was used to estimate the synchrotron emission (j_v^{sy}) and absorption (α_v^{sy}) coefficients for each cell [10], given by

$$j_\nu^{sy} = \frac{4}{9}\left(\frac{q^2}{mc^2}\right)^2 u_B \nu^{\frac{1}{2}} \nu_0^{\frac{-3}{2}} n\left(\sqrt{\frac{\nu}{\nu_0}}\right), \tag{8}$$

$$\alpha_\nu^{sy} = \frac{2}{9}\frac{p+2}{m\nu^2}\left(\frac{q^2}{mc^2}\right)^2 u_B \nu_0^{-1} n\left(\sqrt{\frac{\nu}{\nu_0}}\right), \tag{9}$$

where,

$$\nu_0 = \frac{3qB}{4\pi mc}, \tag{10}$$

represents the electron gyro-frequency. Here q is the charge and m is the mass of the non-thermal electrons in the jet, c is the speed of light, u_B is the magnetic field energy density given by equation 6 and ν is the frequency of emission in the co-moving frame [1].

Since the jet material is moving at relativistic velocities we need to apply Lorentz transformations to each cell. The synchrotron coefficients of each cell transform as,

$$j_\nu^{sy\prime} = \frac{j_\nu^{sy}}{(\Gamma[1-\beta\mu'])^2}, \tag{11}$$

$$\alpha_\nu^{sy\prime} = \alpha_\nu^{sy}(\Gamma[1-\beta\mu']) \tag{12}$$

where the primed quantities are in the observer frame and the unprimed quantities are in the co-moving frame, β is the magnitude of the velocity in units of c and μ' is the cosine of the angle between the observer and the velocity of the fluid in the observer frame. For our initial calculations additional effects such as the light travel time and the expansion of the universe were neglected.

The post-processing code finally integrates the coefficients along a line of sight, s, defined by an azimuth angle ϕ' and a polar angle θ',

$$I'_\nu = \int (j_\nu^{sy\prime} - \alpha_\nu^{sy\prime} I'_\nu) ds', \tag{13}$$

to create a 2D intensity map.

4. Results

The xz-slices of the density, pressure and velocity distributions for the simulation are shown in figure 1. From these figures we can note five distinct regions in the simulation. First we have the outer uniform ambient medium. A bow wave propagates through this medium due to the injection of the supersonic jet material through the nozzle on the initial z boundary. The bow wave increases the pressure of the medium as it propagates creating a high pressure region between the jet and the ambient medium.

The centre of the jet contains collimated jet material moving at a high Lorentz factor through the environment. Surrounding this collimated beam we find a turbulent backflow of material which is generated as the jet material interacts with the shock front, called the working surface, which forms between the jet material and the ambient medium.

Figure 2 shows 1 dimensional plots of the pressure and density in the z direction along the centre of the beam. We note initial oscillation in both pressure and density. The oscillations indicate the formation of stationary re-collimation shocks. The shocks are caused by the over-pressured cocoon acting on the central beam. These shocks are damped as the jet material

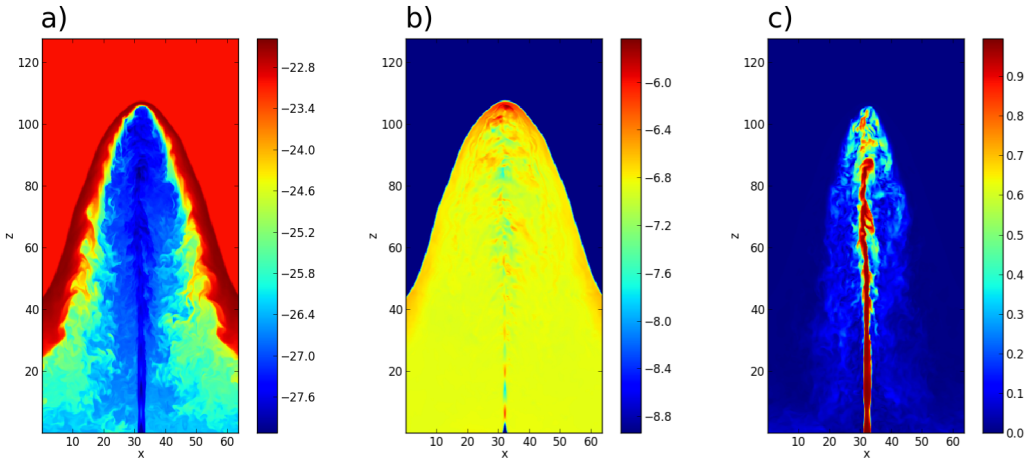

Figure 1. Two dimensional visualizations of the simulation through the xz-plane of the jet, showing a) the density, b) the pressure and c) the velocity component in the z direction. Logarithmic scales are shown for the density and pressure plots in arbitrary units, while the velocity plots have a linear scaling in units of c.

propagates along the z-direction. At larger distances from the injection site turbulence causes the beam of the jet to become unstable. Figure 2 shows this as a rapid change in the density and pressure of the beam. Finally we see a discontinuity in pressure and density at the working surface where the jet material collides with the ambient medium.

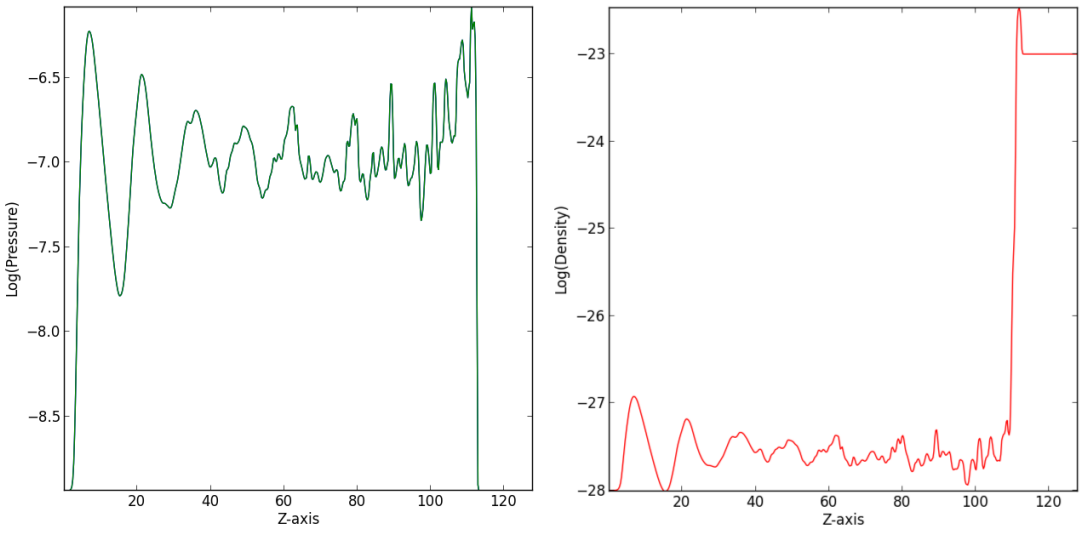

Figure 2. One dimensional plots of the pressure (left) and the density (right) along the central beam.

The emission modelling code was applied to the simulation with a viewing angle of $\psi = 90°$ and $\theta = 90°$. Figure 3 shows 6 sequential frames of the approximated synchrotron emission

at 15 GHz illustrating the time dependence of the main emission regions, or hot spots, in the emission. The hot spot at the head of the jet is shown to change its location, size and maximum intensity. As time progresses we note that the hotspot breaks apart to form several extended emission regions.

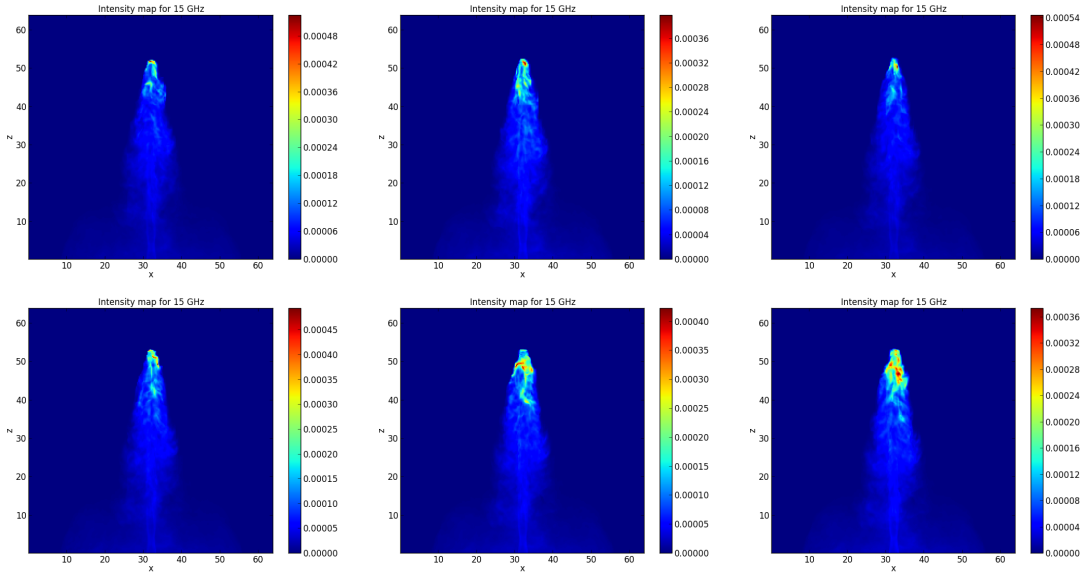

Figure 3. Intensity maps calculated at 15 GHz showing 6 sequential time steps in the numerical simulation.

5. Conclusion

In this paper a numerical model of a relativistic jet was set up and evolved with time using the PLUTO hydrodynamical code. The results showed the formation of a relativistic beam surrounded by a cocoon of backflowing material. Plots of the pressure and density along the central beam revealed the presence of periodic re-collimation shocks within 40 jet radii. Beyond this region the beam becomes turbulent with rapid variations in pressure and density, ending in a shock front at the head of the jet.

A delta-approximation synchrotron model was applied to the simulation to produce a 2D intensity map of an edge-on system. The resulting intensity maps showed time dependent emission regions varying in intensity, position and size. This result indicates that variations in the emission of AGN jets can occur even if the system is fed by a constant injection.

In order to make a precise comparison between the synthetic intensity maps and real observation, however, additional corrections to emission model must be applied for effects such as light travel time and expansion of the universe and radiative losses. The future aim for this project is to include an inverse Compton model into the emission code to investigate the correlation of variability at multi-wavelengths. Based on this we will attempt SED modelling of the simulations in order to produce a better qualitative comparison with observational data. We also plan to include a variable injection rate in the simulation to model how variable injection influences the morphology and stability of the resulting jet. Finally the project can be extended to a much larger scope, including many different astronomical sources such as X-ray binaries and gamma-ray bursts.

Acknowledgments
The financial assistance of the National Research Foundation (NRF) towards this research is hereby acknowledged. Opinions expressed and conclusions arrived at, are those of the author and are not necessarily to be attributed to the NRF.
This work is based on the research supported in part by the National Research Foundation of South Africa for the grant 87919. Any opinion, finding and conclusion or recommendation expressed in this material is that of the authors and the NRF does not accept any liability in this regard.

References

[1] Böttcher M 2011 Modeling the spectral energy distributions and variability of blazars *2011 Fermi & Jansky: Our Evolving Understanding of AGN* (*preprint arXiv:1205.0539*)
[2] Lister M L, *et al.* 2009 MOJAVE: Monitoring of jets in active galactic nuclei with VLBA experiments. V. Multi-epoch VLBA images *ApJ* **137** 37183729
[3] Toro E F 2009 *Riemann Solvers and Numerical Methods for Fluid Dynamics: A Practical Introduction Third Edition* (Berlin: Springer) Chapter 1 pp 1-40
[4] Marti J M, Müller E, Font J A, Ibáñez J M and Marquina 1997 Morphology and dynamics of relativistic jets *ApJ* **479** 151-163
[5] Mignone A, Bodo G, Massaglia S, Matsakos T, Tesileanu O, Zanni C and Ferrari A 2007 PLUTO: a numerical code for computational astrophysics *ApJ* **170** 228-42
[6] Rossi P, Mignone A, Bodo G, Massaglia S and Ferrari A 2008 Formation of dynamical structures in relativistic jets: the FRI case *A&A* **488** 795-806
[7] Mignone A and Bodo G 2006 An HLLC Riemann solver for relativistic flows - II. Magnetohydrodynamics *MNRAS* **368** 1040-54
[8] Gomez J L, Marti J M, Marscher A P, Ibáñez J M and Marcaide J M 1995 Parsec-scale synchrotron emission from hydrodynamic relativistic jets in active galactic nuclei *ApJ* **449** 19-21
[9] Böttcher M and Dermer C 2010 Timing signatures of the internal-shock model for blazars *ApJ* **711** 445-460
[10] Böttcher M, Harris D E and Krawczynski H, 2012 *Relativistic Jets from Active Galactic Nuclei*, Weinheim, Germany: Wiley-VCH Verlag GmbH & Co. KGaA Chapter 3 pp 39-80

PROCEEDINGS OF SCIENCE

Modelling the Synchrotron Emission of AGN with Grid-Based Hydrodynamic Simulations

Izak P. van der Westhuizen*, **Brian van Soelen**, **Petrus J. Meintjes**
Department of Physics, University of the Free State, 9300, Bloemfontein, South Africa
E-mail: VanDerWesthuizenIP@ufs.ac.za, vansoelenb@ufs.ac.za, meintjpj@ufs.ac.za

The spectral energy distributions of AGN have a characteristic double bump structure, with emission at the lower wavelengths being dominated by synchrotron emission from non- thermal electrons in a relativistic jet. In order to investigate possible causes of variability in these systems we model the synchrotron emission from relativistic jets using a 3D hydrodynamic simulation. The simulation was run using the grid based hydrodynamic code PLUTO. The model setup for the simulation consisted of a uniform background medium with less dense jet material injected, at a constant rate, with a Lorentz factor of $\Gamma = 10$. Post-processing calculations were applied to the simulation in order to produce 2D intensity maps at 15 GHz. For this emission we assumed that all of the jet particles had a power-law distribution with no cooling effects. A delta-approximation model was setup to calculate the synchrotron emission and absorption coefficients, and these were then integrated along a user defined line of sight to produce intensity maps. The simulation was evolved until just before the working surface of the jet left the computational domain. The intensity plots show the formation of multiple emission regions at the head of the jet along with a varying intensity.

4th Annual Conference on High Energy Astrophysics in Southern Africa
25-27 August, 2016
Cape Town, South Africa

*Speaker.

1. Introduction

Active galaxies, make up the majority of objects detected in the gamma-ray sky by *Fermi*-LAT [1]. The general properties of these sources can be explained by a unified model that is very dependent on the viewing angle at which the sources are observed. The unified model of active galactic nuclei (AGN) [2] consists of a central super massive black hole (SMBH), surrounded by an accretion disc which powers the emission, beyond which it is surrounded by a dusty torus. The gas which is ionized by the emission from the accretion disc, produces observed broad and narrow emission lines. Sources which are radio loud also produce strong jets, responsible for the non-thermal multi-wavelength emission from radio to TeV gamma-ray energies. Depending on the observing angle of the source, different properties are measured. For example radio loud systems observed close to edge-on are seen as radio galaxies, while for systems where the jet is propagating close to our line of sight, they are observed as blazars. The emission we receive from these objects are dependent on the presence and morphology of a relativistic jet and the angle of observation.

The relativistic jets observed from AGN are highly collimated, and can produce emission over kpc to Mpc scales. In the one-zone model, the non-thermal emission produced from the sources is the result of the acceleration of leptons in the jet in single regions which would cool via synchrotron and inverse Compton scattering. The spectral energy distributions (SEDs) of blazars typically exhibit a double-bump structure, showing a lower (radio to UV/X-ray) and higher (X-ray to gamma-ray) energy component, which can be modelled by these processes (see e.g. [3, 4]). The emission is also highly variable, showing flaring events over all wavelength regimes. However, if the emission was only produced by a single population of electrons this would imply, in the simplest case, that a correlation should exist between the different wavelength regimes. While such correlations are often observed (e.g. [5, 6]) , at other times sources (or the same source) show anti-correlations or flares only at one wavelength (e.g. [7]). This suggests either that there could be multiple zones of emission or that hadronic processes must also be included to explain the higher energy emission (e.g. [8]).

In order to investigate the possible correlation between the lower and higher energy emission in AGN jets we are using relativistic hydrodynamic simulations to model the flow of jets and use these simulations to model the non-thermal emission produced. As a first step we are using the hydrodynamic simulations to model the synchrotron emission from the jet. The hydrodynamic simulations are performed using the PLUTO package [9] while the synchrotron emission is calculated using our post-processing code. The proceedings is structured as follows: in section 2 we briefly summarize the fluid dynamic equations, section 3 describes the setup parameters of the simulation, section 4 summarizes how the synchrotron emission is modelled, the results are presented in section 5 and the final discussion and conclusions in section 6.

2. Fluid dynamics

The flow of the relativistic jet is modelled using relativistic hydrodynamics, under the assumption that on the largest scales this can accurately simulate the bulk motion of the fluid. Within the PLUTO grid-based code the fluid equations are solved and evolved with time following the

Parameter	Value
Lorentz factor (Γ)	10
Jet density (ρ_j)	10^{-1}
Ambient density (ρ_a)	10^4
Pressure (P)	10^{-3}
Mach number	7.8
Adiabatic index (γ_b)	5/3

Table 1: Parameters used in the computational setup of the relativistic jet.

conservation equation [9],

$$\frac{\partial \boldsymbol{U}}{\partial t} = -\nabla \cdot \mathbf{T}(\boldsymbol{U}) + \boldsymbol{S}(\boldsymbol{U}).$$

If the co-moving density is given by ρ, the pressure by P, the enthalpy by h, and the Lorentz factor of the fluid is $\Gamma = (\sqrt{1-|\boldsymbol{v}|^2})^{-1/2}$, (where $\boldsymbol{v}$ is the velocity of the fluid in units of the speed of light), then for relativistic hydrodynamics the conserved variables are given by

$$\boldsymbol{U} = \begin{bmatrix} D \\ \boldsymbol{m} \\ E \end{bmatrix},$$

where $D = \Gamma\rho$, $\boldsymbol{m} = \rho h \Gamma^2 \boldsymbol{v}$, and $E = \rho h \Gamma^2 - P$. The tensor containing the flux terms is given by

$$\mathbf{T}(\boldsymbol{U}) = \begin{bmatrix} D\boldsymbol{v} \\ \boldsymbol{m}\boldsymbol{v} + P\mathbf{I} \\ \boldsymbol{m} \end{bmatrix}^T,$$

where $\mathbf{I}$ is the unit tensor. The final term, $\boldsymbol{S}(\boldsymbol{U})$ contains any sources terms (e.g. gravity); in our simulation we do not include any source terms so in this case $\boldsymbol{S}(\boldsymbol{U}) = 0$.

3. Computational setup

The computational calculations were performed on a three dimensional computational grid of size $64 \times 64 \times 128$ unit lengths (with a computational resolution of 4 points per unit length). All calculations were performed using arbitrary units to avoid computational errors, except for velocity which is given as a fraction of the speed of light.

The simulation was initialized with a uniform stationary medium, and the jet was injected at the centre of the base of the simulation, at $(32, 32, 0)$, at a constant rate with a Lorentz factor of 10, through a nozzle of radius 1. The density ratio between the jet and ambient medium was $\eta = 10^{-5}$ and a pressure match jet was used. The simulation parameters are summarized in table. 1.

The simulation was evolved with time using the HLLC Riemann solver [10] with piecewise parabolic interpolation between cells (see e.g. [11] for a general description of Riemann solvers for fluid dynamics). The simulation was evolved until the working surface of the shock left the computational domain.

4. Synchrotron emission modelling

The synchrotron emission from the relativistic hydrodynamic simulation has been estimated using a post-processing PYTHON code which has been implemented to calculate the emission and absorption coefficients in each cell. The projected 2D image for any viewing angle of the simulation is calculated by integrating over defined lines of sight. Currently, the relativistic effects due to the Doppler boosting of the emission as well as the correction between the emitted and received frequencies are correctly taken into account, while the effects due to light travel time as well as correction due to cosmological redshift have not yet been implemented. However, this is sufficient to investigate where the highest emission regions are occuring and how this will change with time. However, light travel effects may alter the morphology of the observed emission as shown by e.g. [12].

In order to determine the synchrotron radiation, the emission and absorption coefficients must be calculated in each cell and this requires a numerical integration over the particle energy. However, to perform this full calculation is very computationally expensive as the coefficients must be calculated 524 288 ($64 \times 64 \times 128$) times for every time step. Therefore, we have calculate the coefficients in the emitted frame using a δ approximation [4],

$$j_\nu^{\mathrm{em}} = \frac{4}{9}\left(\frac{e^2}{m_\mathrm{e}c^2}\right)^2 u_B \nu^{1/2} \nu_0^{-3/2} n_\mathrm{e}\left(\sqrt{\frac{\nu}{\nu_0}}\right),$$

and

$$\alpha_\nu^{\mathrm{em}} = \frac{2}{9}\frac{p+2}{m_\mathrm{e}}\left(\frac{e^2}{m_\mathrm{e}c^2}\right)^2 u_B \nu^{-2} \nu_0^{-1} n_\mathrm{e}\left(\sqrt{\frac{\nu}{\nu_0}}\right),$$

for the emission and absorption coefficients respectively. Here, e and m_e are the charge and mass of an electron respectively, c is the speed of light, $u_B = B^2/8\pi$ is the magnetic energy density for a field B, ν is frequency and

$$\nu_0 = \frac{3eB}{4\pi m_\mathrm{e} c}.$$

Since the relativistic hydrodynamic simulation does not include a magnetic field, the energy density is calculated as a fraction of the internal energy density. The spectrum of the emitting particles is assumed to follow a power-law of the form,

$$n_\mathrm{e}(\gamma) = n_0 \gamma^{-p},$$

where γ is the Lorentz factor of the particles. For this first approximation we have assumed that the particles have an index of $p = 1.8$ and determine the normalization, following [13], as

$$n_0 = \left[\frac{\mathscr{U}(p-2)}{1-C_E^{2-p}}\right]^{p-1}\left[\frac{1-C_E^{1-p}}{\mathscr{N}(p-1)}\right]^{p-2},$$

where C_E is the ratio of the maximum to minimum energy of the electrons, $\mathscr{U}$ is the electron energy density (approximated by a fraction of the internal energy) and $\mathscr{N}$ is the electron number density (approximated by $\mathscr{N} = \rho/m_\mathrm{p}$ where m_p is the proton mass). The internal energy and proper density is calculated from the numerical simulation, and we assume $C_E = 10^3$.

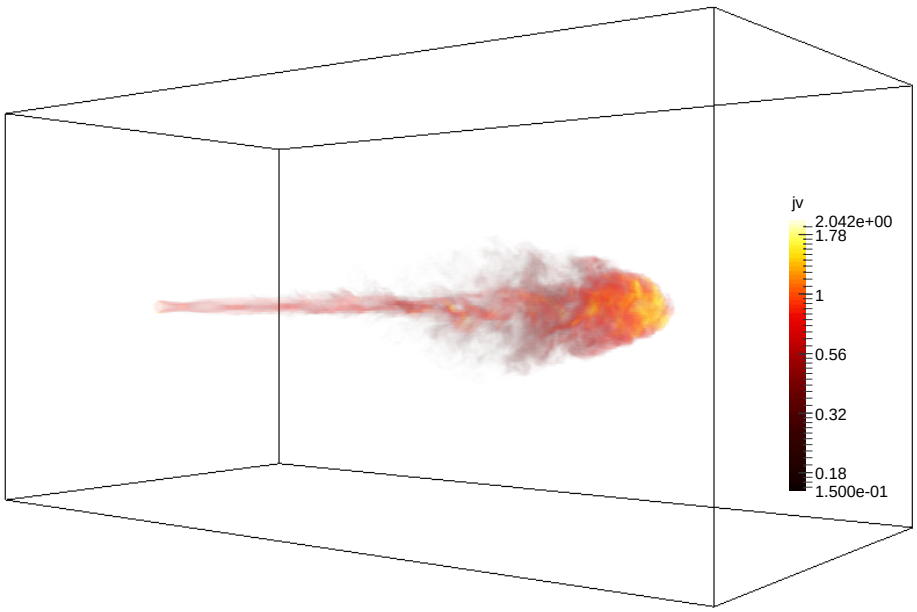

Figure 1: Frame of the three dimension simulation scaled by the co-moving emission coefficient. Please note that the units are arbitrary.

The coefficients are transformed to the observer frame by

$$j_{\nu^{\rm rec}}^{\rm rec} = \delta^2 j_{\nu}^{\rm em},$$

and

$$\alpha_{\nu^{\rm rec}}^{\rm rec} = \alpha_{\nu}^{\rm em}/\delta$$

with

$$\delta = \frac{1}{\Gamma(1-\beta\mu)}$$

where μ is the cosine between the direction of motion of the fluid element and the observer, and β is the speed in units of the speed of light. The change in intensity across a length ds is given by

$$\frac{{\rm d}I_{\nu^{\rm rec}}^{\rm rec}}{{\rm d}s} = j_{\nu^{\rm rec}}^{\rm rec} - \alpha_{\nu^{\rm rec}}^{\rm rec} I_{\nu^{\rm rec}}^{\rm rec}$$

and this is integrated along a user chosen direction to create a two dimension projection.

5. Results

Figure 1 shows a snap shot of the 3D simulation, scaled by the co-moving emission coefficient. This shows the morphology of the jet and the dominance of the emission near the working surface.

Figure 2 shows the 2D projections of the emission from the jet simulation at six equal time steps. This has been calculated for a received frequency of 15 GHz and for a viewing angle which is perpendicular to the direction of the injected jet.

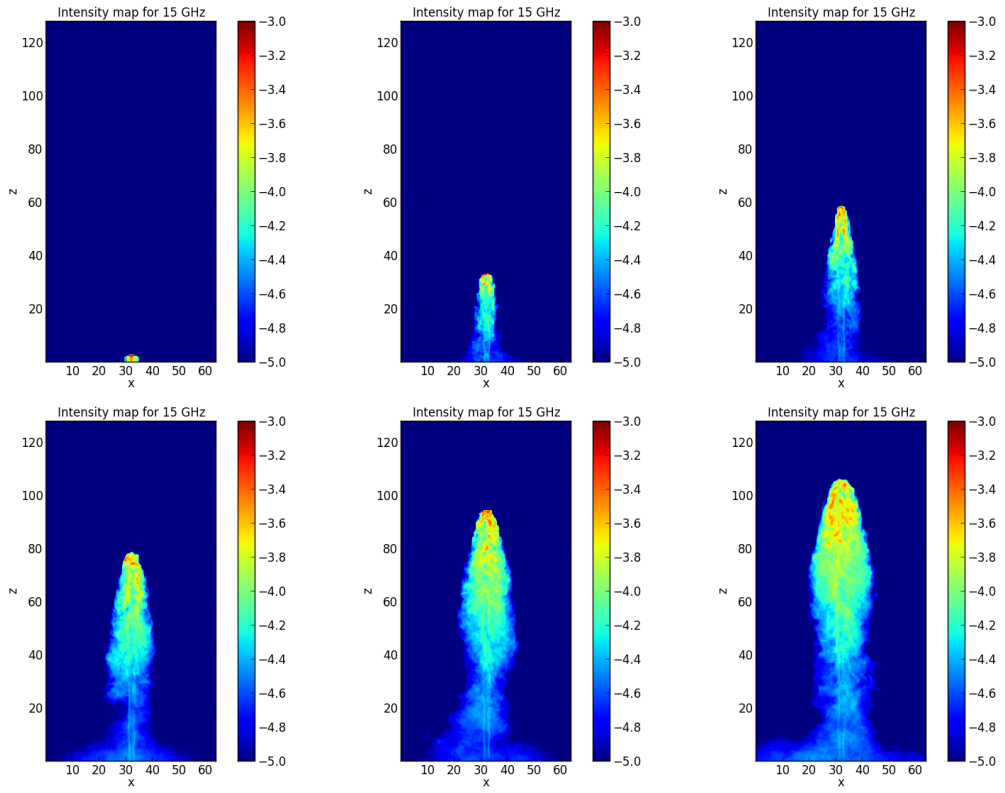

Figure 2: The emission observed from the jet simulation at six equal time steps. The scaling is logarithmic in arbitrary units to highlight the emission regions.

During the initial phase of the jet launch, the jet remains highly symmetrical. The emission is concentrated at the working surface, but is also seen in regions of standing shocks which form in the central beam of the jet. As the working surface propagates through the simulation the distance between the standing shock increases, while the jet remains symmetric.

As the jet continues to propagate through the medium it becomes more turbulent and the jet (and emission) appears less symmetric. While the peak in the emission region remains at the working surface, due to turbulence it is no longer symmetric around the original direction of injection and shifts around. The emission region is also no longer centred at a single location but is more spread out around the jet. The jet fluctuates between periods of lower peak intensity, with multiple "hot-spots" and periods of higher peak intensities which are more focused at the top of the jet.

The growth in turbulence is clearly shown by the variation in the density of the jet. Figure 3 shows the proper density plotted along the central z-axis of the beam (along the initial injection direction) for the same time steps as shown in figure 2. The shock at the working surface, formed by the jet propagating into the ambient medium, shows the progress of the jet through the simulation. The density plots are taken at equal time steps (arbitrary time units) and shows how the propagation speed decreases as the jet moves through the medium, despite a continuous injection. Behind the working surface the standing shocks in the beam, formed due to the pressure difference between the jet beam and ambient medium, are seen as smooth oscillations in the density. The distance between

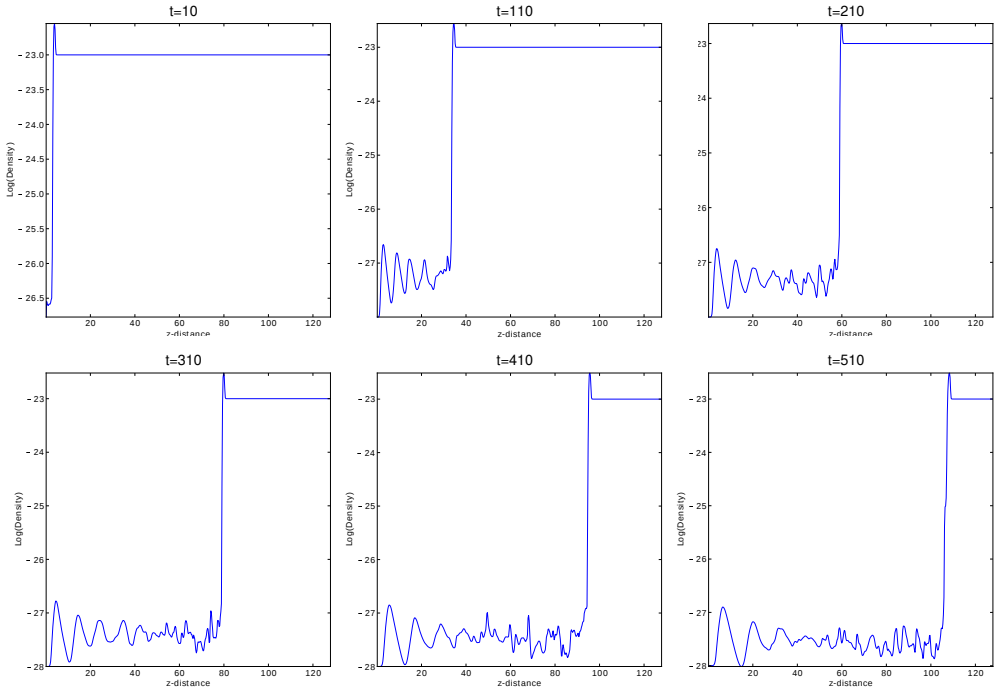

Figure 3: A one dimensional plot of the proper mass density (in arbitrary units) through the central beam of the jet (along the initial injection direction).

the standing shocks increases the further the jet travels and the density shows more turbulence, as is reflected in the emission maps (Fig. 2).

6. Discussion and conclusions

Here we have created an ideal relativistic jet simulation and used a post-processing emission code to produce intensity maps for synchrotron emission. The simulations show that even for this simplified case, of no magnetic field and constant injection the simulation produces variable emission with and changing jet morphology. The morphology of the jet is comparable to an FR II type jet, with the bulk of the emission concentrated at the end of the jet (see [14] for a discussion of forming FR I jets).

The variability observed from AGN is often modelled as the injection of "blobs" into the jet structure. We believe the injection of blob structures into our jet simulation will increase the complication of the simulations and produce more complicated structures.

The simulated emission has been calculated assuming a constant power-law distribution of electrons with an index of $p = 1.8$ that is scaled with with the internal energy density. This first approximation is sufficient to highlight where the emission is most concentrated. This does, however, ignore the effects of cooling in the simulation. In future work we intent to expand the post-processing code to model locations of particle acceleration, due to shocks, as well as the subsequent cooling of the electrons. In addition, here we have only shown the emission at a single frequency

and we intend to expand the post-processing emission code to include inverse Compton scattering to simulated varying SEDs of AGN.

Acknowledgments

This work is based on the research supported by the National Research Foundation (NRF) of South Africa for the grant, No. 87919.

References

[1] F. Acero et al. *Fermi Large Area Telescope Third Source Catalog*, *ApJS* **218** (2015) 23

[2] C.M. Urry, P. Padovani, *Unified Schemes for Radio-Loud Active Galactic Nuclei*, *PASP* **107** (1995) 803

[3] C.D. Dermer and G. Menon *High Energy Radiation from Black Holes: Gamma Rays, Cosmic Rays, and Neutrinos* Princeton Univerisity Press 2009

[4] M. Böttcher, D.E. Harris and H. Krawczynski. (Eds.), *Relativistic Jets from Active Galactic Nuclei* Wiley-VCH 2012

[5] B. Rani et al., *Radio to gamma-ray variability study of blazar S5 0716+714 A&A* **552** (2013) A11

[6] L. Fuhrmann et al., *Detection of significant cm to sub-mm band radio and γ-ray correlated variability in Fermi bright blazars MNRAS* **441**(2014) 1899

[7] M. Błażejowski et al., *A Multiwavelength View of the TeV Blazar Markarian 421: Correlated Variability, Flaring, and Spectral Evolution ApJ* **630** (2005) 130

[8] M. Böttcher et al., *Leptonic and Hadronic Modeling of Fermi-detected Blazars*, *ApJ* **768** (2013) 54

[9] A. Mignone et al., *PLUTO: a numerical code for computational astrophysics*, *ApJS* **170** (2007) 228

[10] A. Mignone and G. Bodo, *An HLLC Riemann solver for relativistic flows - I. Hydrodynamics*, *MNRAS* **364** (2005) 126

[11] E.F. Toro, *Riemann solvers and numerical methods for fluid dynamics : a practical introduction*, Springer, Berlin 2009

[12] M.-Á Aloy et al., *Three-dimensional Simulations of Relativistic Precessing Jets Probing the Structure of Superluminal Sources*, *ApJ* **585** (2003) L109

[13] J.L. Gómez et al., *Parsec-Scale Synchrotron Emission from Hydrodynamic Relativistic Jets in Active Galactic Nuclei*, *ApJ* **449** (1995) L19

[14] S. Massaglia et al., *Making Fanaroff-Riley I radio sources. Numerical Hydrodynamic 3D Simulations of Low Power Jets*, *A&A, in press* [astro-ph/1609.02497]